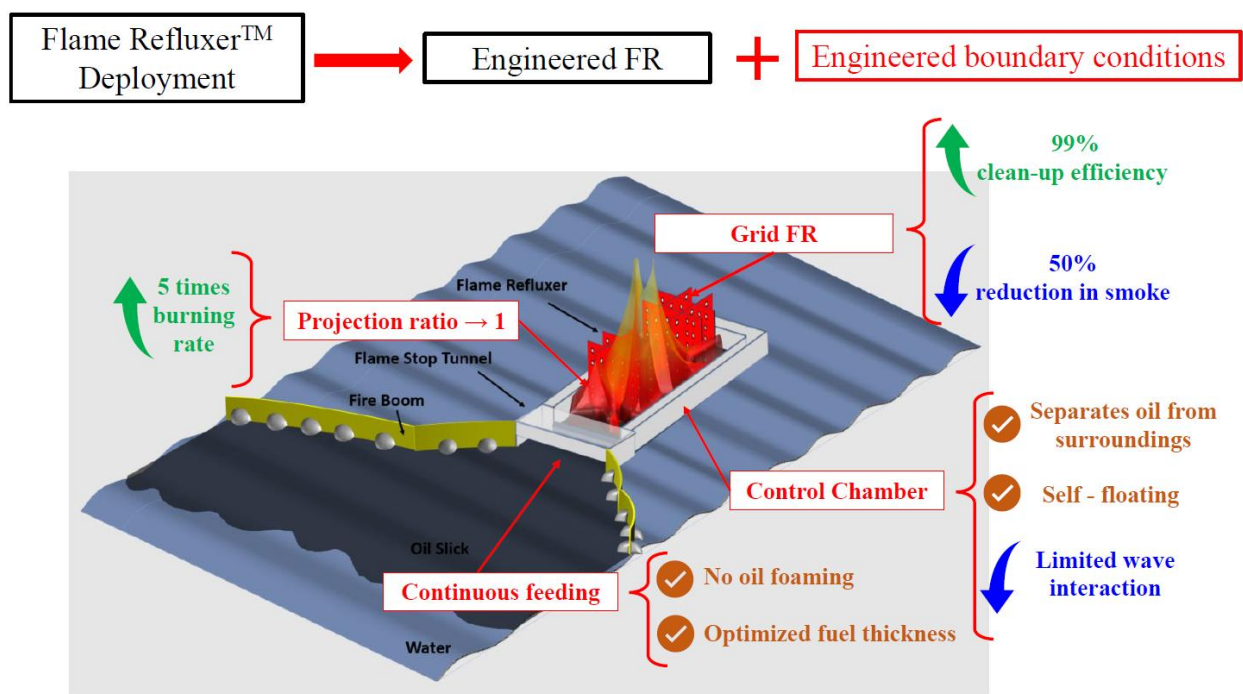


# Bureau of Safety and Environmental Enforcement Oil Spill Preparedness Division Advancing the Maturity of the Flame Refluxer Technology

Final Report

August 2021



(Illustration: WPI, 2021)

Dr. Ali Rangwala, Dr. Kemal Arsava, Nathan G Sauer, Hsin-Hsiu (Matt) Ho, Dr. Sharanya Nair, Glen Mahnken, Mahesh Kottalgi

US Department of the Interior  
Bureau of Safety and Environmental Enforcement  
Oil Spill Preparedness Division



# Advancing the Maturity of the Flame Refluxer Technology

Final Report

OSRR # 1104

August 2021

Authors:

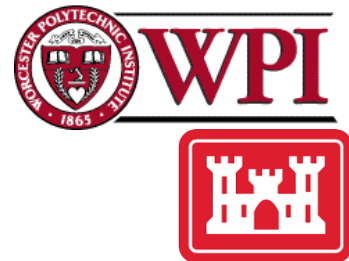
Dr. Ali Rangwala

Worcester Polytechnical Institute

Dr. Kemal Arsava

Cold Regions Research and Engineering

Laboratory (CRREL)



Prepared under **140E0118R0007**

By

Worcester Polytechnical Institute

Department of Fire Protection Engineering

**US Department of the Interior  
Bureau of Safety and Environmental Enforcement  
Oil Spill Preparedness Division**



## DISCLAIMER

Study concept, oversight, and funding were provided by the US Department of the Interior (DOI), Bureau of Safety and Environmental Enforcement (BSEE), Oil Spill Preparedness Division (OSPD), Sterling, VA, under Contract Number **140E0118R0007**. This report has been technically reviewed by BSEE, and it has been approved for publication. The views and conclusions contained in this document are those of the authors and should not be interpreted as representing the opinions or policies of the US Government, nor does mention of trade names or commercial products constitute endorsement or recommendation for use.

## REPORT AVAILABILITY

The PDF file for this report is available through the following sources. Click on the URL and enter the appropriate search term to locate the PDF:

Document Source	Search Term	URL
Bureau of Safety and Environmental Enforcement (BSEE)	Project Number – 1104	<a href="https://www.bsee.gov/what-we-do/research/oil-spill-preparedness/oil-spill-response-research">https://www.bsee.gov/what-we-do/research/oil-spill-preparedness/oil-spill-response-research</a>
U.S. Department of the Interior Library	Advancing the Maturity of the Flame Refluxer Technology	<a href="https://library.doi.gov/uhtbin/cgisirsi/?ps=8L0mpW5uPV/SIRSI/X/60/495/X">https://library.doi.gov/uhtbin/cgisirsi/?ps=8L0mpW5uPV/SIRSI/X/60/495/X</a>
National Technical Reports Library	Advancing the Maturity of the Flame Refluxer Technology	<a href="https://ntrl.ntis.gov/NTRL/">https://ntrl.ntis.gov/NTRL/</a>

Sources: a) BSEE (2019), b) DOI [2021], c) National Technical Information Service (2021)

## CITATION

Rangwala A, Arsava K, Sauer NG, Ho H, Nair S, Mahnkin G, Kattalgi M. 2021. Advancing the maturity of the flame refluxer technology. U.S. Department of the Interior, Bureau of Safety and Environmental Enforcement. Report No.: 1104. Contract No.: 140E0118R0007

## ABOUT THE COVER

Cover image by Worcester Polytechnic Institute (WPI) illustrating conceptual operations of the deployment and burn efficiencies associated with the Flame Refluxer technology.







## **Advancing the Maturity of the Flame Refluxer Technology**

**Contract No. 140E0118R0007**

**Final Report**

**August 15, 2021**

### **WPI Personnel:**

Nathaniel G. Sauer, Hsin-Hsiu (Matt) Ho ,  
Dr. Sharanya Nair, Glen Mahnken, Mahesh Kottalgi

,

Prof. Ali S. Rangwala (PI)

### **Contact Information**

Dr. Ali Rangwala

Worcester Polytechnic  
Institute Department of  
Fire Protection  
Engineering

Phone: (508) 831-6409  
rangwala@wpi.edu

### **CRREL Personnel:**

Dr. Kemal Arsava (Co-PI)

### **BSEE Personnel:**

Karen Stone, Caroline Laikin-Credno

## **Acknowledgements**

This study is funded by the Bureau of Safety and Environmental Enforcement, US Department of the Interior, Washington, D.C., under Contract Number 140E0118R0007. The authors would like to thank Nathan J. Lamie, Brandon K. Booker, Kathryn Trubac, Tyler J. Elliott, William T. (Billy) Burch, and Andrew E. Pohl for their support during large-scale outdoor tests performed at the Cold Regions Research and Engineering Laboratory in Hanover, NH.

Many thanks to the personnel, who made contributions during this study, including:

Albert Simeoni (Department Head of FPE), Raymond T. Ranellone (WPI Fire Laboratory Director), Frederick M. (Fritz) Brokaw (WPI Fire Laboratory Manager), Leonard Zabilansky (Principal Engineer, OMSETT), Dr. Brain k. Gullett (EPA) , Johanna Aurell, Colleen B. Wamback (Public Relations Specialist), Dennis J. Leary, Camden Kulczyk, Adam Saar and Julia M. Cuendet (Undergraduate students), Li Chang, Veronica Kimmerly, Xiaoyue Pi, and Chuming Wei (Graduate students), Dr. Hamed Farahani (Post Doc), Panyawat Tukaew (Sr. Fire Engineer).

## **Disclaimer**

This report has been reviewed by the BSEE and approved for publication. Approval does not signify that the contents necessarily reflect the views and policies of the Bureau, nor does mention of the trade names or commercial products constitute endorsement or recommendation for use.

## 1. Project Overview

This study aims to advance the Flame Refluxer™ technology developed under Contract No: E15PC000004 and E14PC00043 to a maturity level ready for commercialization. The specific objectives were:

1. Determine the optimum material and geometry of FR.
2. Design a new collector for easy storage/deployment.
3. Design, construct and develop a self-floating FR.
4. Perform field trials at CREEL to test the burning and deployment efficiencies in waves.

Answering these questions advanced the FR technology currently at TRL 6 (full-scale technology demonstrated in relevant environments) to TRL 8 (final integrated system tested in real or relevant environment). Worcester Polytechnic Institute (WPI) designed and conducted scaled experiments to evaluate controlling parameters, such as float arrangement, material, and shape. Large-scale burns with the presence of waves were a collaborative study with the United States Army Corps of Engineers, Cold Region Research and Engineering Laboratory (CRREL).

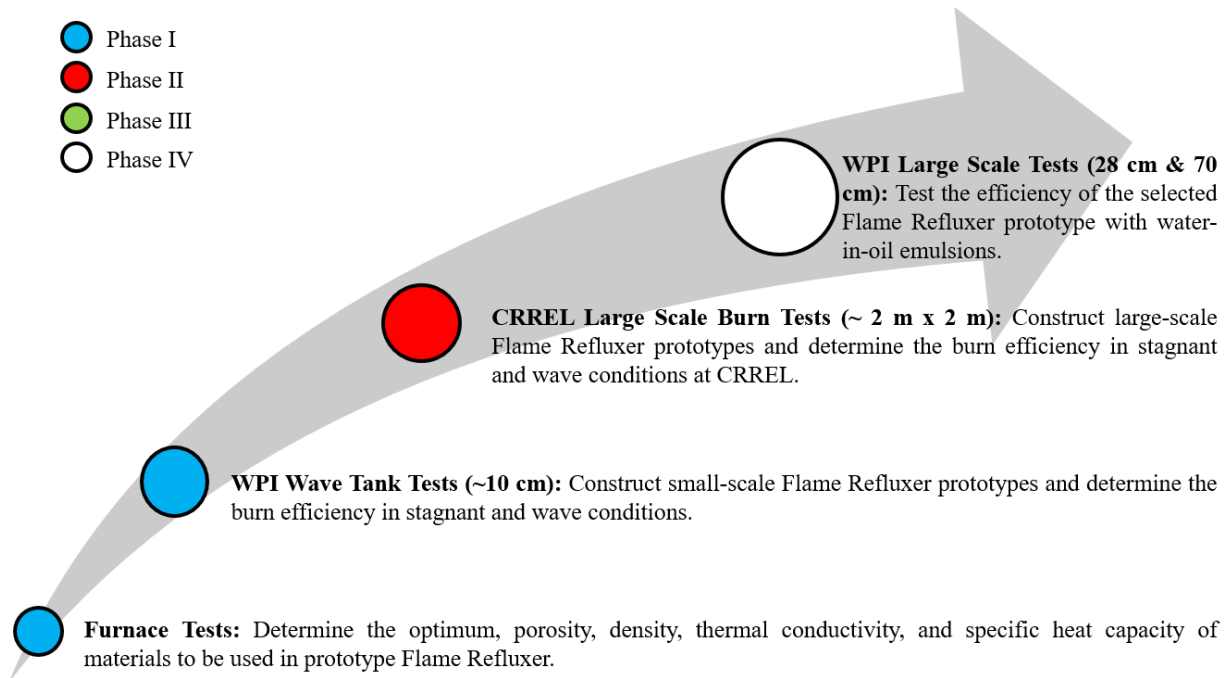
Figure 1 shows the progression of three phases of experimental testing that was adopted in this study:

**Phase I-a:** Initial tests were performed in a bench-scale furnace to identify the optimal material for the FR such that it increases nucleate boiling to promote enhanced burning efficiency and can extend the sustained burning time by retaining heat long enough to fully burn an oil slick.

**Phase I -b:** Phase I-a results were used to design and manufacture the small-scale FR prototypes. The efficiency of FR prototypes was tested in small-scale wave tank experiments of 10 cm diameter at the WPI Combustion Laboratory. The main objective of Phase I was to determine the most efficient FR prototypes and engineer a new float system. Manufacturing the large-scale prototypes started in this phase.

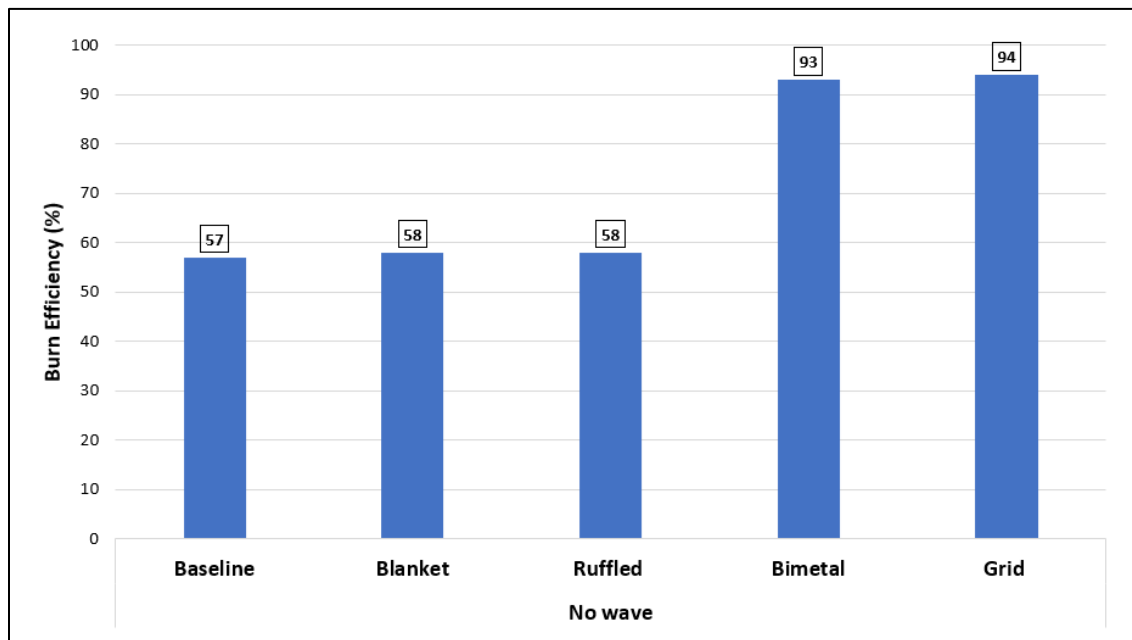
**Phase II:** Deployment of the self-floating FRs at large-scale (1.9 m x 1.7 m) was tested at the US Army Cold Region Research and Engineering Laboratory (CRREL) outdoor wave tank test facility in Hanover, NH (12 m long, 2.4 m wide, and 2.25m deep tank).

**Phase III:** Phase II experiments results were used to design intermediate-scale burn at WPI Fire Science. The main objective of the experiments was to determine the role of fuel thickness, FR placement, and the effect of the projection ratio on the overall efficiency.



**Figure 1- Experiments at small, intermediate, and large-scale**

The experimental results showed that the heat generated by the combustion and directed back to the fuel significantly enhanced the regression rate while reducing smoke emission. In Phase, I (WPI Wave Tank Tests), the regression rate of the fuel (ANS crude oil) was enhanced by 100% with Grid FR, respectively.



**Figure 2 - Phase II - Burn efficiency of FR prototypes with HOOPS crude oil under the no-wave condition**

Phase II tests were performed in the field and resulted in three major outcomes.

The first outcome of Phase II tests was the significant increase in burn efficiency achieved with the Grid FR system as shown in Fig. 2. The burn efficiency was reached 94% at two Grid FRs placed in the hoops crude oil slick. Baseline burn efficiency was measured as 57%.

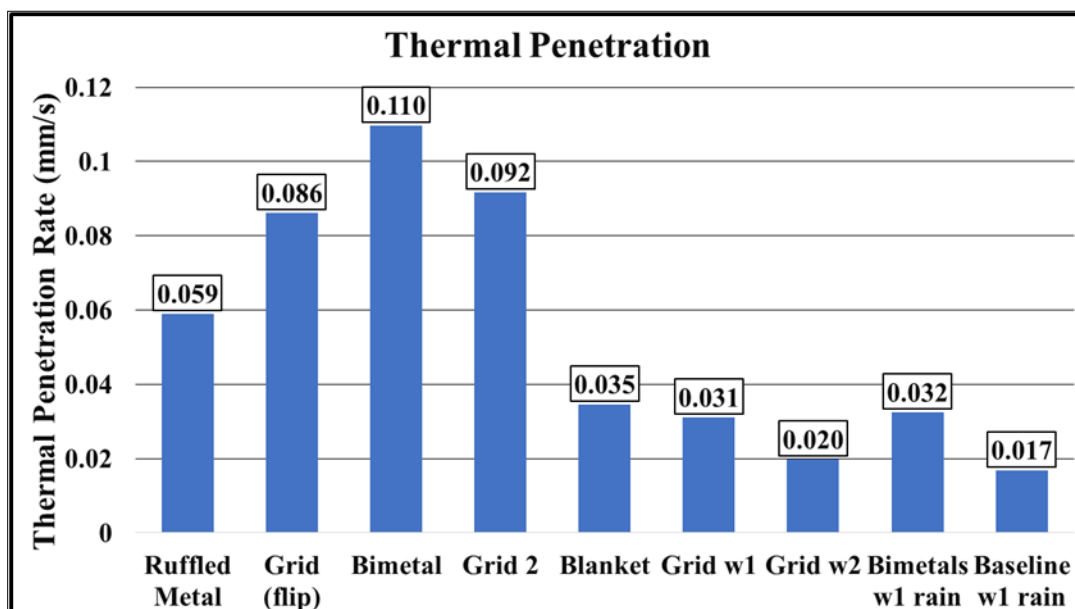


Figure 3 - Thermal penetration rates for FR cases in Phase II

The second outcome, the increase of thermal penetration rate in fuel using the FR, is shown in Fig. 3. The bimetals and grid FR cases demonstrated the highest thermal penetration rate, while the ruffle and blanket FR struggled to reach as high values. The waves reduced the thermal penetration of the grid.

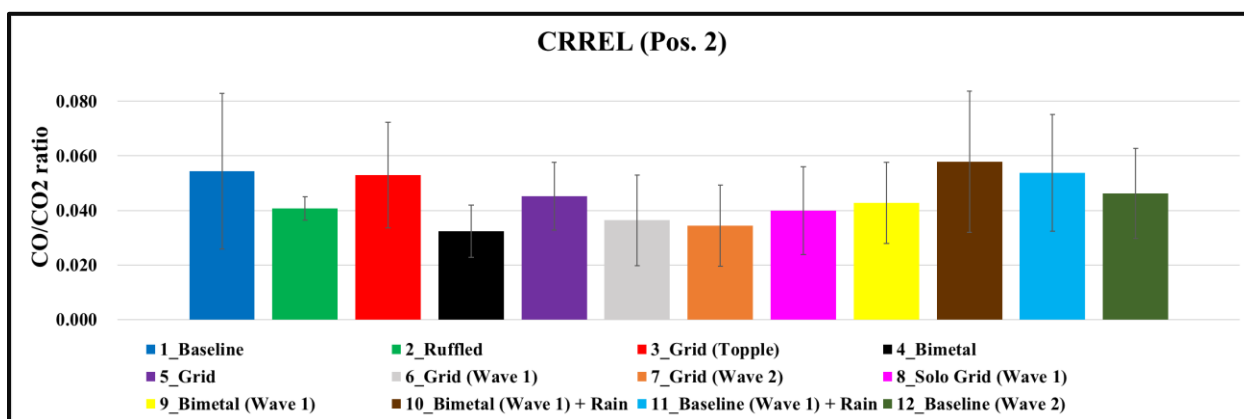


Figure 4 - Phase II – Average CO/CO2 comparison for HOOPS cases sampled at Pos. 2.

The third outcome is the reduction in CO/CO<sub>2</sub> shown in Fig. 4. The cleaner combustion was also observed visually. Figure 5 compares the smoke plume in the steady-state burning regime for the baseline and grid FR cases.



**Figure 5 - Phase II – Smoke visualization of grid FR and baseline case with wave 1**

Figure 5 clearly shows that the color of the smoke plume is much lighter for the Grid FR case. The lighter color of the smoke indicates a reduction in the concentration of carbon particles due to more complete combustion.

In Phase III (WPI large-scale), Flame Refluxers<sup>TM</sup> Rack + Rods enhanced the burning rate by 4.2x and reduced the CO/CO<sub>2</sub> by 50% for a 9 cm crude oil slick on the water layer.

## **2. Phase I - Small Scale experiment (WPI)**

### **Objectives**

The objective of Phase I was to engineer a self-floating FR with an optimum burn efficiency. First, the optimum material and geometry were determined by bench-scale furnace experiments (Phase I-a). Various controlling parameters (density, specific heat, and thermal conductivity) were examined to evaluate materials for their ability to promote nucleate boiling, retain heat, withstand rapid heating and cooling, and enhance the burning efficiency of a pool fire. Bench-scale furnace experiments were performed to determine the most desirable material for the prototype FR, which heats quickly, stores a good amount of heat energy, and dissipates heat at a predetermined temperature. Based on the experimental data, small-scale FR prototypes were manufactured and tested in a small-scale (5 cm x 5 cm) ethanol pool fire and a new Heat Flux experimental setup. The experimental data guided the Phase I-b tests. The burning efficiency of FR prototypes was tested in small-scale (10 cm diameter) crude oil pool fire at the WPI combustion laboratory. Small-scale prototypes were tested under stagnant and wave conditions. Results were used to design and manufacture the large-scale FR prototypes and floatation in Phase II.

This section explains the experimental and numerical study performed in Phase I-a and I-b in detail.

### **Phase I a - Small Scale Furnace Experiments**

The objective of Phase I-a is to determine the optimum materials and geometry for the construction of the small-scale prototype floating Flame Refluxer (FR). Several controlling parameters (density, specific heat, and thermal conductivity) are examined to evaluate materials for their ability to promote nucleate boiling, retain heat, withstand rapid heating and cooling, and enhance the burning efficiency of a pool fire.

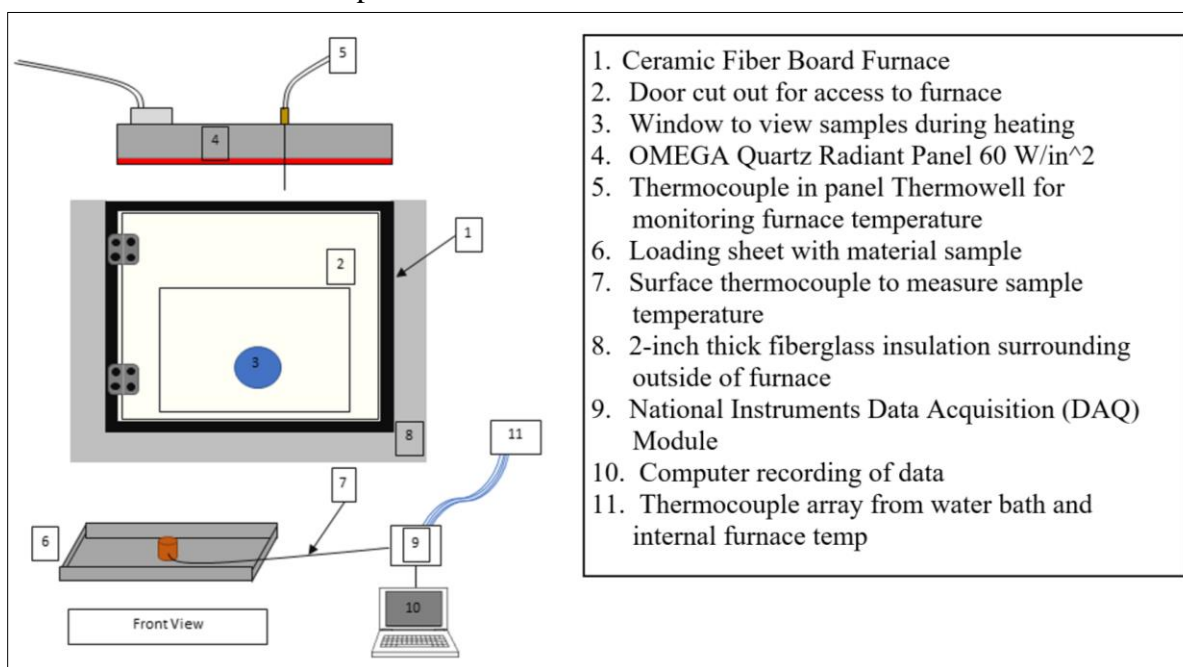
An efficient FR should be able to collect heat from the flame as fast as possible (high heat transfer rates in the gas phase) and dissipate the heat to crude oil slowly in the beginning (high heat retention) but rapidly once the temperature of the immersed portion reaches an optimum temperature range for nucleate boiling. For example, during the field-scale experiments in Mobile, AL (E15PC000004) optimum performance (6 times baseline efficiency) was reached when the temperature of the immersed blanket was in the range of 30- 40 °C above the boiling point of crude oil used (HOOPS). For field deployment, the selection of both the collector and heater components of the FR thus requires careful analysis. The experiments performed in the current phase are a first attempt in providing a universal experimental platform for testing materials for FR design. The experimental platform can also be used for other applications for example fire boom designs where the objectives are resilience and insulation.

This section presents the experimental results from Phase I-a including temperature vs. time profiles, analysis of material thermal integrity, and heat retention capability of samples. 114 small-scale furnace experiments (19 materials, 6 experiments each) were performed with materials of various thermophysical properties, geometries, and porosities. Results show that the porosity of

the material is one of the dominating parameters controlling the heat and mass transfer with respect to FR performance. Quantification of the porosity as a function of gas-phase heat transfer, liquid phase nucleate boiling, and overall heat retention capability is the fundamental knowledge gap with respect to FR design moving forward. Phase I-a is designed to address this knowledge gap.

## Experimental Setup

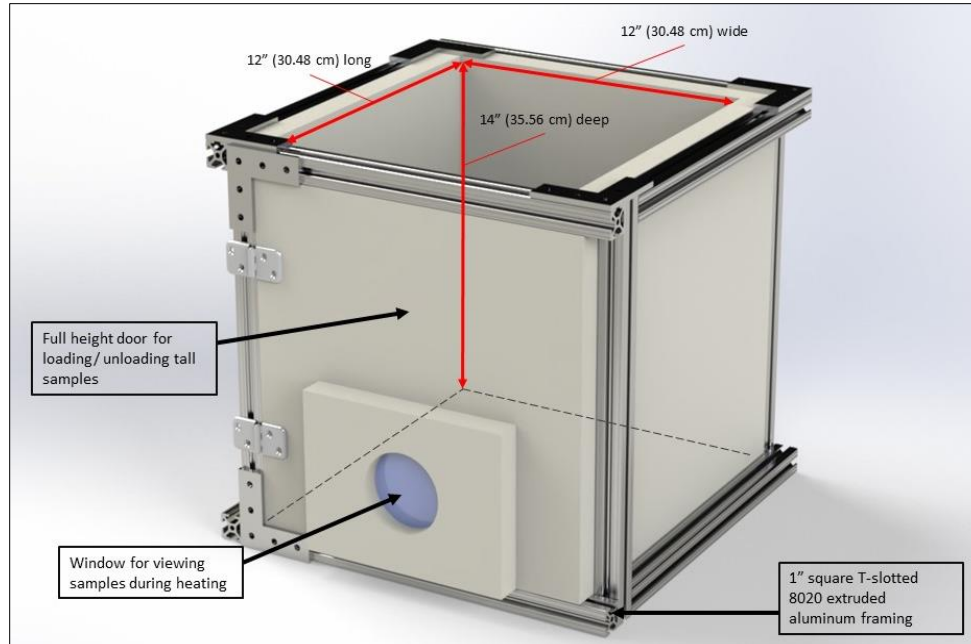
The experimental setup for Phase I-a consists of an electric radiant heat source (OMEGA QH-121260-T panel) and a furnace housing to retain the heat energy (Fig. 6). The radiant panel is 30 cm (12") wide by 30 cm (12") across and 7.5 cm (3") tall (Fig.6). The OMEGA panel is controlled using a Solaira SHP high power heat controller; a phase-angle firing solid-state relay process controller for electric heaters. This combination allows for the precise management of the power to the heater and thus the temperature inside the furnace.



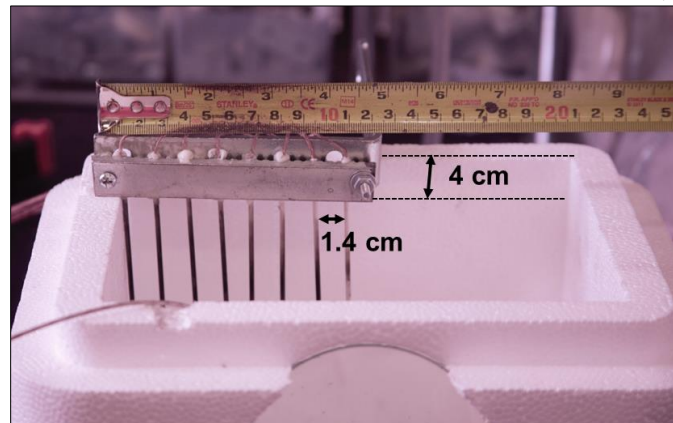
**Figure 6 - Experimental platform and components used in the setup - Phase Ia**

The furnace was constructed of 2.5 cm (1") thick high-temperature ceramic fiberboard insulation (Fig. 7). The internal dimensions of the furnace are 30 cm (12") wide by 30 cm (12") deep by 35 cm (14") tall. With the radiant panel inserted the internal available height is 28.5 cm (11.25"). The ceramic fiberboard insulation and radiant panel were supported by a frame made of 2.5 cm (1") square T-slotted 80/20 aluminum extrusions.





**Figure 7 - Isometric model of the furnace used in Phase I-a (furnace tests)**



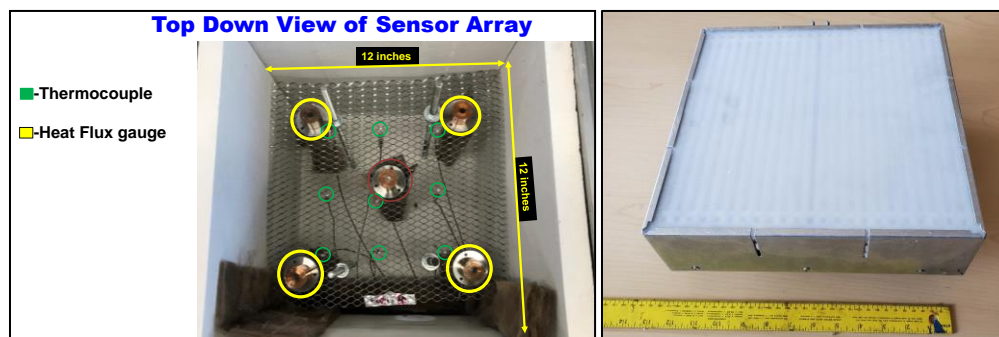
**Figure 8 - Water bath thermocouple arrangement in the ambient water-cooling station**

The ambient air-cooling station consists of a sheet of the same ceramic fiberboard insulation, onto which the samples were placed while the temperature of the sample was recorded for the duration of air cooling. The fiberboard insulation was selected due to its low thermal conductivity. The water-cooling station consists of a 3.7 Liter (1 gallon) expanded polystyrene container, selected for polystyrene's low thermal conductivity and ability to hold water without any absorption (Fig. 8). The temperature of the water-cooling bath was measured using an array of 8 thermocouples (K-Type, AWG 31, 0.0023 mm dia.) held in equal spacing (1.4 cm) by a metal bracket shown in fig. 8. Data acquisition was accomplished using National Instruments Data Acquisition (DAQ) boxes and accompanying LabView software to record data directly to a monitoring computer.

### **Furnace Mapping**

The temperature and the heat flux profiles in the furnace were mapped to quantify the thermal energy exposed to the specimen. Using the sensor array described is shown in fig. 9, the

temperature and radiative heat flux inside the furnace was measured at 9 points in a plane and for 3 different plane heights as measured from the bottom of the radiant panel (8 cm, 16 cm, and 24 cm).



**Figure 9 - Sensor array inside of furnace pre-testing phase (left) and OMEGA radiant panel used as the heat source in the Phase-Ia experiments(right)**

The heat source in these experiments is an OMEGA radiant panel, controlled with a Solaira phase-angle power controller. This power controller allows for adjustment of what percentage of power the panel can draw. At full power, the panel draws 8640 watts, over the panels 12x12 in the face. Meaning a heat flux of 60 Watts/in<sup>2</sup> (93 kW/m<sup>2</sup>) is emitted from the panel. This was confirmed by measurements taken from heat flux gauge data. Typically, during experiments the power controller was set to 40-50% to maintain an average temperature of around 500°C, equating to a total heat flux of 24-30 Watts/in<sup>2</sup> (37-46 kW/m<sup>2</sup>) on the test samples. The heat flux is comparable to values observed in large-scale crude oil pool fires.

### Experimental Matrix

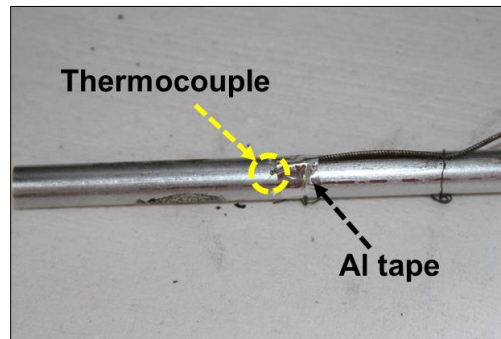
120 small-scale furnace experiments were performed to determine the most desirable material for the prototype FR, which heats quickly, stores a good amount of heat energy, and dissipates heat at a predetermined temperature. Table 1 shows the test samples that have been experimented with.

**Table 1: Materials tested in Phase I-a**

Material	Geometry	Dimensions (cm)		
		Length	Width	Thickness
Aluminum (Al)	Solid Cylinder	15	1.25 dia.	-
	Hollow Cylinder	15	1.25 dia.	-
	Solid Hexagon	15	1.25 dia.	-
	Rectangle	13	13	1.3
	Fiber	-	10 dia.	0.5
	Foam	10	10	2.5
	Honeycomb	10	10	0.3
Copper (Cu)	Solid Cylinder	15	1.25 dia.	-
	Hollow Cylinder	15	1.25 dia.	-
	Solid Hexagon	15	1.25 dia.	-

	Rectangle	13	13	1.3
	Fiber	-	10 dia.	0.5
Bronze	Solid Cylinder	15	1.25 dia.	-
	Hollow Cylinder	15	1.25 dia.	-
Oil Infused Bronze	Solid Cylinder	15	1.25 dia.	-
Ceramic White Board	Rectangle	4	4	1.8
Macor Glass Ceramic	Solid Cylinder	7.7	2.9 dia.	-
Graphite	Solid Cylinder	10	3.7 dia.	-
Carbon Fiber	Solid Cylinder	10	1.6 dia.	-
Bimetal (55% stainless steel ,45% Bronze)	Rectangle	25.4	5	0.254

## Test Procedure



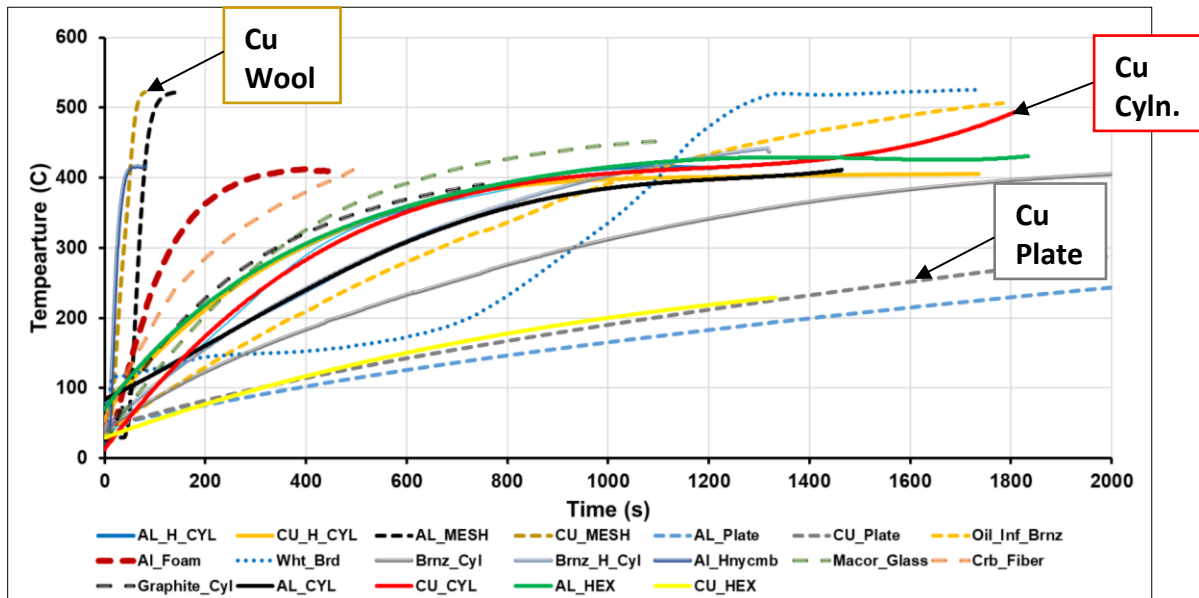
**Figure 10 - Aluminum cylindrical bar showing the thermocouple affixed to the surface for temperature measurement**

Each sample, after being affixed with a thermocouple placed on the surface (Fig. 10), was placed in the preheated furnace at 500°C. Data collection began when the sample was placed inside the furnace. After the heating phase, once the sample had reached the target 500°C, the sample was removed from the furnace. The cooling phase for each sample was conducted in both air and water. For ambient air cooling, the sample was removed from the furnace and placed onto a low thermally conductive insulation sheet, and its temperature was recorded as it cooled. For water cooling the sample was quickly removed from the furnace and placed in a water bath, where the temperature of the sample and the water were both recorded as the sample cooled (Fig. 8). The mass of the samples was recorded before and after the test, and for water cooling experiments the mass of the water was recorded pre and post-test as well.

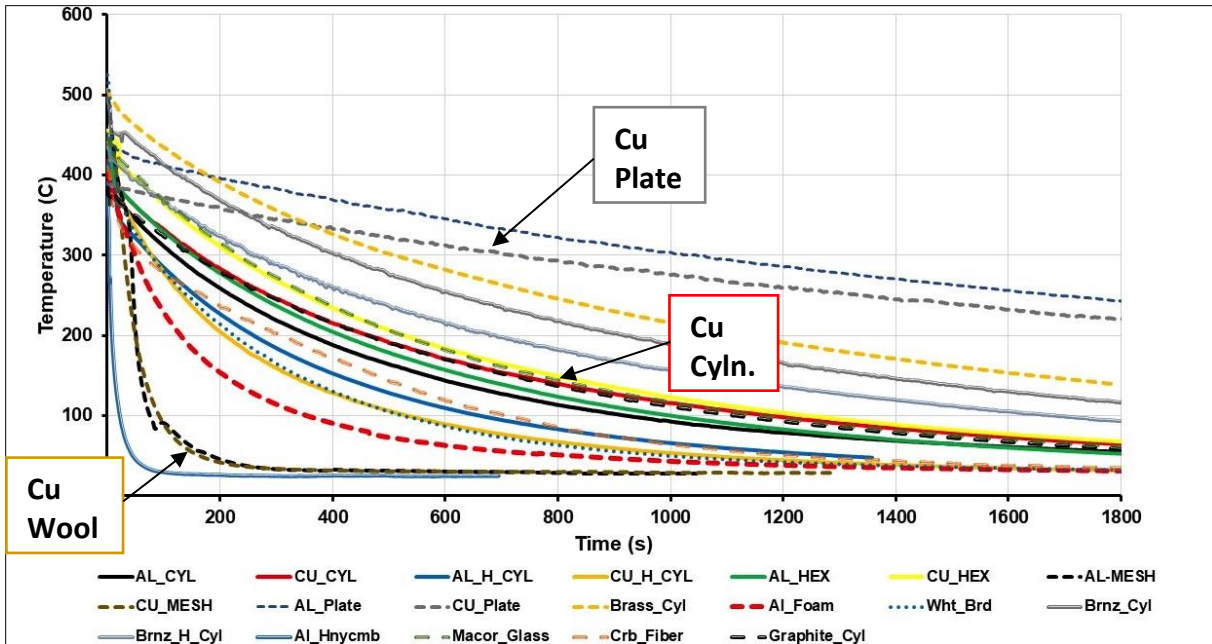
## Experimental Results and Observations

### Material heating and cooling performance

Figure 11 shows temperature profiles during heating of the samples in the furnace. Figures 12 and 13 show the cooling rates in air and water. It is clear that the surface area to volume ratio of the samples is a significant parameter in the heat transfer process. The geometry of the sample is also significant. Materials with high surface area and low mass cool faster than samples with reduced surface area and high mass (denser). For example, the copper wool cools faster than the solid copper rod, which cools faster than the solid copper plate. Figure 11 shows that copper wool is among the fastest to gain heat, heating to over 500°C in about 100 seconds. The copper cylinder takes 12 times longer (1200 s) to reach a similar temperature. Finally, the copper plate is the slowest to heat, barely reaching 300°C in 2000 s. A similar trend is observed with aluminum wool, rod, and plate. Interestingly, aluminum foam is in between aluminum wool and aluminum rod in terms of heating rate. Only the aluminum foam was experimented, as the copper foam was not delivered on time.

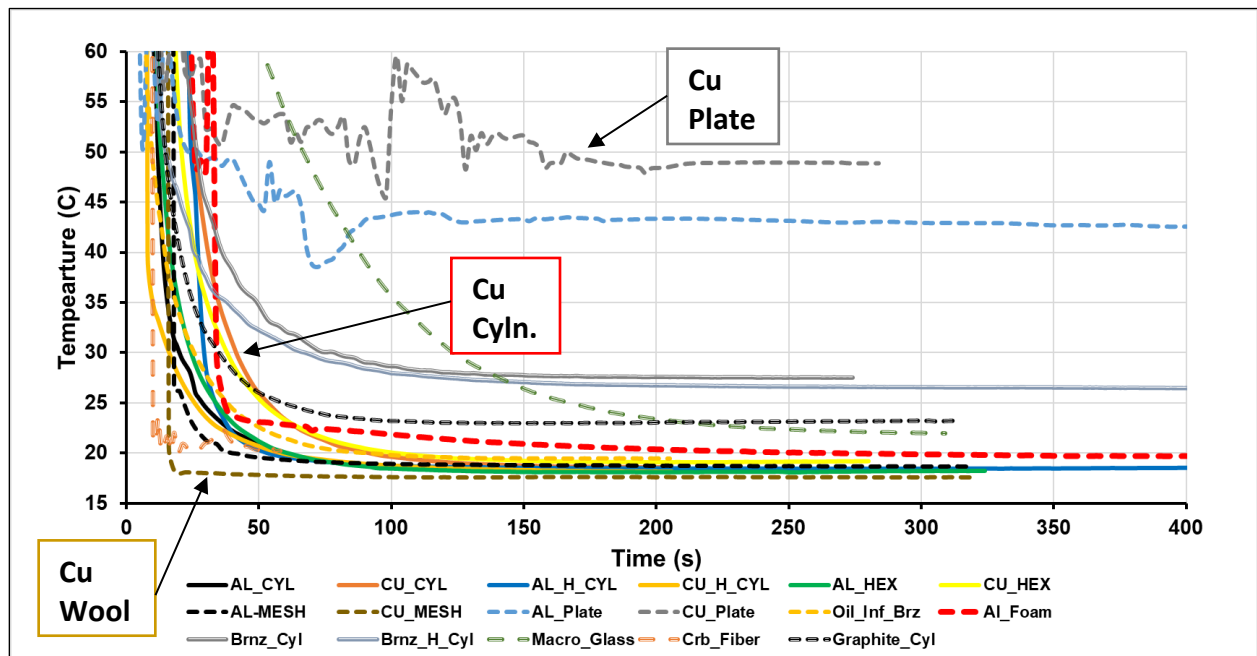


**Figure 11 - Rate of heating for different material samples tested– Phase I a**



**Figure 12 - Rate of cooling for material samples in ambient air – Phase I a**

Figure 12 shows the ambient air-cooling curves for each material tested. Observing the copper samples shows the influence of the material surface area and porosity on the ability of a material to transfer heat. The copper wool is among the fastest to cool and the copper plate the slowest, with the cylinder in between. Aluminum foam, however, cools relatively slowly for its high porosity and low weight.



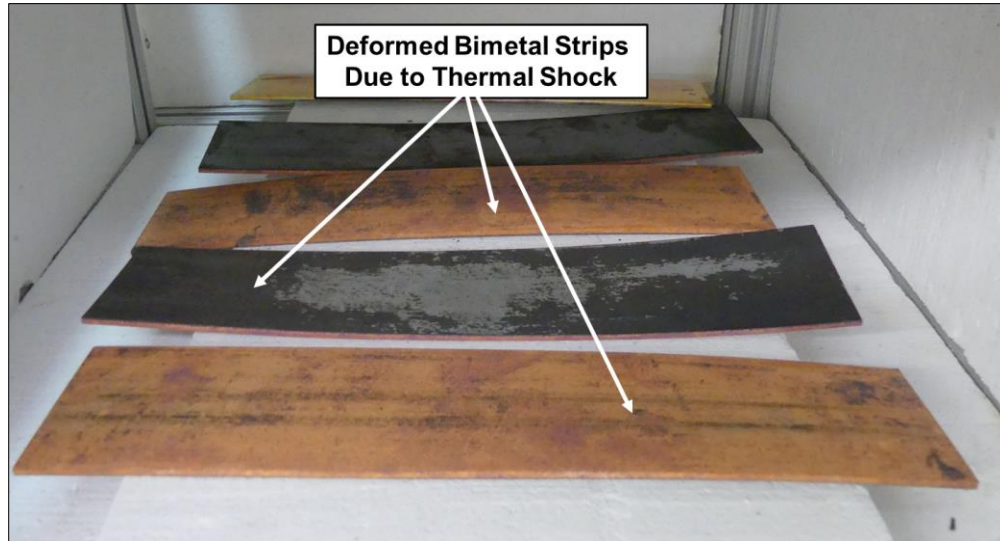
**Figure 13 - Rate of cooling for material samples in a water bath – Phase I a**

Figure 13 shows the cooling curves for the samples in water. Most samples cool very rapidly in water as shown by the sharp decline of temperatures during the first 20 seconds. The aluminum foam although cools much faster in water than expected based on its air-cooling rate, which was slow. This occurs because of its ability to promote nucleate boiling on its surface causing heat transfer rates to increase by a factor of 100. Bubbling was observed in the first few microseconds of the experiment but was too fast to be recorded using the existing camera. Another interesting material is the Macor glass-ceramic, which cools slower in water than other samples. This is because of the low thermal conductivity of ceramic, so heat cannot move as easily from the inside of the rod to the surface in contact with water. So, although the Macor ceramic is highly porous like the aluminum foam, it maintains a much slower cooling rate during water-cooling.

A desirable material for the Flame Refluxer heats quickly, stores a good amount of heat energy, and dissipates heat at a predetermined temperature based on the nature of the oil spill (type of oil, thickness of layer, weathering). The metal wools are promising as demonstrated during the field-scale experiments in Mobile, AL (E15PC000004). However, there are limitations associated with reusability and structural stability for multiple trials. If metal wool were to be used for field deployment, then a protective cover will be needed. On the opposing end, solid metal plates store more heat energy but take a long time to heat up. Of all the materials tested, the metal foam shows the most promise but requires several experiments with different types of metal foam and careful analysis on the role of its porosity with heat transfer and structural integrity in a fire environment (Phase I b). The bronze materials and the Macorglass-ceramic demonstrate desirable characteristics for boundaries in contact with water for example during ocean waves. The furnace tests demonstrated that of all the materials tested, the Al-foam, Al and Cu wools, solid bronze, and Macorglass-ceramic demonstrate the most desirable thermophysical characteristics.

Special importance was given to the bimetals composed of 55% stainless steel and 45% bronze to test for their dual material characteristics and properties. It was observed that the bimetals were efficient to store the heat but were not able to resist the thermal shock. As anticipated and designed, they erected with the exposure to heat but were not able to turn back to their original shape when they dipped into the cold water. Figure 14 shows the deformed bimetals due to rapid temperature change.





**Figure 14 - Deformed bimetal strips (55% stainless steel and 45% bronze) due to thermal shock**

The manufacturer of the bimetals was consulted with the observed thermal failure with the composite material. It was recommended a new composite is made of 72% Cu – 28% stainless steel would better be able to sustain higher thermal conductivity and have better thermal shock resistance.

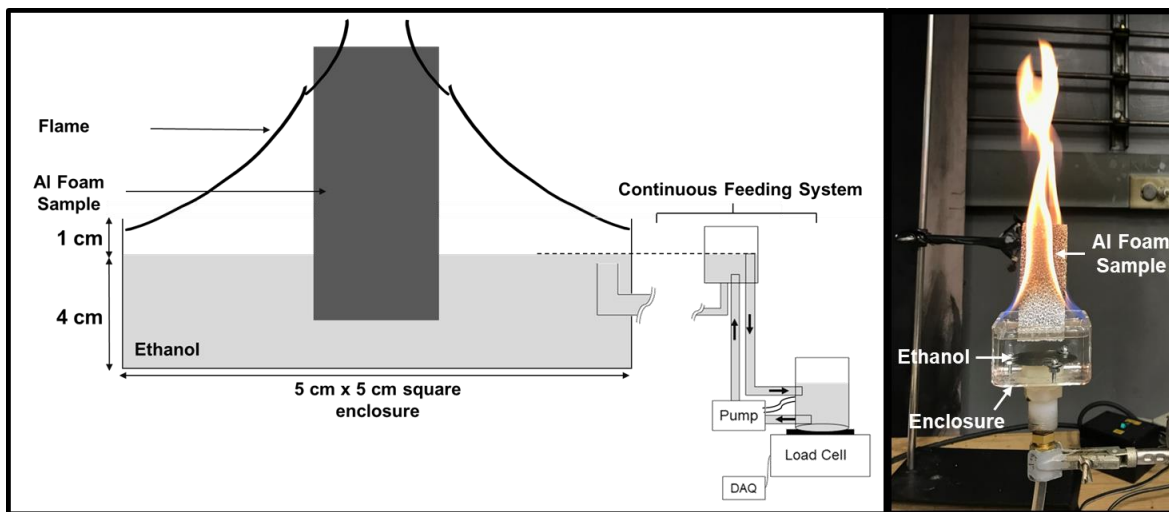
Each material was photographed before and after each test run. None of the metal samples experienced significant deformation or melting of any sort. Most commonly metal samples developed a layer of darker oxidation, particularly the copper samples. The oil-impregnated bronze rod smoldered, and it is believed would have caught fire if the heating of the sample had continued. The ceramic panel sample accumulated some dark sooty looking material on the surface but exhibited no other changes. Materials also developed darker spots on the surface, especially noticeable in the aluminum cylindrical bar and aluminum flat plate photos. These darker spots are an artifact of the adhesive from the tape used to hold on the thermocouples. On aluminum samples, the tape adhesive left dark spots where it burned and charred. On the copper samples, most drastically the copper plate, the tape shielded the area it covered from oxidation. This left a shiny spot on the surface surrounded by darker oxidation, especially noticeable after only 1 test.

### **Further aluminum foam testing**

Experiments were further performed with different types of metal foam to analyze the role of material porosity with heat transfer and structural integrity in a fire environment. In this context, A new experimental burn apparatus, a 5cm x 5cm square glass vessel with a continuous feeding system, was used to investigate the effect of porosity on fuel (ethanol) burning rate. The fuel level is maintained using a gravity feedback system as shown in Fig. 15. An OMEGA FPU5MT peristaltic pump with a constant flow rate overfeeds the fuel supply tank. The overflow rate is measured by Sartorius ED6202S-CW load cell (Capacity of 6.2 kg with a sensitivity of 0.01 g and

a factory uncertainty of  $\pm 0.03$  g). The mass-loss rate is calculated by subtracting the overflow rate from the pumping rate. Figure 11 shows the photograph of the experimental setup.



The ethanol was first burned with nothing placed inside to establish a baseline. Then burning tests were performed with each aluminum foam sample placed into the ethanol with 1 cm submerged beneath the surface (4 cm collector, 1 cm heater). Seven samples with different porosities were tested.



**Figure 15 - Schematic of small-scale (5 cm x 5 cm) experimental setup to test foam materials – Phase I a**

The Al foam samples consisted of 3 ERG aerospace Duocel aluminum foam samples (10, 20, and 40 Pores per Inch or PPI), 3 Cymat Technologies Ltd. Architectural aluminum foams (small, medium, and large cells), and one solid block of aluminum of the same dimensions as the foams. Each foam/ block sample was cut to the same dimensions (8.8 cm tall x 3.6 cm wide x 1.2 cm thick), although each sample has a different weight due to their different porosities and fabrication methods. The details of each sample and pre/post-burn pictures are shown in Table 2.

**Table 2 - Aluminum Foam Burning Test Matrix**

Name	Classification	Wt. Before (grams)	Wt. After (grams)	Before Picture	After Picture
ERG Duocel	10 PPI	8.40	8.38		















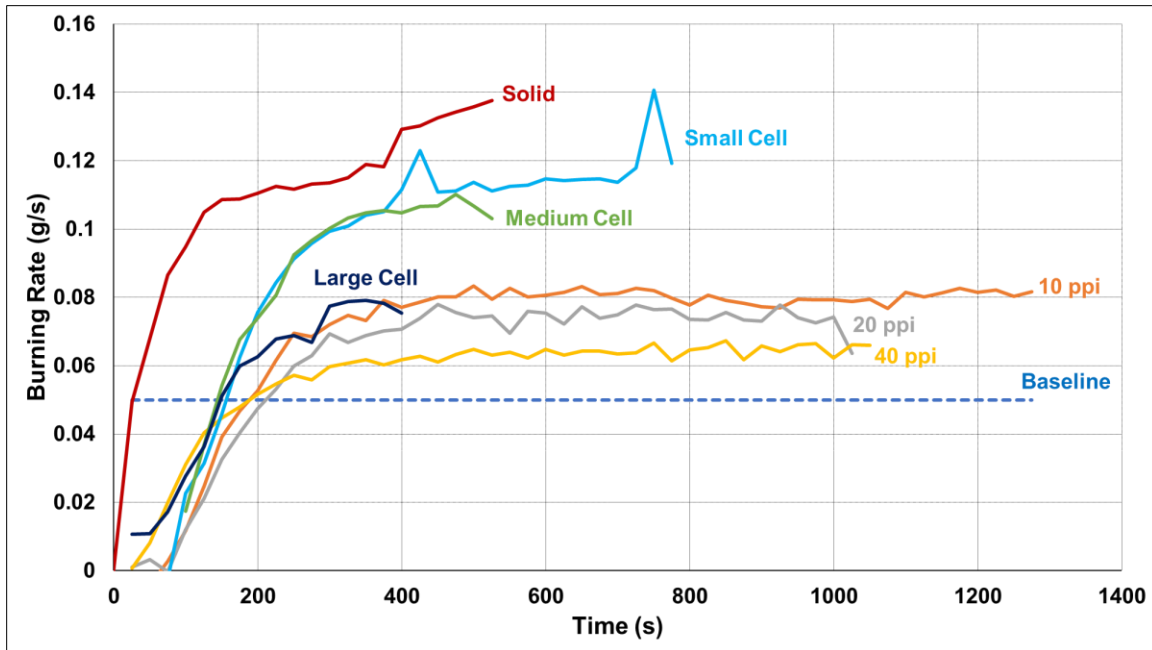
ERG Duocel	20 PPI	6.93	6.91		
ERG Duocel	40 PPI	8.74	8.72		
Cymat Tech.	Small cell	24.27	24.29		
Cymat Tech.	Med cell	24.16	24.16		
Cymat Tech.	Large cell	9.06	9.11		
Solid Al	SOLID	112.01	112.07		

Figure 16 shows the comparison of the mass-loss rates for different porosities. As seen in fig 16, the Al foams do offer an improvement over the baseline burning rate. However, the more dense and solid the foam becomes the better the burning rate improvement. This is emphasized by the solid aluminum block which offers the greatest burning rate improvement of almost 3 times the baseline. Consistently the most porous foams were the worst performing (10 PPI, 20 PPI, 40 PPI, and large cell), and the more solid foams were the best (med cell, small cell, and solid aluminum block).



**Figure 16 - Mass loss rates for different Al porosities – Phase I a**

Experiments demonstrated that the Al foams do offer an improvement over the baseline. However, the more dense and solid the foam becomes, the better the MLR improvement. Due to their low burn efficiency and high cost, foams were eliminated as an option for the FR material.

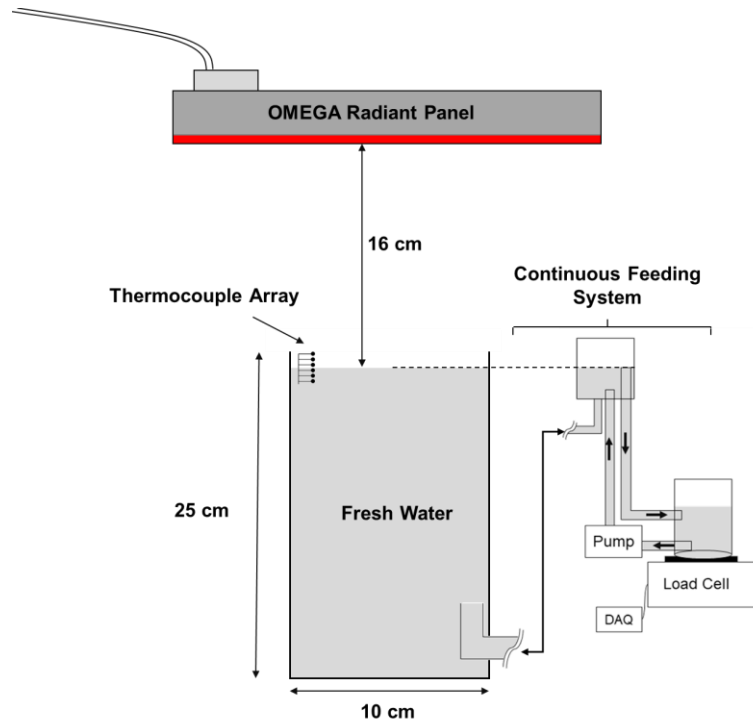
The macorglass-ceramic was also eliminated due to its high cost, while aluminum and brass were not selected due to their low melting point (Melting points of Al = 660 °C, Brass = 900 °C). It was decided to continue with copper (Cu) due to its high thermal conductivity (385 W/mK) and melting point (1,100 °C). A new experimental setup (Heat Flux) was designed, and tests were performed to optimize the geometry of the Cu FR's.

### Heat Flux Tests

A new experimental setup was constructed with the primary objective being to test small-scale prototype FRs in an environment similar to their use case scenario. The test setup consists of the same OMEGA 12" x 12" radiant panel used in Phase I-a, supported by a similar extruded aluminum frame and with insulation sheets to protect test equipment from heat damage. Directly underneath and 16 cm from the bottom surface of the panel, is a constantly refilling fresh water bath in a 10 cm x 10 cm glass enclosure. This sufficiently deep glass, 25 cm, enclosure water bath maintains the water level at a constant height using a constant head device, which allows water to flow between two vessels at the same elevation. The second vessel is being constantly filled and drained with a pumping loop, mass loss rate from the vessel being heated can then be measured as the change in mass in this pumping loop. Fig 17 shows a sketch of the experimental setup.

This experimental setup enables the testing of various small-scale FR prototypes for their effect on water evaporation rate. The temperature in the water layer and the air directly above the water

surface are also measured by a thermocouple array (6 TCs, 0.5 cm spacing, K Type, AWG31 Gauge), allowing analysis of the thermal boundary layer profiles. (Fig. 17)



**Figure 17 - Schematic of small-scale FR prototype testing setup – optimizing FR geometry**

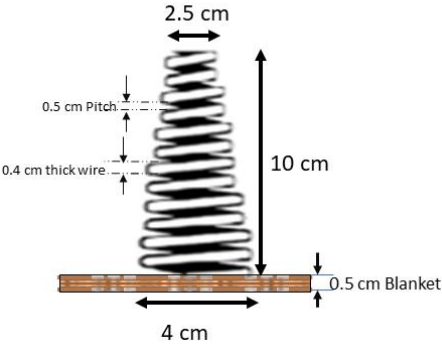
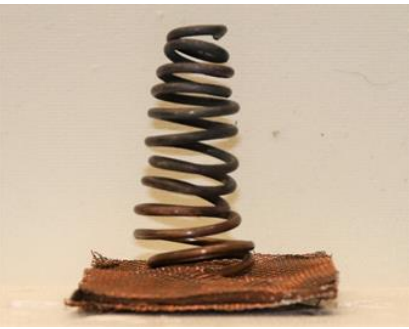
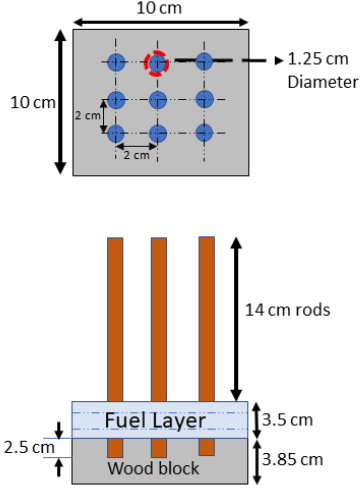

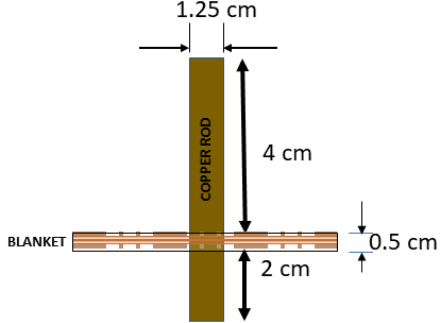
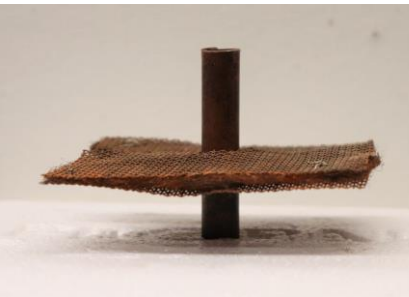
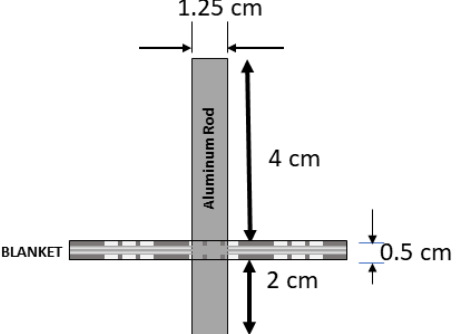
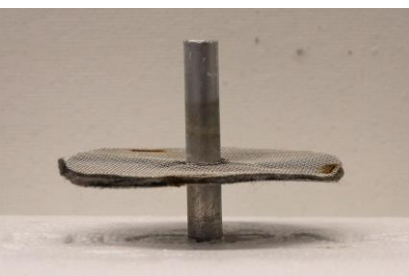
For all tests, the height of the panel off the surface of the water remained the same at 16 cm and the power controller for the radiant panel was set to 100%, equating to a total output of about 70 kW/m<sup>2</sup>.

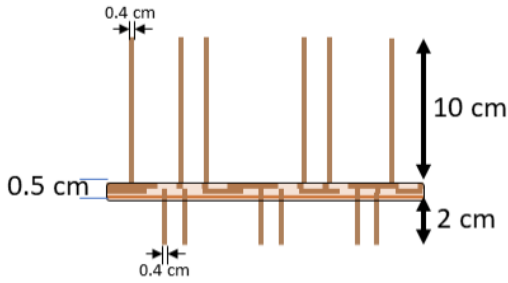

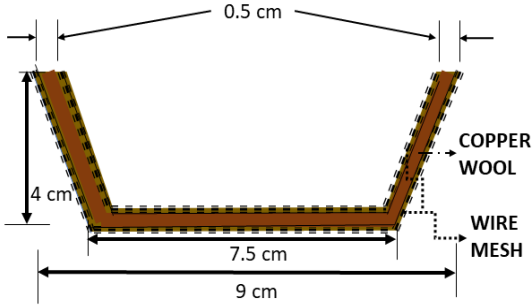

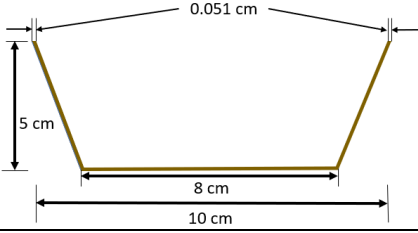

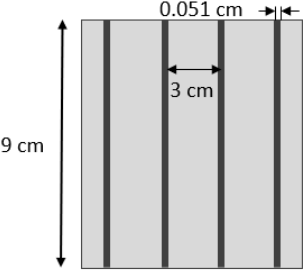

### Flame Refluxer Prototypes

As FR prototypes are generated, we can rapidly produce and test them in this new experimental setup, to date nine prototypes have been created and tested. Each prototype has a footprint of 10 cm by 10 cm, filling the area of the pool it is submerged inside. Each FR prototype was also tested at various submersion depths. None of the prototypes are self-floating in this experiment and are held in place either by friction fit, support from underneath, or suspended from above by a thin wire. The prototypes experimented with are, Cu coil and Cu blanket, single Cu rod, Cu rod array, hollow Cu rod, and Cu blanket, hollow Al rod and Al blanket, Cu wire array, and Cu blanket cup, Cu solid cup, and Cu grid. The details of the prototypes are given in Table 3.

**Table 3: Aluminum Foam Burning Test Matrix**

Name	Sketch	Picture
------	--------	---------

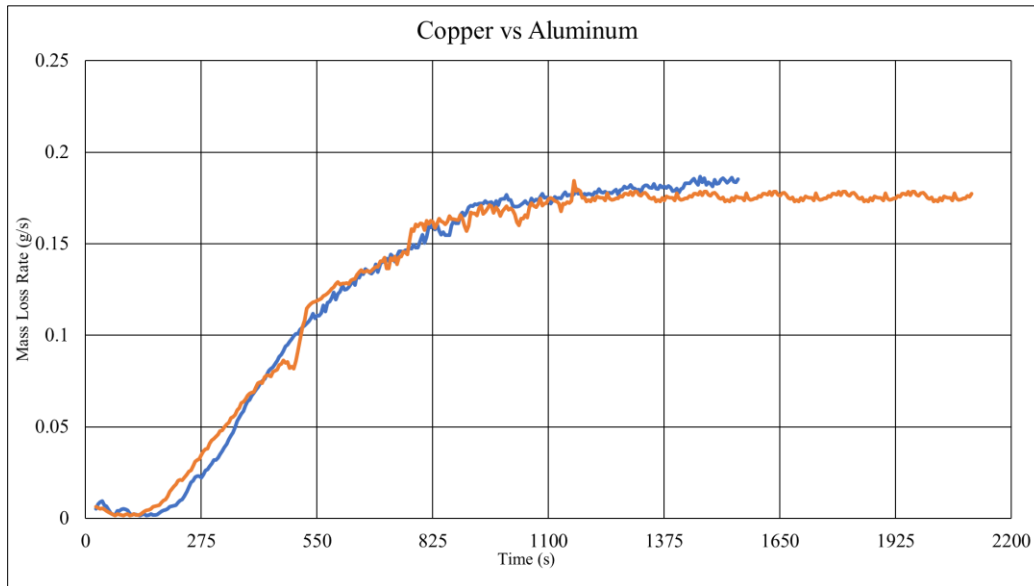
<p>Cu coil and Cu blanket</p>		
<p>Cu rod array</p>		
<p>Hollow Cu rod and Cu blanket</p>		
<p>Hollow Al rod and Al blanket</p>		

Cu wire array		
Cu blanket cup		
Cu Solid Cup		
Grid		

## Experimental Results and Observations

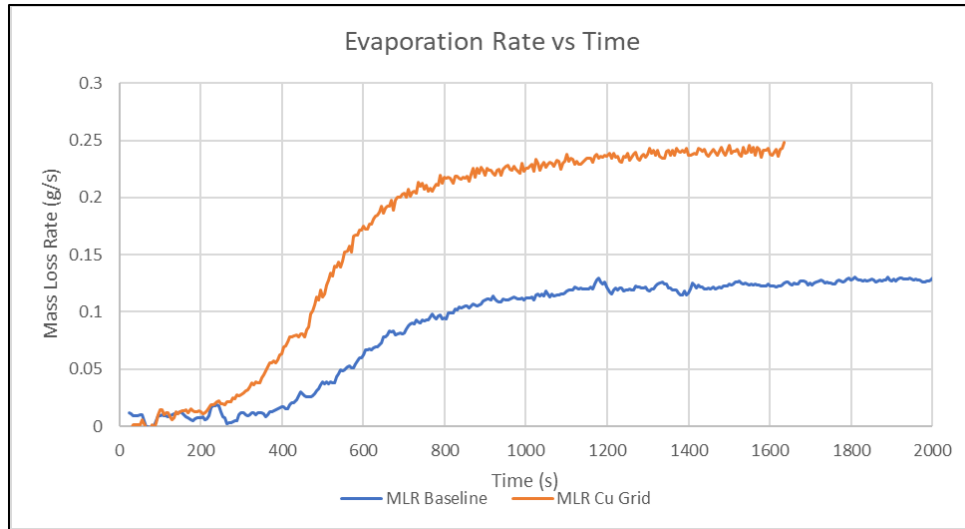
Each prototype was inserted into the glass enclosure directly underneath the panel. The 6 Type K thermocouples on their thermocouple tree were then inserted into position such that 3 were in the water and 3 were above out of the water. Data collection was initiated, and the panel was powered on. Each test was initiated at room temperature, no tests were started while the panel, water, or enclosure were hot to the touch.

Data from each test can be seen plotted in fig 18, 19, and 20 below. Fig 18 and 19 are mass loss rate (evaporation rate) data plotted versus time. This shows the transient mass loss rate that the FR prototype induces in the water layer. The higher the mass-loss rate, the better performing the FR. In figure 18, we compare two identical prototype geometries made from different materials. These prototypes are the hollow rod with mesh type as shown in Table 3 above. These prototypes feature nearly identical shapes and compositions, only one is made from copper and one is made from aluminum. From this comparison, we concluded that there is no significant performance benefit between using copper (blue line) and aluminum (orange line) as an FR material.



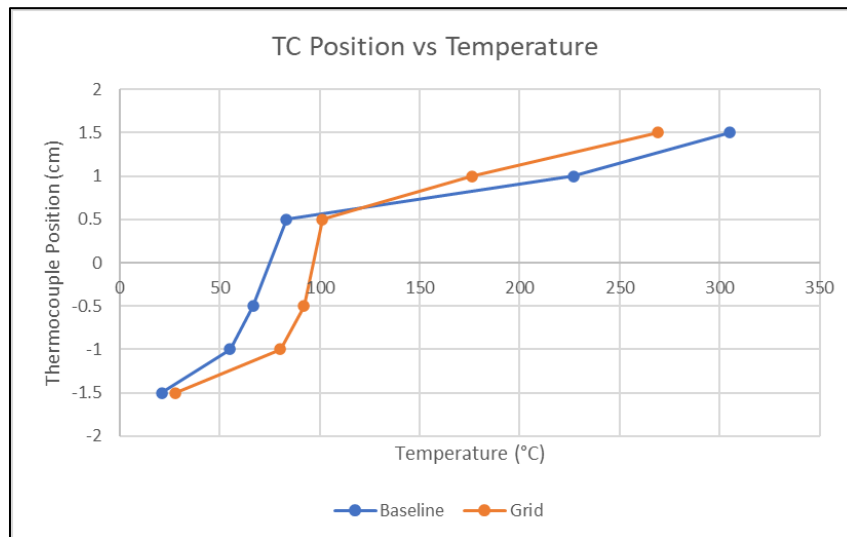
**Figure 18 - Al vs Cu MLR**

In figure 19 below we are comparing the baseline mass loss rate (orange) to the best performing test so far (blue). The best performing test so far consisted of a single 15 cm tall copper rod which was placed 80% out of the water (12cm exposed 3 cm submerged). This arrangement offered a 68% improvement over the baseline mass loss rate.



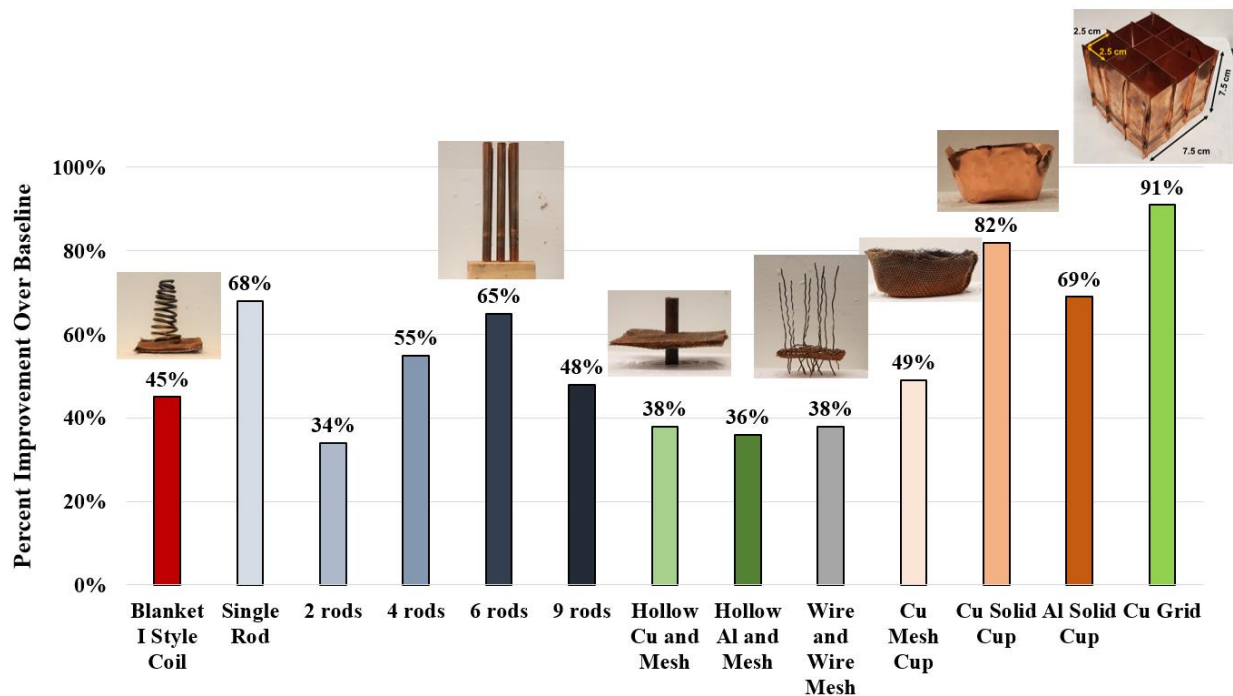
**Figure 19 - MLR for best performing FR vs baseline**

In figure 20 we are comparing the temperature profiles for the baseline experiment (blue) and the best performing experiment thus far (orange). The thermocouple tree used in the experiments enabled the placement of 3 thermocouples above the water and 3 thermocouples in the water with all thermocouples spaced evenly at 0.5 cm apart. In this figure, the y-axis is the thermocouple position in cm, with 0 cm being the water line. Here we can see that the grid FR maintains significantly higher temperatures in the liquid phase. The temperatures higher in the gas phase are slightly lower. This is consistent with expectations that the grid FR efficiently transfers heat from the gas phase to the liquid phase.



**Figure 20 - Temp. of best performing FR vs baseline**

Results demonstrated that the maximum evaporation rate was obtained with the grid FR with over 91% improvement over the baseline case (Fig. 21).



**Figure 21 - Performance of the different FR's tested in heat flux tests**

Based on the results, a scaled-down grid FR, a single pike ruffled metal FR and multiple pikes ruffled metal FR were manufactured to be tested in the wave tank in Phase I-b.

### Outcomes of Phase I-a

Phase I-a aimed to explore the parameters controlling heat collection and transfer back to the fuel by the FR. In Phase I-a, various materials (with different porosity, density, thermal conductivity, specific heat, and durability to thermal shock) were tested in a 30 cm x 30 cm x 35 cm radiative furnace. The following key conclusions were drawn from Phase I:

1. Experiments demonstrated the Al-foam, Al and Cu wools, solid bronze and Macorglass-ceramic demonstrate the most desirable thermophysical characteristics for FR. They heat quickly, store a good amount of heat energy, and dissipate heat slowly.
2. Further experiments demonstrated that the more dense and solid the foam becomes, the better the MLR improvement. Consistently the most porous foams were the worst performing (10 PPI, 20 PPI, 40 PPI, and large cell), and the more solid foams were the best (medium cell, small cell, and solid aluminum block).



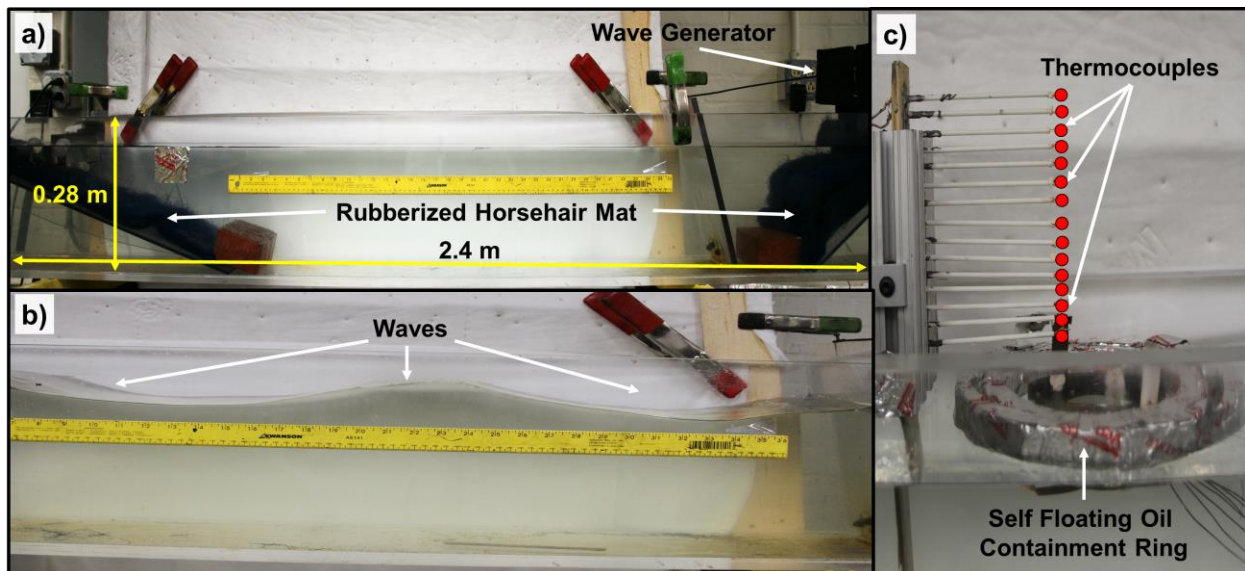
3. The macorglass-ceramic was eliminated due to its high cost, while aluminum and brass were not selected due to their low melting point (Melting point of Al = 660 °C, Brass = 900 °C). It was decided to manufacture FRs with copper (Cu) due to their high thermal conductivity (385 W/mK) and melting point (1,100 °C).
4. The effect of collector geometry on evaporation rate was investigated by the heat flux tests. The grid FR performed best by increasing the evaporation rate by 91% over the baseline.

The results of Phase I-a (such as material, and optimum collector geometry) were used in the development of the small-scale FR prototypes that were tested in Phase I-b.

### Phase I b - Wave Tank Experiments

#### Experimental Setup

The test setup for Phase I-b consists of a small-scale wave tank and a self-floating fuel containment ring. The wave tank allows for precise control of model wave parameters and small-scale burning inside of the wave tank. The wave tank's internal dimensions measure 2.4 meters long, 0.24 m wide, and 0.28 m deep (Fig. 22). The walls and floor of the tank consist of 2.5 cm thick acrylic glued together at the edges. The tank is filled with 33 ppt (parts per thousand) saltwater. A 1:6 sloped beach covered with a rubberized horsehair mat acted as the wave absorber at the end of the tank opposite the wave generator (Fig. 22a). Another section of rubberized horsehair mat was placed behind the wave paddle to prevent reflections behind the paddle as well. The beaching method of wave absorption was used to minimize the wave reflections.

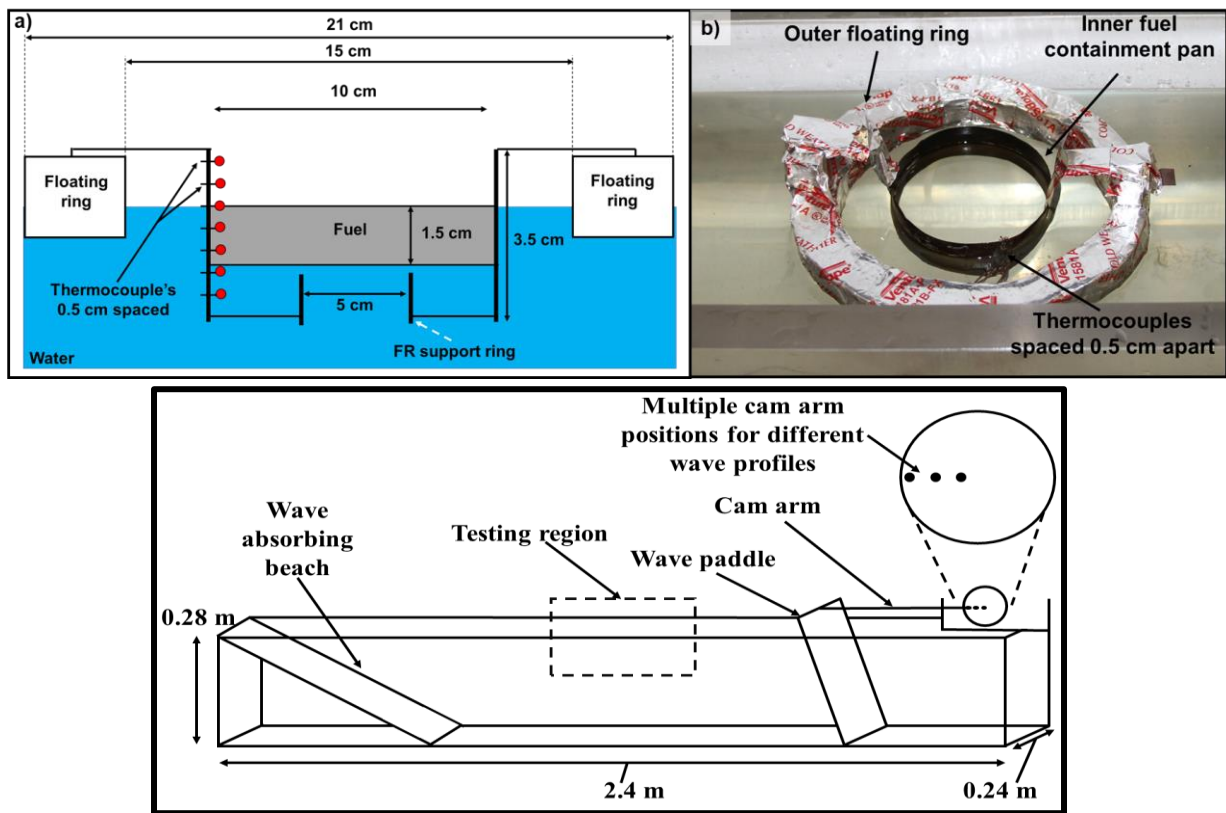


**Figure 22 - a) Phase I-b experimental setup, b) Waves created by the wave generator, c) Thermocouple array used to measure plume temperatures- TC array was placed 25 cm above the fuel surface while conducting tests.**

Waves were generated using a paddle or flapper type wave generator, powered by an electric motor (Fig. 22a & 22b). In this method, an electric motor turns a cam which in turn drives an arm and pushes the wave generating paddle. This method of wave generation produces regular sinusoidal wave motion with larger circular particle movements closer to the surface, and smaller circular particle movements closer to the bottom of the tank (Fig. 22b). Cam size and motor turning speed can both be adjusted to create different wave profiles. Data on these wave profiles were measured both by video and an Akamina AWP-24-3 dual-sensing wire wave height gauge.

The floating containment ring consists of a 10 cm diameter inner stainless-steel pan to contain the fuel and a 5 cm diameter submerged stainless steel ring to support small-scale FR prototypes (Fig. 23a). The inner pan and submerged ring were connected via metal arms to a Styrofoam floating ring with an inner diameter of 15 cm and an outer diameter of 21 cm. This floating ring surrounds and supports the inner pan and the submerged ring. This setup allows the inner fuel containment pan to float on the water's surface and move with the waves, staying at a relatively constant position relative to the water surface.

Temperature measurements in these experiments were gathered through 22 K-Type AWG31 thermocouples. Seven of them were inserted 0.5 cm apart vertically through the fuel pan to measure the hot gas, oil, and water temperature (Fig. 23), while 15 placed 2 cm above the fuel surface with 1 cm spacing to measure the hot plume temperature (Fig. 22c).



**Figure 23 - Self-floating setup with TC configurations and containment pan - Phase I-b**

Two distinct wave profiles were chosen for scaling purposes from the 10 cm pool size to a 10 m pool size with full-scale ocean waves. Scaling was accomplished using the Froude number, which ensures proper scaling of gravity forces between a model “M” and full-scale “F”. For Phase I-b wave tank the Froude number can be calculated by the following equation.

$$Fr_M = \frac{U}{\sqrt{gL_M}} = 0.86 - 0.95$$

where U is the wave velocity, g is the gravitational acceleration (9.81 m/s<sup>2</sup>) and L<sub>m</sub> is the characteristic length of the model. For Phase I-b tests the L<sub>m</sub> is the pool fire size which is 10 cm.

Thurman’s Introductory Oceanography describes a moderate ocean wave as having a wavelength of 61.8 meters, a period of 7 seconds, and a height of 4.5 meters. Wave velocity can be calculated by dividing the wavelength by the wave period. For the Thurman wave, this would be a wave velocity of 8.82 m/s. Using a full-scale pool fire size of 10 meters the full-scale Froude number becomes 0.89, sufficiently in the range that we see for small-scale waves as well. In this way, we can ensure proper scaling similarity between our scale and the full scale.

$$Fr_F = \frac{U}{\sqrt{gL_F}} = 0.89$$

Table 4 shows the wave profiles used in Phase I-b.

**Table 4 - Wave profiles used in Phase I-b**

Wave Name	Rotational Speed (ω) rpm	Wave Length (L) cm	Wave height (H) cm	Wave velocity (cm/s)	Freq. Waves/sec	Froud Number for small scale tests
Wave 1	37.8	147	0.9	85.47	0.58	0.86
Wave 2	87	66	0.7	94.2	1.41	0.95

### Experimental Matrix

A total of 114 experimental tests were performed. All tests were performed with a 1.5 cm initial fuel slick thickness. Initially, the baseline tests were performed with pure Alaska North Slope (ANS) crude oil and emulsion consist of 25% saline water (33 ppt) and 75% ANS by volume. Then the influence of blanket coverage area on the burn efficiency was investigated. Blankets comprise of 1 cm thick Cu fibers (0.0127 cm wire diameter) sandwiched between two Cu meshes (wire diameter of 0.058 cm and has an opening of 0.13 cm between wires) were manufactured with various diameters (10 cm, 7 cm, and 5 cm) and tested. Kapok fiber, which is a plant-based, non-toxic, naturally hydrophobic, oleophilic, and self-buoyant material, was added to the blanket to improve burn efficiency. In two cases, 0.2 cm kapok fiber placed at the top and bottom was tested. Then different collector types such as solid rods at the center, ruffled plate, and grid plate

were tested. Each test was repeated three times. Details of the experimental matrix are given in Table 5.

An analysis of the area ratios on evaporation rate was also performed. The ratio of the collector area to the pool surface area ( $\alpha_1$ ) was calculated and correlated with the burn efficiency.  $\alpha_1$  values obtained from Phase I-b will be used to design the large-scale FR prototypes.

**Table 5 - Experimental Matrix of Phase I-b**

Case	Heater			Collector		Wave	Fuel
	Blanket Dia. (cm)	Blanket Thickness (cm)	Blanket Material	Type	Height		
Baseline	-	-	-	-	-	-	ANS
						Wave 1	
						Wave 2	
						-	25 % Saline Water - 75 % ANS
						Wave 1	
						Wave 2	
Only Blanket	10	1	Cu	-	-	-	ANS
	5	1	Cu	-	-	-	
	7	1	Cu	-	-	-	
						Wave 1	
						Wave 2	
	7	1.2	1 cm Cu, 0.2 cm Kapok fiber at the top.	-	-	-	ANS
	7	1.2	1 cm Cu, 0.2 cm Kapok fiber at the bottom	-	-	-	
						Wave 1	
						Wave 2	
						-	
						Wave 1	
						Wave 2	25 % Saline Water - 75 % ANS

**Table 5 - Experimental Matrix of Phase I-b (Cont.)**

Case	Heater			Collector		Wave	Fuel	$\alpha_1$
	Blanket Dia. (cm)	Blanket Thickness (cm)	Blanket Material	Type	Height			
Blanket with FR	7	1.2	1 cm Cu, 0.2 cm Kapok fiber at the bottom	Cu rod placed at the center	3	-	ANS	0.266
					5			0.432
					7			0.597
					9			0.763
	7	1.2	1 cm Cu, 0.2 cm Kapok fiber at the bottom	Ruffled Cu plate with 1 pike	3	-	ANS	1.301
					5			1.681
					7			2.120
					9			2.587
	7	1.2	1 cm Cu, 0.2 cm Kapok fiber at the bottom	Ruffled Cu plate with 3 pikes and holes	3	-	ANS	2.150
						Wave 1		
						Wave 2	25 % Saline Water - 75 % ANS	
						-		
						Wave 1		
						Wave 2		
	7	1.2	1 cm Cu, 0.2 cm Kapok fiber at the bottom	Cu Grid	3	-	ANS	1.23
						Wave 1		
						Wave 2	25 % Saline Water - 75 % ANS	
						-		
						Wave 1		
						Wave 2		

## Small-scale FR prototypes

Five FR prototypes were designed and tested in Phase I-b. Figure 24 shows the details of the small-scale FRs.

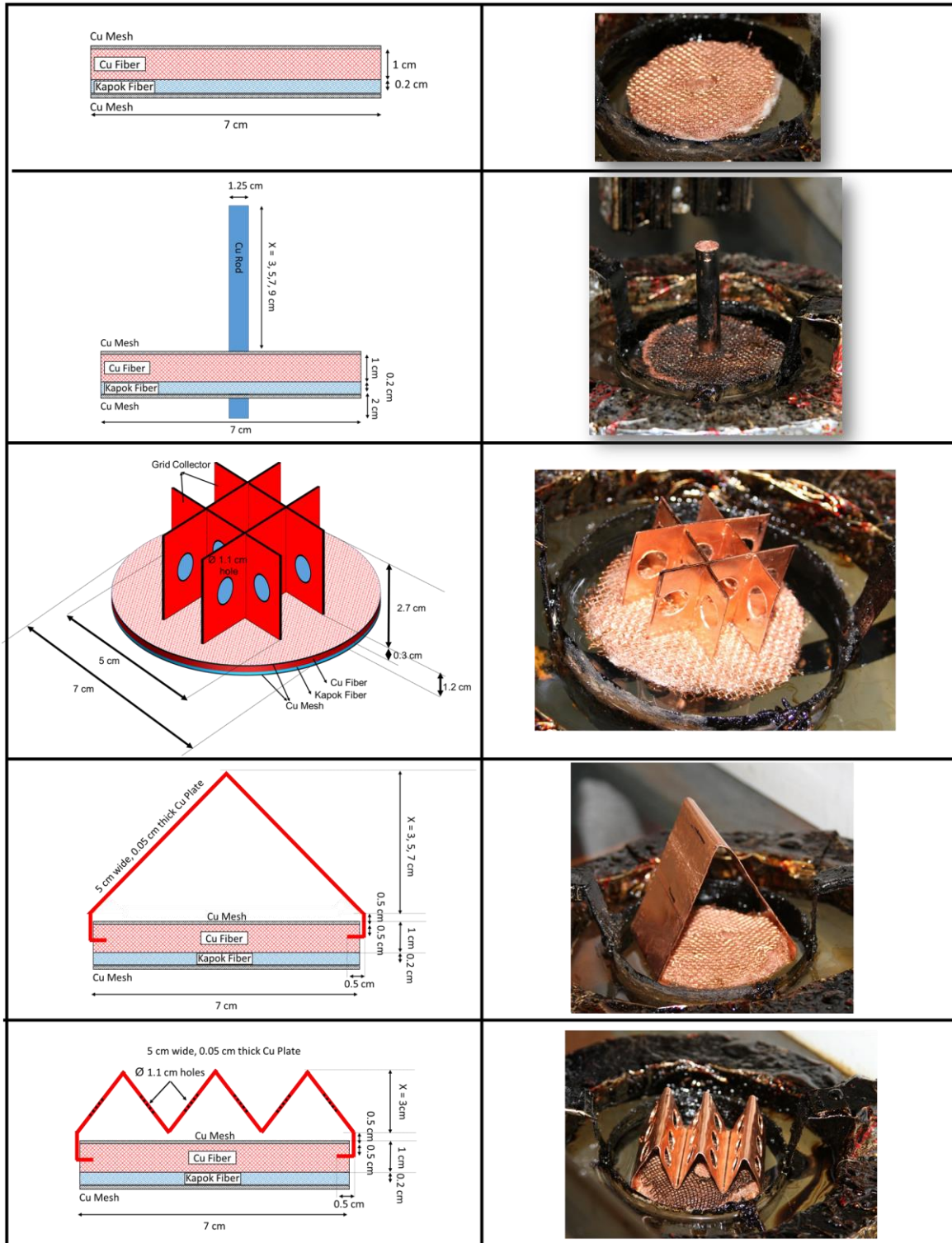


Figure 24 - Small-scale FR prototypes tested in wave tank - Phase I-b

## Experimental Results and Observations

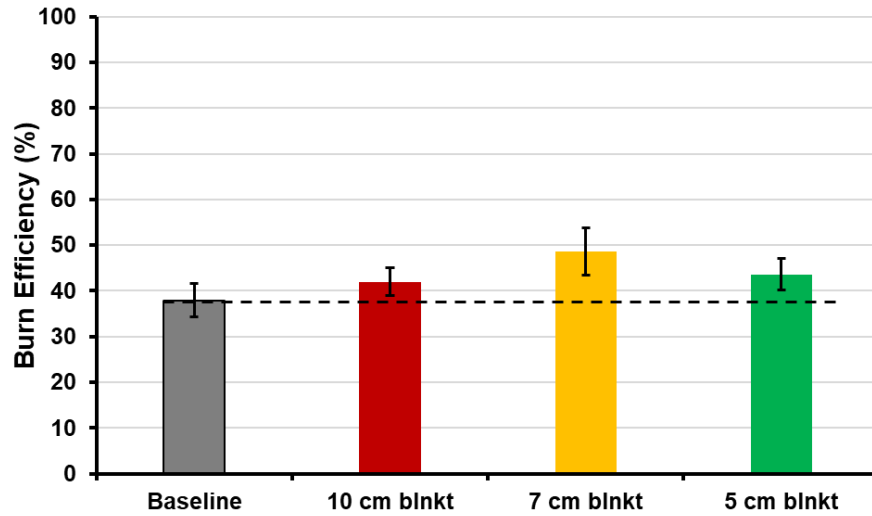
### Burn Efficiency

Burn efficiency is the ratio of the mass of oil burned to the initial oil mass:

**Burn Efficiency (%)**

$$= \left[ \frac{\text{Initial Oil Mass} - \text{Burnt Mass}}{\text{Initial Oil Mass}} \right] \times 100$$

Initially, the influence of blanket coverage area on burn efficiency was investigated. Blankets (1 cm thick filled with Cu fibers) with different diameters (10 cm, 7 cm, and 5 cm) were manufactured. Figure 8 compares the burn efficiency of the baseline and 1 cm thick Cu blanket with different diameters for ANS crude oil. Error bars show the standard deviation between three replicates.

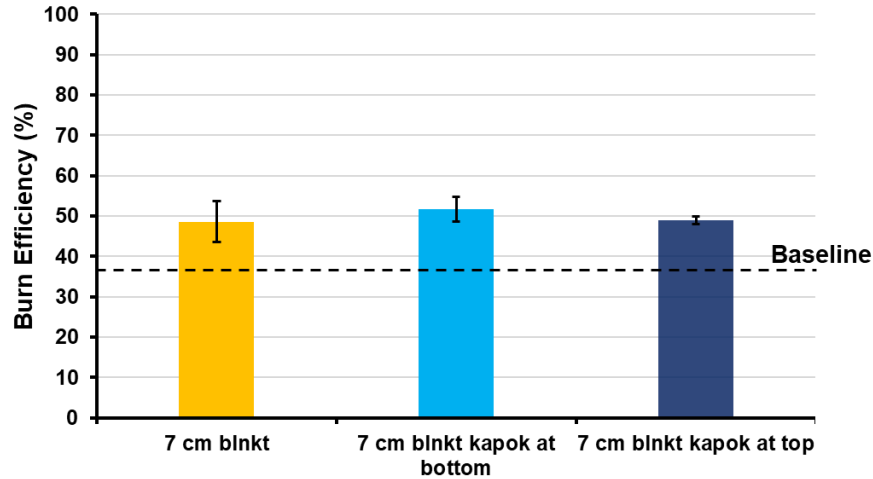


**Figure 25 - Burn efficiency of the baseline, and 1 cm thick Cu blanket with different diameters (10 cm, 7 cm, and 5 cm)**

When the Cu blanket with a 7 cm diameter is placed in the fuel, it is observed that the burn efficiency increased to 48%, while it was 38% for the baseline case. Covering the pool surface with the blanket (10 cm blanket case) limited the rise of the fuel vapor from the bottom of the blanket. Although the burn efficiency was ~42%, the improvement was not significant as the 7 cm diameter blanket case. Using a smaller blanket than the pool diameter allowed fuel vapor to rise easier and promoted a higher flame temperature and higher heat feedback from the flame to the pool surface. In this context, a 7 cm diameter blanket was used in all the small-scale prototypes.

Then kapok fiber was added to the blanket to wick the oil during the burn and sustain the fire longer even with the thin oil slicks. Two cases, 0.2 cm layer of kapok above the 1 cm Cu fiber and 0.2 cm layer of kapok below the 1 cm Cu fiber, were tested. Figure 26 shows the effect of kapok fiber on the burn efficiency for ANS crude oil.

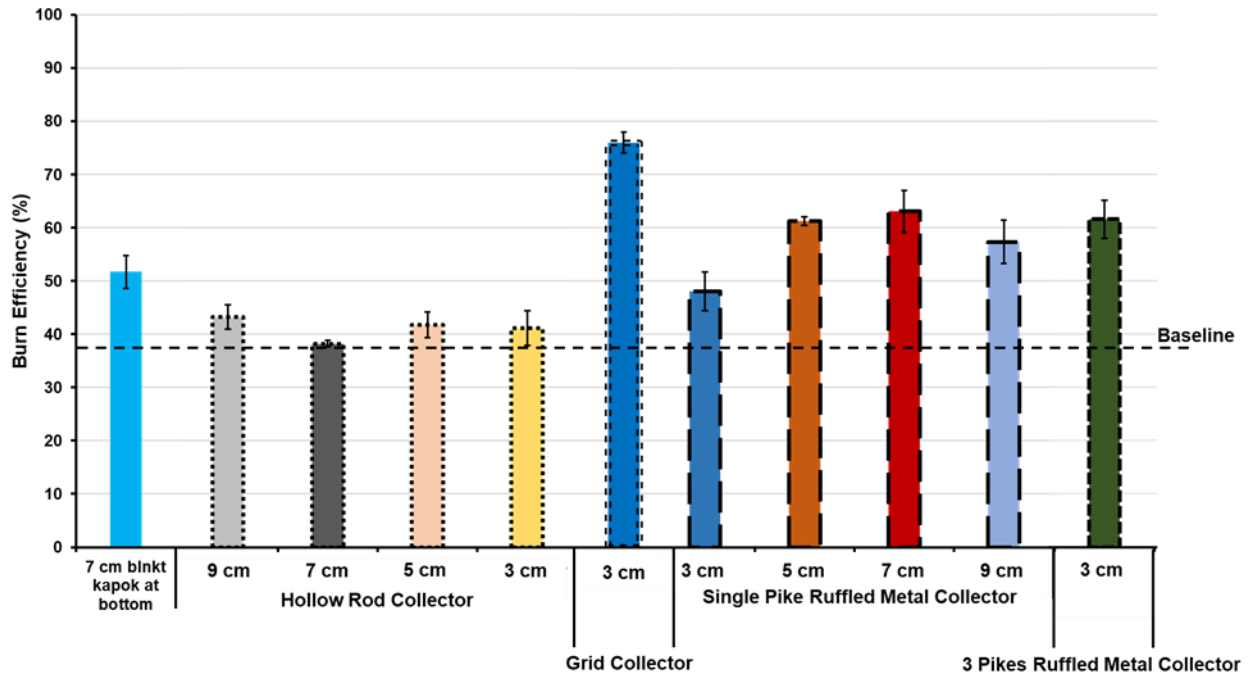




**Figure 26 - Burn efficiency of the 7 cm diameter blanket with and without kapok fiber. Orange: No kapok fiber, Light Blue: Kapok placed below the Cu fiber, Dark Blue: Kapok placed above the Cu fiber. (Horizontal dotted line shows the baseline)**

It is observed that adding 0.2 cm thick kapok fiber (light blue) increased the burn duration (due to the wicking effect) and further enhanced to burning rate to ~ 52%.

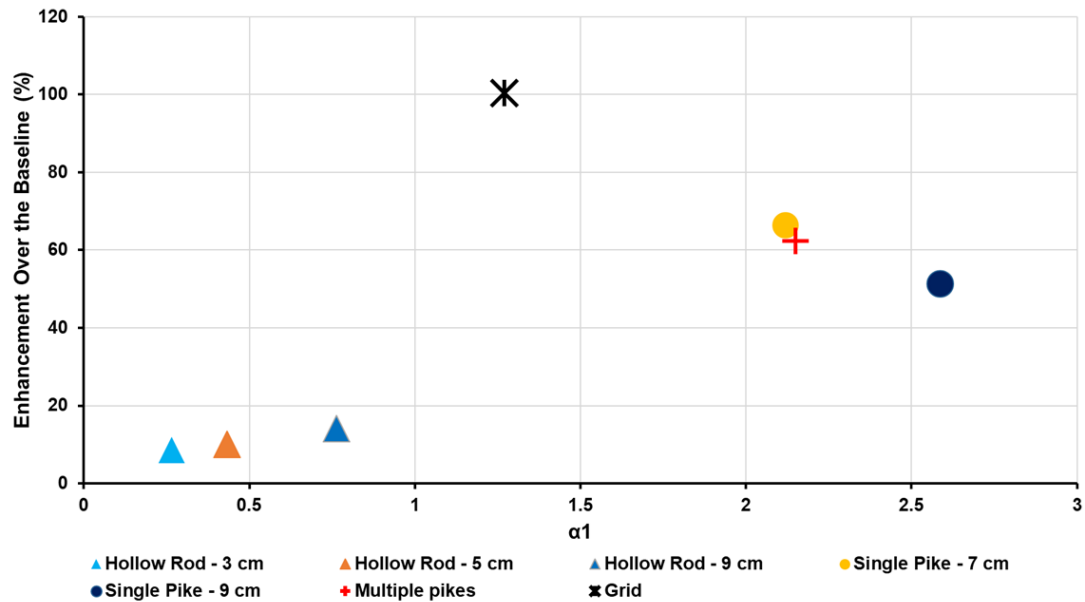
After optimizing the blanket area and the material, FRs with different collector types were tested (Fig. 24). Figure 27 compares the burn efficiency of different FRs in stagnant water conditions for ANS crude oil.



**Figure 29 - Burn efficiency of the small-scale FRs with different collector types and heights for ANS crude oil. (Horizontal dotted line shows the baseline)**

First, FRs composed of a single hollow Cu rod (0.92 cm inner diameter, 1.25 cm outer diameter) attached on a 7 cm diameter blanket (1 cm thick Cu fiber standing on 0.2 cm kapok fiber sandwiched between two Cu meshes) were tested (Fig. 20). Different collector heights were investigated (3, 5, 7, and 9 cm). It is observed that enhancement in burn efficiency was not significant with the hollow rod FRs. It was decided to use thin Cu plates as collectors due to their lightweight and high burn efficiency. A 3 cm high (2.7 cm collector, 0.3 cm heater) grid FR (this configuration showed the best performance in heat flux tests) was manufactured. Holes (1.1 cm diameter) were drilled to increase the airflow into the flame (Fig. 20). Experiments demonstrated that the burn efficiency reached its optimum value of 76%, which is a ~ 50% increase over the baseline case. Base on the grid FR a new FR made of single pike ruffled metal (5 cm wide, 0.05 cm thick Cu plate) attached on a 7 cm diameter blanket were manufactured (Fig. 20). The ruffled collector is selected for easy storage and deployment. Tests with different collector heights (3, 5, 7, and 9 cm) were performed. It is observed that the short pikes, 3 and 5 cm, blocked the air entrainment into the flame and caused lower burn efficiencies. The maximum burn efficiency, 63%, was achieved by the 7 cm high single pike (Fig. 29). However, using the same aspect ratio (1:1) of the optimum pike height (7 cm) and the blanket diameter (7 cm) for the large-scale tests will increase the center of gravity of the FR that might cause tilting in wave conditions. In this context, a 3 cm high 3 pikes ruffled metal collector was designed and manufactured by keeping the optimum pike surface area. Like in the grid FR, holes were drilled to increase the airflow into the flame (Fig. 24). The tests demonstrated that the new multiple pike collector achieved the same burn efficiency as the 7 cm high single pike collector.

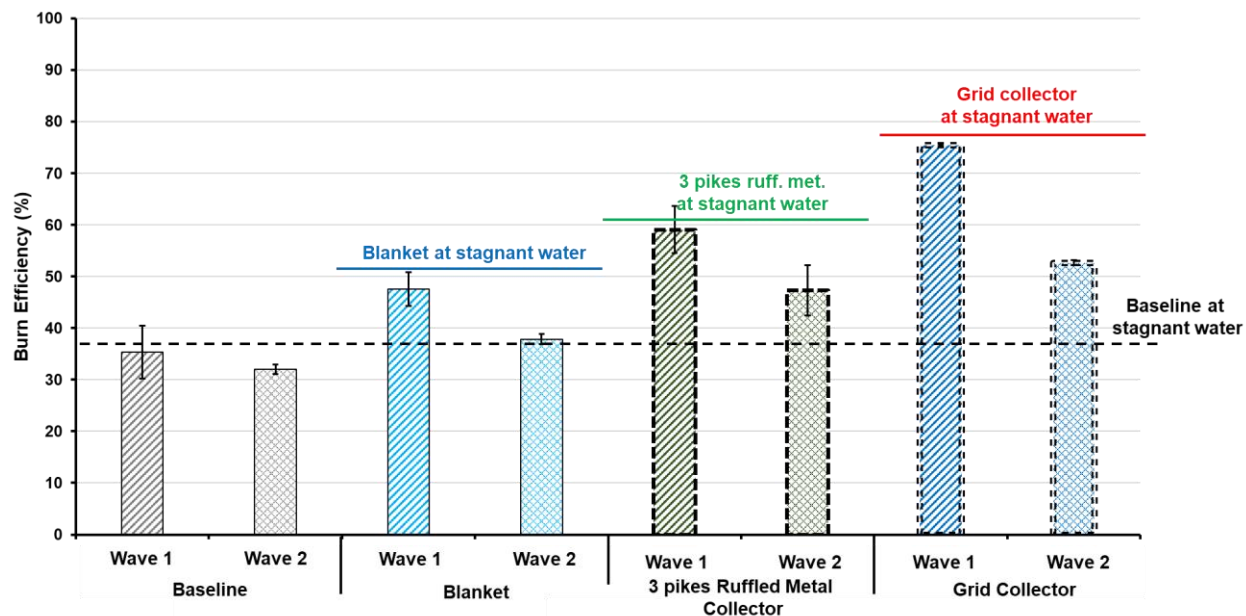
Figure 30 shows the correlation between the  $\alpha_1$  and burn efficiency.



**Figure 30 - Influence of  $\alpha_1$  (Collector area/pool surface area) on burn efficiency**

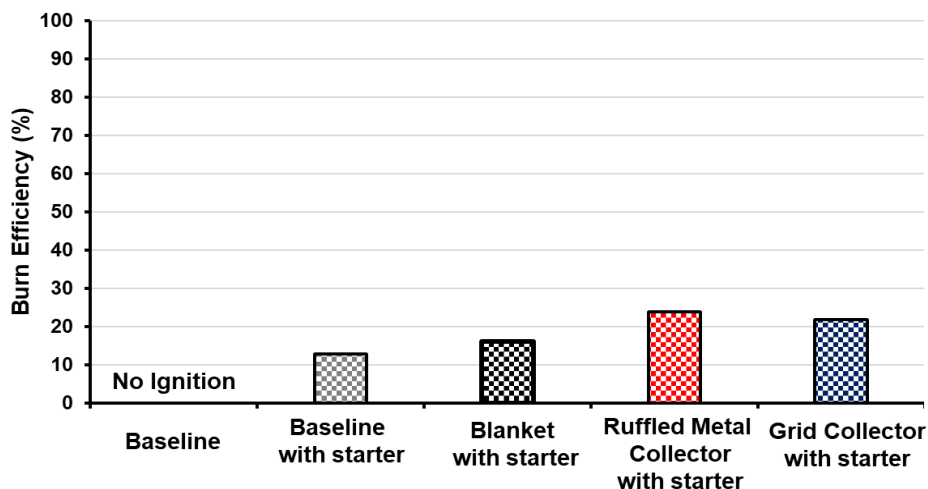
As shown in Fig. 30 the maximum enhancement in burn efficiency was obtained when  $\alpha_1$  (Collector area/pool surface area) is about 1.3. The optimum  $\alpha_1$  value will be used as a guideline to manufacture large-scale prototypes.

Figure 31 compares the burn efficiency of the baseline, blanket, multiple pike collector, and grid collector FRs in wavy water conditions with ANS crude oil.



**Figure 31 - Burn efficiency of the baseline, blanket, multiple pike collector, and grid collector FRs in wavy water conditions with ANS crude oil**

As shown in Fig. 31, the FRs were able to maintain the high burn efficiency even in high waves (Wave-2 in Table 4). Figure 32 compares the burn efficiency of the different FRs in stagnant water conditions with water-ANS emulsion. The procedure of creating emulsions is described in Appendix B.

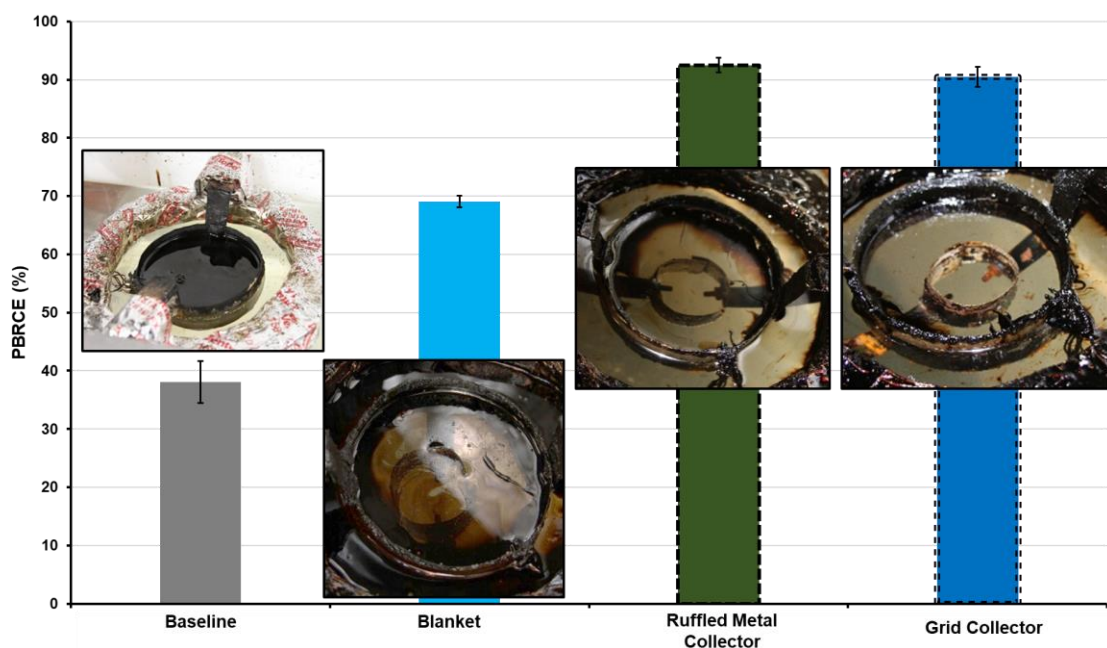


### Figure 32 - Burn efficiency of the baseline, blanket, multiple pike collector, and grid collector FRs in stagnant water conditions with water-ANS emulsion

As a first attempt, a torch was used to ignite the 25% emulsion. The emulsion could not be ignited with a torch. In this context, a 0.4 cm heptane layer was added as a starter fuel to the surface of the emulsion. The objective was to ignite the emulsion and achieve a self-sustaining steady-state burn. As shown in Fig. 31, self-sustained burning was achieved with the addition of a starter. With the introduction of FR with multiple pikes ruffled collectors the burn efficiency of the emulsion increased to 22%.

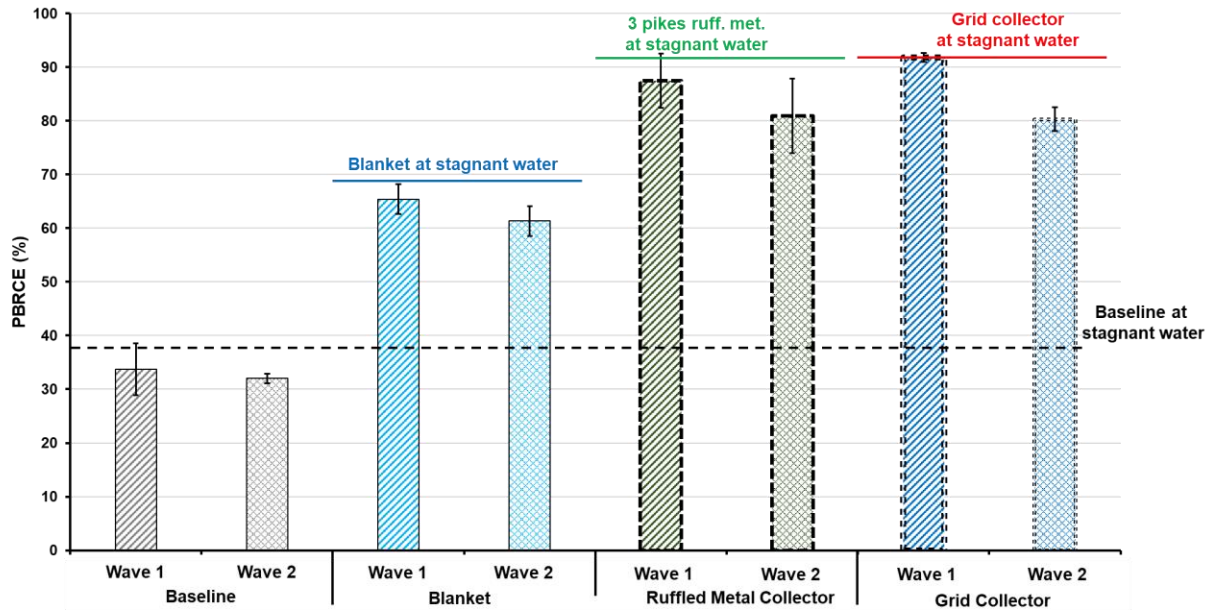
### Post-burn Residue Clean-up Efficiency

Post-burn residue clean-up efficiency (PBRCE) is the ratio of the mass of residue that remains on the water surface to the initial oil mass. PBRCE considers both the burnt residue and the residue stuck in the blanket. Figure 33 compares the PBRCE of different FRs in stagnant water conditions with ANS crude oil.



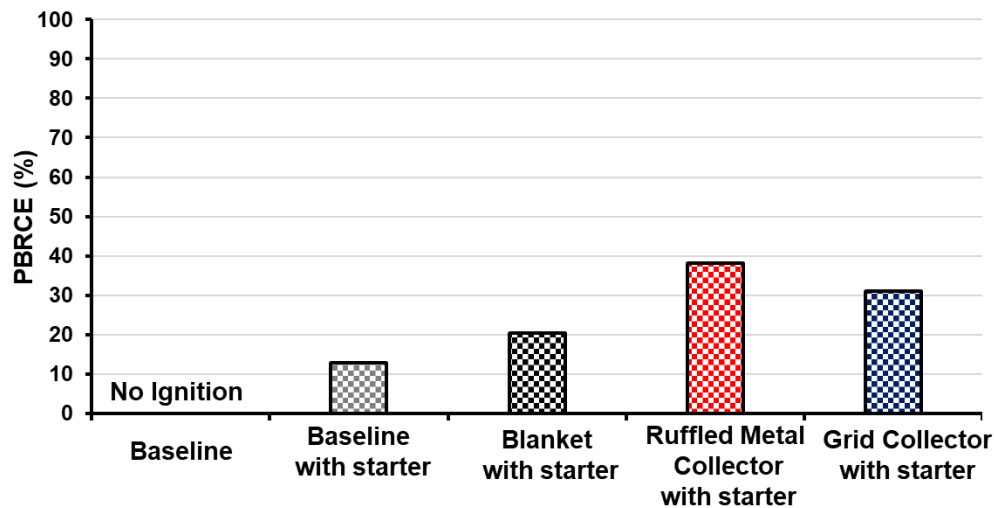
**Figure 33 - PBRCE of the baseline, blanket, multiple pike collector, and grid collector FRs in stagnant water conditions with ANS crude oil**

As seen from Fig.33, FRs with ruffled metal (3 cm high 3 pikes) and grid collectors removed ~90% of the oil from the water surface. This is about 3 times the baseline case. Figure 34 shows the PBRCE for the wavy conditions.



**Figure 34 - PBRC of the baseline, blanket, multiple pike collector, and grid collector FRs in wavy water conditions with ANS crude oil**

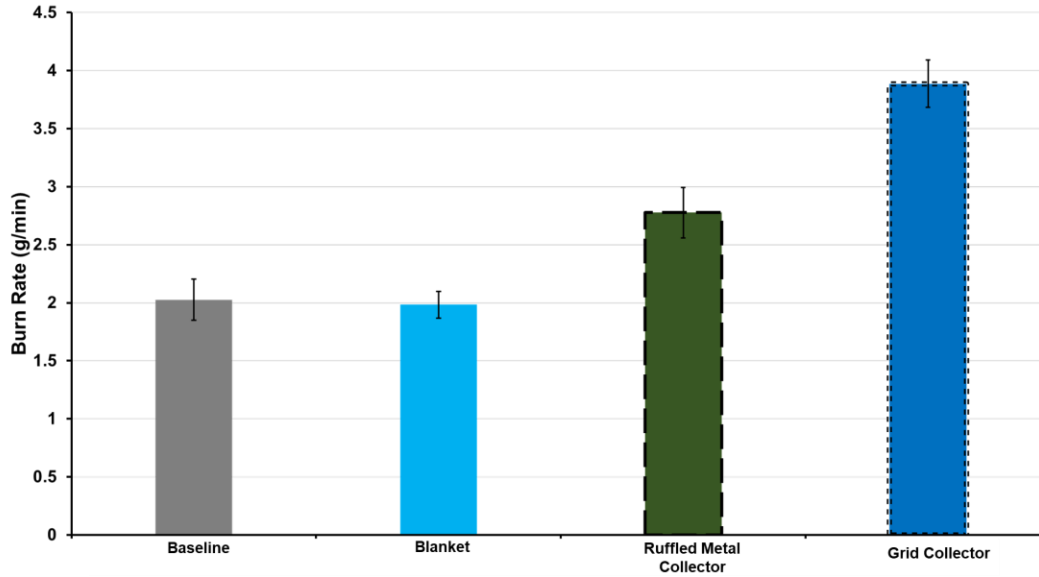
The wave action did not affect the PBRSE of the FRs with ruffled metal and grid collectors. Most of the oil (~90 %) was removed from the oil surface (Fig. 34). Figure 35 shows the PBRCE for the emulsion tests under stagnant water conditions.



**Figure 35 - PBRC of the baseline, blanket, multiple pike collector, and grid collector FRs in stagnant water conditions with water-ANS emulsion**

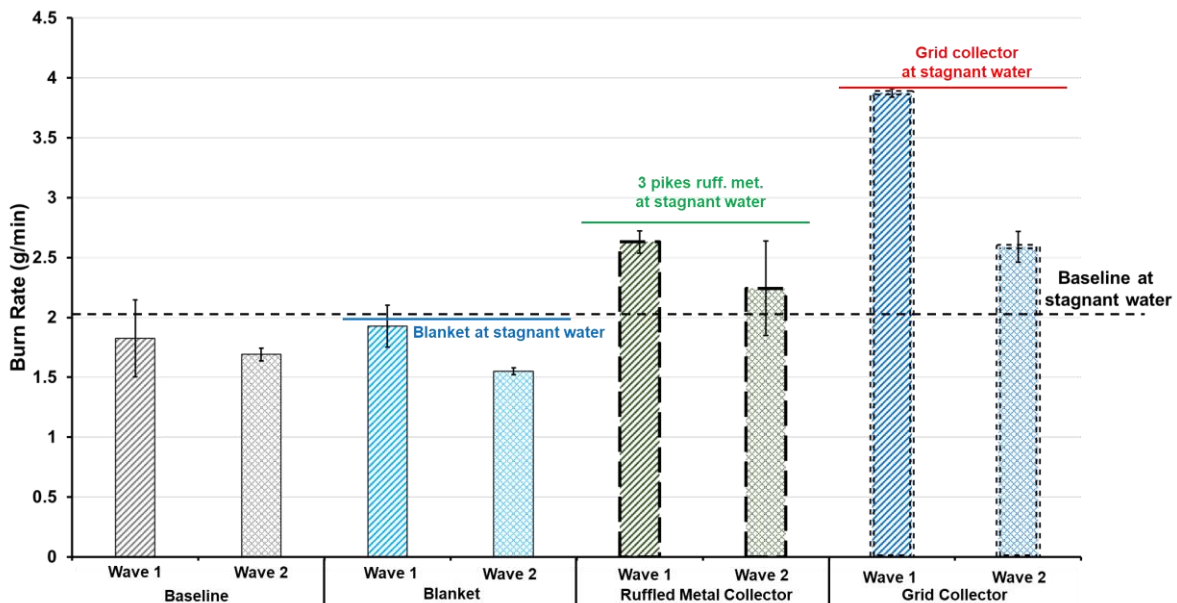
### Burn Rate

The burn rate for the experiments is determined both experimentally and numerically. Experimentally the mass of oil consumed by burning is measured as the mass put into the pan minus the mass of oil remaining at the end of the experiment. Figure 36 compares the burn rate of different FRs in stagnant water conditions.



**Figure 36 - Burn rate of the baseline, blanket, multiple pike collector, and grid collector FRs in stagnant water conditions with ANS crude oil**

Although the burn efficiency was increased with the introduction of the blanket, the burn rate did not change. The blanket promoted a longer burn with the same burn rate as the baseline. The burn rate significantly increased for the grid collector by reaching a maximum value of 3.8 g/min. This is about 2 times the baseline case. Figure 37 compares the burn rate of different FRs in wavy water conditions.



**Figure 37 - Burn rate of the baseline, blanket, multiple pike collector, and grid collector FRs in wavy water conditions with ANS crude oil**

As shown in Fig. 37, the ruffled metal and grid collector continued to burn faster in wavy conditions. To validate the experimental data a numerical study was performed. Numerically a correlation developed by Garo et al. which was developed to predict the time to boil over of crude oil spilled on water, was used. Using the temperature data acquired from the thermocouples inserted into the floating pan the regression rate/the mass burning rate of the oil was calculated.

In the correlation  $T_b$  is the boiling point of the fuel,  $T_1$  is the measured temperature at  $x$  depth from the surface,  $\alpha$  is the thermal diffusivity of the fuel, and  $T_\infty$  is the temperature as  $x \rightarrow \infty$  or as we get as far from the surface as possible. Using these parameters and the equation below we can calculate regression rate  $r$  (m/s), and then find mass burning rate (g/s).

$$\frac{T_1 - T_\infty}{T_b - T_\infty} = \exp\left(-\frac{r}{\alpha}x\right)$$

We performed this calculation on a select number of FR types and only on the no wave case tests. The correlation predicted mass-loss rate well (10-25% error) until the highest performing FR's. At this point, where the FR has such a strong impact on the fuel temperatures, that the correlations assumptions no longer remain valid, and the results start to break down.

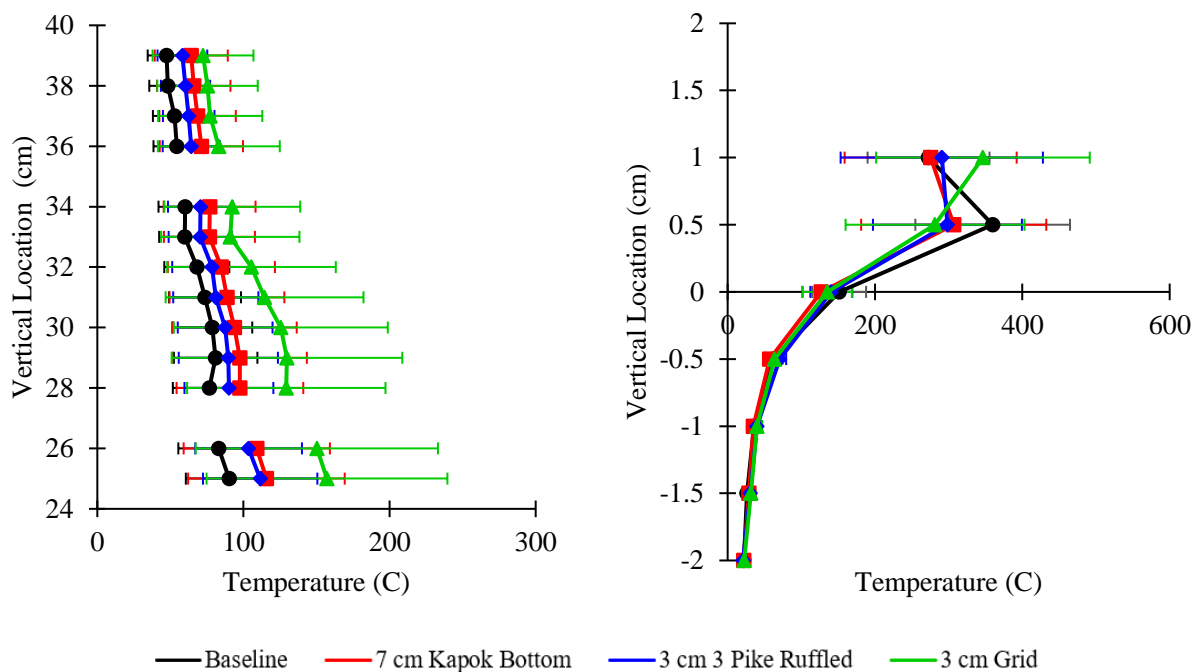
**Table 6 - Comparison of the experimental vs numerical MLR**

Mass Loss Rate (g/s)			
Test ID	Experimental (g/s)	Numerical (g/s)	Error
Baseline	0.0325	0.0371	12%
Blanket	0.0331	0.0374	12%
Multiple pikes ruffled metal collector	0.0463	0.0319	45%
Grid collector	0.0648	0.0325	100%

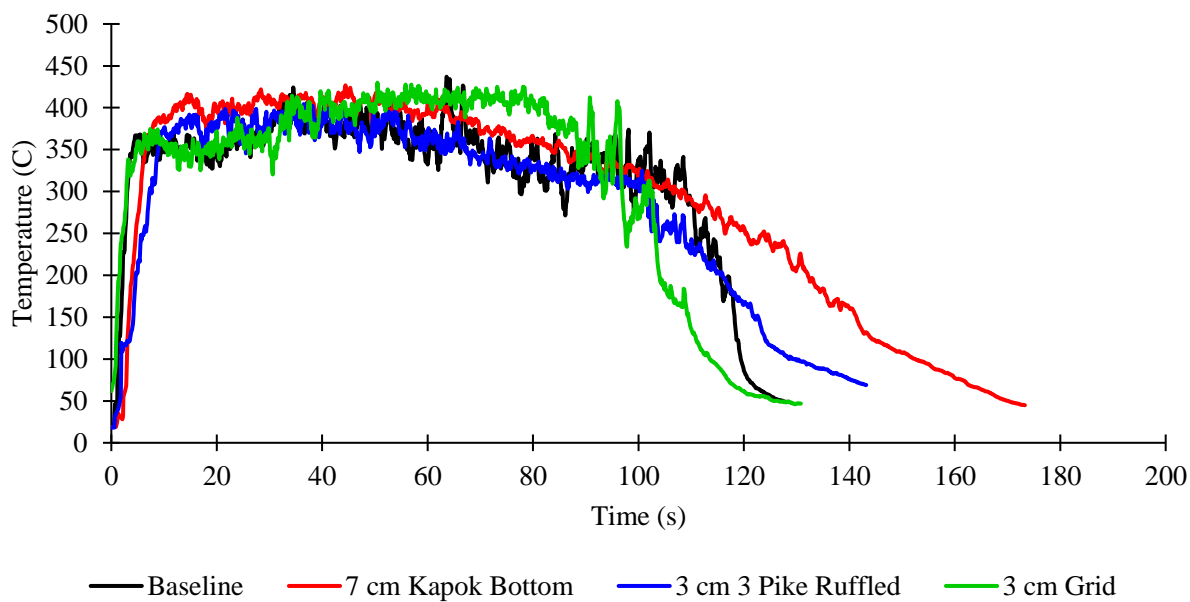
### Temperature Profiles

The thermocouple data is averaged in two ways, in time and space. The time-averaged data is averaged over the whole burn time for a given location while space averaged data is the average at each time step of two locations in the flame region. For both of these methods, the data of at least two runs is also averaged.

For the time-averaged data, there are two regions of interested the plume locations (25 to 39 cm above the fuel surface) and the near flame region (1 cm above to 2 cm below the fuel surface). Figures 38 and 39 represent 4 cases – baseline, blanket FR, ruffled FR and the grid FR. In the stagnant water conditions (no waves) the 3 cm grid (green line) performs the best, with the highest temperatures in the plume and near flame region and the shortest burn time.



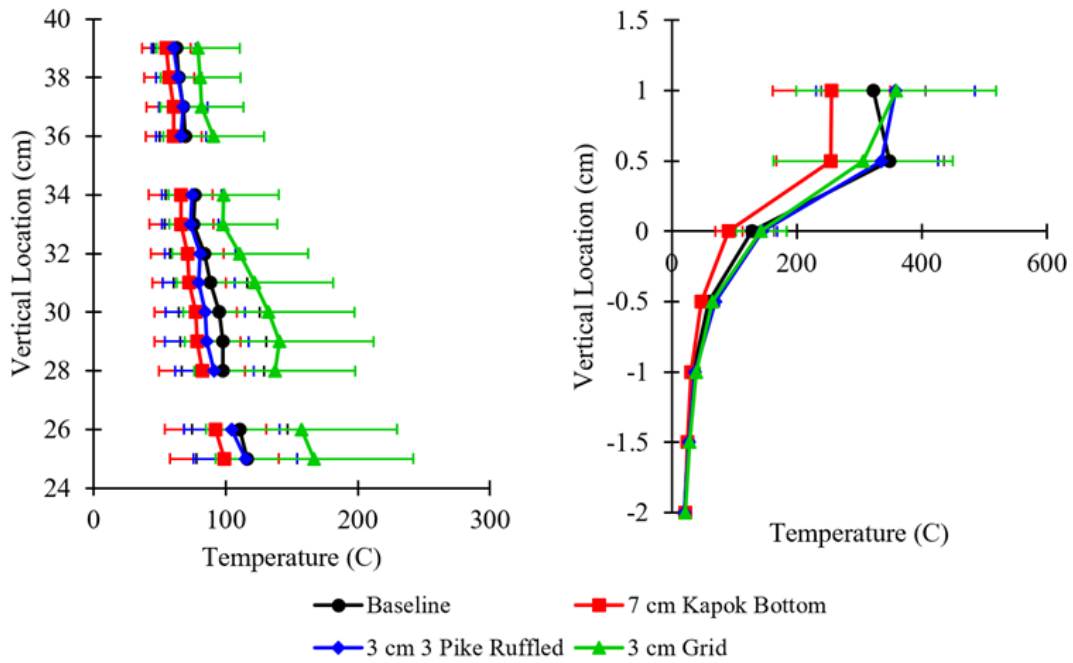
**Figure 38 - Time-averaged temperature data for plume and near flame regions for no wave tests**



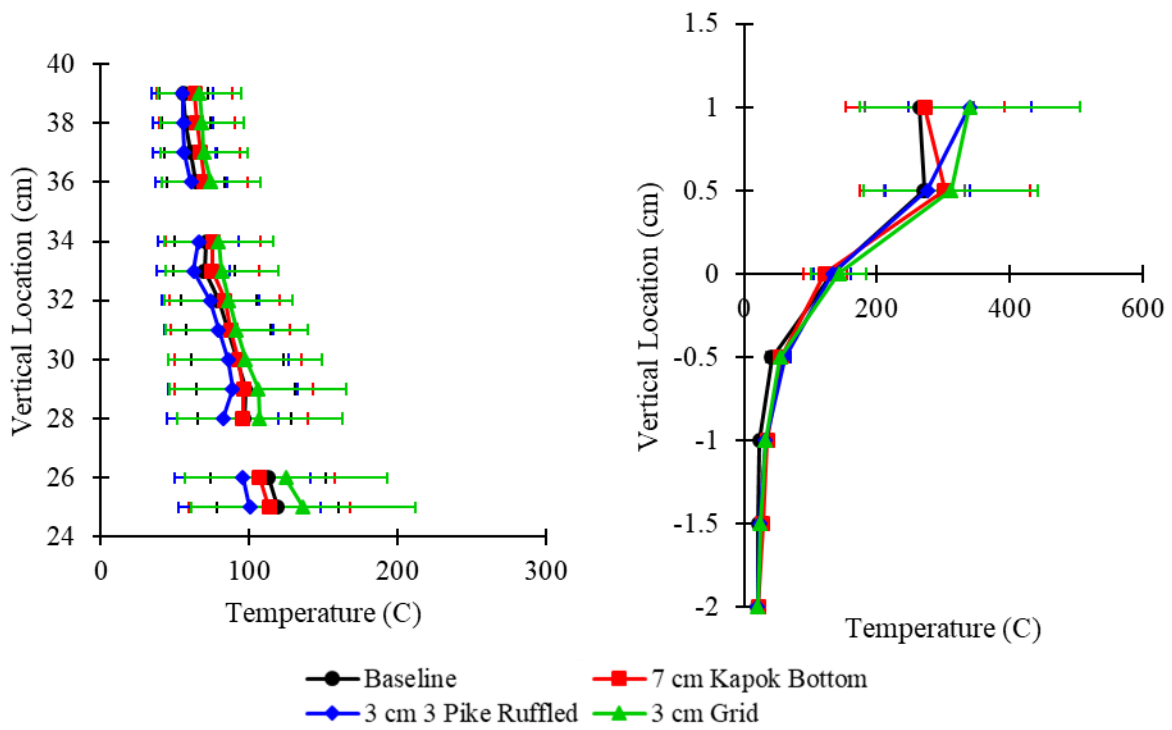
**Figure 39 - Flame region averaged for whole burn duration for no wave tests**

Two wave conditions are shown in Figures 40 and 41. From these figures, it is clear that the grid FR increased the plume temperature over the baseline and has comparable flame region (1 to 0 cm) temperatures to the baseline, while the multiple pikes ruffled, and the blanket has lower temperatures than the baseline. This increase is larger at Wave 1 than Wave 2 but is still significant at higher waves.



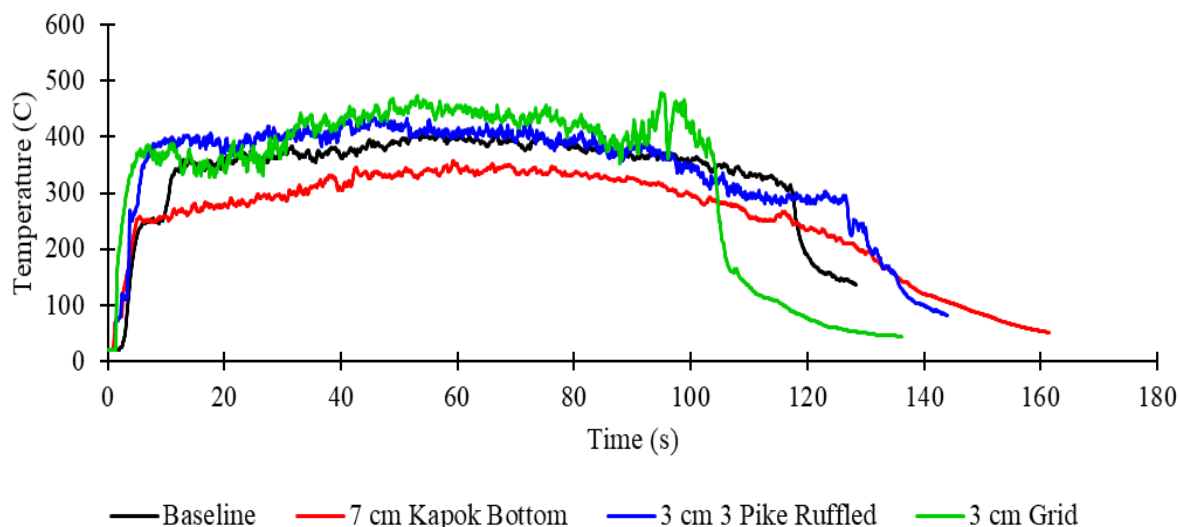


**Figure 40 - Time-averaged temperature data for plume and near flame regions for Wave – 1**

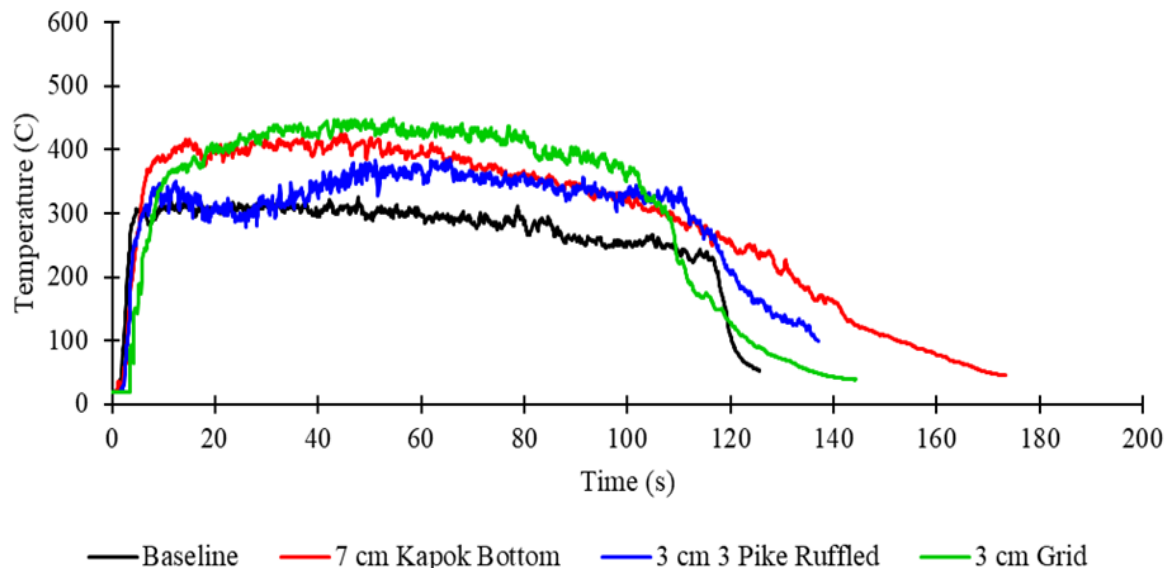


**Figure 41 - Time-averaged temperature data for plume and near flame regions for Wave – 2**

The data from the two thermocouples in the flaming region (1 and 0.5 cm above the fuel surface) are averaged together and plotted for the entire burn duration in figures 42 and 43. This look at the temperature data shows that the grid has the highest flame region temperatures and has a comparable burn time to the baseline. The blanket with the kapok at the bottom has the longest burn time and has lower temperatures than the baseline at Wave -1 but is hotter than the baseline at Wave -2. The multiple pikes ruffled metal FR is hotter than baseline for both wave conditions but has a longer burn time and lower temperatures than the grid FR.



**Figure 42 - Flame region averaged for whole burn duration for Wave – 1**



**Figure 43 - Flame region averaged for whole burn duration for Wave -2**

In total, from the temperature data for crude oil burn in wavy water, the grid FR provided hotter plume temperatures across the burn duration, short burn duration, and hotter near flame

temperatures when compared to the baseline cases. This is in line with the burn efficiency and clean-up efficiency data that shows the grid FR as most effective.

### **Outcomes of Phase I-b**

In Phase I-b a wave tank was designed and constructed to test small-scale prototype FR for their ability to burn fresh and emulsified crude oil under various wave conditions. Based on the small-scale tests 4 prototypes were chosen to advance to large-scale crude oil burning experiments into Phase II.

### 3. Phase II – CRREL Testing

#### Site Overview

Phase II experiments were conducted at the Cold Regions Research and Engineering Laboratory (CRREL) in Hanover, NH between 9/21/2020 and 10/9/2020. The CRREL facility possesses a large wave tank capable of conducting burning experiments, which was critical for this stage of development of the Flame Refluxer. The first week of testing (9/21-9/25) consisted of setup and preparation for the resulting two weeks of testing to be conducted. The second week (9/28-10/2) consisted of HOOPS crude oil burning experiments with and without Flame Refluxers. The third week (10/5-10/9) moved forward to testing with 25% water emulsions and bunker fuels.

The main testing facility for this phase of experiments consisted of the large wave tank and surrounding facilities. The wave tank is located on a concrete pad, with an observation hill at one end, and observation scaffolding placed at the other end. A shed sits next to the tank to house instrumentation and data collection equipment, as well as the wave generation equipment.

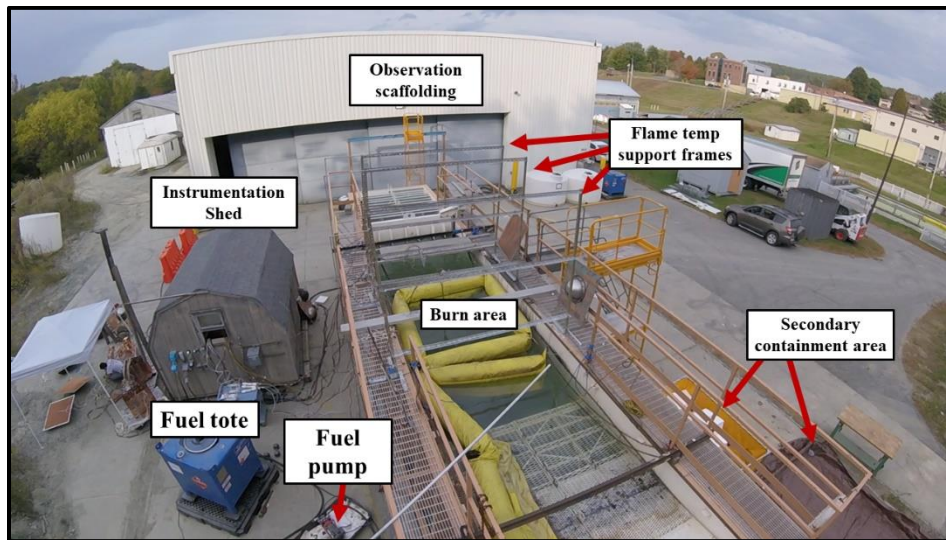


**Figure 44 – Cold Regions Research and Engineering Laboratory wave tank facility, the testing site for Phase II**

The CRREL wave tank has a total length of 15.5m (50.8 ft), a width of 2.5m (8.2 ft), and a depth of 2.25m (7.4 ft). The tank is fitted with a hydraulically driven wave board at one end. Passive wave absorbers at both ends suppresses the reflected waves. With 1.8 m (5.9 ft) of water depth in the tank, the wavemaker can generate waves with heights to 0.6 m (2') with periods ranging from 1.7 to 3.3 seconds. An American Fire boom was used to create a 1.9 m x 1.7 m contained burn area inside the wave tank. A large field of view cameras was placed on the scaffolding as well as on the hill, both looking over the tank into the testing area. Distances from these cameras to the burn area are shown in Fig 44 with another overview perspective in Fig 45.



**Figure 45 - Overhead view of the wave tank site, showing linear distances to key locations**



**Figure 46 - View of fully prepared testing location, showing fuel containment boom and other testing apparatus**

## Instrumentation Overview

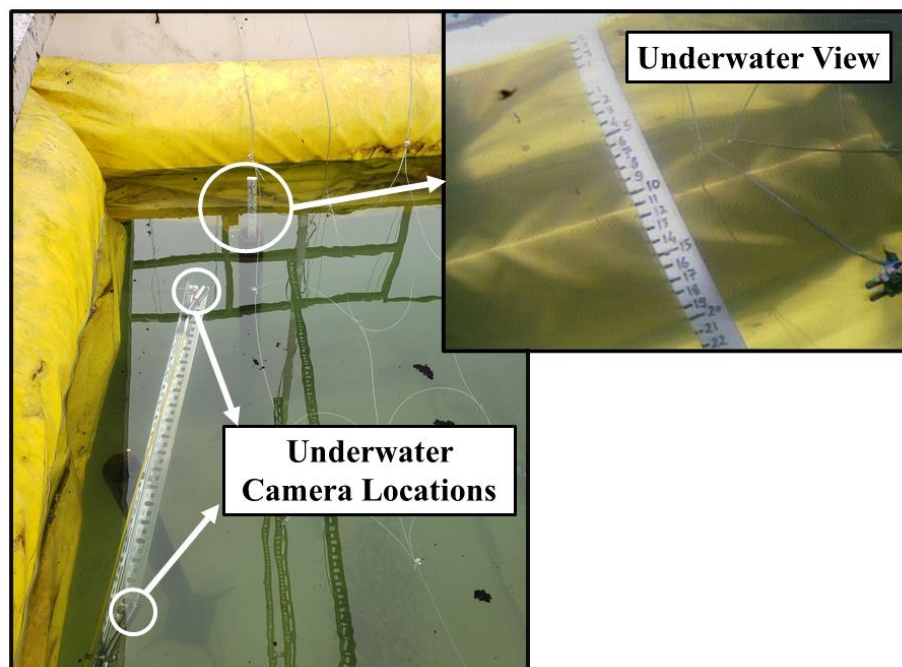
A large collection of instrumentation was used to capture data about the Phase II experiments. An Akamina AWP 24-3 wave gauge and a 1m wave probe were used to verify wave heights and periods. Initial fuel content for each experiment was measured by weight using a Computer scales Accuset II load cell set as the fuel was pumped into the experiment containment area. The remaining fuel residue was measured post-experiment using a similar load cell, set up inside of a secondary containment area.





**Figure 47 - (left) Fuel tote placed on load cells to measure the amount of fuel added to each experiment. (right) Load cells in a secondary containment area to measure fuel residue on FR's**

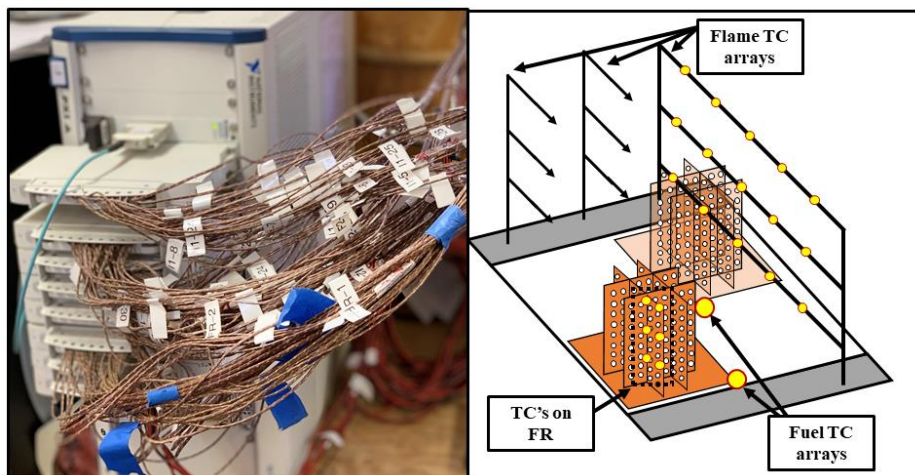
Two underwater cameras were placed in the wave tank along with an accompanying Teflon linear measurement scale, shown in Fig 48. The objective of this equipment was to get live-feed information about the fuel thickness and resulting regression rate. The method was used with varying levels of success throughout the course of the two burn weeks.



**Figure 48 - Underwater cameras placed with a view of a teflon measurement stick to monitor fuel thickness throughout the experiments.**

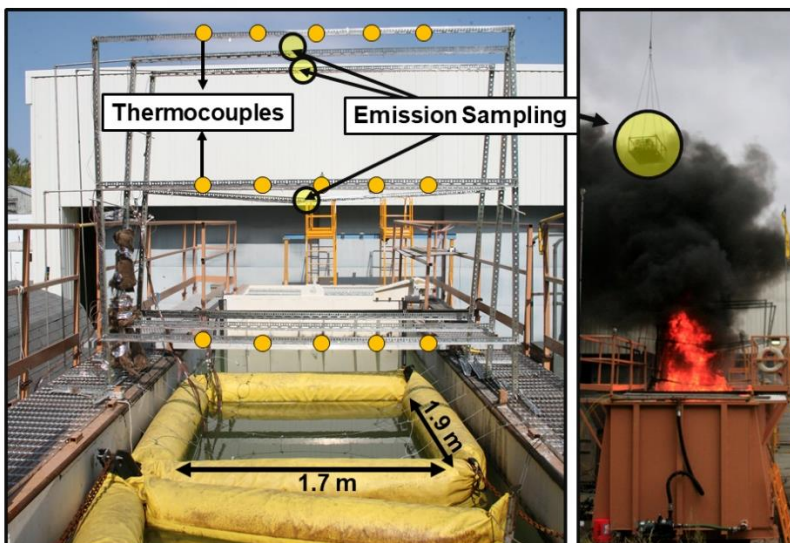
## Thermocouples

Over 140 thermocouples (TC's) were used to monitor temperatures over the course of the experiment. The three thermocouple groups consisted of the flame TC array, liquid TC array, and FR TC array.



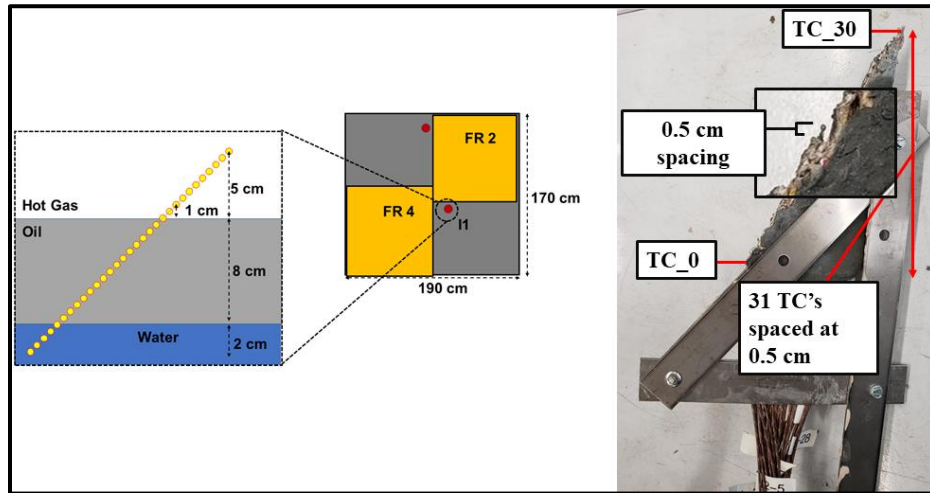
**Figure 49 - (left) Data acquisition module with thermocouple wires (right) Sketch showing TC locations in yellow**

As shown in Fig. 50 the flame TC array consisted of 45 thermocouples secured to a water-cooled metal support frame placed above the burning pool in the flaming region. Three emission sampling points were also placed on this metal frame as shown.



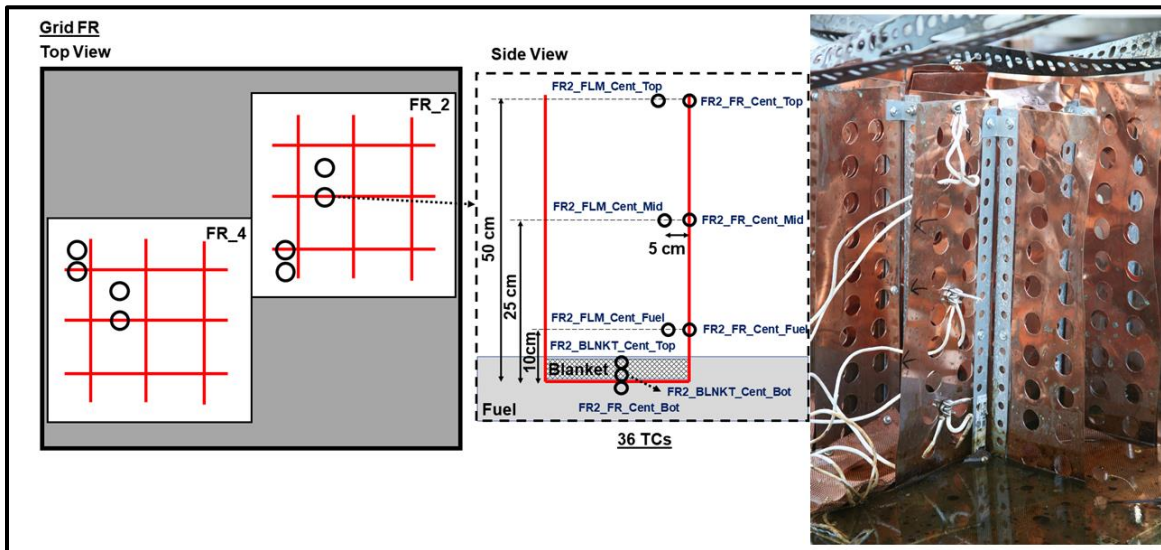
**Figure 50 - (left) flame thermocouple array placed over the burn area, with TC locations outlined in yellow, and emissions sampling points also labeled. (right) Crane emissions sampling point.**

The liquid TC arrays consisted of two custom fabricated TC ‘trees’ which contained 31 thermocouples, each spaced precisely 0.5 cm apart. One of these TC arrays was placed as close as possible to the center of the burn area, and the other was placed towards the edge of the burning pool. These thermocouples successfully measured the fuel and water temperatures over the course of the experiments.



**Figure 51 - Liquid TC arrays were used to monitor temperatures inside of the fuel layer.**

The final TC array consisted of the thermocouples placed on the FR's themselves. Each FR had 36 thermocouples placed at strategic locations along its height and width. Some TC's measured the metal temperature of the FR directly, while others measured the gas or liquid fuel temperatures directly adjacent to the FR. Shown for demonstration in Fig. 52 below is the grid FR with its TC locations.



**Figure 52 - 36 Thermocouples were placed on the FR's to monitor metal temperatures and adjacent gas temperatures.**



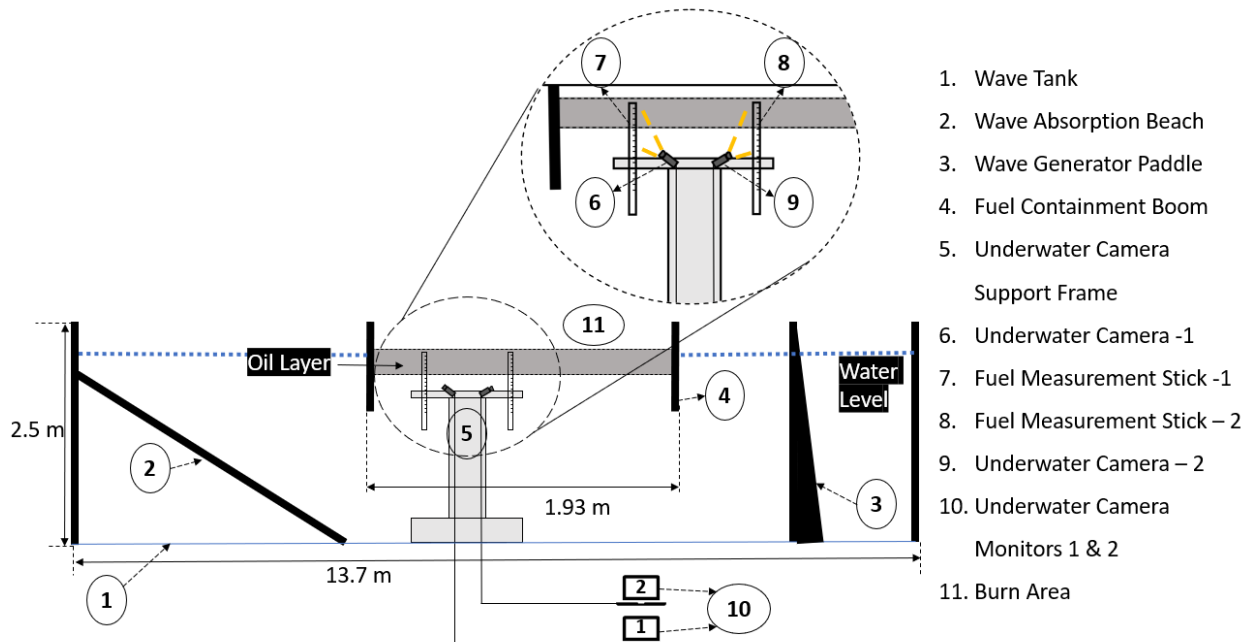
In total 24 experiments were conducted over the two-week burning period. Cases with and without FR's, with and without waves, and with various fuels and thicknesses were all tested. The full experimental matrix is detailed in Table 7.

**Table 7 - Phase II Experimental Matrix**

Name	Date	Fuel	Fuel Weight (kg)	Density (kg/l)	Slick Thickness (cm)	Rain	Wave	
							Period (s)	Wave Height (cm)
Baseline	9/28	HOOPS	225	0.784	8.10	No	-	
Ruffled	9/28		221	0.784	7.96	No	-	
Grid	9/28		225	0.784	8.10	No	-	
Bimetal	9/29		223	0.784	8.03	No	-	
Grid	9/29		226	0.784	8.14	No	-	
Blanket	9/30		230	0.784	8.28	No	-	
Baseline	10/2		228	0.784	8.21	Yes	2.5	7
Baseline	10/5		225	0.784	8.10	No	4	14
Grid	10/1		226	0.784	8.14	No	2.5	7
Grid	10/1		225	0.784	8.10	No	4	14
Solo Grid	10/1		229	0.784	8.24	No	2.5	7
Bimetal	10/1		227	0.784	8.17	No	2.5	7
Bimetal	10/2		227	0.784	8.17	Yes	2.5	7
Baseline	10/5	Emulsion (25% salt water – 75% HOOPS)	68	0.86	2.45	No	-	
Baseline	10/5		77	0.86	2.77	No	1	4
Baseline	10/5		73	0.86	2.63	No	2.5	10
Baseline	10/5		73	0.86	2.63	No	2.5	20
Baseline	10/6		68	0.86	2.45	No	-	
Bimetal	10/8		109.3	0.86	3.93	No	-	
Baseline	10/8		110.2	0.86	3.97	No	-	
Baseline	10/6	Bunker	27.3	0.94	0.90	No	-	
Baseline	10/7		35.4	0.94	1.17	No	1	4
Bimetal	10/7		36.1	0.94	1.19	No	1	4
Bimetal	10/7		33	0.94	1.09	No	-	

## Regression Analysis

An underwater camera was used to monitor the regression of the fuel layer overtime for the experiments conducted at CRREL – phase II of the project. The setup consists of 2 fuel gauge sticks ( measuring stick 1 & measuring stick 2) seen in Fig. 53, made of Teflon material because of its hydrophobic surface properties and ability to withstand high temperatures. Both the measuring sticks (gauge) were indented with markings to distinguish the fuel level in cms and placed at a position to cover both the fuel and the water layer under it.



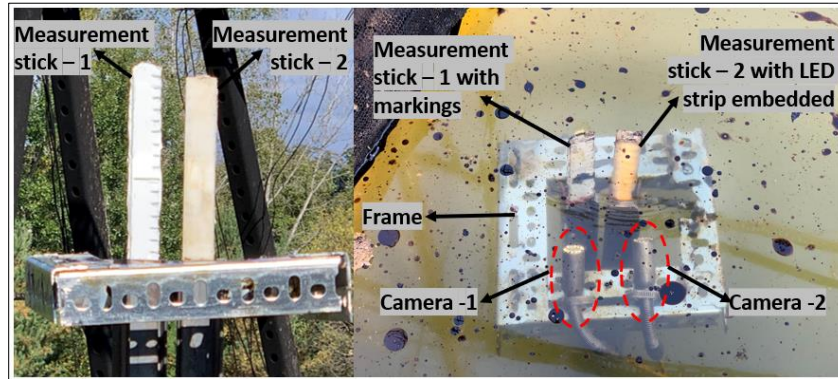
**Figure 53 - Cross-sectional representation of the wave tank with the underwater camera setup used to monitor the fuel level regression**

The measuring stick – 2 was grooved and embedded with a 12 v LED strip inside the stick (fig 54), with the advantage of illuminating in dark and providing clear visuals of the fuel level.



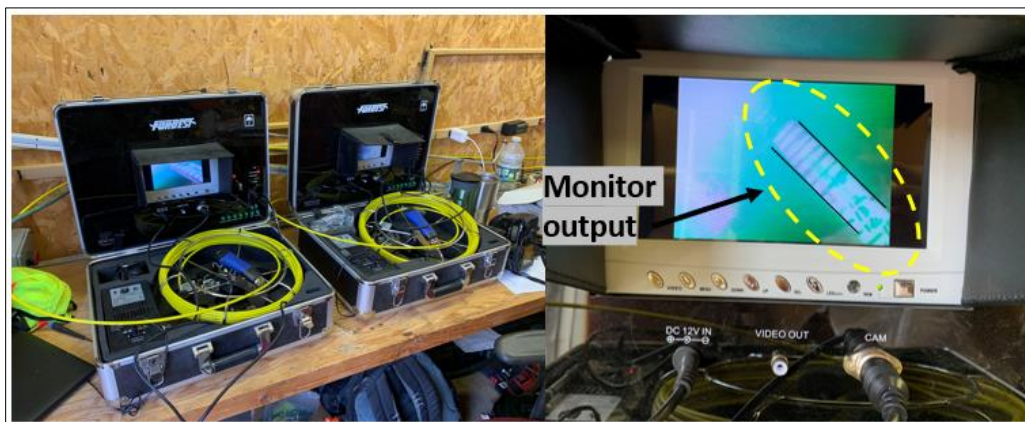
**Figure 54 - Measuring stick – 2 fitted with LED strip; measuring with grooves for LED strip that is to be embedded (left), LED strip (mid), and completed measuring stick fitted with LED's**

The measurement sticks were monitored by two Forbest 23 mm CMOS underwater cameras (0.3 MP, color) with built-in white LED lights. The cameras that were mounted were equipped with 120° field of view and vision capability up to 400 mm. The cameras were supported by a rigid metal frame, able to withstand different waves tested in the wave tank seen in fig 55.



**Figure 55 - Measurement sticks 1 & 2 used for recording regression rate mounted on the metal frame (left) and complete set with the cameras pointing towards the measurement stick (right)**

The metal frame supporting the fuel measurement cameras rested at the bottom of the wave tank in the boom containment area under the FR prototypes as seen in Fig 53. The cameras communicated through fiber optic cables and the visuals from the underwater camera setup were monitored outside the wave tank. The monitors from the cameras were capable of outputting video images of 1140 x 234-pixel resolution and with an inbuilt ability to record images and videos in real-time seen in fig. 56 below.

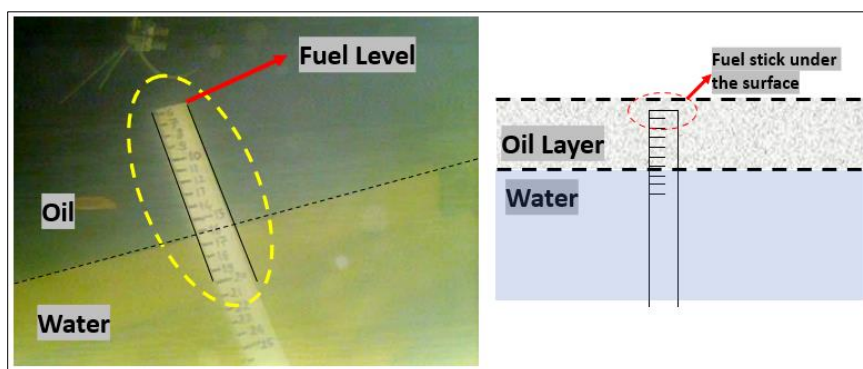


**Figure 56 - Underwater camera output stations used to record regression rates**

## Regression rate measurement

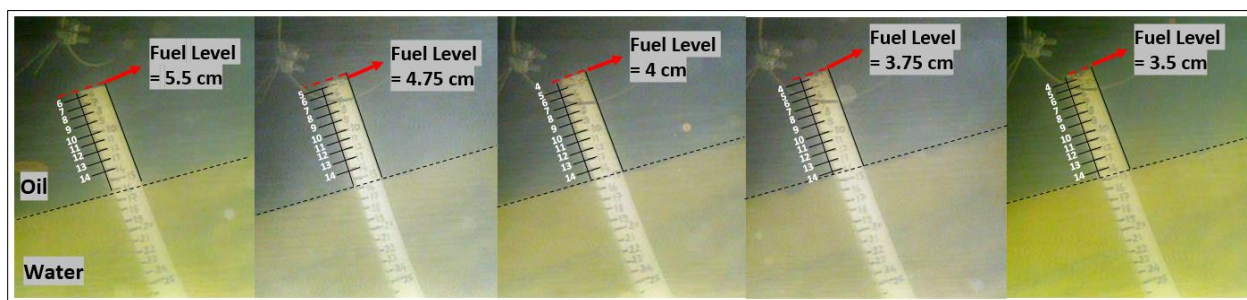
The 2 underwater cameras were used simultaneously to record the fuel regression rate depending on the view the camera provided. From fig 57 it can be seen that the receiving monitors provided a definitive view of the fuel thickness, the water layer, and the markings on the stick captured the exact fuel levels.

The position of the measurement sticks does not necessarily measure the exact fuel thickness of the experiment but is only used as a reference to monitor the regression of fuel over a time period. Fig. 57(right) shows the line diagram of the placement of the measuring stick, it can be seen that the measuring stick is not exactly at the fuel surface but below the fuel surface with a clearance between the measuring stick and the fuel surface.



**Figure 57 - View from the camera output outlining the clear view of oil, water, and fuel level from the scale (left), the placement of the measuring stick in the fuel water layer (right)**

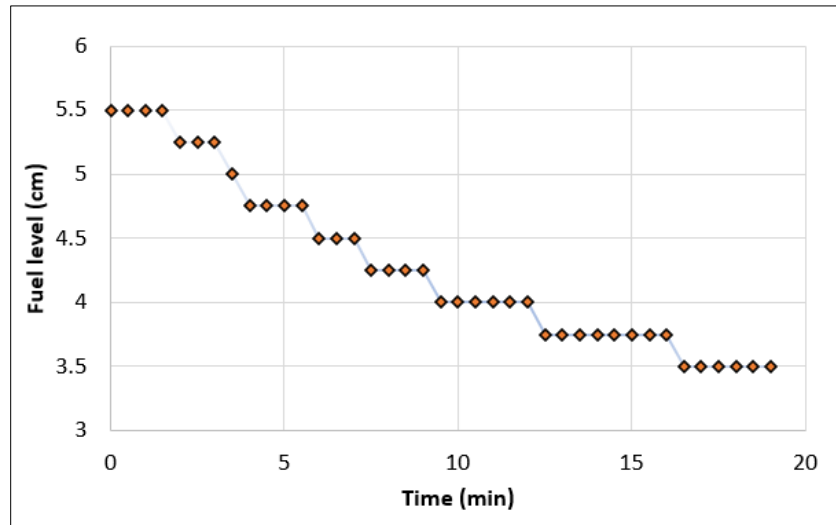
Figure 58 shows the example of the visuals seen on receiving monitors for the baseline case – no wave with HOOPS crude oil at 5-minute intervals. Fuel thickness regressing over time can clearly be seen from the fig below



**Figure 58 - View from the camera output outlining the clear view of oil, water, and fuel level from the scale for baseline case with HOOPS crude oil without waves observed at 5-minute intervals**

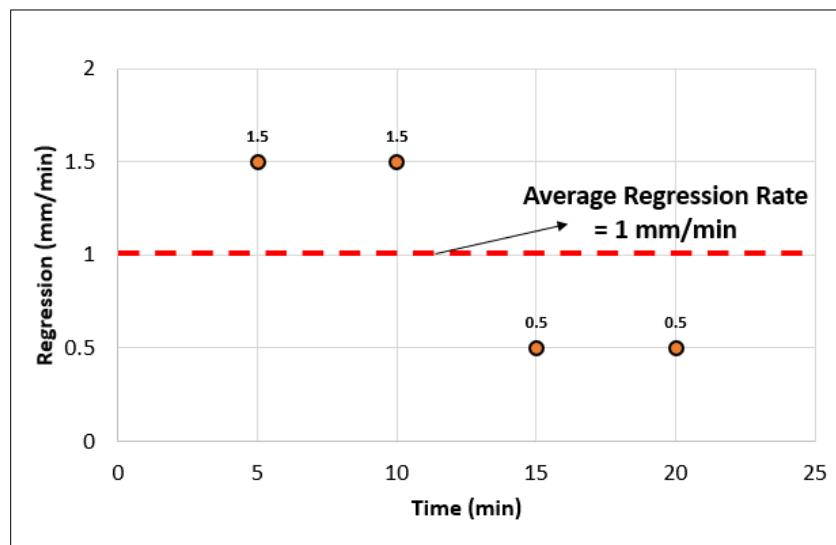
Experiments were monitored and recorded from the underwater cameras at 30 second time intervals to study regression of fuel level systematically and the same observed recordings were

used to calculate the average regression rate for most of the cases. Figure 59 below represents the recordings from the baseline experiment with HOOPS crude oil without the presence of waves, the corresponding change in fuel thickness vs time plot recorded from the underwater cameras. It can be seen that regression for baseline case progresses negatively from 5.5 cm to 3.5 cm over time, also seen in the captured pictures in fig. 6 at 5-minute intervals.



**Figure 59 - Plot for fuel level vs time - measurements recorded with an underwater camera in 30 second time intervals**

Figure 59. is then converted into a regression rate (mm/min) plot. Fig 60 below shows the regression rate plotted vs time at 5 min intervals for baseline case with HOOPS crude oil without the presence of the waves as an example. The corresponding regression plot gives the overall distribution of the regression rate at 5 min intervals, and the average of the distributed regression rate gives the average regression rate of the experiment.

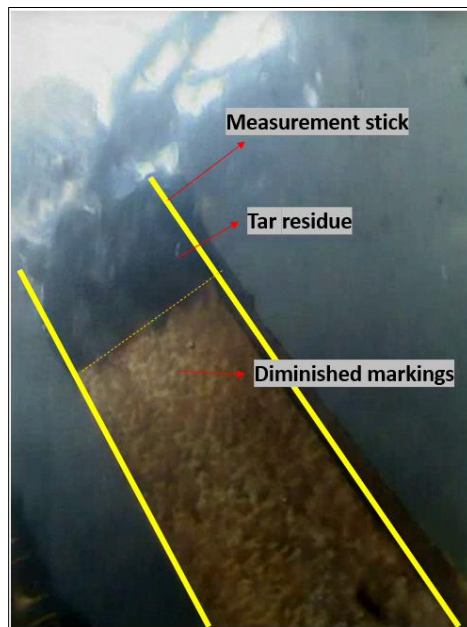




**Figure 60 - Plot for regression rate vs time - measurements recorded with an underwater camera for 5 minute time intervals**

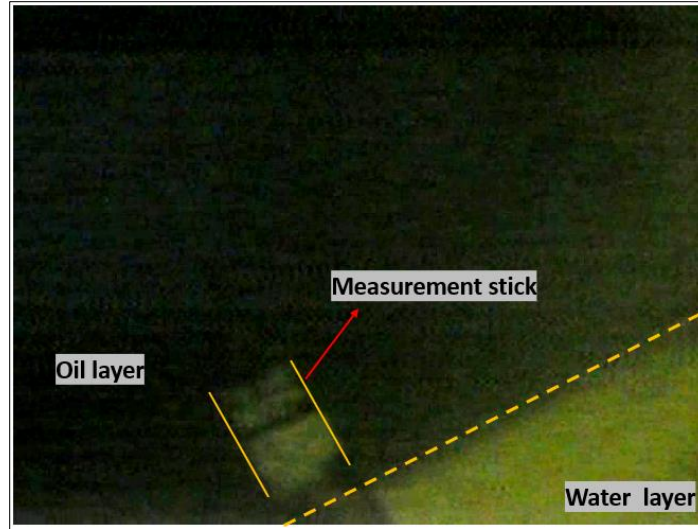
The underwater camera with the progressing number of experiments started to wear out with time and also the influence of the waves on the camera had adverse effects. The camera setup worked best when the burn area was not subjected to any turbulence. The underwater camera in the further tests was not used because of the following reasons,

- i. As the number of experiments increased the markings on the measuring stick started to wear out and the left-over residue from the burn eventually clouded the measuring stick with tar seen in fig 61. The addition of the wave also added to the complexity.



**Figure 61 - Unclear view of the measurement stick clouded with tar residue from the burn**

- ii. Since the tank was filled only once with fresh water at the start of the first experiment, It is most clear for test 1 and the clarity of water deteriorates as the number of tests increases. The addition of high turbulence in the system results in a bad depth of view of the camera and the residue particles from the tests also start moving in random motion, thus making it difficult to register any clear images of the measuring stick. From fig. 62 it can be seen that the camera fails to register a clear view of the measuring stick because of cloudy water, the demarking lines for fuel regression are also blurry.



**Figure 62 - Unclear view of the underwater camera with prolonged use of the measurement stick and cloudy water surrounding it.**

The experiments after the underwater camera measurements were deemed unreliable, the regression rate is calculated as global regression rates instead of the average regression rate calculated previously. The global regression rate was calculated using the following equation,

$$\text{Global Regression Rate (mm/min)} = \left( \frac{\text{Fuel Thickness} \times \text{Burn Efficiency}}{\text{Total Burn Time}} \right) \times 10$$

Table 8 shows the summary of the tests performed at the CRREL – Phase II (1m scale). The regression rates calculated using the average regression rate from the underwater cameras are highlighted. And the remainder of the experiments that are not highlighted are calculated as global regression rate using the equation shown above

**Table 8 - Summary of experiments with wave profile, burn duration, regression rate, and their respective efficiency – CRREL Phase II (1 m burn)**

Fuel	FR	Wave Profile	Total Fuel Added (kg)	Fuel Thickness (cm)	Total Burn Time (min)	Residue Left (kg)	Regression Rate (mm/min)	Burn Efficiency (%)	Weather Condition
HOOPS	Baseline	-	225	8	16	97	1	57	Sunny
	Ruffled	-	221		19	93	1.4	58	
	Grid	-	225		20		-	-	
	Bimetal	-	223		39	16	1.8	93	
	Grid	-	226		84	14	1.8	94	
	Blanket	-	230		23	97	1.4	58	
	Baseline	(Wave 1) Period: 2.5 s Height: 7 cm	228		42	11	1.2	95	60% Rain 0.04 inch – Total Precipitation
	Baseline	(Wave 2) Period: 4 s Height: 14 cm	225		54	7	1.5	97	Sunny
	Grid	(Wave 1) Period: 2.5 s Height: 7 cm	226		48	2	1.5	99	
	Grid	(Wave 2) Period: 4 s Height: 14 cm	225		55	2	1.5	99	
	Solo Grid	(Wave 1) Period: 2.5 s Height: 7 cm	229		43	2	1.5	99	
	Bimetal		227		31	2	2	99	
	Bimetal		227		32	4.5	2.3	98	60% Rain 0.04 inch – Total Precipitation
25% Emulsion	Baseline	-	68	2.5	7	2.5	3.2	96	Sunny
	Baseline	(Wave 3) Period: 1 s Height: 4 cm	77		6	5	4.2	93	
	Baseline	(Wave 4) Period: 2.5 s Height: 10 cm	73		8	3.5	3.1	95	
	Baseline	(Wave 5) Period: 2.5 s Height: 20 cm	73		12	3.5	2.1	95	
	Baseline	-	68		7	4	3.2	94	
Bunker	Baseline	-	27	1	5	7	1.2	74	
	Baseline	(Wave 3) Period: 1 s Height: 4 cm	35		6	5	1.7	86	
	Bimetal		36		8	3.5	1.2	90	
	Bimetal	-	33		6	3	1.7	91	
25% Emulsion	Bimetal	-	109	4	12	18.5	2.6	83	
	Baseline	-	110		9	23	3.7	79	

From Table 8. we can see that the grid FR and the bimetal FR outperformed the baseline case with HOOPS crude oil without the presence of the waves. Both the grid FR and the bimetal FR performed higher with an overall efficiency of 93% and 94% respectively while maintaining an average regression rate of 1.8 mm/min until the first extinctions.



The grid and the bimetal FR still outperformed the baseline case with HOOPS crude oil in the wavy condition regressing at 1.5 mm/min and 2 mm/min respectively, while the baseline case regressed at 1.2 mm/min. That's a healthy 25% increase in burn rate for the grid FR and a 91% increase in the burn rate for the bimetal FR (rain conditions) compared to the baseline case with the wave 1 scenario. While the bimetal with 25% emulsions without the presence of the waves increased the burn time also increasing the efficiency of the burn, which in turn reduced the overall residue left at the end of the experiment.

Even with the heavier fuel like bunker crude oil, the bimetal FR without the presence of the waves showed a 30% increase in the burn efficiency, 42% increase in the burn rate from 1.2 mm/min with baseline case to 1.7 mm/min with bimetal FR.

## Flame behavior analysis

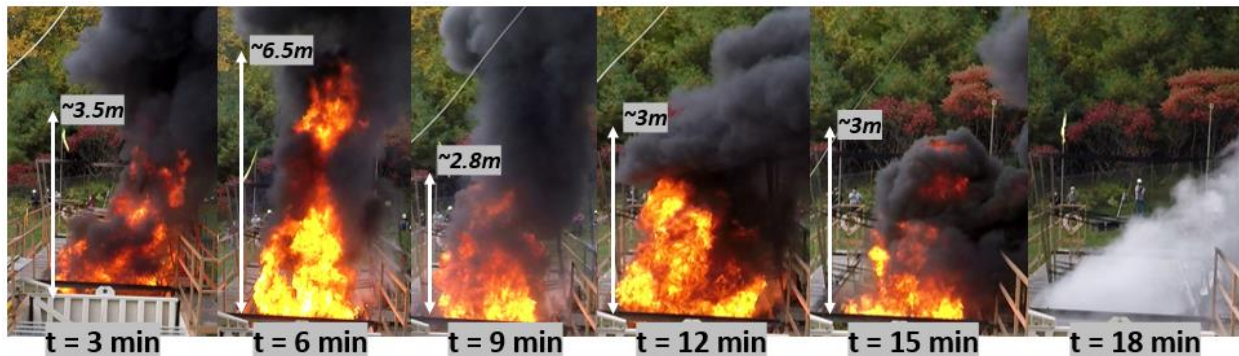
### Baseline

This section will discuss the propagation of the flame height for the baseline experiments also discuss the fire behavior in brief for different fuels and wave cases with no FR's.

#### 1. HOOPS crude oil

##### a. Baseline - No wave

In the baseline case with no wave conditions, the flames start with tall flames of ~3.5m in height from  $t = 0$  to  $t = 3$  min, then peaks to ~6.5m high flames at  $t = 6$  min. Then fire steadies itself from  $t = 9$  min to  $t = 15$  min with an average ~3m flame height, before it self-extinguishes at  $t = 16$  mins as seen in Fig 63.

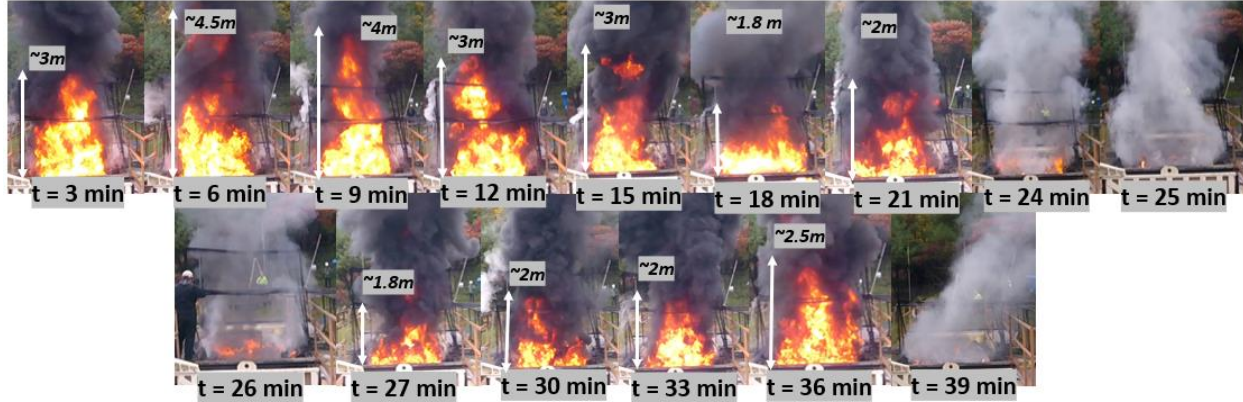


**Figure 63 - Flame behavior for baseline case – no waves with HOOPS crude Oil**

##### b. Baseline - Wave 1

The weather conditions for this particular test were rainy with 1 mm of total precipitation observed for the day. The baseline case with wave 1 starts with low flame (Fig. 64) height (~3m – ~4m) and propagates to tall flames at the quarter of the experiment from  $t = 10$  to  $t = 15$  min. The flames descent suddenly to a scenario with no flames at the center, flames can be only observed on the

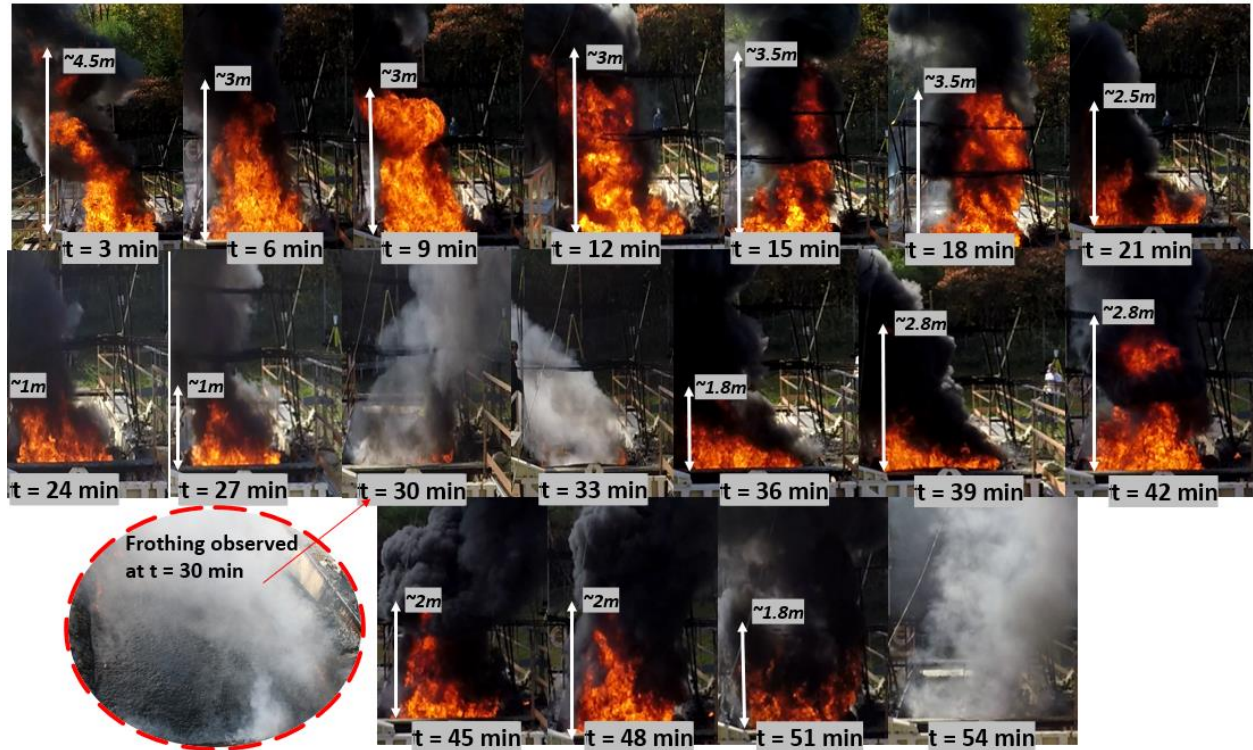
periphery. This might be caused due to foaming phenomenon, resulting in fuel to expand and extinguish the flames. Also, it is suspected the cooling effect and the flames held on the sides of the boom cause the fuel to cool down and reignite the fire in baseline case at  $t = 27$  min. the flames continue to grow until they self-extinguish at  $t = 39$  min.



**Figure 64 - Flame behavior for baseline case – Wave 1 with HOOPS crude Oil**

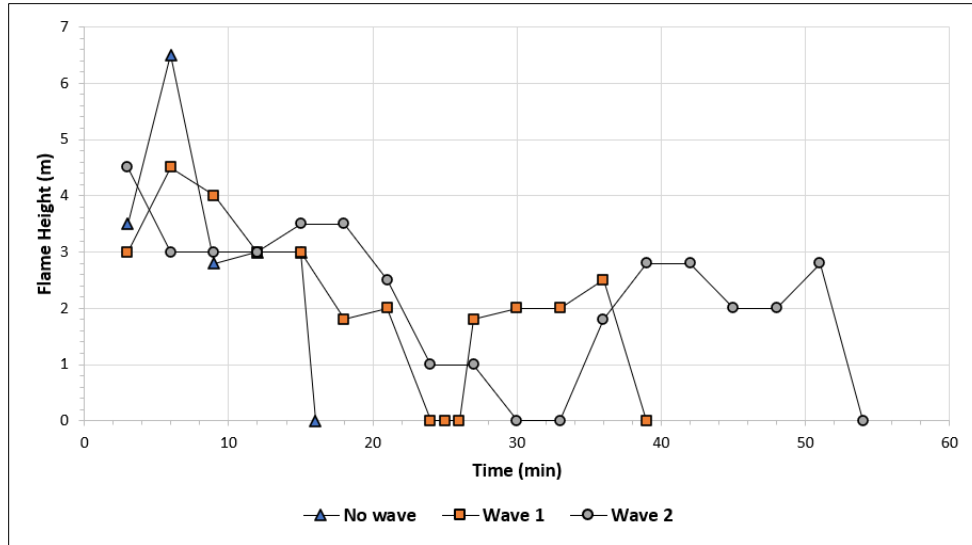
c. Baseline – Wave 2

The baseline with wave-2 behaves similarly and follows a trend alike wave 1 case where the flames start tall ~4.5 in and sustain an average flame of ~3m from  $t = 6$  to  $t = 18$  min. From  $t = 18$  min the flames start to reduce in height to a minimum and extinguish completely due to the foaming phenomenon observed at  $t = 30$  min, the flames remain subdued until  $t = 33$  min. The fire then comes back to reach steady flames of ~2m before it self-extinguishes at  $t = 54$  min.



**Figure 65 - Flame behavior for baseline case – Wave 2 with HOOPS crude Oil**

Figure 66 shows the summary of the fire behavior of all the baseline cases with HOOPS crude oil. For all the cases with waves, the flames start tall and reduce and steady themselves before extinction, with the cases with no waves the flame height peaks with 6.5 m fire and dip to self-extinction at  $t = 16$  min. while both wave 1 and wave 2 cases behave similarly; both start with tall flames, decrease to a steady flame height. At the midpoint during the experiment the flames reduce to a minimum and flames die at  $t = 24$  and  $t = 30$  for wave 1 and wave 2 respectively, raise again higher before they self-extinguish at  $t = 42$  min and  $t = 54$  min respectively. The timeframe where the flames virtually die as seen in the graph can be attributed to foaming which can be also seen in fig 65.



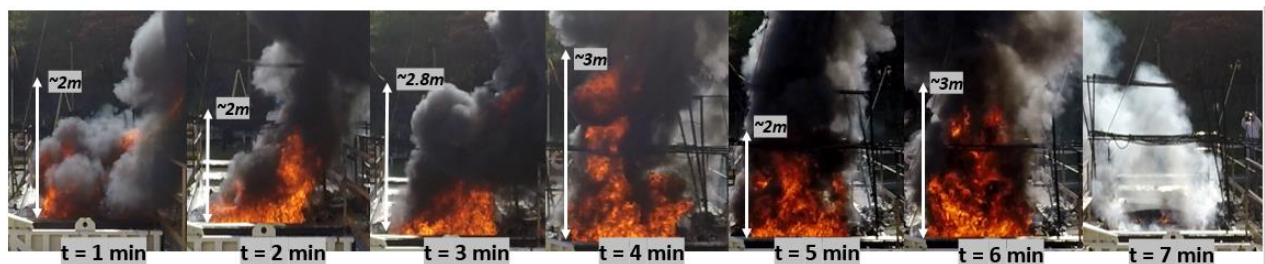
**Figure 66 - Flame heights for baseline cases –HOOPS crude Oil with 3 cases – no wave, wave 1, and wave 2.**

## 2. 25% Emulsions

### a. Baseline – No wave

The baseline case with 25% emulsion was tested with 2 different fuel thicknesses starting with 2.5cm fuel slick and 4 cm fuel slick thickness

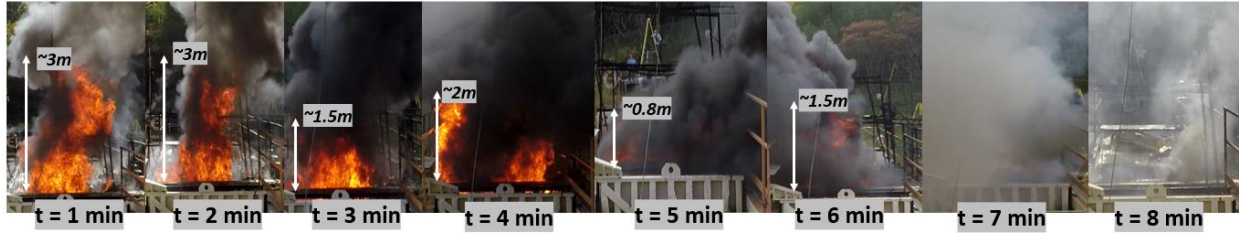
For the case with 2.5 cm fuel thickness, the experiment was repeated, and two sets of data were collected to see the repeatability of the burns. The fire starts with a steady flame of ~2m in height and increases gradually to up to ~3m tall. The fire stays consistent at an average flame height of ~2.5m throughout the first run of the test until it self-extinguishes at  $t = 7$  min (Fig. 67)



**Figure 67 - Flame behavior for baseline case – No wave for 2.5 cm slick thickness (run1) with 25% emulsion mix**

The repeated test showed slightly different behavior in terms of flame height. The flames start tall and slowly diminishes until the fire self-extinguishes at  $t = 8$  min.

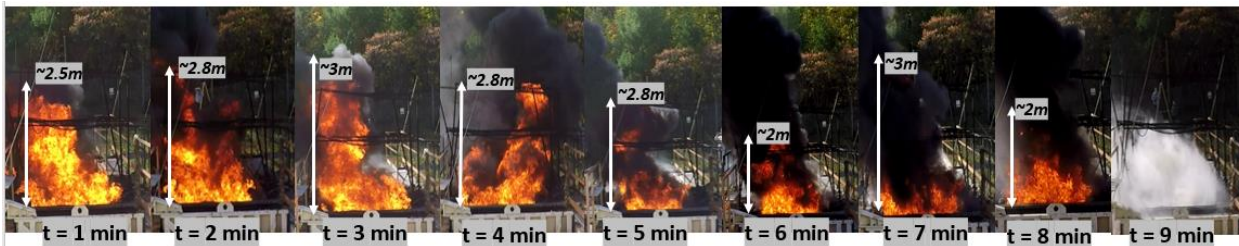




**Figure 68 - Flame behavior for baseline case – No wave for 2.5 cm slick thickness (run 2) with 25% emulsion mix**

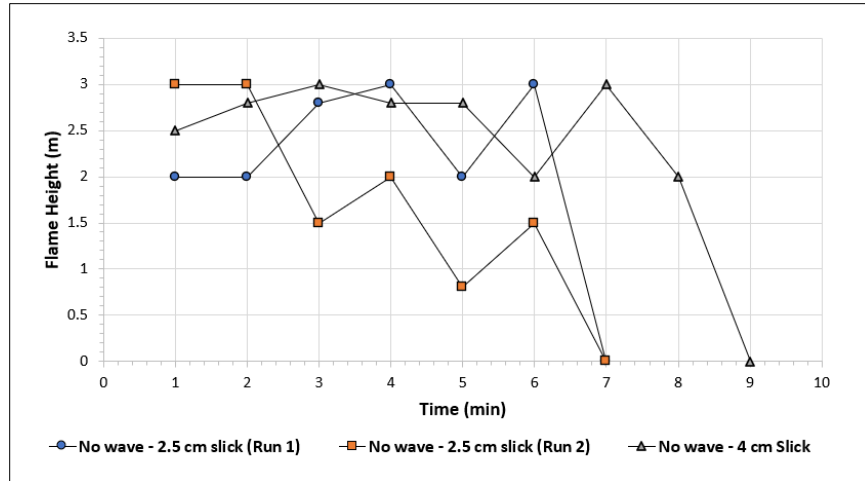
For the case where the slick thickness increased to 4 cm, the fire behaves similarly to that of the case earlier with 2.5 cm fuel thickness. The flames start slow and steady at around ~2.5 m compared to ~2m previous case with lower fuel thickness. The flames hold steady for most of the burn with an average flame height of ~2.5m from t = 3 min to t = 8 min before it self-extinguishes at t = 9 mins.

The 2.5 cm and 4cm fuel thicknesses behave similarly in terms of behavior as observed in Figures 68 and 69 where the fire starts steady, flames peak, and self-extinguishes at the end.



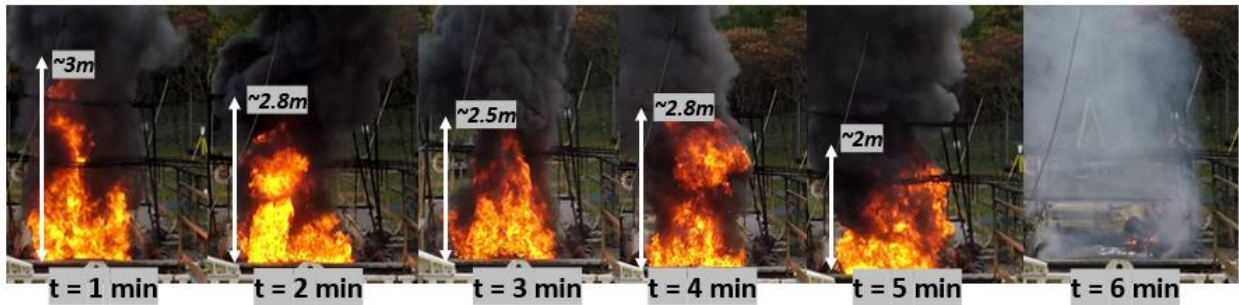
**Figure 69 - Flame behavior for baseline case – No wave for 4 cm slick thickness with 25% emulsion mix**

The no wave case (run 1) with 2.5 cm fuel thickness and no wave 4 cm fuel thickness behaves similarly in terms of flame behavior. While run 1 and run 2 behave differently in terms of flame heights, they yield a similar burn efficiency and burn rate at the end of the test after self-extinction.



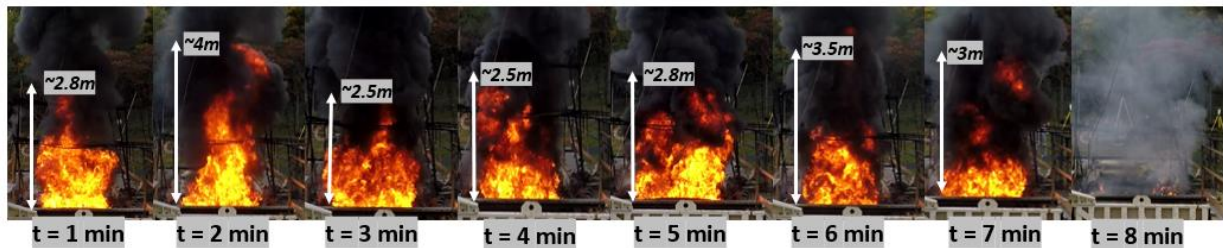
**Figure 70 - Flame heights for baseline cases –25% emulsion with 3 cases – no wave 2.5 cm oil thickness (run 1), no wave 2.5 cm oil thickness (run 2), and no wave 4cm oil thickness**  
b. Baseline - Wave 3

In the case with wave 3, the flames start high and tall reaching up to ~3m in length as seen in Fig. 71 at  $t = 1\text{min}$  and gradually decrease to ~2m until it self-extinguishes at  $t = 6\text{ min}$ .



**Figure 71 - Flame behavior for baseline case – Wave 3 with 25% emulsion mix**  
c. Baseline – Wave 4

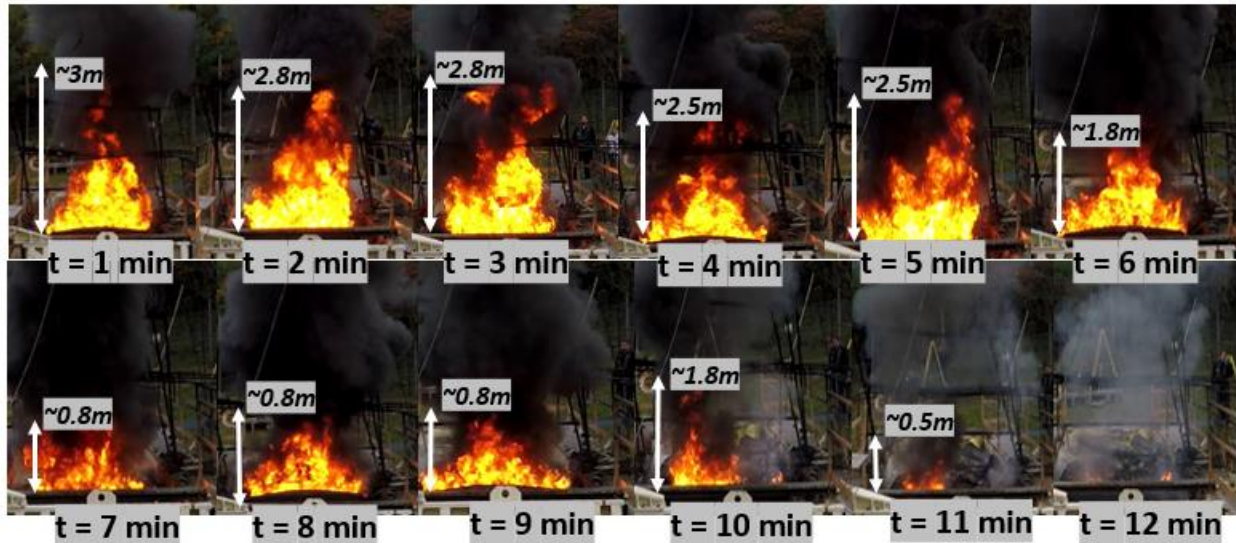
In the case with wave 3, the fire tends to delay reaching maximum flame height ~4m tall at  $t = 2\text{ min}$ , compared to wave 1 case where the flame reaches its maximum height at the  $t = 1\text{ min}$  mark. Soon after the flame height peaks ( $t = 2\text{ min}$ ), it drops to its lowest ~2.5m at  $t = 3\text{min}$  and holds steady until  $t = 5\text{ mins}$ . The flames rise again an average of ~3m height before it self-extinguishes at  $t = 8\text{ min}$



**Figure 72 - Flame behavior for baseline case – Wave 4 with 25% emulsion mix**

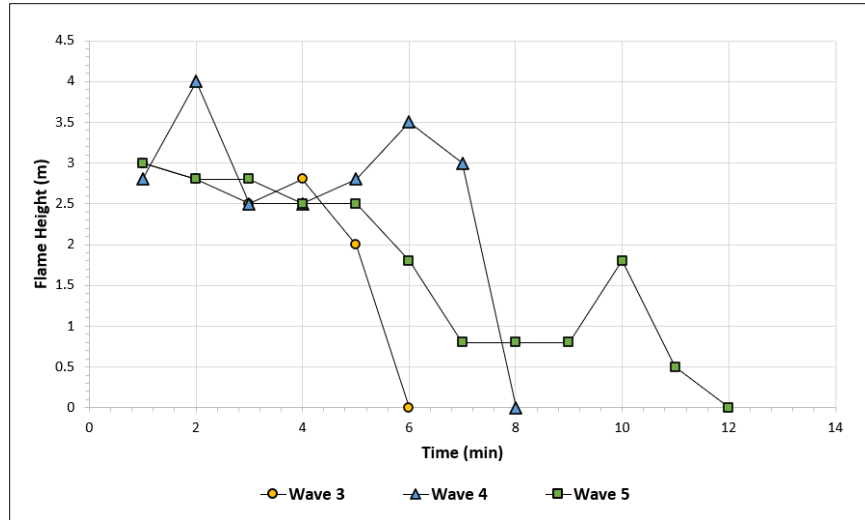
d. Baseline – Wave 5

For the case with wave 5, the flames start tall and steady at around ~2.8m from  $t = 1$  to  $t = 5$  min. The flames then start to decline from  $t = 5$  to  $t = 6$  mins from ~2.5m to ~1.8m, the flames drop even lower and hold steady ~0.8m height from  $t = 7$  to  $t = 9$  min before it self-extinguishes at  $t = 12$  min. It is important to note that the containment boom disintegrated at  $t = 10$  min where it was observed the flames increase to ~1.8m and flames die soon after.



**Figure 73 - Flame behavior for baseline case – Wave 5 with 25% emulsion mix**

In Summary, wave 3 and wave 4 behave similarly in a pattern where the flame starts steady, and it is observed that flames peak right before they self-extinguish. For the case with wave 5, the test sustains a bit longer than the wave 3 and wave 4 cases. The flames start steady at ~3m height and gradually decrease over a period. The flame again steadies and quickly shoots before it drops and self-extinguishes at  $t = 12$  min.



**Figure 74 - Flame heights for baseline cases –25% emulsion with 3 cases –wave 3, wave 4, and wave 5**

### 3. Bunker Fuel

#### a. Baseline – No wave

Bunker fuel being heavier and hard to ignite, and starter fuel was used as an ignitor to start the fire. The case with no waves for bunker fuel starts to sow with ~1.8m flame height, then peaks at around t = 3mins and drops to ~2m flames before self-extinguishing at t = 6min.

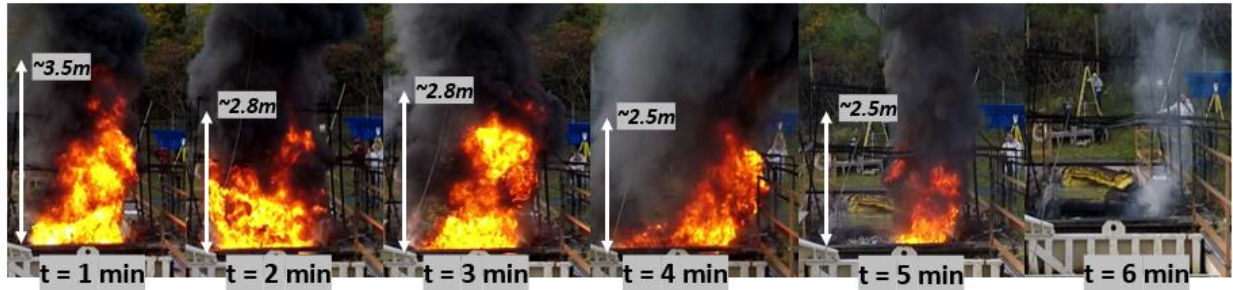


**Figure 75 - Flame behavior for baseline case – No wave with bunker fuel**

#### b. Baseline – Wave 3

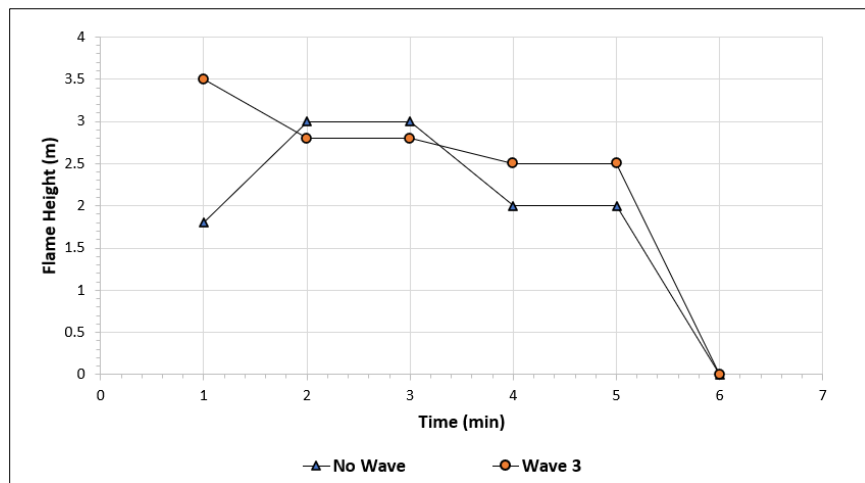
For the case with waves, the flames behave differently compared to the no waves with bunker fuel. The flames peak at the start with a tall ~3.5m fire and holds steady from t = 2min to t = 5min at ~2.8m to ~2.5m flame height before self-extinguishes at t = 6 min.





**Figure 76 - Flame behavior for baseline case – Wave 3 with bunker fuel**

The flames heights for no wave and wave 3 vary initially as the case with no waves starts with low flames and peaks before descending while the wave 3 case peaks initially and descends from the peak flame height. From  $t = 2$  mins both the cases behave quite similarly in terms of flame height and self extinguish at the same time at  $t = 6$  min



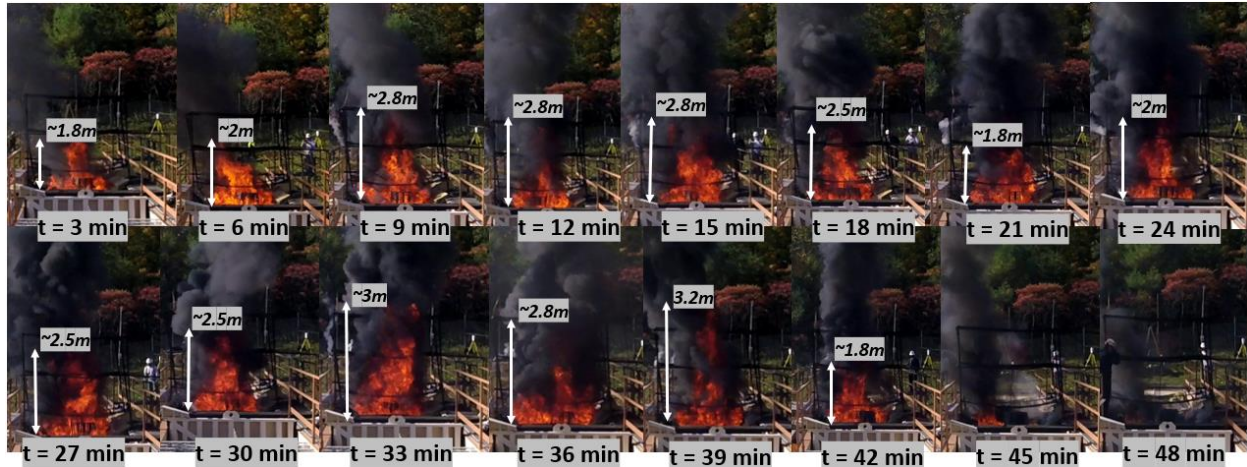
**Figure 77 - Flame heights for baseline cases –Bunker fuel with 2 cases – no wave, and wave 3**

## Flame Refluxers

### 1. Wave 1 - Hoops Crude Oil

#### a. Grid FR

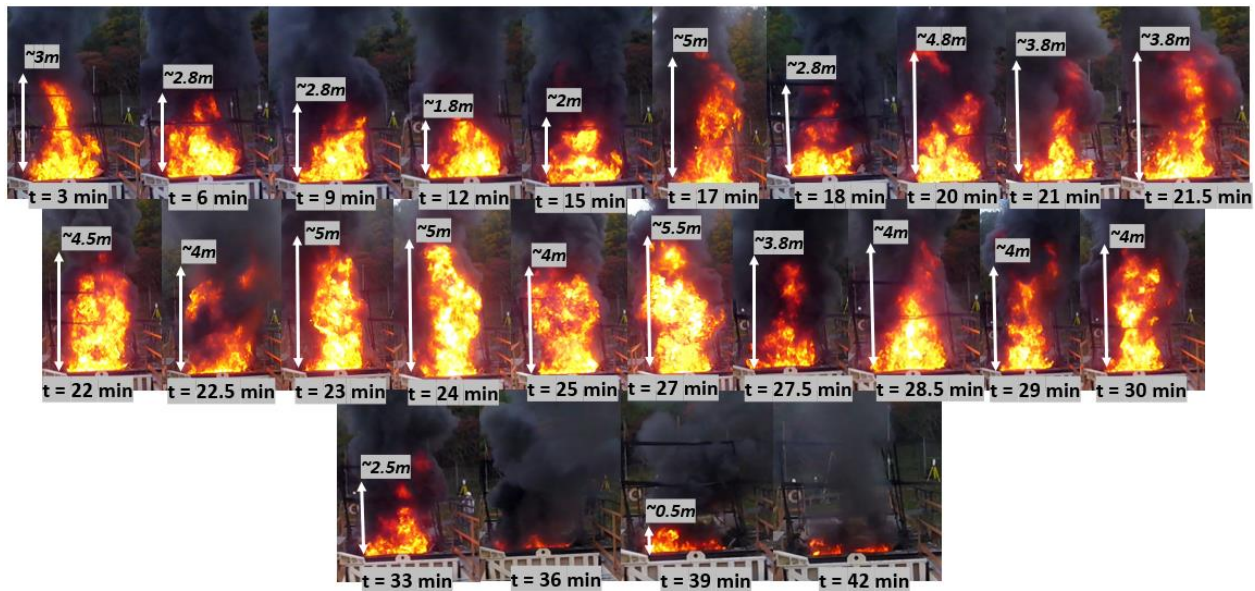
Compared to the baseline case we do not see any cyclic behavior that was observed in baseline where the flames peak and fall to a minimum, and peaks again before self-extinction. The Grid FR with wave 1 does not fluctuate much, the flames start small at ~1.8m and relatively stays at steady with an average flame height of ~2.5m throughout the test before one of the FR fails to maintain its buoyancy and sinks at  $t = 45$  min and the experiment concludes with self-extinction at  $t = 48$  min.



**Figure 78 - Flame behavior with grid FR case – Wave 1 with HOOPS crude Oil**

b. Bimetal –

The wave 1 case with bimetal FR, starts tall with ~3m flame height with steady average flame heights of around ~2m high from t = 2 to t = 15 min. It was observed that the flames suddenly erupted to high up to ~5m intermittently from t = 18 min to t = 30, with flames averaging about ~4m high. Before it self-extinguishes at t = 42 min.



**Figure 79 - Flame behavior with bimetal FR case – Wave 1 with HOOPS crude Oil**

The bimetal FR is an alloy of 2 different materials (Cu and SS), characteristics of the bimetal FR allow it to contract and expand differently. We can also see that bimetal FR works as intended, rising when subjected to high-temperature conditions.

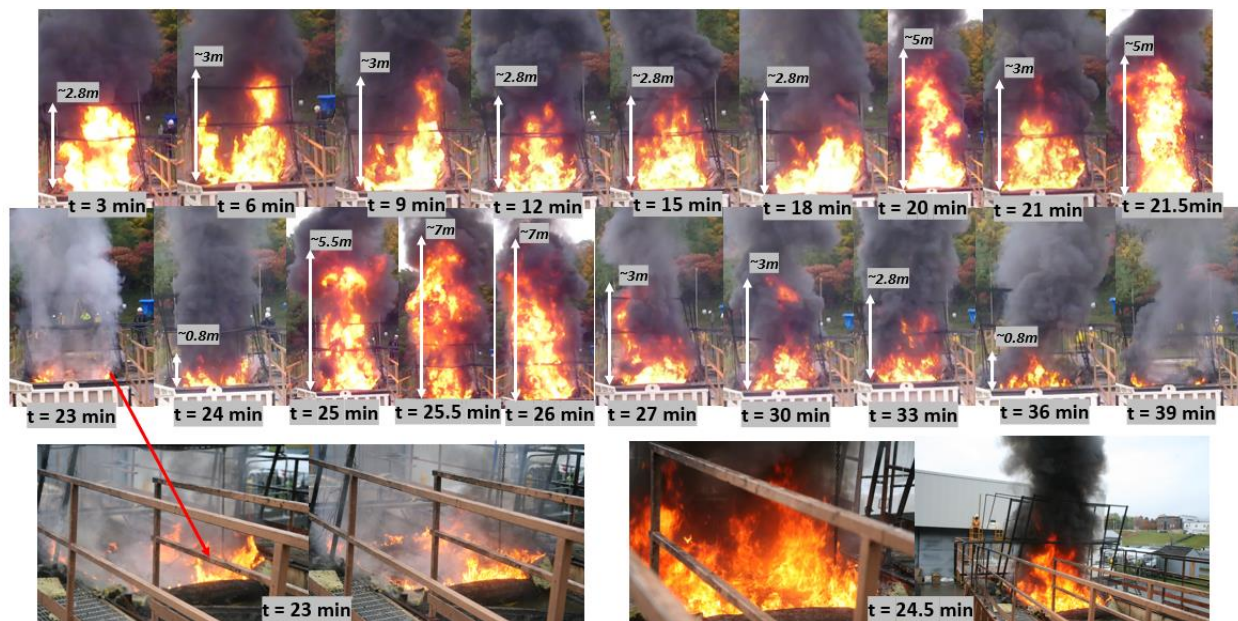




**Figure 80 - Bimetal FRs raising with high temperatures – Wave 1 with HOOPS crude Oil**

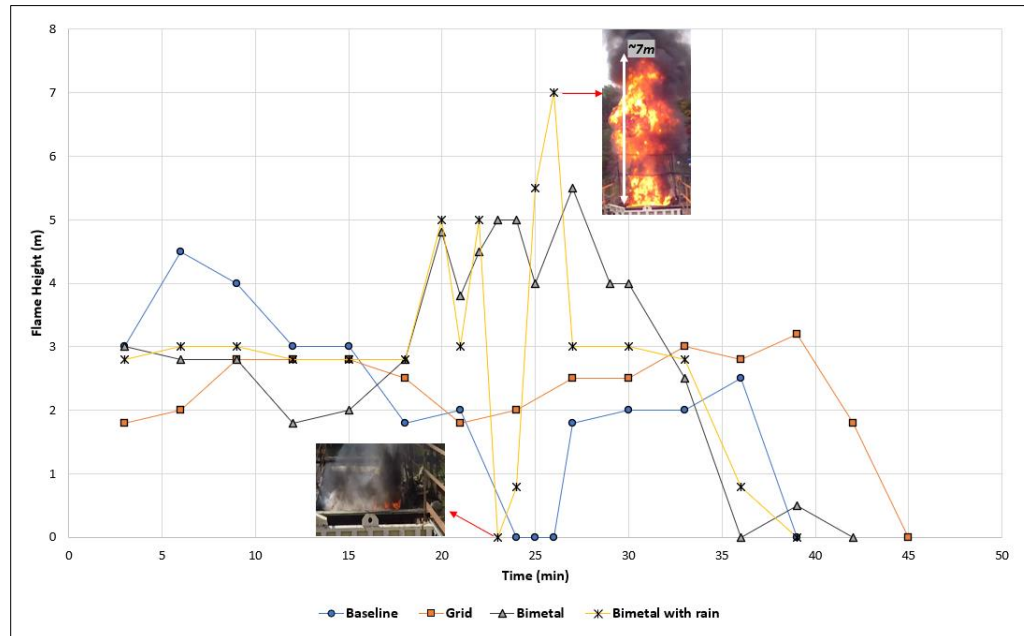
c. Bimetal – (rain case)

The experiment with the Bimetal FR case with wave 1 does follow a trend similar to the baseline case but the fluctuations are much erratic. The fire with bimetal FR starts steadily at ~2.8 m from  $t = 2$  min to  $t = 18$  min, an unusual erratic behavior is observed with bimetal FR where sudden pops of flames reach close ~5m to 7 before and the after the flames are extinguished by to foaming. It can be seen that flames pops are frequent from  $t = 20$  to  $t = 21.5$  before the flames are subdued. At  $t = 23$  min it can see that flames are only observed in the FR periphery and not that the center, flames start coming back to the center towards the FR at  $t = 24$  min and then propagate to higher flames. Soon after the flames mature at the end of the cyclic behavior, pops of fire flashes are observed again after the following 2 mins from  $t = 24$  to  $t = 26$  min. The flames then die gradually, and self-extinguishes at to = 42 min.



**Figure 81 - Flame behavior with bimetal FR case – Wave 1 with HOOPS crude Oil**

The case with baseline with wave 1 profile follows a sinusoidal trend with average flame heights of ~3m. while the FR (Bimetal & Grid) sustain taller fires and longer fires with an increased burning rate. The grid resulting 25%, and bimetal cases without and with rain resulting 67% and 92% higher burning rate than the baseline case.



**Figure 82 - Flame height comparisons for baseline, grid FR, and bimetal FR case – Wave 1 with HOOPS crude Oil**

Also, it can be seen from the observed figure 83 comparing grid FR and baseline case with wave 1, that the grid is visibly burning with clear white smoke indicating complete combustion, while the baseline case is still inefficient visible from the black smoke.



Figure 83 - Smoke visualization of grid FR and baseline case with wave 1

## 2. Wave 2 – HOOPS Crude Oil

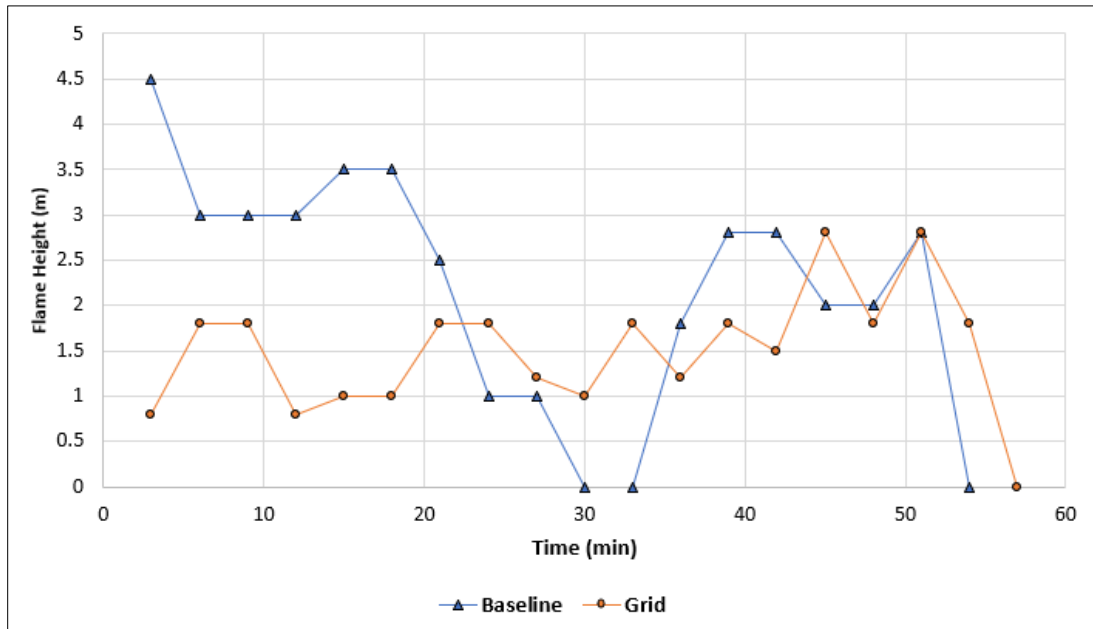
### a. Grid

Compared to the baseline case the FR with wave 2 profile has an overall reduced flame height. The flames start low at ~0.8m high at  $t = 3$  min and keep fluctuating between 0.8 and 1.8 for the entire burn period, except at  $t = 45$  min and  $t = 51$  min where the peaks at ~2.8m before extinguishing at  $t = 57$  min



**Figure 84 - Flame behavior with grid FR case – Wave 2 with HOOPS crude Oil**

The Baseline follows a clear trend where the flames peak, reduce to no flames, and peak again before extinction. Whereas the bimetal FR again stays relatively low compared to the baseline case but sustains the fire longer and with steady flame height. The fluctuations in the flame are very subtle and do not vary much throughout the experiment with the FR case still maintaining high efficiency.

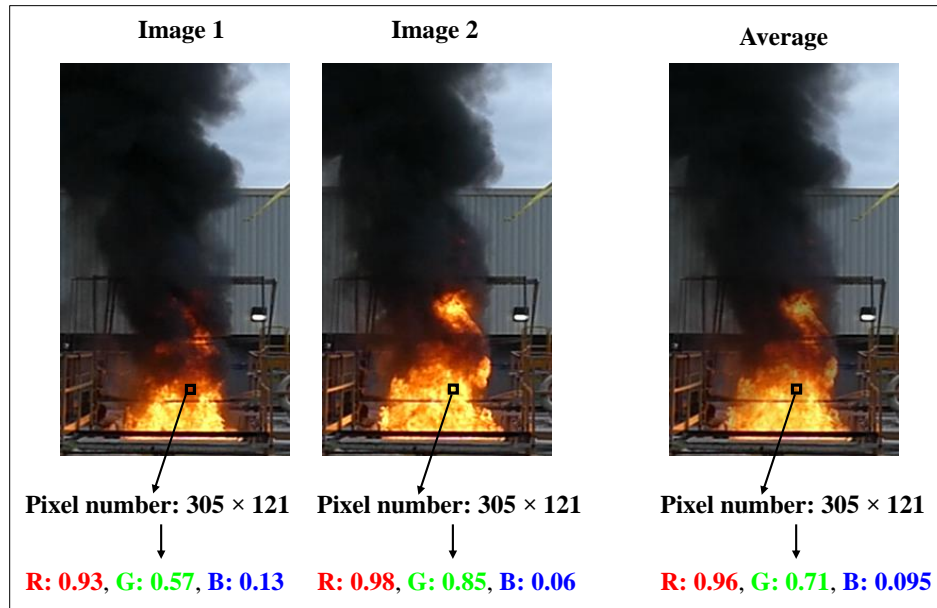


**Figure 85 - Flame height comparison for baseline, and grid FR– Wave 2 with HOOPS crude Oil**

### Average Flame Height analysis

Figure 87 shows the evolution of stages for the different experiments with HOOPS crude oil. The burn phases portray the continuous burning regime in the different cases. The time-averaged flame height (in m) is shown in each of these burn phases. Time averaging of flame photographs is done every second through an in-house MATLAB code through image processing for every burn duration as shown in Table 9. Figure 86 shows the image averaging procedure in the MATLAB code. Consider a pixel in image 1 as shown at location  $305 \times 121$ . For this pixel, the Red-Green-Blue components of each pixel are stored in a three-dimensional where  $[0,0,0]$  and  $[1,1,1]$  represent black and white colors, respectively. Each of the RGB components for the other colors lies in between 0 and 1. The RGB components of the pixel in image 1 and image 2 are averaged to obtain the RGB value for the same pixel in the average image. This procedure is followed for the required number of figures, for each of the test cases to obtain an average image in that duration.





**Figure 86 –Image averaging procedure in MATLAB**

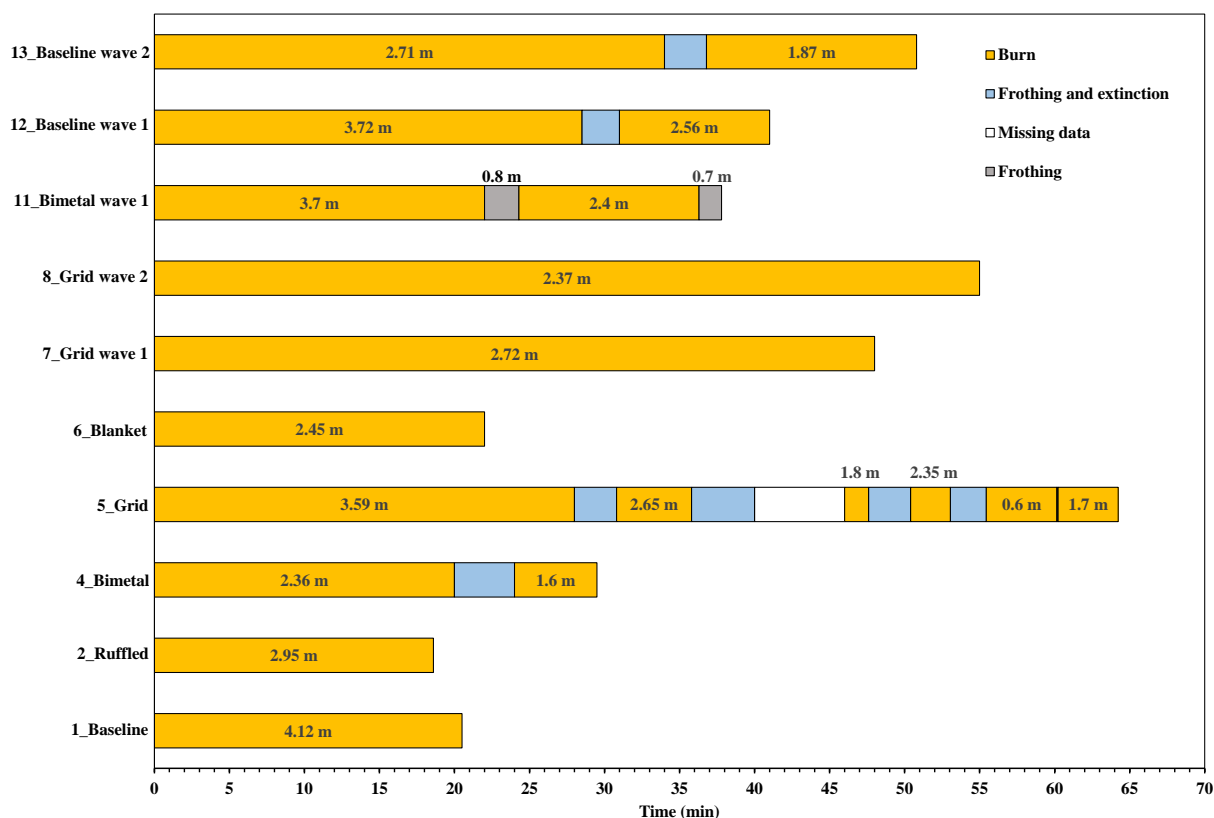
For example, during 0 - 20.5 min, the baseline no-wave case as shown in the first row of Table 9, the photograph shows a superimposed image of 1230 images taken from the time of ignition to extinction. The camera location does not change. Similar photographic averages are shown for all 13 experiments performed with HOOPS crude oil during week 1 and week 2 at CRREL. In some cases, the photographs are split into phases, for example with Bimetal and Grid FR's to show behavior during re-ignition caused because of foaming.

For the baseline case (Test 1), foaming occurs, and the flame extinguishes at around 20 minutes leading to only 57% burn efficiency. The ruffled and blanket cases (Tests 2 and 6) were extinguished in about 20 minutes with 58% efficiency with the oil froth preventing re-ignition. This behavior was overcome in cases with bimetal (Test 4) and grid (Test 5), with multiple extinction and re-ignition cycles being observed for the grid case, where the heat as contained by the refluxers was able to break down the froth. The flames are observed to be shorter after re-ignition. It is also worthwhile to note that the foaming period is usually in the order of 2.5 - 4 minutes, and then the reignition occurs.

For the baseline with wave cases (Test 12, 13) as shown in Fig. 87, the flame extinguishes at around 30 min (wave 1) and 35 min (wave 2). However, the wave motion causes the froth to break down more quickly compared to baseline no-wave cases thereby leading to a reignition in 2.5 minutes as shown in Fig 87. The flames are shorter as compared to the pre-foaming period. For the cases with bimetal with wave 1 (Test 7), the flame does not extinguish completely even during the foaming period. Even though the flames were shorter than 1 m in the foaming time period, the fire sustained over the pool to attain a burn efficiency of 98%, which is higher than the baseline wave cases of ~95%. For the grid cases with waves (Tests 7 and 8), the flames sustained throughout

the burn without any foam-induced quenching, leading to a burn efficiency of 99%. Finally, the average flame photographs clearly show that the burning is much cleaner for the Grid FR for all cases. The smoke plume is light gray compared to the black smoke observed in baseline cases. The emission data from OGES and EPA also show the same result, where the particulates with the Grid FR are nearly 50% lower than the baseline cases.


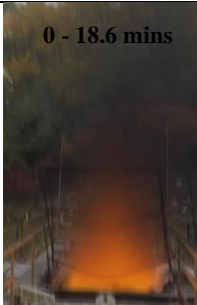
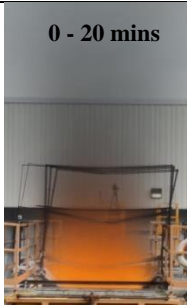







Finally, Fig 88 shows a comparison of the average photograph flame method with the Blanket with 48 coils test performed at Mobile, AL [Fig. 88 (a), (b)] with the CRREL experiment [Fig. 88 (c), (d)] performed currently. Even in Mobile, the case with the flame refluxer showed cleaner burning as compared to the baseline case with light gray smoke in Fig. 88(b).












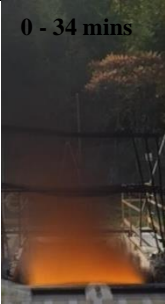
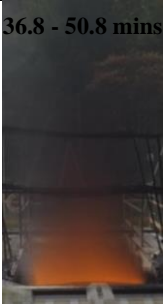
**Figure 87 - Time evolution of burning stages for HOOPS crude oil cases (Numbers indicate average flame height during the burn time)**

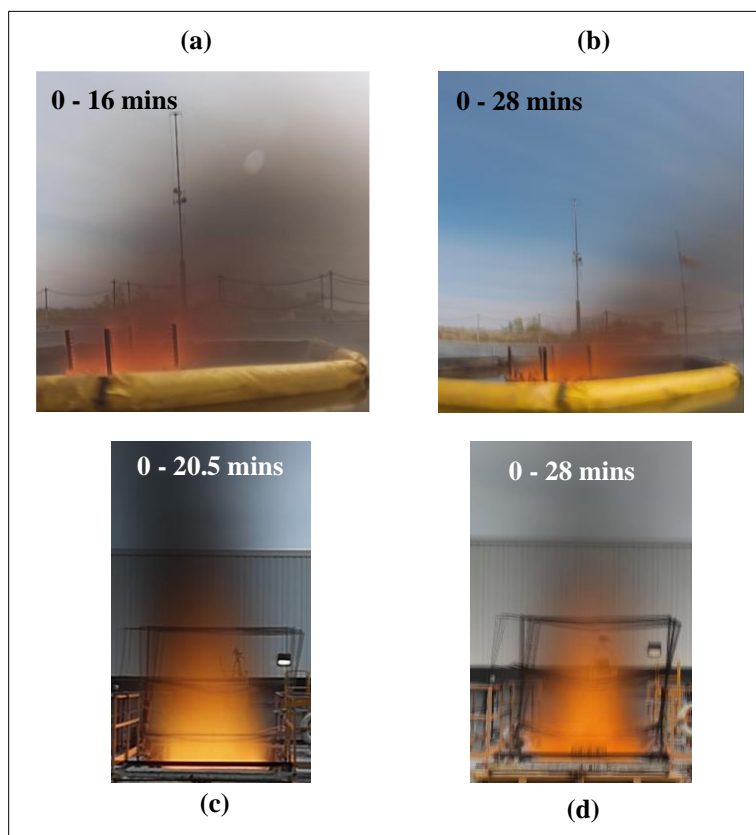
**Table 9 - Time-averaged flame photographs**



1_Baseline	<p><b>Burn time:</b> 0 - 20.5 minutes</p> <p><b>Burn efficiency:</b> 57%</p> <p><b>Visible flame height:</b> 4.12 m</p>	<p>0 - 20.5 mins</p> 		
2_Ruffled	<p><b>Burn time:</b> 0 -18.6 minutes</p> <p><b>Burn efficiency:</b> 58%</p> <p><b>Visible flame height:</b> 2.95 m</p>	<p>0 - 18.6 mins</p> 		
4_Bimetal	<p><b>Burn times:</b> 0 -20 minutes, 24 - 29.5 minutes</p> <p><b>Burn efficiency:</b> 93 %</p> <p><b>Visible flame height:</b> 2.36 m, 1.6</p>	<p>0 - 20 mins</p> 	<p>24 - 29.5 mins</p> 	
5_Grid	<p><b>Burn times:</b> 0 - 28, 30.8 - 35.8, 46 - 47.6 minutes</p> <p>50.4 - 53, 55.4 - 60.1, 60.2 - 64.2 minutes</p> <p><b>Burn efficiency:</b> 94 %</p> <p><b>Visible flame height:</b> 3.59 m, 2.65 m, 1.8 m, 2.35 m. 0.6 m. 0.7 m</p>	<p>0 - 28 mins</p> 	<p>30.8 - 35.8 mins</p> 	<p>46 - 47.6 mins</p> 
		<p>50.4 - 53 mins</p> 	<p>55.4 - 60.1 mins</p> 	<p>60.2 - 64.2 mins</p> 

6_Blanket	<p><b>Burn time:</b> 0 - 22 minutes</p> <p><b>Burn efficiency:</b> 58%</p> <p><b>Visible flame height:</b> 2.45 m</p>	
7_Grid Wave 1	<p><b>Burn time:</b> 0 - 48 minutes</p> <p><b>Burn efficiency:</b> 99%</p> <p><b>Visible flame height:</b> 2.72 m</p>	
8_Grid Wave 2	<p><b>Burn time:</b> 0 - 55 minutes</p> <p><b>Burn efficiency:</b> 99%</p> <p><b>Visible flame height:</b> 2.37 m</p>	
11_Bimetal Wave 1	<p><b>Burn times:</b></p> <p>0 - 37.8 minutes</p> <p>(Foaming: 22 - 24.3 mins, 36.3 - 37.8 mins)</p> <p><b>Burn efficiency:</b> 98 %</p> <p><b>Visible flame height:</b></p> <p>3.7 m, 0.8 m,</p> <p>2.4 m, 0.7 m</p>	<div>   </div> <div>   </div>

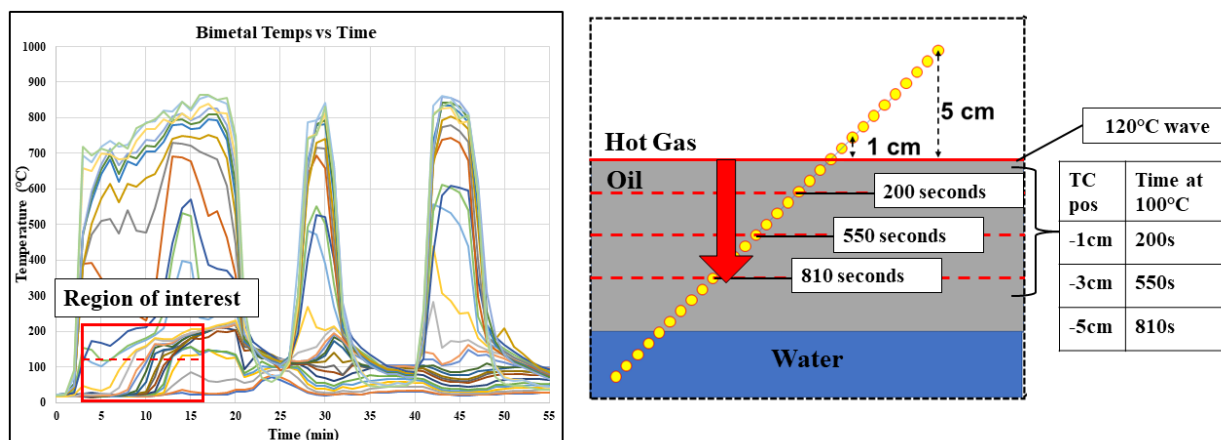
12_Baseline Wave 1	<b>Burn times:</b> 0 - 28.5, 31 - 41 minutes <b>Burn efficiency:</b> 95 % <b>Visible flame height:</b> 3.72 m, 2.56 m	 
13_Baseline Wave 2	<b>Burn times:</b> 0 - 34, 36.8 - 50.8 minutes <b>Burn efficiency:</b> 97 % <b>Visible flame height:</b> 2.71 m, 1.87 m	 



**Figure 88 - Average flame photograph for (a) Mobile baseline test, (b) Mobile blanket with 48 coils test, (c) CRREL baseline test, and (d) CRREL grid test**

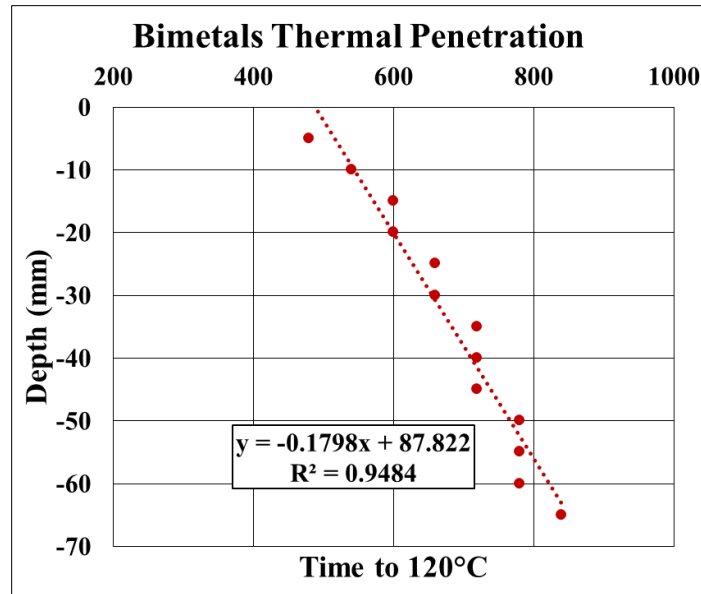
## Thermal Penetration Rate

The temperature data played a key role as one of the integral instrumentation methods to monitor the performance of the burning behavior since the thickness of the fuel layer was difficult to monitor with waves. We developed a method of analysis to evaluate the thermal penetration performance for each of the experiments. As the fuel layer heats this method ‘tracks’ a threshold temperature as it moves down the thermocouple array. For these experiments, this thermal penetration threshold temperature was 120°C. This method is shown as an example for the bimetals case. Fig. 89 (left) shows the temperature of the bimetal vs time plot for the fuel thermocouple array. The large fluctuations are present due to the extinction and reignition behavior of the bimetals case. The heating region of interest is outlined in a red box on the temperature vs time plot, the in-depth thermocouples are visible rising in this region of interest and crossing the red-dashed line which denotes 120°C.



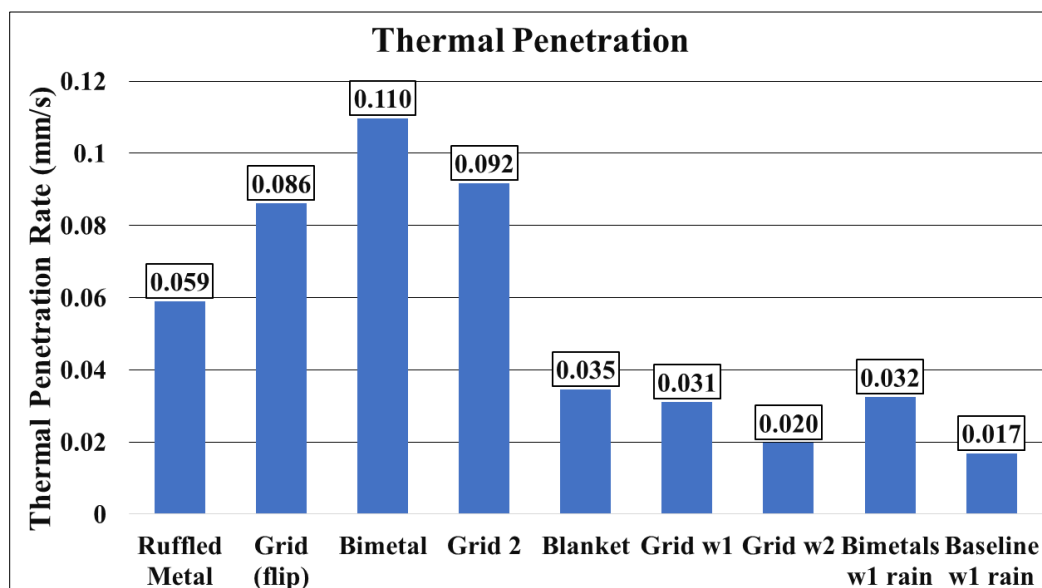
**Figure 89 - (left) Bimetal temp vs time with thermal penetration rate area of interest highlighted. (right) Thermal development in the fuel layer over time**

The time at which each thermocouple reached 120°C were tabulated and used to create charts that plot thermocouple depth and time to 120°C. This plot is shown as an example for the bimetals case in Fig. 90. A linear trendline then fits this data, and the slope of this line is the thermal penetration rate in millimeters per second (mm/s). This thermal penetration rate was obtained for both the outer and center fuel thermocouple arrays wherever available and then averaged to obtain a single value for each FR. Extensive thermal penetration plots for each FR prototype and the individual center and outer fuel thermocouple arrays are available in the appendix.



**Figure 90 - Example thermal penetration chart for bimetals case**

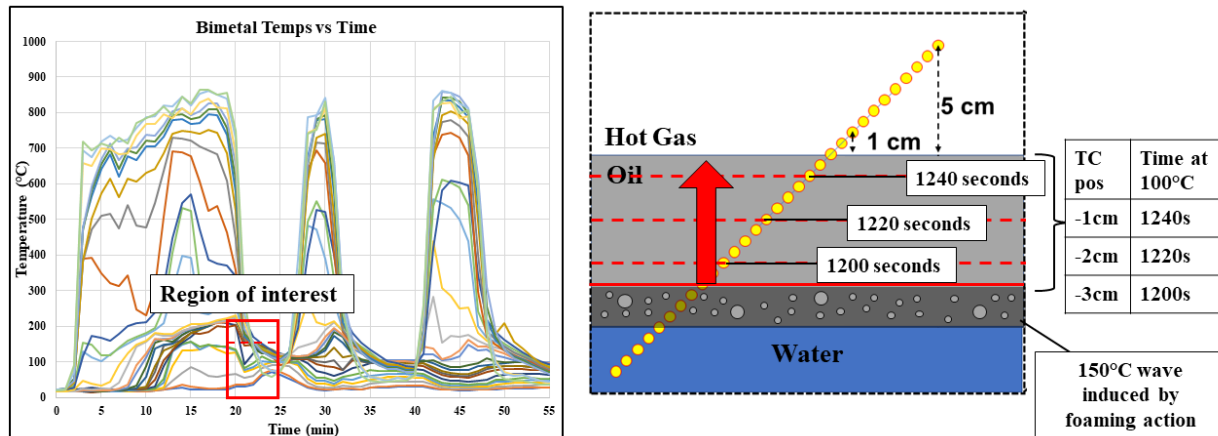
This analysis was conducted for the first 12 experiments conducted in Phase II at CRREL. This data is presented in Fig. 91 below. Solo grid wave 1 has been omitted due to unreliable data. The Bimetal and second Grid experiments both experienced extinction and reignition behavior not seen in other experiments. For these cases, the thermal penetration for this chart was only calculated using the first initial burning period. The Bimetals and Grid cases demonstrated the highest thermal penetration rate, as anticipated. While the ruffle and blanket struggled to reach as high values. The waves reduced the thermal penetration of the grid, with wave 2 being more detrimental than wave 1. Although both the bimetal and grid FR performed very similarly under the impingement of wave 1.



**Figure 91 - Thermal penetration rates for FR cases in Phase II**

## Foaming Speed

A similar method to the thermal penetration rate can be applied to measure the speed at which the foaming moves through the oil layer. As the foam rises through the fuel the presence of the bubbles limits the maximum temperature that can be present in the fuel layer. This resultingly cools the fuel and thermocouples. This threshold temperature was discovered to be 150°C and could then be tracked moving back up through the fuel layer, as seen in Fig. 92 this region of interest is outline by the red box.



**Figure 92 - (left) Bimetals temp vs time with foaming speed area of interest highlighted.  
(right) Foaming development in the fuel layer over time**

In the same fashion as the thermal penetration rate, these points representing TC position and time to 150°C were then plotted, and the slope of the linear fit being the foaming speed in mm/s. This calculation was conducted for the ruffle case, as well as for all the foaming events in both the grid and bimetal cases (8 from grid, 3 from bi-metal). It was found that there may be a slight decline over the course of multiple extinctions and reignitions, but largely the speed of foaming was constant and independent of the FR. The decrease in foaming speed may be in part due to the increase in viscosity of the oil, which would slow down the terminal bubble rise velocity.



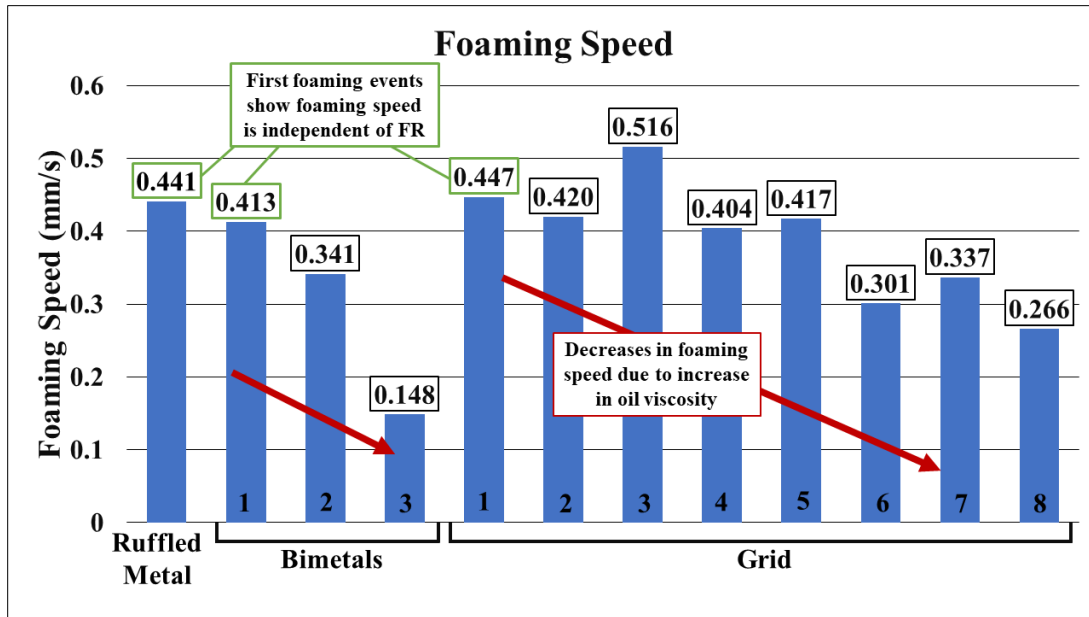


Figure 92 - Foaming speeds for the Ruffle, Bimetal, and Grid cases

### Cooling by Waves

Some cases never extinguished due to foaming behavior and thus the cooling behavior for these cases needed to be captured as well. The cases examined which did not experience foaming were grid - wave 1, grid wave - 2, and baseline wave - 1 in rainy conditions. These 3 cases were then analyzed to find the speed at which a 120°C threshold moved back up the TC array once the heating penetration had stopped.

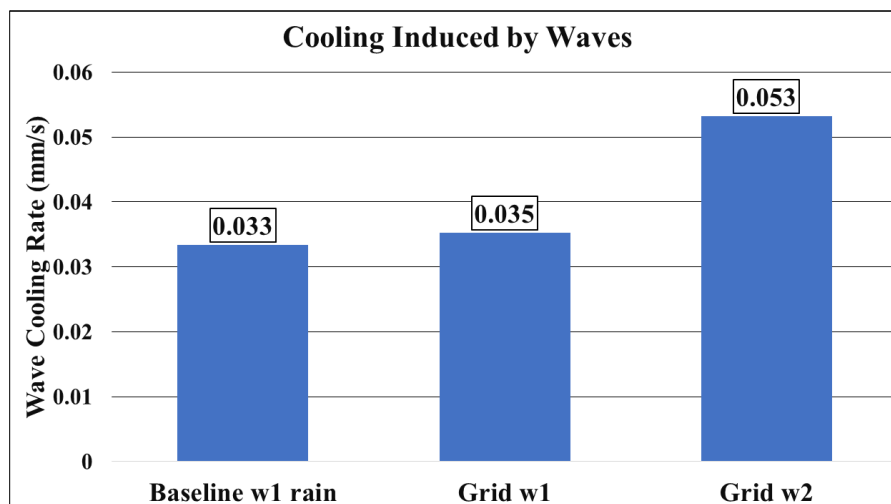


Figure 93 - Wave induced cooling speeds for the available wave cases

An interesting observation is that the cooling rate seems to be independent of whether the FR is present in the experiment. This behavior seems to be dominated by which wave is impinging on the fuel layer. Both wave 1 cases exhibit almost identical cooling rates, and the more aggressive

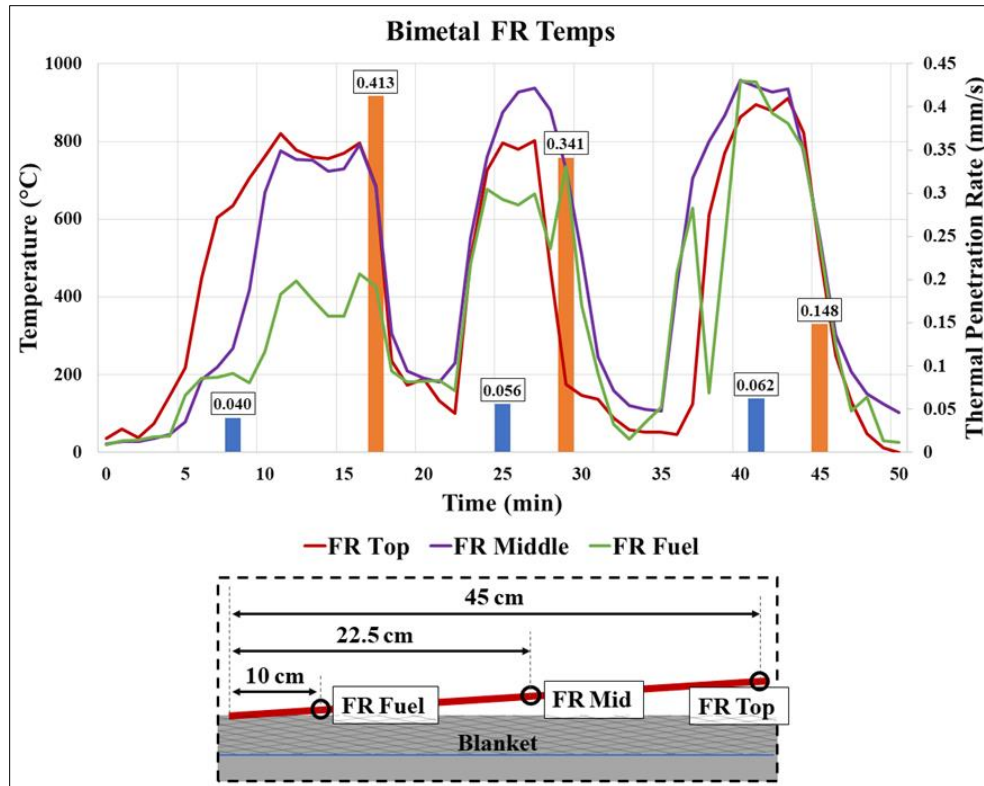
wave 2 has a higher cooling rate than both as expected. Although it is difficult to make concrete statements with only 3 data points.

### **Extinction and Reignition Events**

The two most promising FR types produced experiments with never-before-seen behavior. Both the bimetal and grid cases experienced a foaming-driven extinction and then multiple reignitions and extinctions subsequently. Each of these foaming and reignitions was analyzed for their respective thermal penetration rate and foaming speed. These rates were then plotted on the same chart with three select FR metal temperature thermocouples.

#### **Bimetal**

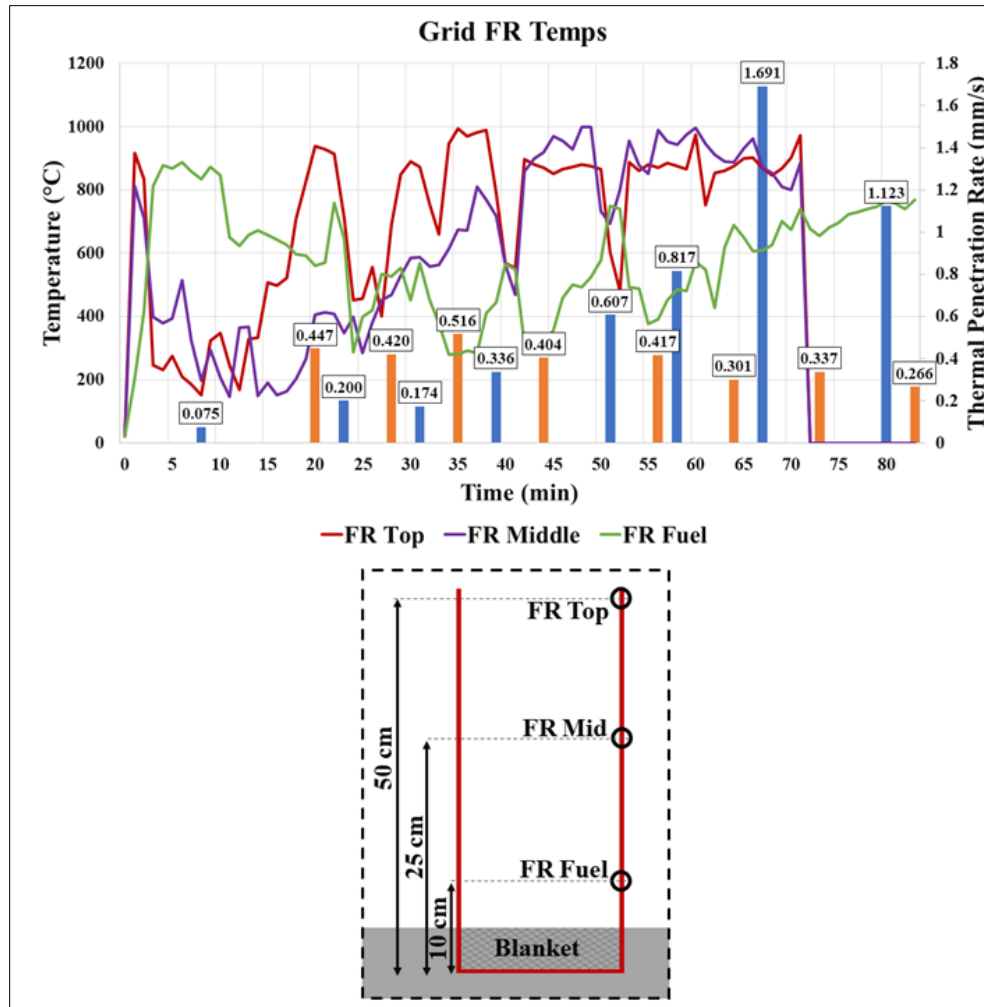
Fig. 94 shows this combination of data points. The blue bars represent thermal penetration speeds, and the orange bars represent foaming speeds. The 3 lines represent the temperatures of the FR Top (red), FR Middle (purple), and FR Fuel (green) thermocouples. The thermal penetration rates slightly rise over the course of the experiment, and the foaming speeds decline. The bimetal FR is at least partially responsible for the rise in thermal penetration rates over the course of the reignitions. This is evident because of the rising peaks observed in the overlaid temperature data. This suggests that even though the flames are extinguished the FR is retaining heat and overall heating up over the course of the experiment.



**Figure 94 - Evolution of FR temps, thermal penetration rate, and foaming speed for the bimetals case**

## Grid

Just as shown in the bimetal section, Fig. 95 shows the same chart now generated for the grid case. The grid case experienced 8 foaming extinctions and 7 reignitions. Here the rise in thermal penetration rate is much more exaggerated than in the bimetal case. This may be because of the longer duration, higher number of reignitions, or higher thermal capacity of the grid FR. The drop in foaming speed is similar to what was observed with the bimetal case. Just as in the bimetal case the FR metal temperatures suggest that even through the extinctions the FR is heating up and driving the faster thermal penetration rates. This is especially evident in the FR Middle (purple) line.



**Figure 95 - Evolution of FR temps, thermal penetration rate, and foaming speed for the grid case**

## Temperature Plots

Comparing each experiment more appropriately required the generation of temperature-depth plots. Temperatures in these plots are obtained from 1-minute averages for each experiment, and the plots are then color-scaled for visualization of the temperature bands. Plots were generated for 5-, 10-, 15-, and 20-minute time stamps for the ruffle, bimetals, grid, blanket, grid wave 1, grid wave 2, and baseline wave 1 rain cases, these plots are shown in Fig. 96. It can be seen from these charts that the grid wave cases present the highest temps in-depth initially, although these temperatures are not very high, they do penetrate quite deep. However, at 15 and 20 minutes, once the bimetals and grid have had sufficient time to develop heat, they present much higher overall temperatures than any case. Meanwhile, the grid wave 1 and grid wave 2 cases do not show much overall change in temperature development into the later timestamps. It should also be noted that the threshold temperature for calculating thermal penetration rate was 120°C. Thus, the wave cases

do not present faster penetration rates because this 120°C threshold is not reached any faster than in the Grid and Bimetal FR cases.

Temps at 5-min							
TC pos (cm)	Ruffle	Bimetals	Grid	Blanket	Grid w1	Grid w2	Base w1 r
0	179.7	248.1	195.4	165.6	124.4	107.2	141.4
-0.5	99.2	168.1	125.4	101.6	129.6	96.4	59.7
-1	77.3	118.5	88.7	43.4	128.3	85.7	59.7
-1.5	45.1	100.2	59.6	26.7	132.2	87.8	33.9
-2	22.5	34.2	44.4	19.9	134.8	94.3	33.7
-2.5	19.0	23.7	29.3	20.7	108.3	53.2	33.4
-3	15.9	19.6	27.9	19.9	88.1	63.8	24.1
-3.5	11.4	18.5	22.3	21.8	75.6	68.3	26.6
-4	16.3	17.8	19.6	18.5	70.0	73.4	18.3
-4.5	14.8	16.4	16.4	17.2	65.8	69.4	19.6
-5	14.0	20.3	16.6	16.7	61.5	63.6	19.7
-5.5	13.8	19.8	15.0	18.4	51.8	48.6	19.6
-6	14.0	16.3	22.5	16.3	46.7	47.7	18.5
-6.5	13.3	24.8	19.2	12.6	38.1	37.4	19.5
-7	12.7	14.1	17.2	14.1	30.6	27.6	14.8

Temps at 10-min							
TC pos (cm)	Ruffle	Bimetals	Grid	Blanket	Grid w1	Grid w2	Base w1 r
0	185.7	229.7	251.6	217.8	119.6	148.9	146.1
-0.5	153.0	211.9	197.9	204.0	102.5	120.8	136.2
-1	156.6	181.1	190.7	160.8	133.2	92.7	102.8
-1.5	131.4	176.3	187.6	138.8	163.8	101.7	129.6
-2	125.7	160.2	151.9	21.9	163.8	119.4	85.4
-2.5	109.9	156.2	112.8	27.4	122.6	93.8	69.6
-3	91.1	122.7	100.3	25.1	114.9	106.2	61.8
-3.5	50.8	113.0	90.0	24.9	107.1	91.8	41.3
-4	27.9	88.9	38.7	22.2	99.7	91.9	33.4
-4.5	24.7	57.1	31.7	26.3	73.1	85.6	21.5
-5	22.5	30.2	27.0	22.5	83.3	88.7	22.1
-5.5	26.9	26.8	26.6	20.5	54.9	58.0	19.6
-6	17.1	25.1	21.4	16.4	49.6	45.4	20.6
-6.5	17.7	24.3	19.7	15.9	27.9	36.7	19.7
-7	16.9	21.1	18.0	21.7	18.4	33.6	18.3

Temps at 15-min							
TC pos (cm)	Ruffle	Bimetals	Grid	Blanket	Grid w1	Grid w2	Base w1 r
0	234.9	263.1	219.5	220.6	222.5	229.6	223.6
-0.5	177.2	205.1	192.8	226.3	219.9	126.3	164.6
-1	169.1	194.6	183.3	211.6	195.5	61.1	141.5
-1.5	164.9	193.8	181.9	207.4	99.6	91.6	132.7
-2	163.9	181.3	178.9	159.0	138.1	113.3	148.5
-2.5	163.3	188.4	176.1	96.8	122.6	109.9	124.6
-3	160.0	181.5	175.8	44.6	109.6	100.3	126.6
-3.5	151.4	192.4	175.3	35.6	109.6	99.6	89.4
-4	138.3	180.5	172.3	29.7	105.1	90.8	69.6
-4.5	122.7	188.0	168.6	55.3	71.7	96.9	88.1
-5	94.1	171.0	161.8	31.9	97.0	110.6	69.6
-5.5	67.5	157.1	146.1	25.6	91.4	68.9	33.4
-6	32.2	156.6	137.3	41.9	45.0	46.4	19.6
-6.5	22.9	130.4	132.7	48.4	27.9	36.7	20.6
-7	16.7	84.5	119.7	39.8	18.4	33.6	19.7

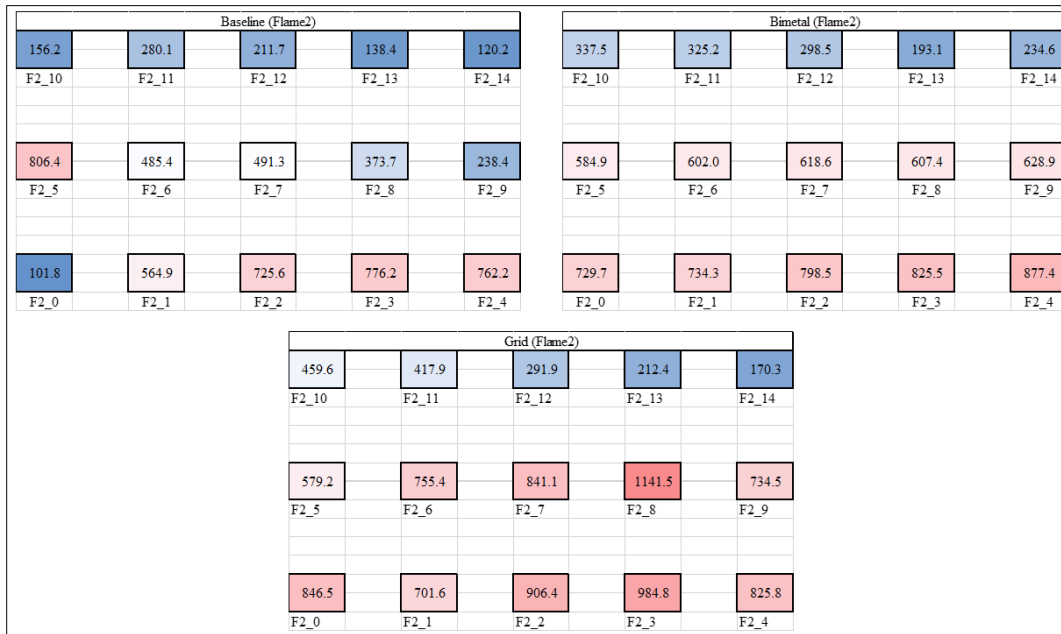
  

Temps at 20-min							
TC pos (cm)	Ruffle	Bimetals	Grid	Blanket	Grid w1	Grid w2	Base w1 r
0	223.8	282.9	185.3	232.4	199.3	218.2	221.2
-0.5	164.2	256.8	162.0	231.0	148.5	171.5	197.7
-1	174.1	216.3	163.3	230.6	163.3	165.8	183.6
-1.5	187.3	240.4	171.9	226.2	132.7	160.0	155.5
-2	167.2	229.6	160.7	208.7	122.6	140.1	141.5
-2.5	158.0	219.4	160.2	153.1	120.4	102.1	109.5
-3	167.3	224.2	156.5	45.2	113.7	101.1	95.0
-3.5	169.6	218.3	158.3	33.8	107.2	99.8	88.1
-4	92.6	218.5	155.0	75.1	100.1	99.0	73.7
-4.5	135.7	218.5	155.4	64.7	93.2	96.1	69.6
-5	120.0	203.4	109.1	46.6	77.6	96.0	20.6
-5.5	54.1	217.9	140.9	46.7	64.9	91.3	19.7
-6	74.8	225.0	155.9	32.7	46.5	71.4	18.3
-6.5	40.3	202.8	129.2	47.4	27.9	62.6	18.8
-7	23.8	133.3	91.9	37.4	18.4	33.6	18.9

**Figure 96 - Temperature color vs depth plots for CRREL FR cases**

## Flame Temperatures

Flame temperatures were recorded for each experiment with the array placed over the burning area. Using this flame temperature data plots were generated showing the position of each sampling point, with the temperatures at each point color-scaled for ease of comparison. For the following comparison, only the middle flame temperature array (Flame\_2) will be shown, with the remaining flame temperature plots included in the appendix. The middle array was chosen as this array is most likely to be exposed to consistent flame and hot-gas heating. The experiments chosen for comparison were the baseline, bimetal, and grid cases. The temperatures for these plots are 1-minute averages of the temperatures present at 15-minutes post ignition. The baseline case presents the lowest flame temps both close to the burning pool and higher on the array away from the fuel. Both the bimetal and grid have significantly higher gas temperatures throughout the plume. However, the grid FR demonstrates the highest temps at the 15-minute mark, both close to the burning surface and higher in the gas temperature array.

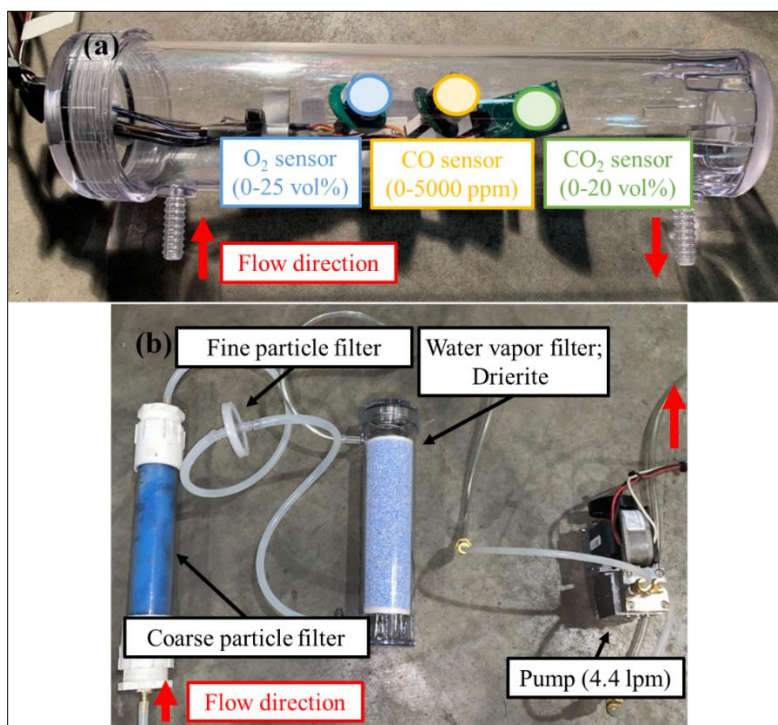


**Figure 97 -Flame temperature comparison with data plots showing the position of each sampling point, color scaled temperatures at each point with baseline, bimetal, and grid FR**



## Outdoor Gas Emission Sampling (OGES) CRREL - Phase II Tests

In addition to temperature and regression rate data, gas emission sampling would act as another data set to determine the burning performance enhancement of the different FR's. Fig. 98 depicts the gas sensor sampling chamber as well as the sampling filter 'train used for the CRREL tests.



**Figure 98 - (a) Gas sensor sampling chamber (b) Filter train**

The large-scale nature of the CRREL tests piqued interest in not only the study of gas emission distribution along the centerline of a fire, which can then be compared to multiple plume theories from prior research but also the study of gas concentration distribution along the horizontal direction as well. Therefore, three points on the TC tree were chosen as sampling points for the tests at CRREL, labeled Pos 1, 2, and 3 respectively (Fig. 99). Sampling points were selected in locations with a TC present so that gas emission data could be compared to temperature data during data analysis.

Environmental Protection Agency (EPA) was present for the first week of testing (Sep 28 – Oct 2) and performed burn emission sampling with the aid of a crane at much higher locations than the TC tree. A fourth sampling point was added in the crane to provide an additional data set for the WPI studies and comparison with EPA data when needed. Fig. 99 shows all the sampling points. Table 10 lists the locations of the sampling points relative to the fuel surface.

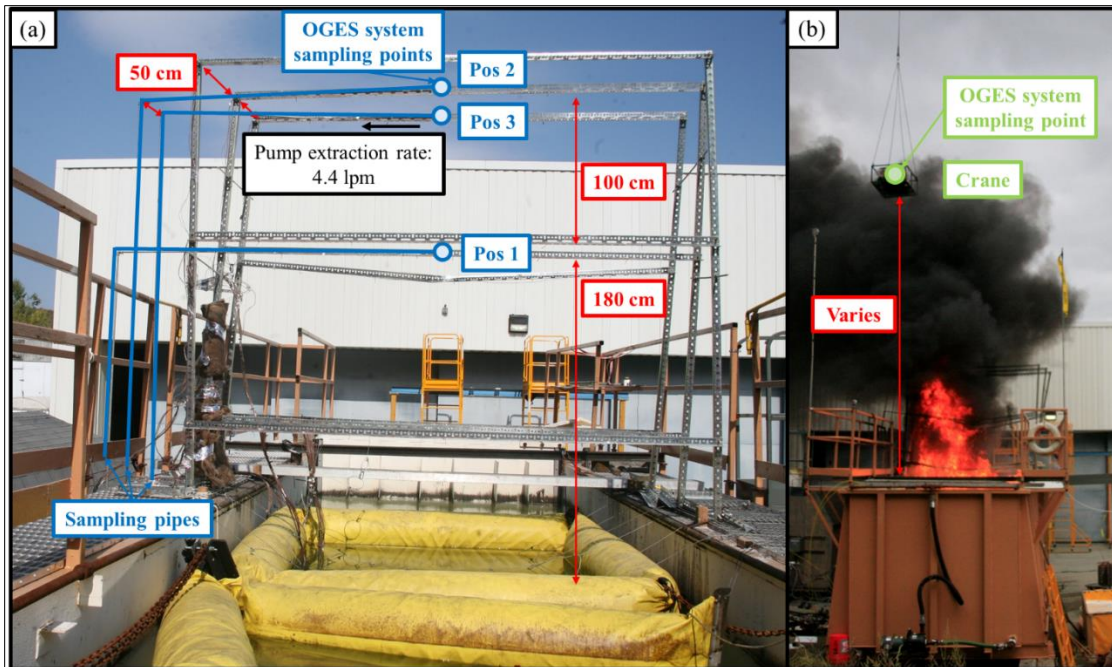


Figure 99 - OGES setup on (a) TC tree (b) Crane.

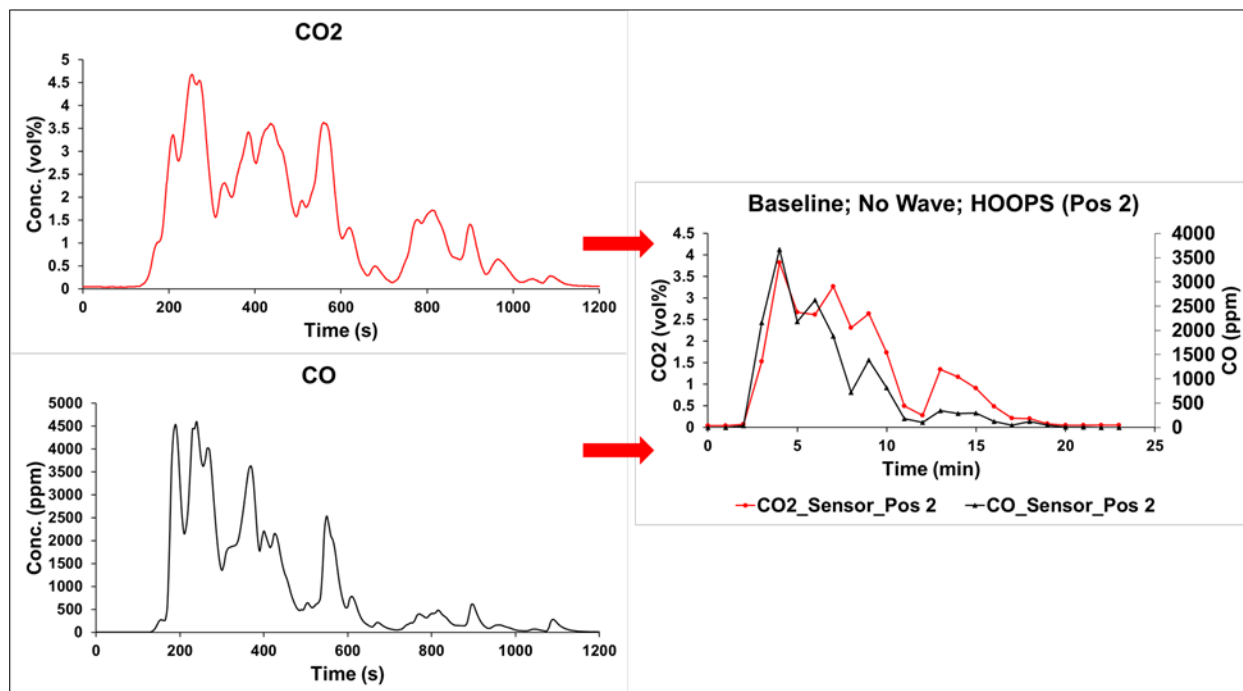
Table 10 - Sampling points for CRREL tests.

Sampling Point	Location
Pos 1	Height: 180 cm Position: Centerline
Pos 2	Height: 280 cm Position: Centerline
Pos 3	Height: 280 cm Position: 50 cm from Centerline
Crane	Location varies: Crane operator attempts to keep payload within plume as much as possible

### OGES Data Averaging

To ensure all data sets had the same starting point, all data sets were moved so that only 2 minutes of pre-ignition time remained. The burn tests at CRREL had durations between 20 to 65 minutes depending on the fuel type, fuel thickness, wave setting, and FR prototype deployed. To decrease the amount of noise in the data, all data was averaged to 1-min time steps to simplify data analysis.

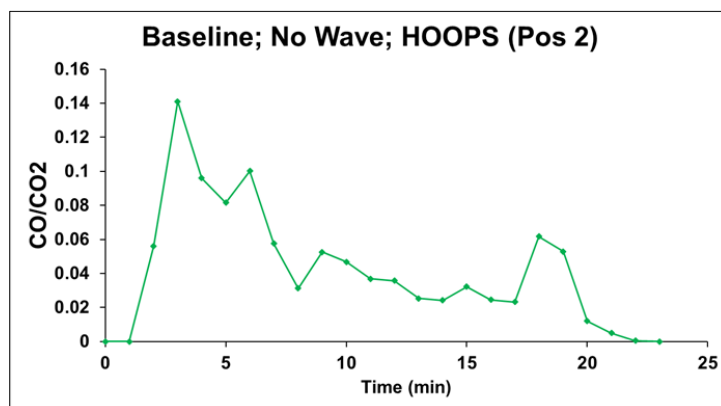
Fig. 100 below is a representation of the data after it is averaged for CO<sub>2</sub> and CO concentrations. The data shown is from the Baseline; No Wave; HOOPS test at Pos 2.



**Figure 100 - Averaging technique for gas emission data.**

## Results CO/CO<sub>2</sub>

After obtaining the averaged data, other values such as CO/CO<sub>2</sub> were calculated and graphed based on this data. Fig. 101 is an example of a CO/CO<sub>2</sub> graph based on averaged CO<sub>2</sub> and CO data. The data shown is from the Baseline; No Wave; HOOPS test at Pos 2.

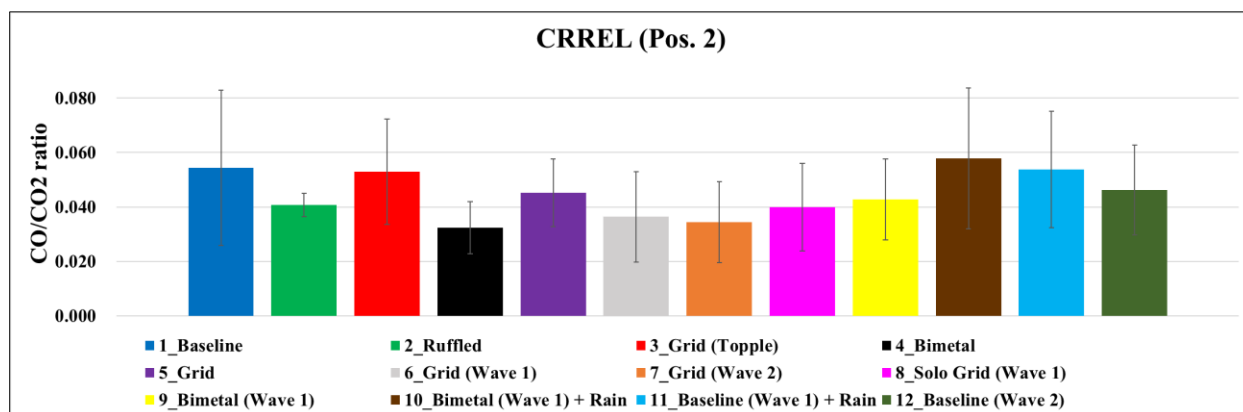


**Figure 101 - CO/CO<sub>2</sub> for Baseline; No Wave; HOOPS test at Pos 2.**

CO/CO<sub>2</sub> was then averaged over the entire burn, where a representative single value was obtained to quantify the overall burning behavior of a given experiment. These average values are shown in bar graphs to visually compare the burning performance enhancement of the FR prototypes.

Higher CO/CO<sub>2</sub> ratio, in general, represents a higher degree of inefficient burning. The expectation of FR deployment was an increased enhanced burning behavior, meaning the CO/CO<sub>2</sub> ratio should be lower than the baseline case.

A total of 12 burn experiments were performed in collaboration with EPA at CRREL. Five experiments were performed without waves being made by the large wave tank; the remaining seven experiments comprised of two different waves, referred to as Wave 1 and Wave 2 in the experimental matrix. Wave 1 is a smaller wave with a period of 2.5 s and wave height of 7 cm; Wave 2 is a larger wave with a period of 4 s and wave height of 14 cm. Fig. 102 shows all tests performed with HOOPS crude oil sampled at Pos 2 by OGES system.



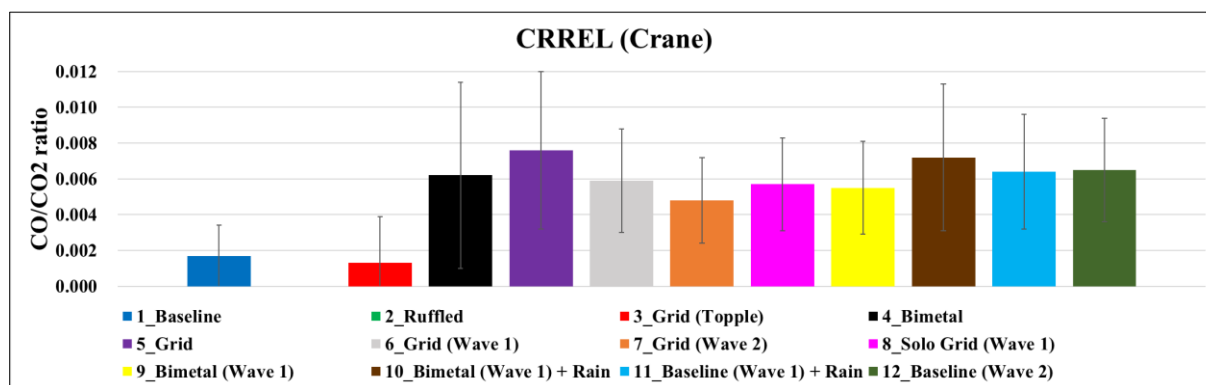
**Figure 102 - Average CO/CO<sub>2</sub> comparison for HOOPS cases sampled at Pos. 2**

For experiments with no waves, all cases where an FR was deployed yielded a lower CO/CO<sub>2</sub> ratio. This makes sense since the function of the FR prototype is to redirect heat back to the fuel layer and subsequently improve burning behavior, with the added anticipation of reduced emissions.

Overall, the Bimetal FR provided the most improvement in terms of emissions over the Baseline case, an over 40% in reduction of CO/CO<sub>2</sub> ratio, and is overall the best performing FR prototype when there are no waves. A notable observation is that the Grid FR toppled over within a short period in Set 3, and therefore it is observed that the CO/CO<sub>2</sub> ratio is essentially identical to the Baseline case. This is reasonable since a toppled FR is underwater and is no longer functioning as intended to enhance the burning behavior of the fuel, reverting this data set back to a pseudo-Baseline case. This demonstrates the repeatability of using the new OGES system to evaluate CO/CO<sub>2</sub> ratio or degree of burning behavior improvement, for large-scale outdoor burn experiments.

For experiments with waves, the Grid FR provides the most improvement in terms of emissions over the Baseline case, even with different waves. Focusing on Wave 2, the improvement in CO/CO<sub>2</sub> ratio with the Grid FR is over 25%. However, the Bimetal FR still provided a slightly lower but comparable decrease in CO/CO<sub>2</sub> over baseline cases involving waves, and therefore other factors such as temperature data needed to be considered when deciding the best-performing FR for future work and commercial deployment.

Fig. 103 shows a comparison of average CO/CO<sub>2</sub> for the same experiment matrix, but for the Crane sampling point instead. For these cases, a similar trend to the Pos 2 sampling point is observed except for the first three experiments. During the first day of experiments, the crane operator required some repetitions to maintain the sampling apparatuses within the smoke plume. In addition, obstruction from the dark smoke limited visibility and required external communication. This caused slight delays, which would result in gaps of missing data points during sudden wind shifts. Average CO/CO<sub>2</sub> values were outside of the reasonable range for these experiments since these values approach zero. This means CO concentration readings tended to approach zero, which is not reasonable for a fire of this size.



**Figure 103 - Average CO/CO<sub>2</sub> comparison for HOOPS cases sampled at Crane.**

It was observed that overall CO/CO<sub>2</sub> values were lower at the Crane position compared to on the TC tree at Pos 2. The hypothesis is that CO concentrations decay at a much faster rate with respect to height compared to CO<sub>2</sub>. Once past a certain reasonable height, it becomes more difficult to quantify burning behavior based on CO/CO<sub>2</sub> because CO concentrations begin to approach zero from ambient dilution. Figures 102 and 103 conclude that real-time gas sampling should be above the flame tip of a fire, but not too far from the fire where ambient dilution and wind shifts become a limiting factor. A discussion on CO<sub>2</sub> and CO concentration decay with respect to height as well as optimal sampling height is shown in the appendix section of this report as a publication.

This research originally included Pos 1 and 3 on the TC tree for a more systematic study on combustion product spatial distribution, however, equipment issues at Pos 3 resulted in missing data sets while the sampled gas concentrations at Pos 1 far exceeded the sampling capabilities of the gas sensors. The deployment of FR prototypes yielded flame heights that were higher than anticipated, and therefore resulted in Pos 1 no longer being in the intermittent flame zone but in the continuous flame zone. As mentioned in the publication in the appendix, the sampling point cannot be in the continuous flame zone to minimize the effect caused by flame chemistry.

As noted previously, EPA was present for the first week of experiments. The same publication in the appendix provides a section that compares gas emissions data between EPA and WPI. EPA data suggests that Grid FR provides the most improvement in emissions, particularly the

significant decrease in particulates compared to other FR's. This makes the case for Grid FR as the overall best performing FR for future work and commercialization.



## 4. Phase III

### Overview

In the Phase II experiments at CRREL, it was observed that foaming was frequent with best working prototypes (Grid and Bimetal FR) and the FR coverage area to the pool area (Projection Ratio) might affect the overall efficiency of the FR prototype.

Using this information from Phase II, the experiments in Phase III were designed to answer the following questions:

1. Does fuel thickness and placement of the FR in the fuel region play a role in burning?
2. Does the projection ratio<sup>1</sup> of the system play an important role in enhancing the overall efficiency of the FR prototype?

The Phase III experiments were divided into 2 sections with one set of experiments performed in December 2020 and the second set in February 2021. Notable points between the December experiments and the February experiments are:

- i. The December experiments did not have a continuous feed replicating CRREL experiments, while the February experiments were conducted with a continuous fuel feeding setup to achieve a steady state during the combustion.
- ii. December experiments were performed with a pool diameter of 70 cm, while the February experiments were performed with a pool diameter of 28 cm. The smaller diameter burn allowed floating the FR in a pool of water.
- iii. The December experiments had a projection ratio of 0.1, while the February experiments had a projection ratio of 0.6. Note that CRREL experiments during Phase II had a projection ratio equal to 0.25 – 0.5.

The results in Phase III of the experiments in December showed that placement of the FR played a significant role in achieving higher efficiency and overall reducing emissions (CO/CO<sub>2</sub>). Projection ratio of 0.6 in the February tests yielded higher regression rates (4.8x with kerosene fuel and 4.2x with HOOPS crude oil).

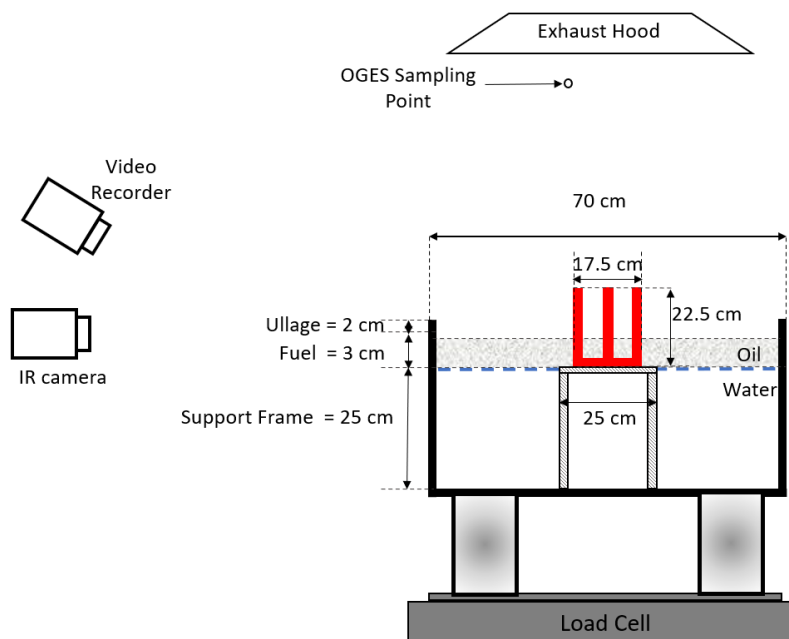
---

<sup>1</sup> The projection ratio is the area projected by the FR on the fuel surface divided by the total fuel surface area. A projection ratio = 1 means the FR is covering the entire fuel surface.

### PHASE III Experiments at WPI (0.7 m scale) (December 2020)

#### Experimental Setup

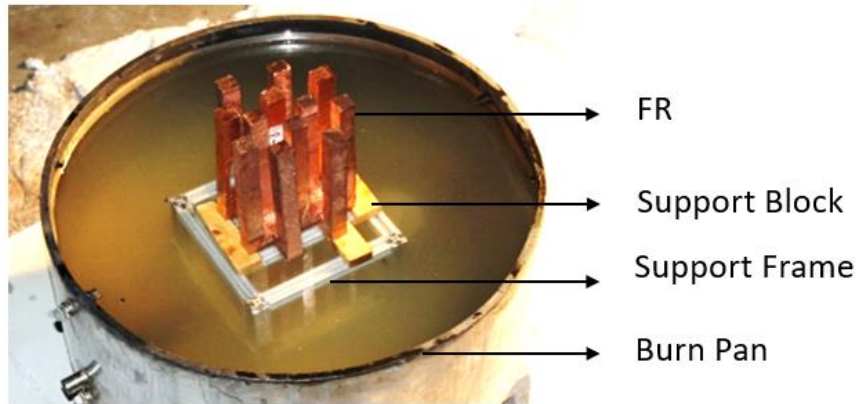
The experimental setup consists of a stainless-steel burn pan 70 cm wide and 30 cm deep (Fig. 104). The burn pan houses a stationary 8020-aluminum frame 25 cm x 25 cm wide and 30 cm tall that sat in the water layer at the bottom of the pan, the frame was used to support the FR's during the experiments. The projection ratio of the FR's tested varied from 0.04 to 0.12.



**Figure 104 - Experimental setup for Phase III experiments performed at WPI during Dec 2020**

The experimental setup was instrumented with thermocouples to record FR temperatures. Mass loss data was collected from the load cell placed underneath the burn pan and emissions were monitored from the OGES sampling point for every experiment to validate the efficiency of the FR's. Additionally, an infrared camera and digital video recorder were used to capture flame behavior and corresponding temperature profiles for the experiments done.

A total of seventeen experiments were performed with HOOPS crude oil and kerosene in an experimental platform shown in Fig.104. Five FR prototypes were tested, three with blanket bases and two standalone with different fuel thicknesses and configurations.



**Figure 105 - Experimental setup for Phase III experiments performed at WPI during Dec 2020. The diameter of the vessel is 70 cm. The FR was supported on an aluminum frame, as shown in the photograph. The initial fuel slick thickness for all experiments was 3 cm.**

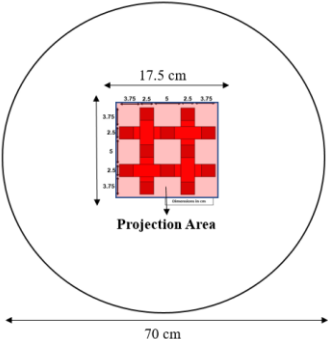
Blanket case FRs comprised of 1 cm thick Cu fibers (0.0127 cm wire diameter) sandwiched between two Cu meshes (wire diameter of 0.058 cm and has an opening of 0.13 cm between wires) manufactured for coils (wire thickness 0.4 cm) and grid FR (plate thickness 0.08 cm and 1 cm). The coil and grid structure sat on top of the blanket as collectors. Rack (plate thickness of 2.5cm) and rod (diameter of 3.81cm) FRs were used as standalone prototypes with no blanket underneath them, as they act as collectors and heaters coupled together. Table 11. shows the detailed test matrix in the order of testing and corresponding initial results. The projection ratio, defined as the ratio of the FR coverage area to the total pool area, is shown in Table 12.

**Table 11 - Experimental matrix for Phase III experiments at WPI (0.7 m scale) – December 2020**

#	Fuel	Prototype FR	Prototype Placement	Collector Height (cm)	Heater Height (cm)	Fuel Thickness (cm)	Burn Efficiency (%)	Burn Duration (min)
1		Baseline	-	-	-		58	11
2	HOOPS Crude Oil	Rack	Center	19.5	3	3	81.2	23
3		Rack	Corner	19.5	3		58	17
4		Rack – Raised	Center	20.5	2		88	28
5		Rod	Center	12	4		64	14
6		Thick Grid & Blanket	-	9	3		73	21

7		Thick Grid – no Blanket	-	9	3		52	10
8		Thick Grid & Blanket	-	10.5	1.5		68	24
9		Thin Grid & Blanket	-	9	3		64	12
10		Coils & Blanket	-	11	1		61	12
11	Kerosene	Baseline	-	-	-	2	99	12
12		Rack – Raised	Center	21.5	1		99	14
13		Rack separated	4 Corners	20.5	2		99	30
14		Rack separated	4 Corners	20.5	2	4	99	63
15		Rack Immersed	Center	19	2	2	99	31
16		Baseline	-	-	-	4	99	28
17		Rack – Raised	Center	21.5	1		99	51

**Table 12 - Projection ratios of FR's during Phase III experiments at WPI (0.7 m scale) performed in December 2020**

FR Prototype	Projection View	$\frac{\text{Projection Area}}{\text{Total Pool Area}} = \text{Projection Ratio}$
Rack		$\frac{(17.5 \times 17.5)}{(\pi \times 35^2)} = 0.08$

Rack – Distributed		$\frac{(\pi \times 35^2) \times (\pi \times 32.75^2)}{(\pi \times 35^2)} = 0.12$
Grid – no blanket		$\frac{(12 \times 12)}{(\pi \times 35^2)} = 0.04$
Grid – with the blanket		$\frac{(\pi \times 8.75^2)}{(\pi \times 35^2)} = 0.06$

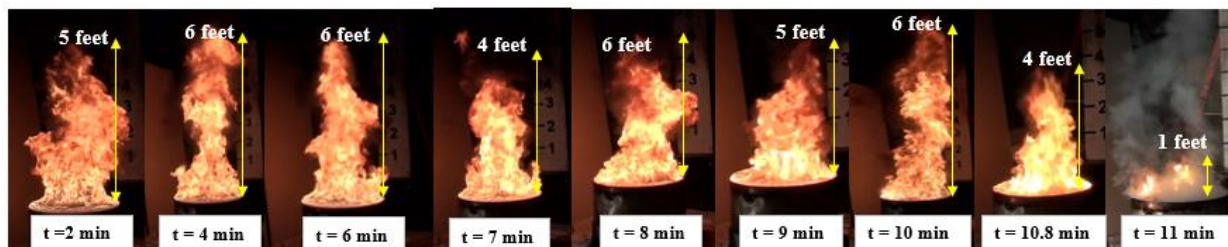
## Analysis of Burning Behavior

The section discusses the burning behavior of the 2 FR prototypes, analyzed in different working conditions. The experiments are not replenished with fuel and are transient in nature where the fuel layer regresses with time.

Experiments with HOOPS crude oil

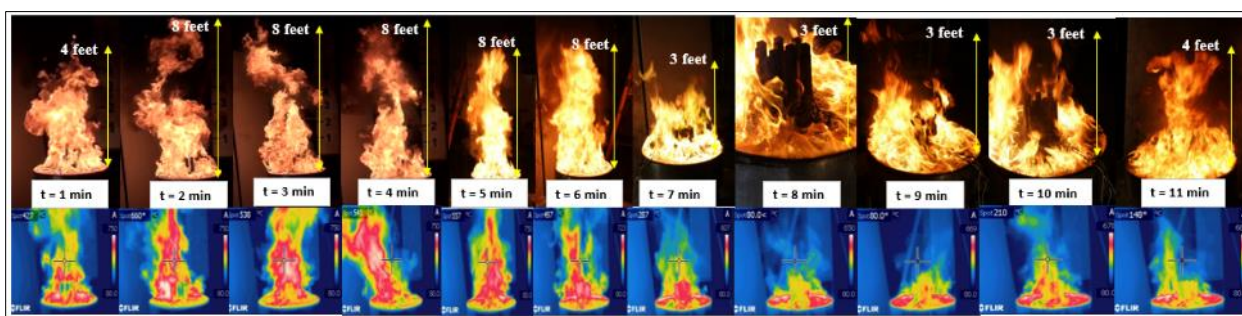
### i. Rack FR

The yellow highlighted cases in Table 11 of baseline, the Rack FR and Grid FR with its heater partially and fully immersed in the fuel slick of thickness 3 cm are analyzed in detail for HOOPS crude oil. This is done to demonstrate the influence of initial and boundary conditions on the efficiency of the FR. The fuel is constant at 3 cm thickness for all the cases discussed in this section.



**Figure 106 - Flame height progression and analysis for baseline case with 70 cm crude oil pool fire.**

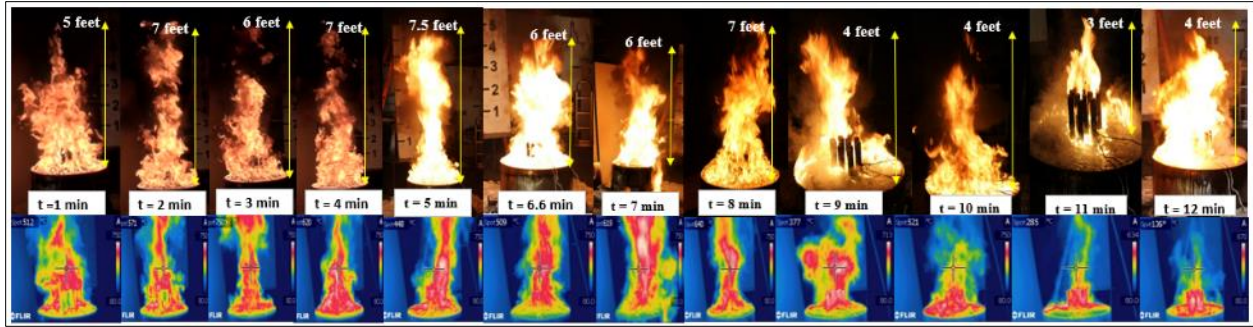
The burning behavior of HOOPS crude oil slick floating on water with an initial fuel thickness of 3 cm and a pool diameter of 70 cm is shown in Fig. 106. The flame height hovers consistently around 5 – 6 feet for the duration of the experiment. At  $t = 7$  min, small crackling sounds are observed and continue until  $t = 10$  min, where a boilover is observed. The flame height does not increase substantially, and the fire extinguishes within 1 min after boilover, as shown in Fig. 106.



**Figure 107 - Flame height progression and analysis for rack FR case with 70 cm crude oil pool fire with FR placed water fuel interface.**

Figure 107 shows the burning behavior of the case where the FR is immersed in the fuel slick with its bottom touching the water-fuel interface. The burning is much more intense than the baseline case with the presence of the FR, with flame heights reaching 8 feet compared to the 5 – 6 feet observed during the baseline. Since the heat transfer rate into the pool increases, crackling sounds of water boiling are observed earlier at  $t = 5$  min, with intense crackling around  $t = 6$  min. However, since the water boiling is localized around the FR and the FR does not cover the entire pool surface area (projection ratio = 0.08, Table 12) at  $t = 7$  min, foaming behavior is observed, and the flame height decreases to 3 feet from 8 feet. The rest of the burn occurs with the average flame height around 3 feet to 4 feet and extends to 23 minutes of total burn duration. Also, from 8 min to 24 min, the flames tend to move away from FR at the onset of foaming and come back in around 1 min intervals in a cyclic way. This behavior is clearly observed in the photographs at  $t = 10$  min and  $t = 11$  min in Fig. 107 (visible and IR). This cycle continues until the fire is extinguished at  $t=23$  min. IR camera images also show the reduction in the overall flame heat transfer after the 7 min. A similar pattern was also observed during the CRREL experiments of Phase II.

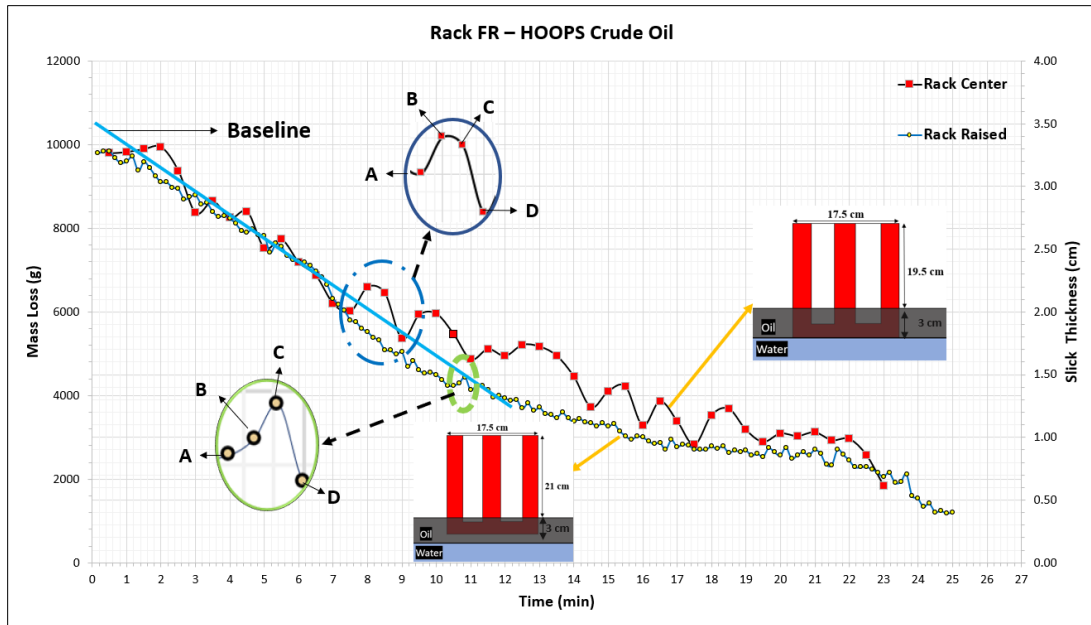




**Figure 108 - Flame height progression and analysis for rack FR case with 70 cm crude oil pool fire with FR raised 1.5 cm midway in the fuel layer.**

Figure 108 shows the burning behavior under similar conditions but with the FR raised midway in the fuel layer. Thus, the heater of the FR is not fully utilized as half of the fuel slick  $\sim 1.5$  cm is not exposed to it. In this case, the burning behavior is again higher than the baseline, with the flame height around 6 to 7 feet. Surprisingly, intense crackling is observed much earlier for this case at  $t = 5$  min, and at around 6.6 min, the fuel starts bubbling out of the container. A cyclic pattern of flame moving back and forth from the FR serving as an anchor is observed in this case after  $t = 7$  min. The burning slows down and continues till the fire self-extinguishes at  $t = 28$  min. The cyclic movement of the flame is because of the formation of water vapor that bubbles through the oil slick rather than causing boilover has never been reported in the literature. It is a unique phenomenon first observed during CRREL experiments (Phase II) and then re-confirmed during the WPI experiments (Phase III).

Figure 109 shows a 10 second moving average of the mass loss data vs. time for the three cases discussed earlier. These include baseline, a rack FR placed in the center with the base touching the water sub-layer, and a rack FR placed in the center with its base raised, as shown in the inset sketches of Fig. 109. The fuel slick thickness is also shown in Fig. 109 on the alternate Y-axis on the right-hand side. The three experiments analyzed in Fig. 109 are also highlighted in Table 11.



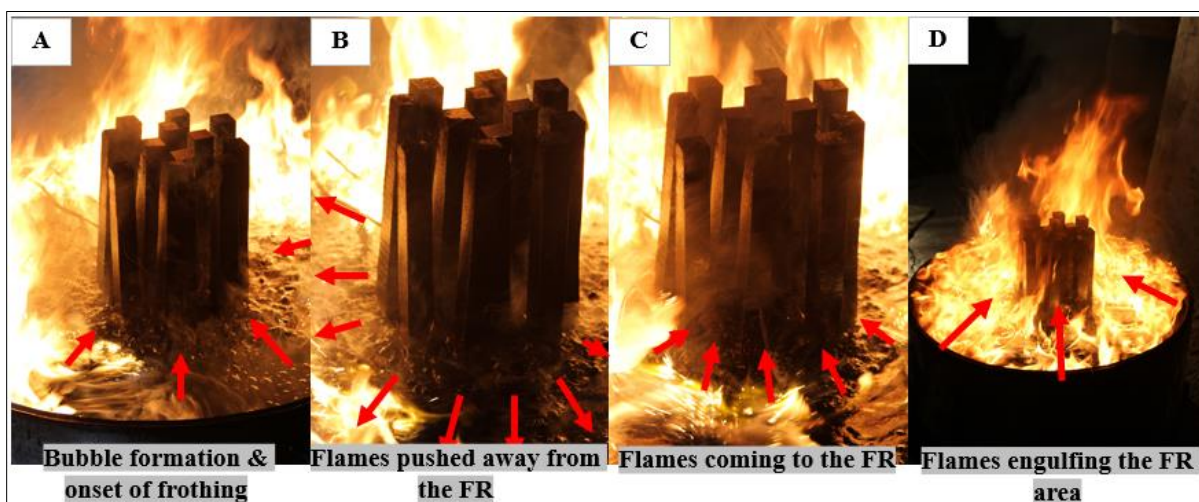
**Figure 109 - HOOPS crude oil mass loss vs. time for baseline (blue curve), Rack FR placed at the fuel-water interface (red), and Rack FR placed midway in the fuel layer (green). Initial oil slick thickness equals 3 cm. Pool diameter equals 0.7 m.**

As shown in Table 13, the burn efficiency of the rack FR placed at the water-fuel interface equals 81.2%, while the FR placed midway in the fuel layer has a higher efficiency equal to 88%. Both burn efficiencies are significantly higher than the baseline case of 58 %. The FR's are thus able to burn off the higher boiling point tar-like fuel in the crude oil. However, the low projection area of the FR's causes boiling of the water sublayer. Since the boiling point of water is lower than that of crude oil, the subsequent water boiling causes the heat from the FR to be predominantly directed to the water sub-layer. The nucleate boiling in the crude oil ceases, and instead, water starts boiling. This leads to foaming and foaming behavior, causing the burning to occur in a cyclic fashion with ups and downs, as shown in the mass loss vs. time graph in Fig. 109. This cyclic motion also delays the duration of the burn because of the flame cycling, as shown in Fig. 109. This back-and-forth movement is related to the initial and boundary conditions.

**Table 13 - Duration, efficiency, and rate of combustion for HOOPS crude oil slicks floating on water, with an initial thickness of 3cm and pool diameter of 70 cm.**

Prototype	Configuration	Burn Duration (min)	Burn Efficiency (%)	Burn rate (g/min)
*	Baseline	11.3	58	1.62
Rack FR	Center	23.3	81.2	1.02
	Center – Raised	28.2	88	0.91

Figure 110 shows the fire behavior during foaming for the rack FR when placed at the water-fuel interface. The FR heats the water layer creating a regular stream of water vapor bubbles around the FR and pushes the fire away from the FR. A recent study at WPI shows that the frequency of the water bubbles is around 60 Hz with an average bubble size of approximately 1 mm. The significant quantity of bubbling causes the fire to be quenched around the refluxer region, as shown in Fig. 110A. The burning slows down from Fig. 110A to 110C, also demonstrated by the positive slope on the mass loss vs. time curve shown in Fig. 109. With no flame around the FR, it cools, and this causes a reduction in the water vapor. The fire then comes back radially to the center towards the FR as shown in Fig. 110C and 110D. The corresponding burning rate increases as shown by the negative slope of the mass loss vs. time when traversing through points C and D in Fig. 109. The cycle repeats throughout the burning duration, with the frequency changing because of the fuel layer thickness not being constant. Thus, in this case, the localized heating of the water sublayer caused by the flame refluxer results in a cyclic burning behavior.



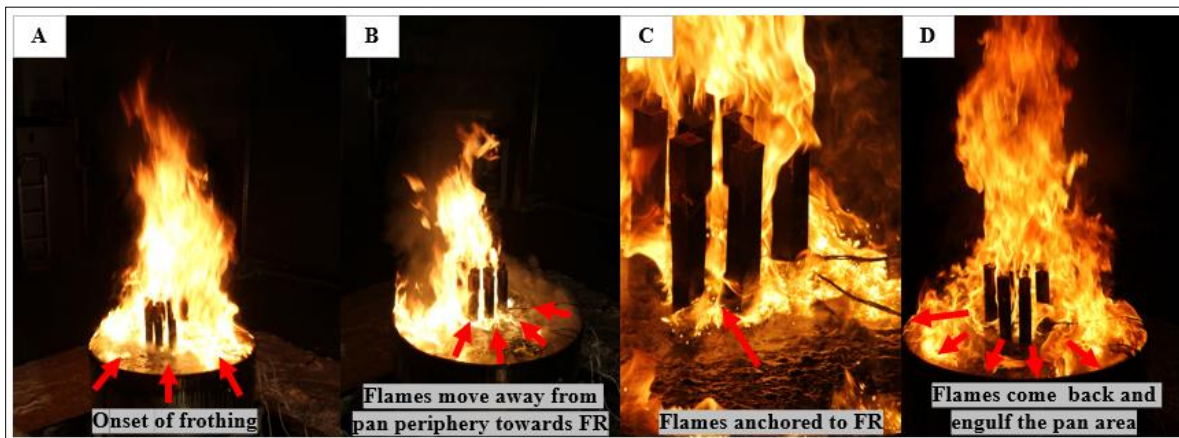
**Figure 110 - Foaming cycle observed with Rack FR with a center configuration where the FR bottom sits at the water-fuel interface.**

The Fig 111. shows the similar pattern that was observed with bimetal FR in wave 1 condition, where the flames were observed to die from the center and propagate towards the periphery and come back to the center towards FR to form a fully mature fire. This phenomenon at that time was only attributed to the foaming and not attributed to the placement of the FR, from the experiments concluded in December the results reconfirmed this behavior observed in Phase II.



**Figure 111 - Foaming cycle observed in Phase II experiments at CRREL with bimetal FR in wave 1 condition with Hoops crude oil**

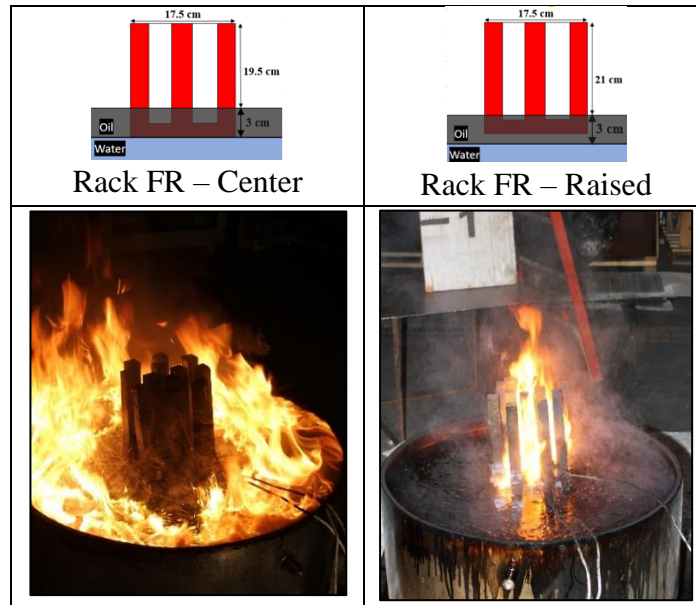
Figure 112. shows that the behavior of the cyclic motion is also a function of the initial and boundary condition. When the rack FR is placed midway on the oil surface, the burning efficiency improves by ~10%, as observed in Table 11. However, the burning behavior is still cyclic, with the FR serving as an anchor to the flames and the flames moving away from the burn pan towards the FR. This behavior is observed because after the fuel regresses by 1.5 cm (around 7 min) the FR heater is no longer immersed in the fuel surface. Instead, it is above the fuel (see Fig. 112B) and is only radiatively heating the oil slick at this time.



**Figure 112 - Foaming cycle observed with Rack FR - raised configuration where the FR bottom sits midway in the fuel layer**

Fig 113. Shows the flame behavior observed in the cases with rack FR at the onset of foaming behavior. The key difference between the two cases where the FR is placed at the water-fuel interface and FR is raised midway in the fuel is that they behave oppositely. In the case where the FR is raised, the flames are anchored to the FR while in the case where the FR is at the interface the flames move away from the FR. This behavior can be attributed to the initial boundary conditions and heat transfer feedback of the FR discussed in Fig 110 and Fig 112.

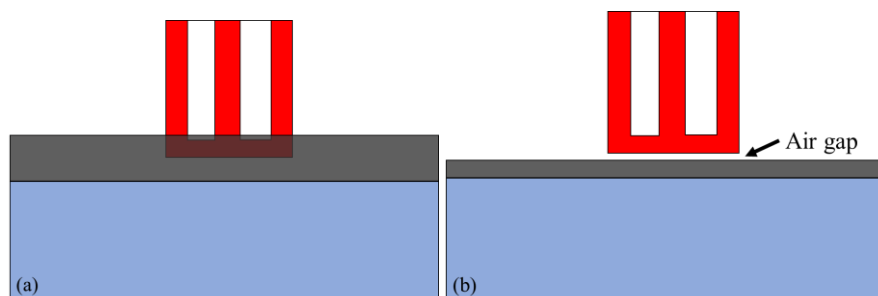




**Figure 113 - Flame behavior observed at the onset of the Foaming cycle observed with Rack FR – i. Center case – FR sits at the fuel-water interface ii. Raised case - FR bottom sits midway in the fuel layer**

### **Transient behavior of CO/CO<sub>2</sub> using OGES**

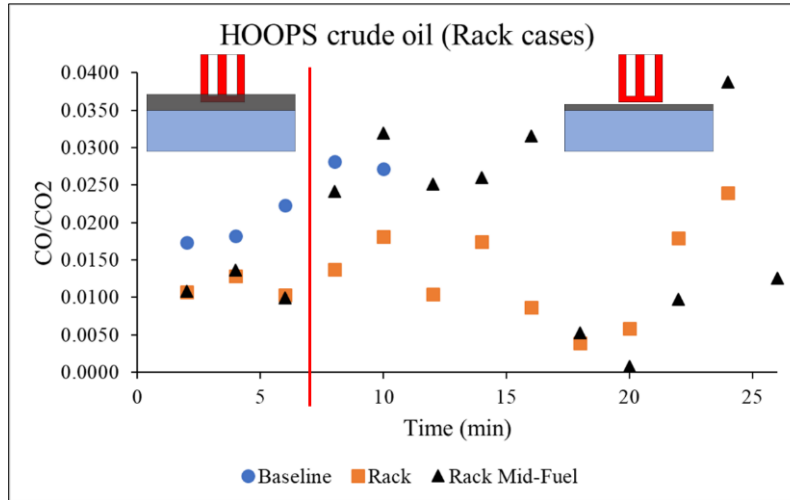
A time-dependent study was performed on the Rack cases with HOOPS crude oil as the fuel to investigate the transient changes in CO/CO<sub>2</sub> ratio as the fuel regresses throughout the burn. For “Mid-fuel” cases, the fuel regresses to a certain point throughout the burn so that the FR is no longer in contact with the fuel. When this air gap is created, the lower heat transfer coefficient of air allows it to act as an insulation that hinders heat transfer from the FR to the fuel layer. An illustration of this description is shown in Figure 114.



**Figure 114 - FR placement within fuel for Rack Mid-Fuel case during (a) early (b) late-stage**

Figure 115 shows the CO/CO<sub>2</sub> values in the plume region at 2 minutes increments for the Rack cases using HOOPS crude oil. Figure 8 shows that during the initial stages, the Rack FR can provide heat to the fuel layer, substantially decreasing unwanted emissions, or lower CO/CO<sub>2</sub> ratios. This results from direct contact resulting in effective heat feedback via conduction, which holds true for both placements of the FR, as the values are in close agreement. However, as indicated by the red line, after 7 min, it can be observed from the Rack Mid-Fuel case that it is no

longer providing a sufficient amount of heat feedback to reduce the CO/CO<sub>2</sub> ratio. The reason for this conclusion is that the CO/CO<sub>2</sub> ratio after 7 min reverts to values similar to that of baseline. It is deduced that there is an air gap present. However, due to the lack of this air gap in the FR case with complete immersion, it is still able to effectively reduce the CO/CO<sub>2</sub> ratio throughout the entirety of the burn, as shown by the significantly lower CO/CO<sub>2</sub> ratios after 7 min.

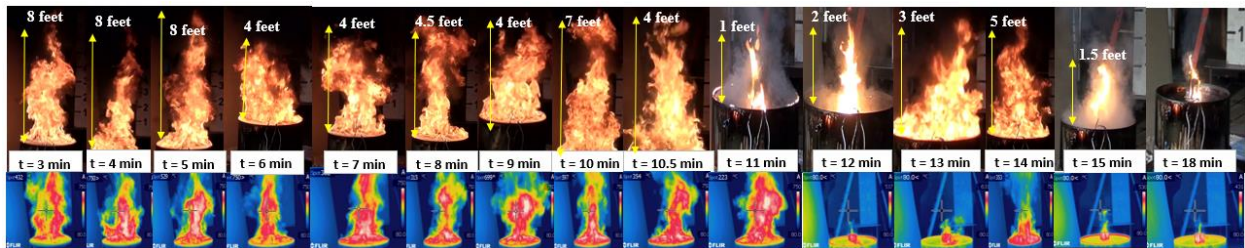


**Figure 115 - Transient CO/CO<sub>2</sub> comparison for Rack cases using HOOPS crude oil**

However, when the FR is placed too close to the fuel-water interface, the emission of water vapor creates other complications not associated with the improvements observed from sampled gas emissions. Further studies are required to improve knowledge regarding the placement height of FR within the fuel layer, and its effects on burning mass loss rate as well as gas emissions, especially when the fuel layer thickness is transient in nature.

## ii. Grid FR

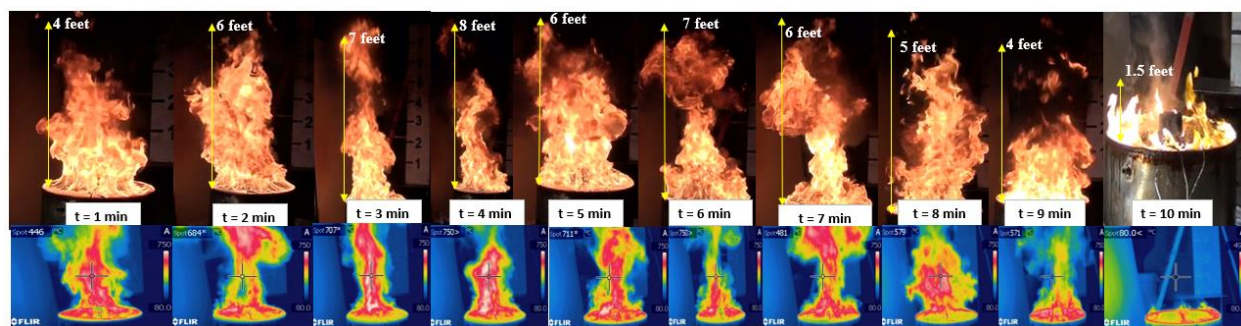
The same conditions that were previously experimented with rack FR were used as a reference point to understand if grid FR also exhibited the same occurrences that were seen in rack configurations. The grid FR was investigated with two configurations starting with grid FR with blanket and grid without a blanket, both the FR's placed at the fuel-water interface.



**Figure 116 - Flame height progression and analysis for grid FR with a blanket with 70 cm crude oil pool fire with FR at water fuel interface.**



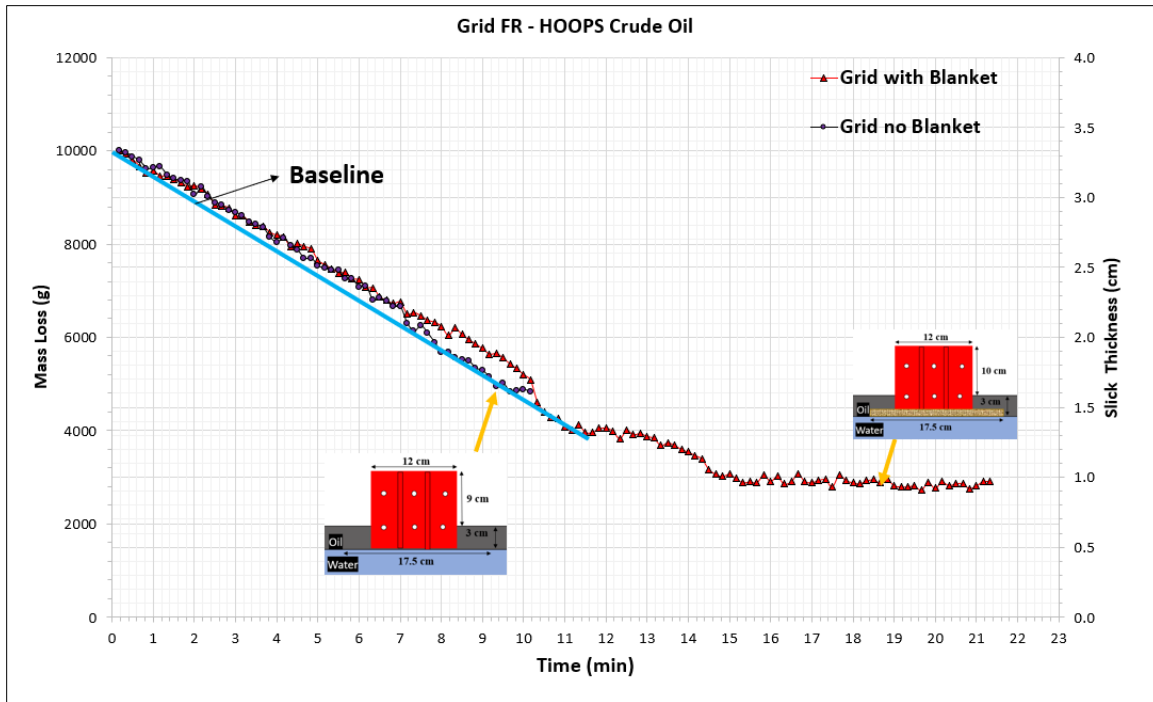
Figure 116. shows the burning behavior of Grid FR with a blanket, placed at the fuel-water interface. The flame height starts high with 8 feet tall fires and suppresses to steady 4 feet tall flames from  $t = 5$  min to  $t = 9$  min. Intense cracking sounds were observed at  $t = 9$  min due to the boiling of the water sublayer and soon after boilover was observed at  $t = 10$  min with intense tall flames reaching 7 feet, once the boilover was reached the flames anchored to the FR from  $t = 11$  to  $t = 12$  min; also visible on the mass loss vs time curve. The fire engulfs the burn area from the FR radially from  $t = 13$  to  $t = 14$  min and mellows with a small burst, the fire then subdues and stays just on the FR for the remainder of the burn from  $t = 15$  min to until it self-extinguishes at  $t = 22$  min.



**Figure 117 - Flame height progression and analysis for grid FR without a blanket with 70 cm crude oil pool fire with FR at water fuel interface.**

The burning behavior for the grid FR with no blanket showed a different behavior compared to that of the blanket case. The flame height for this experiment constantly hovered between 6 to 8 feet high from  $t = 2$  min to  $t = 7$  min before the onset of foaming behavior, intense cracking sounds were observed from  $t = 8$  min to  $t = 9$  min while also seeing a gradual reduction in flame height from 6 feet to 4 feet tall at  $t = 9$  min. The flames moved away from the FR at the onset of foaming and the flame's self-extinguished in 30 seconds after the onset of foaming. This was also observed with rack FR placed at the water fuel interface, where the heat from the FR creates localized boiling and pushes the flame away from the FR since rack FR had higher heat retention, a cyclic behavior was observed where the flames returned when the localized boiling reduced. While it was observed that the grid FR loses its heat feedback to the water sublayer significantly and fails to sustain the fire before it self-extinguishes soon after foaming at  $t = 10.5$  min.

Figure 118 shows a 10 second moving average of the mass loss data vs time discussed for the 2 FR cases with the grid. The figure shows the mass loss behavior of baseline, grid FR with a blanket placed in the center with the base touching the water sub-layer, and a grid FR without the blanket placed in the center with the base touching the water sub-layer. The fuel slick thickness is also shown in Fig. 118 on the alternate Y-axis on the right-hand side.



**Figure 118 - HOOPS crude oil mass loss vs. time for baseline (blue curve), Rack FR placed at the fuel-water interface (red), and Rack FR placed midway in the fuel layer (green). Initial oil slick thickness equals 3 cm. Pool diameter equals 0.7 m.**

The grid FR case with blanket performed higher than both baseline and Grid FR with no blanket case with 75% efficiency. While the grid without blanket performed similarly to the case with baseline. In no blanket, the FR case, the majority of the heat is lost to the water sublayer, which was also observed with rack FR with a configuration where the FR was placed the water-fuel interface.

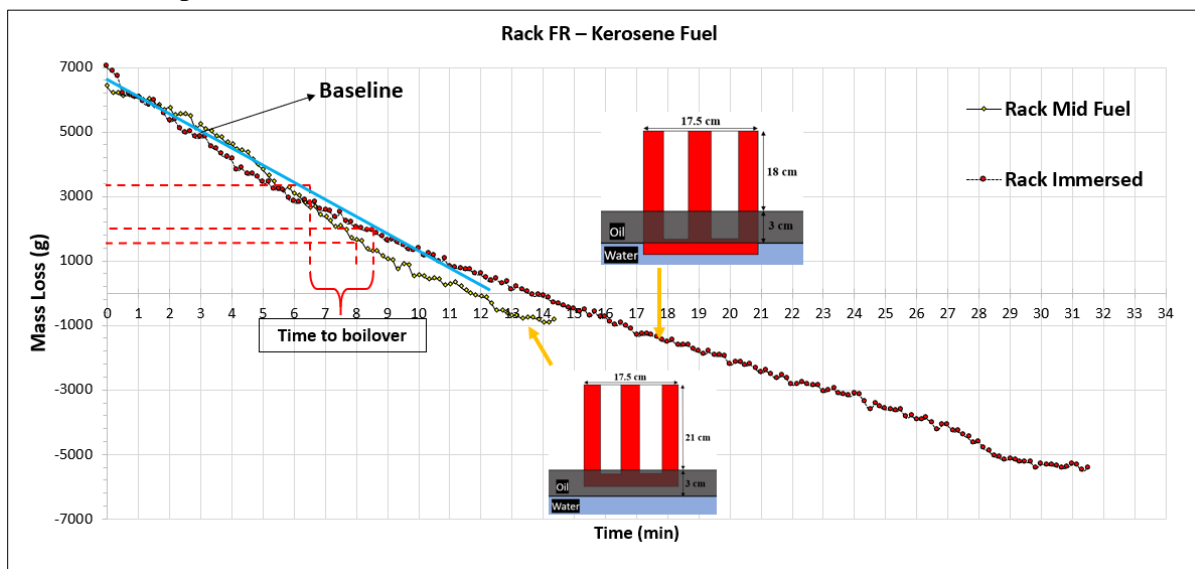
While the grid with a blanket observed a boilover, the case without a blanket did observe foaming. This can be attributed to the slowly rising temperatures in the water layer, which is not enough to cause foaming behavior.

**Table 14 - Duration, efficiency, and rate of combustion for HOOPS crude oil slicks floating on water, with an initial thickness of 3cm and pool diameter of 70 cm.**

Prototype	Configuration	Burn Duration (min)	Burn Efficiency (%)	Burn rate (mm/min)
*	Baseline	11.3	58	1.62
Grid FR	With blanket	21.4	75	0.98
	No blanket	10.35	53	1.5

## Experiments with Kerosene fuel

A similar data analysis method was used to study the burning behavior of Kerosene with FR's. Kerosene was chosen because it has a high boiling point (200 – 300 °C range). It also burns with an efficiency of 99% as it does not have tarry compounds like crude oil. Thus, the aspect of “burn efficiency” can be excluded from the analysis, and the focus on “burning rate” can be made. Kerosene also does not degrade such that lighter volatiles escapes first, as observed in the crude oil case. Kerosene is also transparent and allowed a more accessible analysis of the influence of initial conditions and water evaporation. Figure 119 shows the mass loss vs. time for two FR initial conditions compared with the baseline.



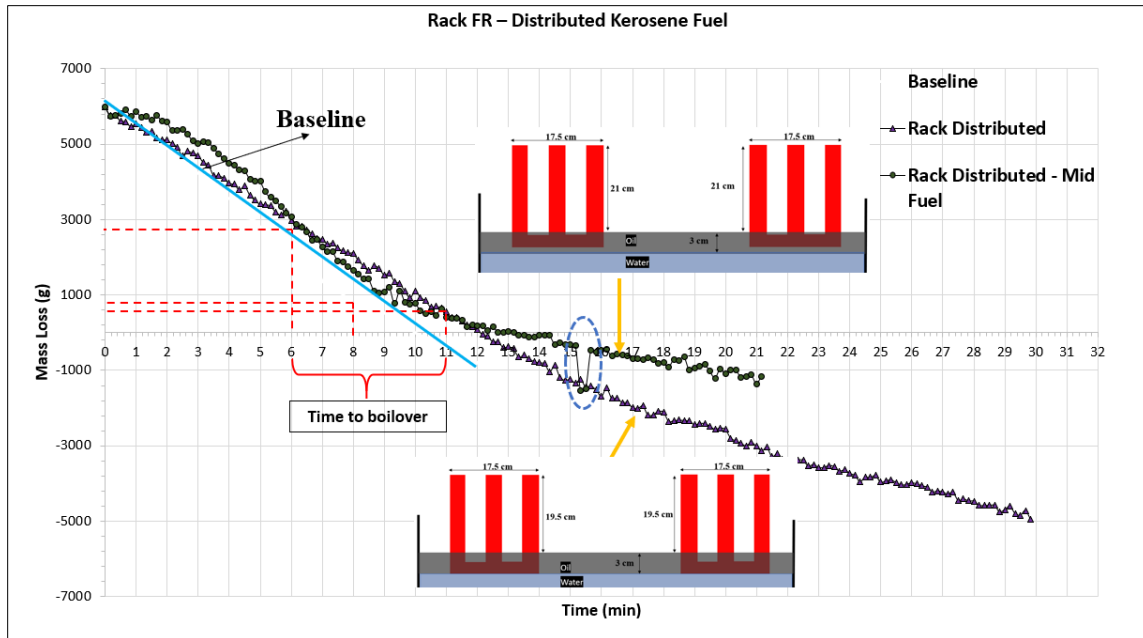
**Figure 119 - Kerosene mass loss vs. time. 1. Baseline (blue curve), 2. Rack mid fuel - FR placed midway in the fuel layer, and 3. Rack immersed - FR sits 1.5cm in the water sublayer**

Like the crude oil case, the Rack FR placed midway into the fuel captures and transfers heat to the fuel layer efficiently, thus yielding sustained burns with a higher burn rate throughout the test. Interestingly, when the FR was immersed in the water layer, the burn duration almost doubles! The slow-burning occurs because of water vapor evaporation. Thus, with the initial condition where the FR is in contact with the water sublayer during burning, most of the heat transferred by the FR is to the water sublayer. This is also evident from the time to boilover for this case, where boilover is observed in the shortest time of 6.5 min. However, not all kerosene can boil over. After this local increase in the burning rate, the heat from the FR is dissipated to the water, the water bubbles, the bubbles move through the kerosene layer, and superheated steam is mixed with the kerosene vapor, thereby diluting the flame and causing a reduction in the overall burning rate. This behavior extends the burning of the 2 cm layer of kerosene to 32 minutes! The mass loss is also negative on the Y-axis of Fig. 119 because of water vapor formation. Table 15 shows the pre and post-boil-over summary that shows the rack FR in different configurations for kerosene.

**Table 15 - Duration, efficiency, and rate of combustion for Kerosene slicks floating on water, with an initial thickness of 3cm and pool diameter of 70 cm.**

Prototype	Configuration	Burn Duration (min) Efficiency]	Water evaporated (g)	Time Boil over (min)	Mass loss Pre -Boil over (g)	Pre Boil over - Burn rate (mm/min)	Mass loss Post - Boil over (g)	Pre Boil over - Burn rate (mm/min)
-	Baseline	12.23 [99%]	740	8	5322.88	2.21	1617.77	1.34
Rack	Center - Mid Fuel	14.27 [99%]	888	8.5	4980.04	1.94	2308.00	1.28
	Center - Immersed 1.5cm	31.47 [99%]	5434	6.5	4195.27	2.14	8238.83	1.09

As for the cases where the rack FR was broken up into pieces and placed in corners of the burn area to see the influence of the projection area and placement of the FR in the burn area. It was again observed from Figure 120. that the FR in contact with the water sublayer had higher evaporation rates and longer burn durations as observed in all the cases with FR's placed at the water sublayer for all the above cases. The FR raised mid-way delays the onset of boilover considerably from the baseline and the corresponding case where the FR touches water sublayer by 3 and 5 min respectively. As can be seen from the mass loss is also negative on the Y-axis of Fig. 120, but higher evaporation rates are only observed where the FR is closer to the water layer, while the mid fuel placed FR performed par with FR placed at water interface in terms of regression rate observed in Table 16.



**Figure 120 - Rack distributed FR kerosene fuel mass loss data for 2 different configurations 1. Rack distributed - FR placed water-fuel interface and 2. Rack distributed mid fuel - FR sits midway 1.5 cm in the fuel layer.**

Table 16. below shows the pre-and post-boil-over summary that shows the rack FR in different configurations.

**Table 16 - Duration, efficiency, and rate of combustion for Kerosene slicks floating on water, with an initial thickness of 3cm and pool diameter of 70 cm.**

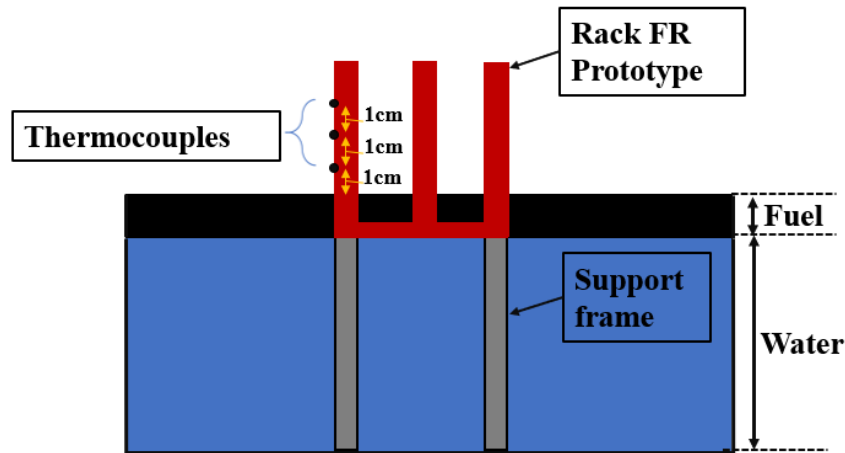
Prototype	Configuration	Burn Duration (min) [Efficiency]	Water evaporated (g)	Time Boil over (min)	Mass loss Pre -Boil over (g)	Pre Boil over - Burn rate (mm/min)	Mass loss Post - Boil over (g)	Pre Boil over - Burn rate (mm/min)
-	Baseline	12.23 [99%]	740	8	5322.88	2.21	1617.77	1.34
Rack	Distributed	29.92 [99%]	4831	11	5360.97	1.62	5470.11	0.96
Rack	Distributed - Mid fuel	21.15 [99%]	1150	6	2811.96	1.56	4338.56	0.93

In summary, the cases with FR placed at the water-fuel interface reached boilover earlier and foaming was observed for most cases because of the heat feedback to the water sublayer rather than to the fuel completely. while the cases where the FR was raised, the heat from FR was largely

distributed to the fuel layer yielding sustained burns with higher efficiency. Also, the higher evaporation rates from kerosene experiments showed clearly the heat dissipation to the water layer is higher in cases where the FR is at the fuel-water interface.

## Temperature Data

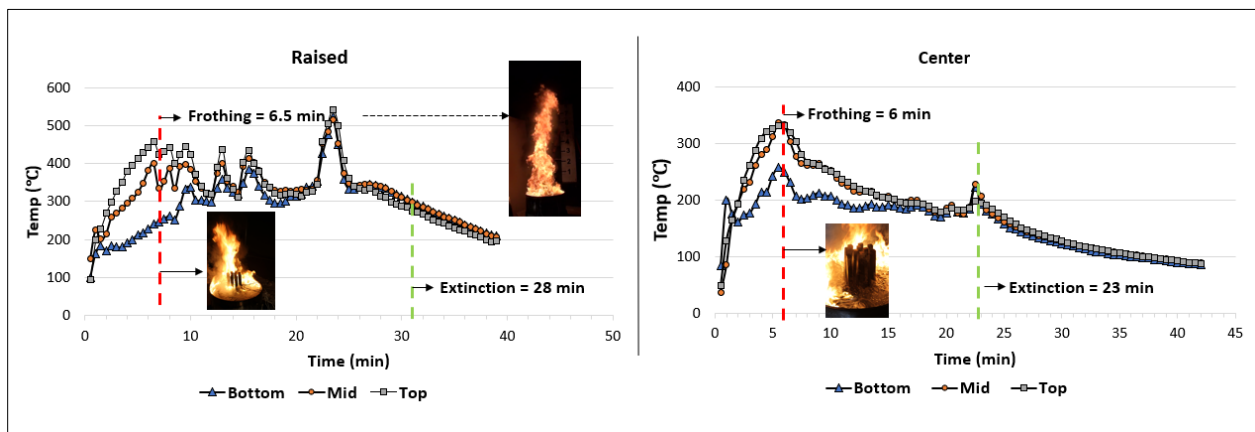
The experiments conducted in December were instrumented with 3 thermocouples spaced 1cm apart, shown as an example for the rack configuration in the figure below. These 3 Type K thermocouples were firmly anchored to the body of the FR itself and sampled at a rate of 1 Hz over the entirety of each experiment.



**Figure 121 - December experiments FR thermocouple arrangement, shown for Rack FR**

A 30-second moving average was done with the temperature measurements and plotted. These thermocouple measurements were used to assess the performance of each FR prototype, by both the rate at which they initially heat up during the beginning of the experiment and how they may be transferring heat to the fuel layer. A

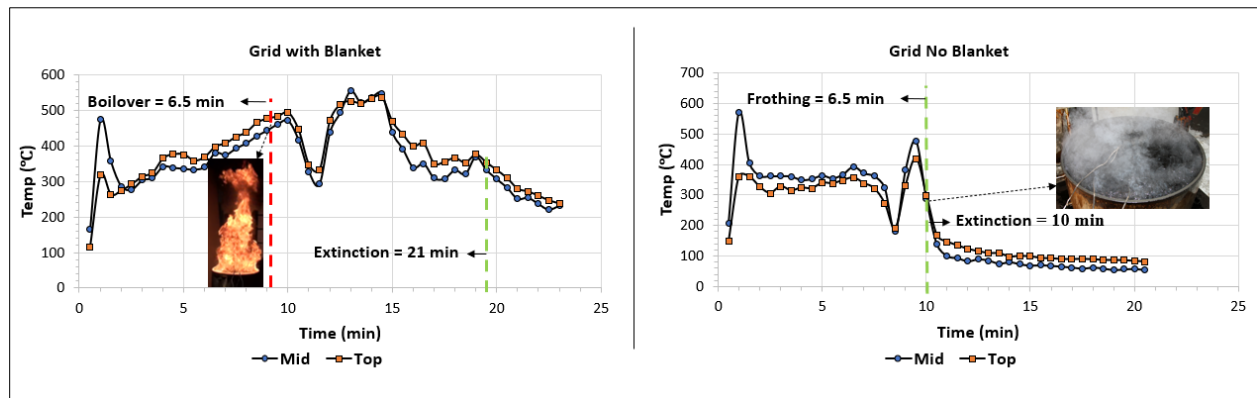
## Experiments with HOOPS crude oil





**Figure 122 - HOOPS crude oil temp vs. time for Rack FR placed at the fuel-water interface, and Rack FR placed midway in the fuel layer. Pool diameter equals 0.7 m.**

As seen in Fig. 122 the rack FR raised midway in the fuel heats up quickly reaching average temperatures of 300°C before 5 minutes from the ignition, while the FR placed at the water fuel interface only reaches roughly 250°C until the onset of the foaming. Temperatures in the raised configuration are higher since the flames anchor to the FR during the cyclic behavior that is previously covered in flame behavior analysis. It can be seen that the raised case also sustains constant average temperatures of ~350°C throughout the entirety of the test, while the configuration where the FR placed at the water sublayer. It gradually keeps reducing until it is self-extinguished. The average temperature sustained in this configuration is around ~220°C. Showing that a greater amount of heat is being lost to the water layer.



**Figure 123 - HOOPS crude oil temp vs. time for grid FR placed at the fuel-water interface i. with blanket ii. Without blanket - Pool diameter equals 0.7 m.**

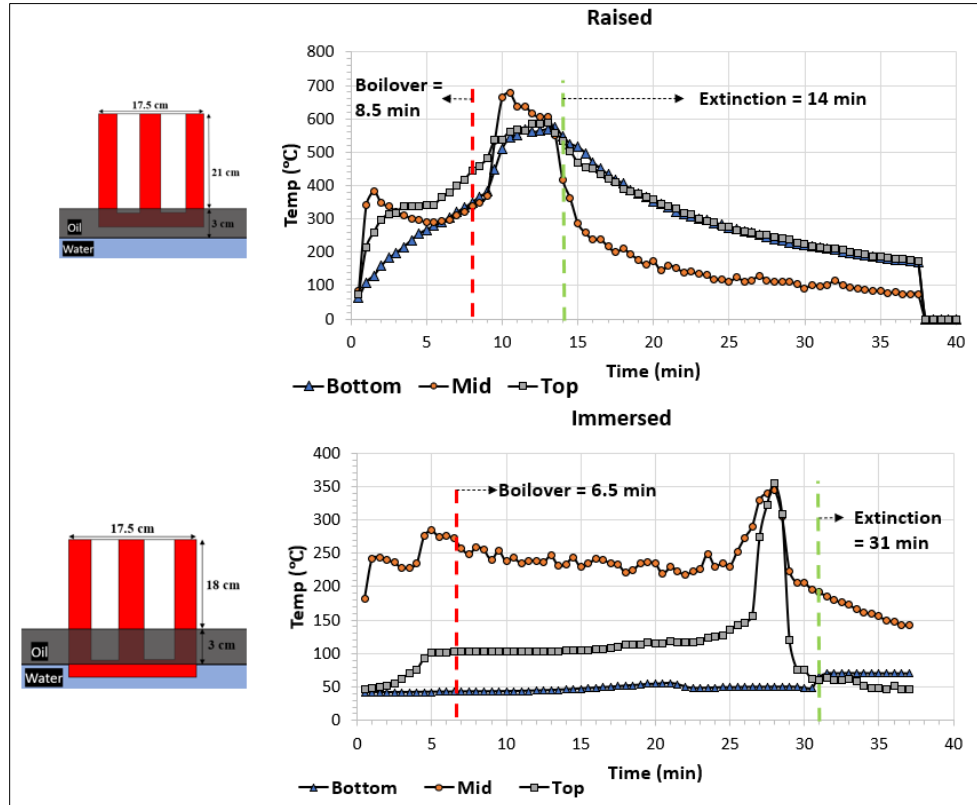
From fig. 123, the grid FR with the blanket case again achieves higher temperatures as the Grid FR is not in direct contact with the water layer, keeping the FR relatively at higher average temperatures of ~410°C. While the case with no blanket stays steady throughout the tests (~315°C) until foaming onsets and self-extinguish as temperatures drop in seconds of the onset of foaming.

### Experiments with kerosene

The experiments with crude oil showed that the rack FR was the best performing FR, and it also presented the configuration and placement of the FR had significant importance on the performance of the FR. Hence, experiments were further conducted to validate the data seen in crude oil experiments.

Figure 124. shows the 2 configurations of the rack FR raised midway in the fuel layer and the other case where it is immersed 1.5 cm in the water layer. As we can see from fig. 124 the temperatures go higher with the progression of the experiment for the raised case, while the temperatures remain relatively steady and low for the immersed case. The bottom TC in the immersed case never reaches the boiling point while the mid-TC which is at the water fuel interface reaches boiling

point throughout the experiment, confirming that a greater amount of heat is directed to the water layer causing the flames to dilute with water vapor and prolonging the experiment to 31 minutes in the case with FR immersed 1.5 cm in the water layer. The average temperatures for the raised case are also higher compared to that of the immersed case.



**Figure 124 - HOOPS crude oil temp vs. time for Rack FR placed midway in the fuel layer and rack FR submerged 1.5 cm in the water layer. Pool diameter equals 0.7 m.**

The experiments further showed similar results, the configurations closer to the water layer lost a significant amount of heat to the water layer. The FR takes a longer time to reach peak performance, as compared to the FR raised above the water layer (Fig 125).

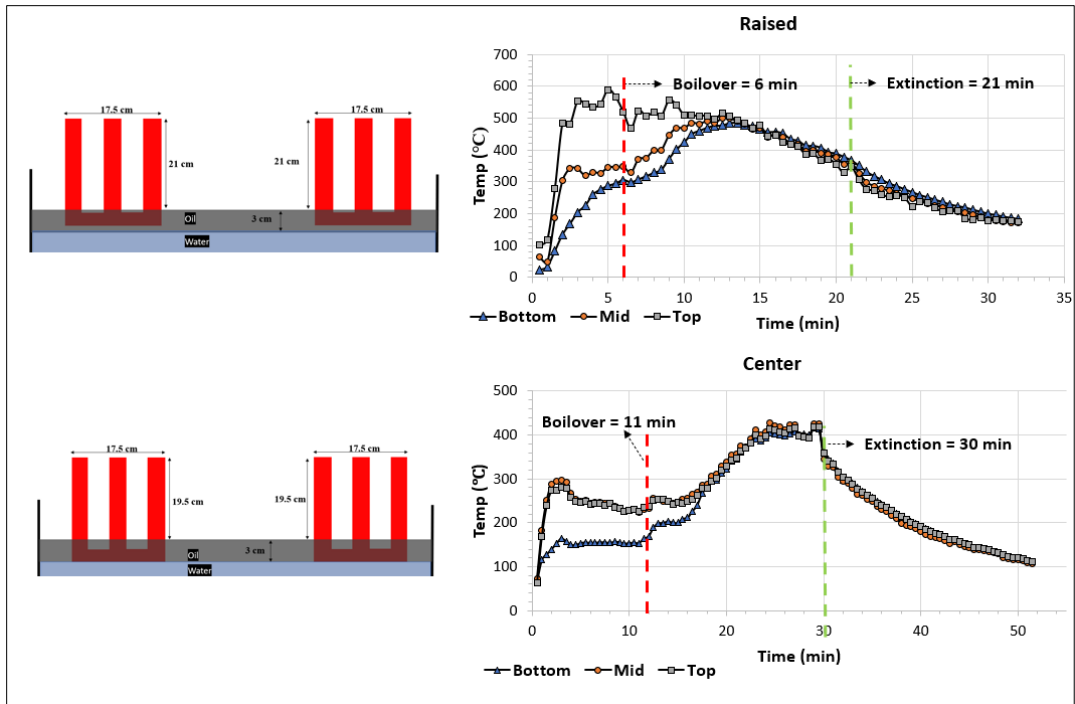
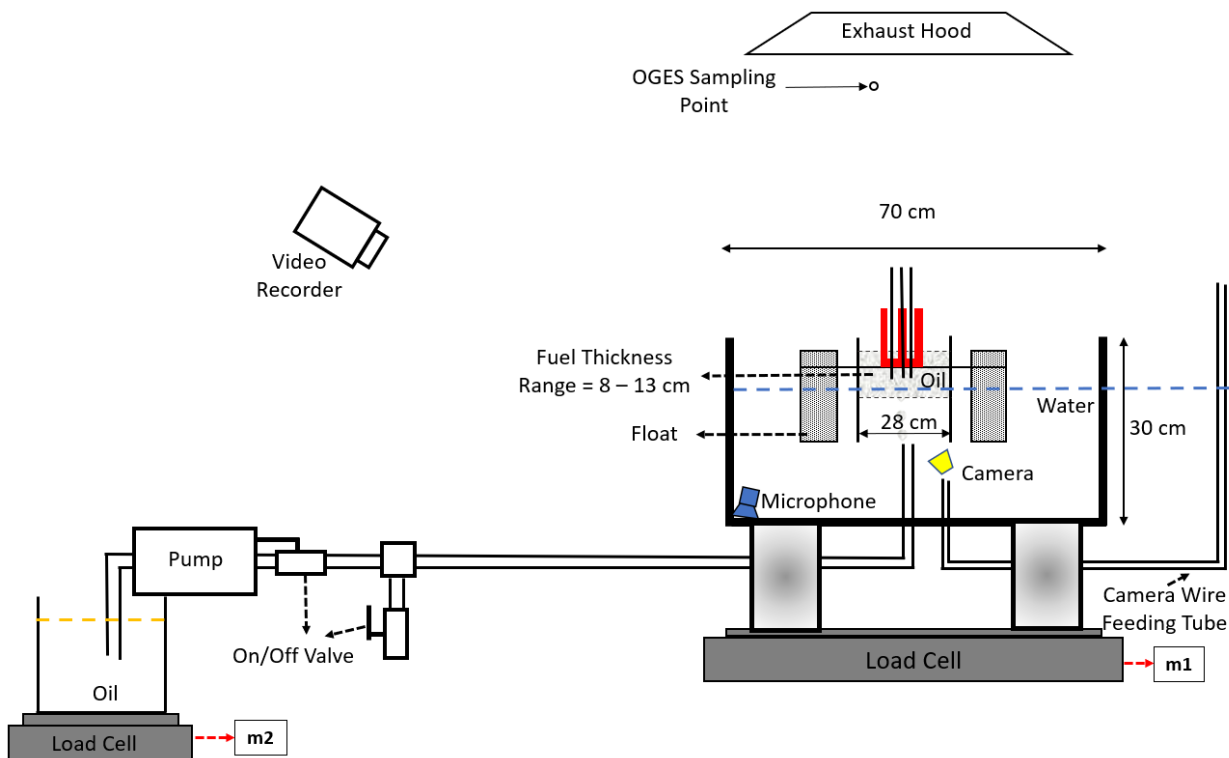


Figure 125 - HOOPS crude oil temp vs. time for distributed rack FR placed midway in the fuel layer and rack FR placed at the interface of the fuel-water layer. Pool diameter equals 0.7 m.

## PHASE III experiments at WPI (0.3 m scale) – February 2021

### Experimental Setup

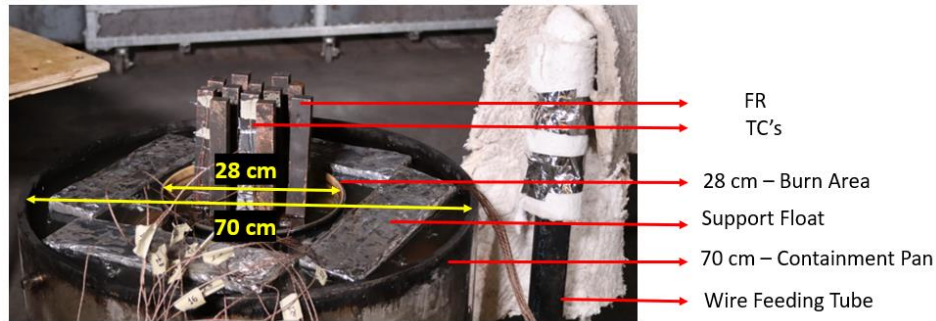
Figure 126 shows the experimental setup used for the second stage of Phase III experiments performed at WPI during Feb 2021. The FR's were contained in a 28 cm diameter burn pan that was floating in a water bath of 70 cm diameter, as shown in Fig. 126. The projection ratio was around 0.6 for these experiments.



**Figure 126 - Experimental setup for experiments performed during Phase III at WPI at 0.3 m scale. The FR was self-floating, and a steady state was achieved by continuously feeding fuel.**

The fuel is pumped to the burn area via a peristaltic pump that is controlled by manipulating the speed of the pump. The 70 cm diameter pan houses a 28 cm diameter steel ring that constitutes a burn area, as shown in Figure 127. The FR sits on a mesh supported by stainless steel rods held in place by high-density foam floats. The floats keep the FR neutrally buoyant.

The experimental setup is instrumented with thermocouples to record fuel, water, and FR temperatures. Mass loss data is collected from both the burn pan and the fueling station, and emissions are monitored for every experiment to validate the efficiency of the FR's in addition to the underwater microphone, to study acoustics and fire behavior correlations further.



**Figure 127 - Experimental burn pan for floating FR experiments performed at WPI in Feb 2021.**  
**Burn diameter = 28 cm, fuel slick thickness ~ 10 cm.**

Eight experiments were performed with HOOPS crude oil and kerosene. With information from tests conducted in December 2020, it was clear that Rack FR and Grid FR gave the highest efficiency of around 88 % compared to the baseline efficiency of 58 % for HOOPS crude oil. Therefore, experiments were performed with Rack FR and Grid FR's with various configurations shown in Table 17.

**Table 17 - Experimental matrix for Phase III experiments performed at WPI (0.3m scale) in February 2021**

#	Fuel	Prototype FR	Collector Height (cm)	Heater Height (cm)	Fuel Slick (cm)	Steady State MLR (g/min)	Burn Duration (min)
1	Kerosene	Baseline (70 cm)	-	-	9.5	414	82
2		Baseline (28 cm)	-	-	10	100	17
3		Grid + 6 Rods	Grid = 8.5, Rods = 30.5	Grid = 3.5, Rods = 8	10	147	81
4		Rack	14.5	5.5	8	211	54
5		Rack + 14 Rods	Rack = 17, Rod = 32.5	Rack = 5.5, Rods = 6	12	<b>476</b>	81
	HOOPS	Baseline2 (70 cm)			9	302 <sup>2</sup>	
6	HOOPS	Baseline (28 cm)	-	-	11	86	33
7		Rack	18	4.5	7	140	39

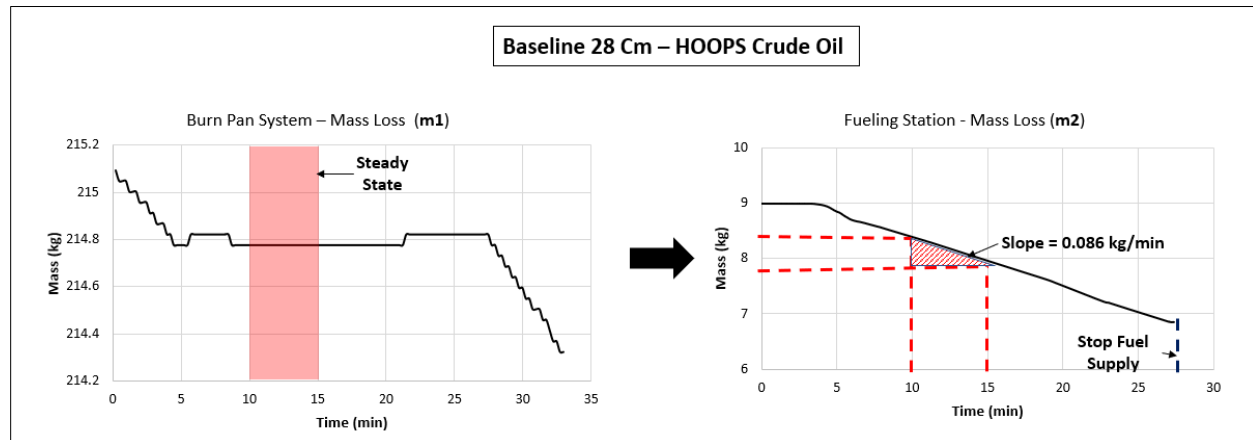
<sup>2</sup> Calculated from observed on Phase II baseline experiments at CRREL (~ 2 m scale), with HOOPS crude oil

8		Rack + 14 Rods	Rack – 17, Rods – 32.5	Rack- 5, Rods – 6	8	358	35
---	--	-------------------	---------------------------	----------------------	---	-----	----

## Analysis of Burning Behavior

### The methodology used to calculate steady mass loss rate

Figure 127 shows the methodology used to identify the steady-state region for each experiment and the corresponding mass loss rate is shown in Table 17 in g/min for all experiments.



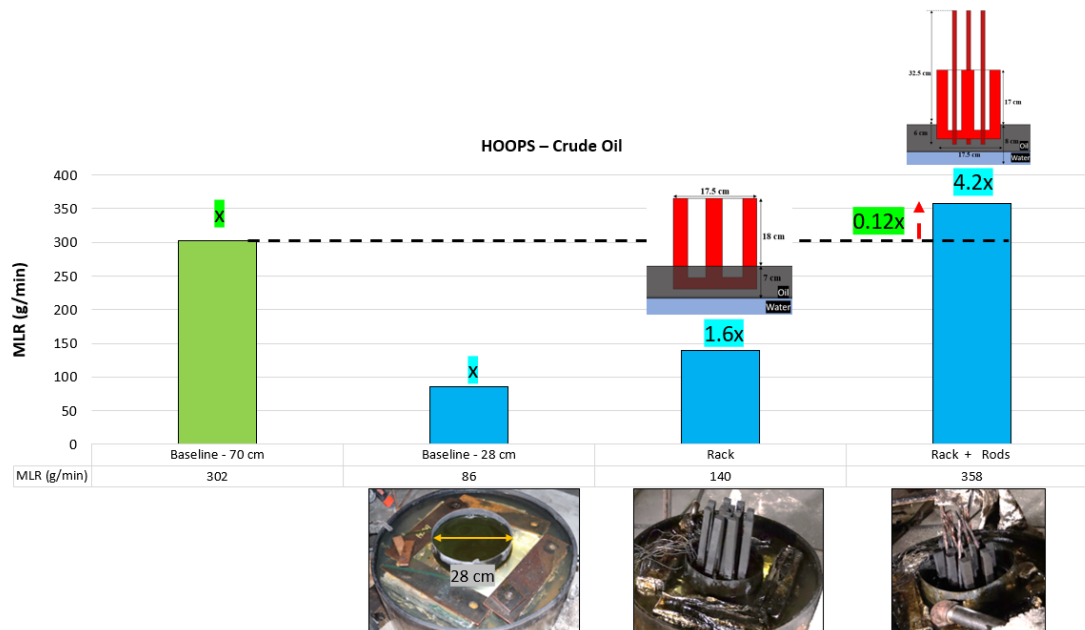
**Figure 128 - Steady-state mass loss data interpretation and regression rate sampling for baseline with 28 cm burn area for HOOPS crude oil.**

Figure 128 shows an example case for the experimental data recorded by the load cells at stations m1 and m2 shown in the schematic for the experiment in Fig. 126. m1 represents the overall mass of the system measured by weighing the burn pan containing the water and fuel. It is clear that when a steady mass loss rate is achieved, the incoming fuel delivered from the fueling station should balance the vaporized fuel at the burn pan. In other words, m1 will not record any change in mass. As shown in Fig. 128 (LHS), this occurs at ~9 min and continues till around 22 min. A five-minute window is identified by the shaded band from 10 – 15 min during this steady-state regime, as shown in Fig. 128. The steady mass loss rate in kg/min is estimated from the load cell station m2 as shown in Fig. 128 (RHS). The slope of the mass loss vs. time curve at station m2 equals 0.086 kg/min and is recorded as the steady-state mass loss rate in g/min in Table 17. The procedure is repeated for all the nine experiments shown in Table 5. The burning rate enhancement with the FR is observed for all cases with kerosene by comparing the baseline cases (shaded gray) with the experiments with FR's.

### Experiments with HOOPS crude oil

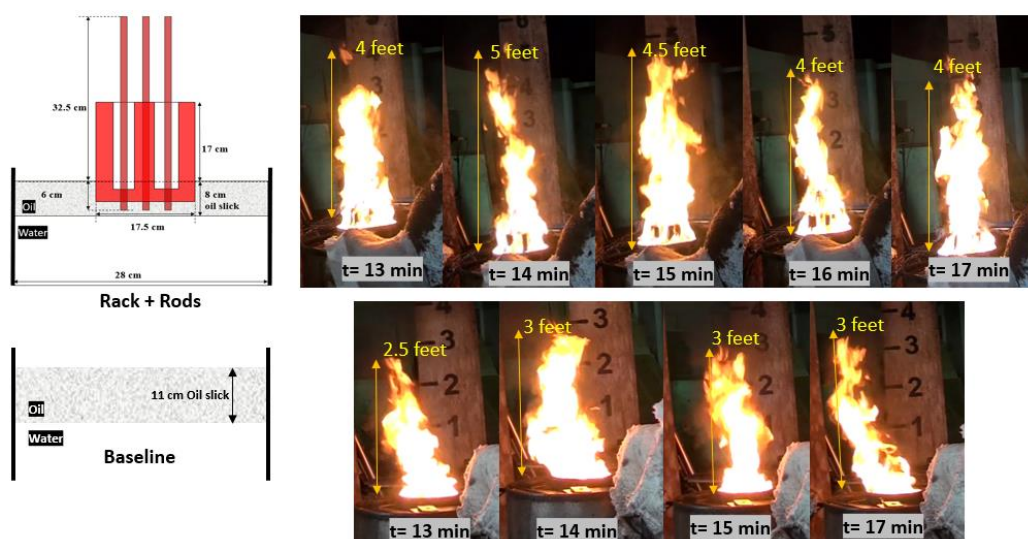
Figure 129 shows the experimental regression rate for HOOPS crude oil.





**Figure 129 - Steady-state regression rate for HOOPS crude oil.**

It can be seen that the combination of Rack and rod FR resulted in a 4.2x higher regression rate compared to the baseline case. Fig. 130 shows the flame behavior for the best performing case and the baseline. It can be seen that the flames average 4 to 5 feet tall for the best performing FR while the baseline steady-state only manages to peak about 3 feet tall.

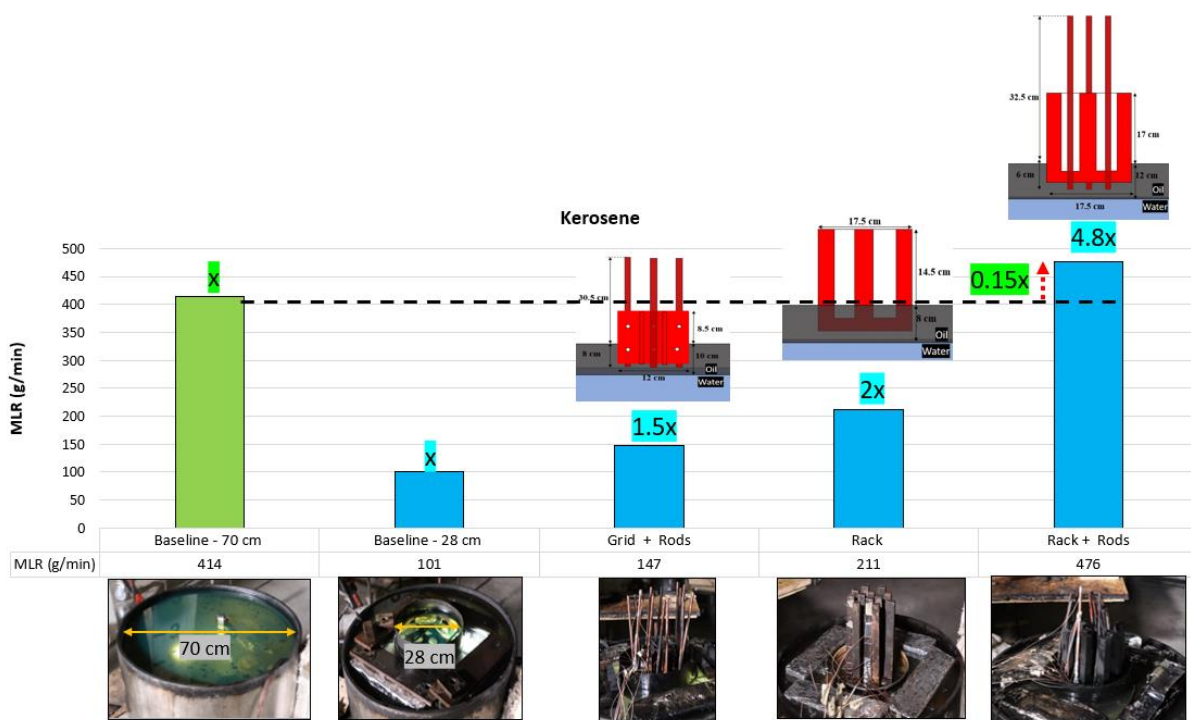


**Figure 130 - Flame height analysis of the best performing FR (rack + rods) and baseline case**

## Experiments with Kerosene

A total of 5 experiments were performed with kerosene as fuel. Two baselines with 70 cm burn area and 28 cm burn area, along 3 FR cases starting with a combination of grid and rods, rack and with the last combination of rack and rod FR's. The additional rods were added to the FR to

provide heat transfer at different depths of the fuel slick, as the fuel slick thicknesses were significantly higher compared to the 3 cm thickness used during the experiments performed in Dec 2020.



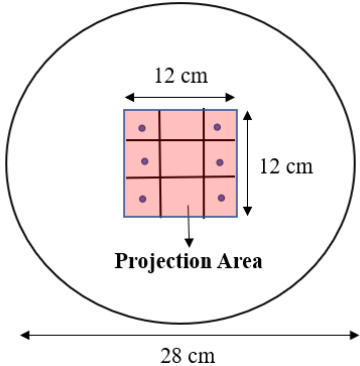
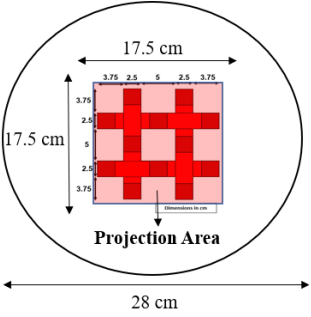
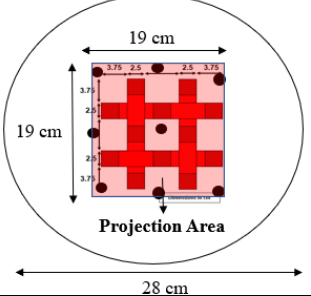
**Figure 131 - Steady-state regression rate for kerosene with a floating FR.**

From Figure 131, it can be seen the rack and rod combination FR performed the best yielding a 4.8x times higher regression rate than the corresponding baseline case. The rack and rod combination FR aggregated 0.15x higher regression rate even outperforming the baseline case with 70 cm burn area. Additionally, even just the rack FR in itself had 2x times the regression rate than the baseline case.

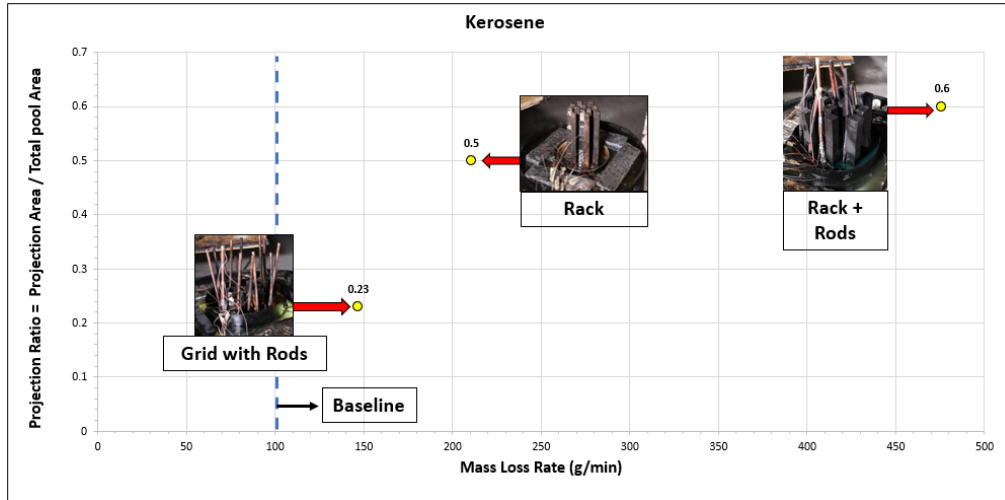
### Importance of Projection Ratio

Projection ratio refers to the ratio of the FR coverage area to the total pool area. Since the FR’s tested both with crude oil and kerosene fuel presented various dimensions, the projection area investigates the influence of the coverage area over efficiency. Table 18 shows the different FR’s and their respective projection areas.

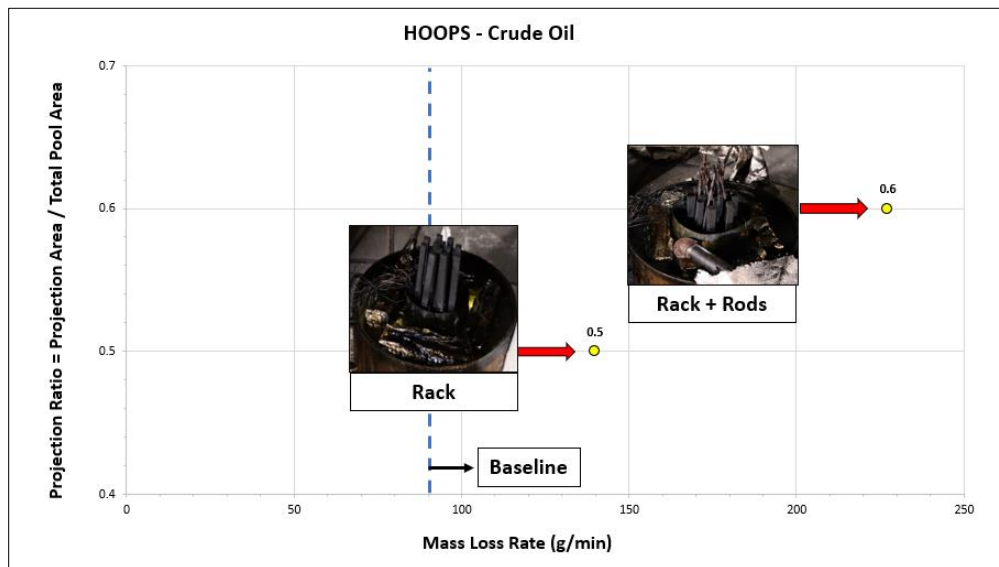
**Table 18 - Projection ratios for FR's tested in February - 2021**

FR Prototype	Projection View	Projection Ratio = $\frac{\text{Projection Area}}{\text{Total Pool Area}}$
Grid + Rods		0.23
Rack		0.5
Rack +Rods		0.6

Figures 132 and 133, show the influence of the projection ratio over the efficiency of the prototype in terms of regression rate.



**Figure 132 - Influence of projection ratio over the efficiency of FR's tested for kerosene fuel**

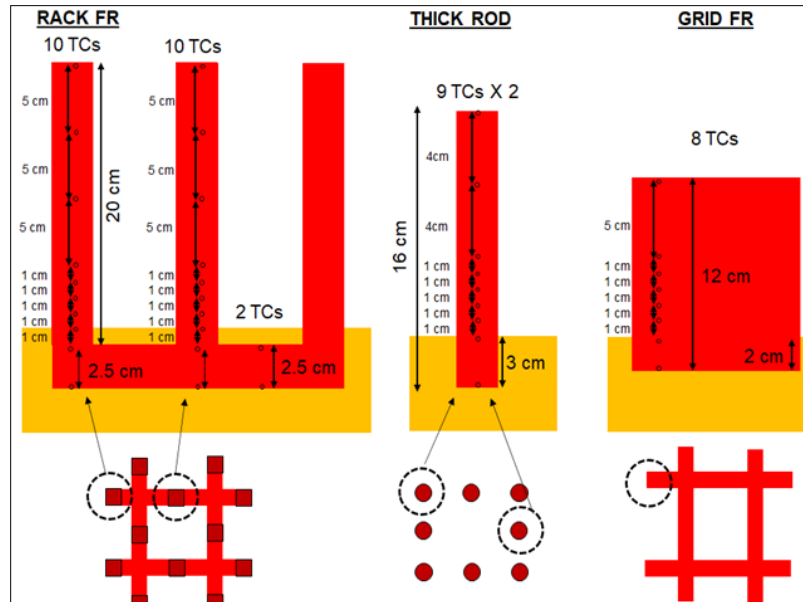


**Figure 133 - Influence of projection ratio over the efficiency of FR's tested for HOOPS crude oil fuel**

As shown in 132 and 133, it is evident that as the projection ratio increases the efficiency in terms of regression increases, and this is observed both in kerosene and crude oil fuel FR cases.

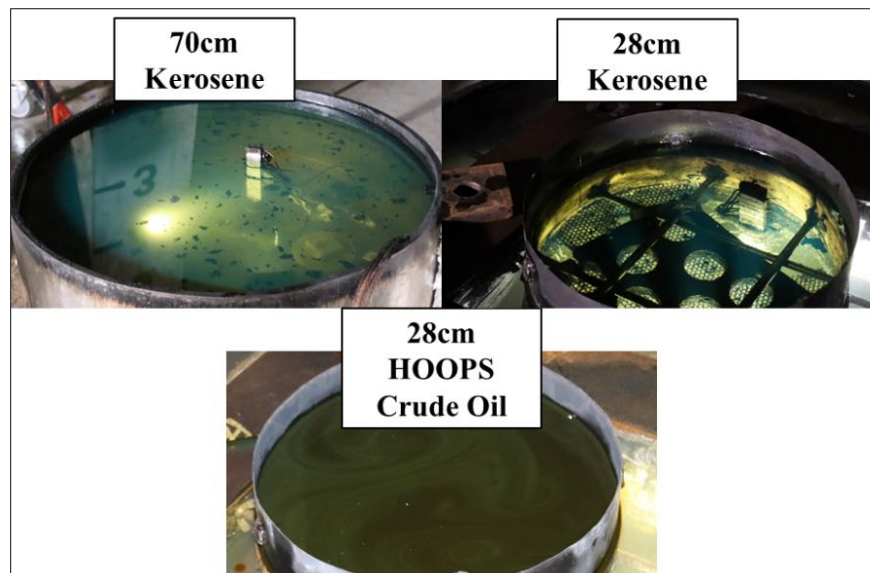
### **Temperatures – Phase III**

For the February Phase III experiments temperature data was determined to be of interest. Temperatures were collected from both the fuel/ water layers as well as from the FR's themselves. The variety of FR prototypes tested required slightly different FR thermocouple (TC) arrangements for each prototype, but generally, the layout was similar. Fig. 134 below shows the TC arrangements for the fuel layer, as well as the Rack, Rod, and Grid FR's.

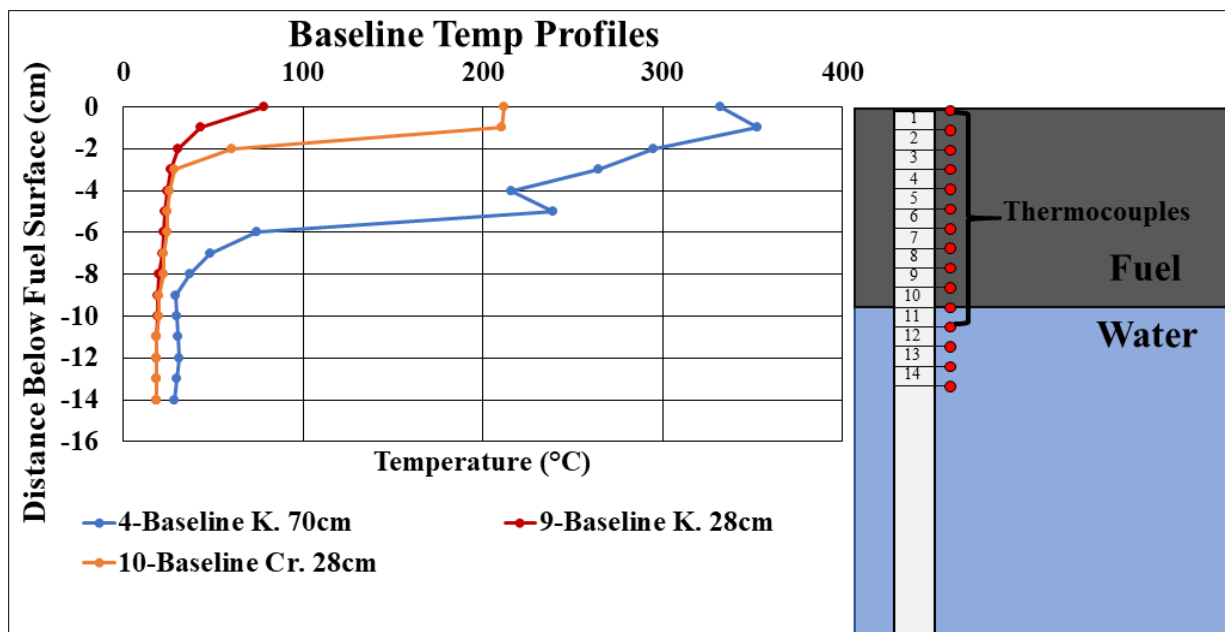


**Figure 134 - Flame Refluxer (FR) thermocouple arrangements for the Feb Phase III Experiments.**

The fuel thermocouple array consisted of 14 TC's affixed to a Teflon bar which was then submerged so the topmost TC remained at the fuel surface for each experiment. This thermocouple array was used to measure the temperature distribution in the fuel/ water layers and would prove especially important in the baseline cases. The three baseline case fuel arrangements are seen in the images below.



**Figure 135 - Images showing the 3 baseline cases examined in the Feb experiments.**



**Figure 136 - Baseline temperature profiles (left) and thermocouple array diagram (right)**

The temperature distributions for the 3 baseline cases are seen in Fig. 136 above (left) and the fuel TC array (right). The three baseline cases were 70cm diameter Kerosene, 28cm diameter Kerosene, and 28 cm Crude Oil. Plotting of the temperature vs depth for the baseline cases confirms what we would expect about the heat transfer from the burning region back to the liquid fuel. The 70cm Kerosene case yields the hottest temperatures in-depth, the burning area for this case is significantly larger and thus so is the resulting heat feedback. The 28cm Kerosene and Crude baselines are very similar, but the Kerosene maintains a slightly higher surface temperature which is expected.

### Fuel Temperatures

Temperature depth color plots were then generated for the various FR and baseline cases for Kerosene and HOOPS crude to better visualize the FR prototype's impact on temperature in-depth. It should be noted that the "fuel depth" noted on the charts is an approximation as the various tests had slightly varying initial fuel depths. Additionally, these tests had were conducted using constant filling aimed at maintaining 8 to 13 cm fuel depth. These temperature profiles were taken at the steady-state times during the experiment, as determined earlier in this section. The Kerosene experiments are shown first in Fig. 137 below.



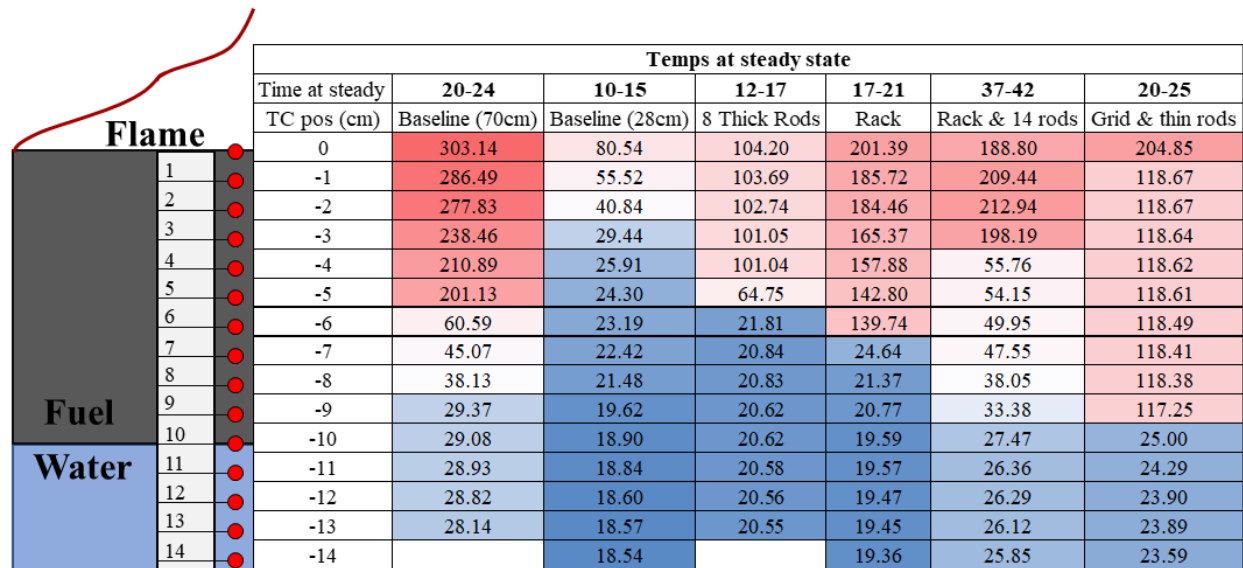


Figure 137 - Temperature depth color plots for Kerosene Feb Phase III Experiments.

First to note is that all cases except for the 70 cm baseline were conducted with a 28cm diameter burn area. With this plot, it can be observed that the baseline 28cm case has the lowest heat penetration of all the cases, and the 70cm is the highest heat penetration. It can also be observed that the best performing FR's (Rack and Grid) are reaching the same internal fuel temperatures as the 70cm baseline. This further supports the conclusion that the best performing FR's can compete with larger burning diameters, at least from a thermal perspective.

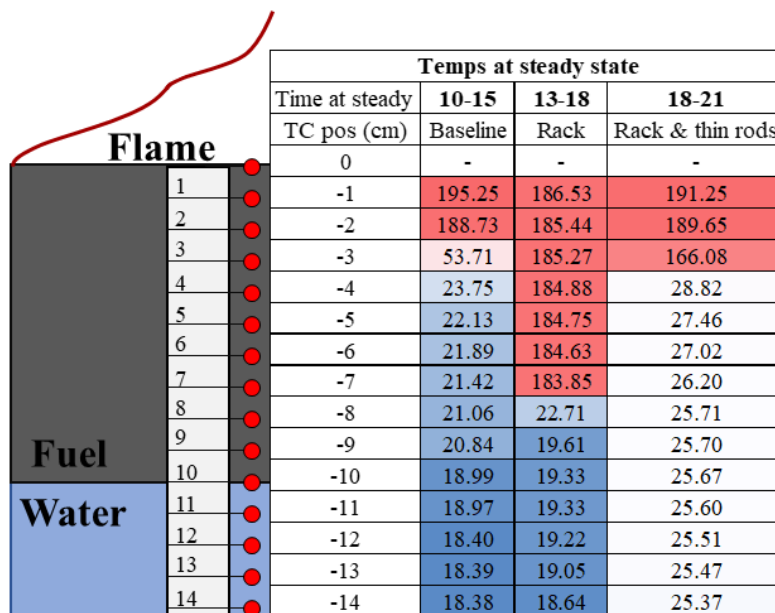


Figure 138 - Temperature depth color plots for HOOPS Crude Oil Feb Phase III Experiments.

The crude cases show a similar result to the kerosene cases. The baseline case shows the lowest heat penetration of the cases presented. The Rack FR in both configurations shows significant heat penetration over the baseline case.

## FR Temperatures

The following plot in Fig. 139 shows the FR temps vs distance from fuel surface for each of the selected cases. On this chart (K.) denotes a kerosene fuel experiment, and (Cr.) denoted a HOOPS crude oil experiment. Although this is not a decisive analysis it can be observed that at the steady-state portion of the experiments the best performing FR's are maintaining the highest fuel temps and the highest FR temps. The thick rods, which showed the lowest fuel temps among the selected cases, also shows the lowest FR temps. While the Rack and Rack with rods cases consistently show high fuel temps and high FR temps.

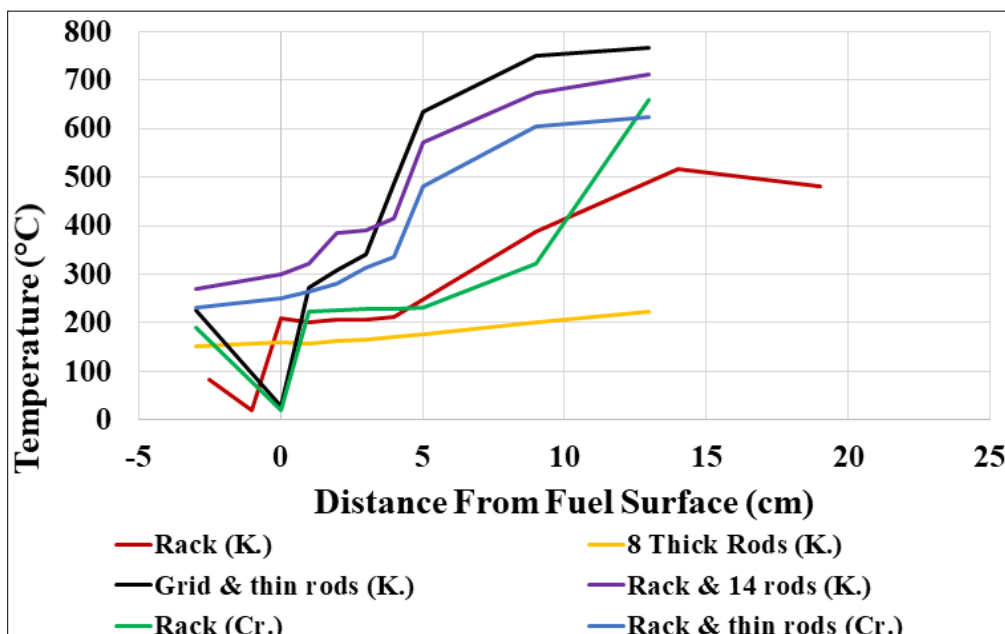


Figure 139 - FR Temperatures for select cases from Feb Phase III Experiments.

## Audio Sensors and Preliminary Analysis

### Objective

Previous studies have used sound signals for the analysis of crude oil burns in various ways. Labourer et al. conducted thin layer boilover experiments to study boilover as a function of reservoir size and material. Sound signal in this study was collected from an external sensor, different regimes of burning and boiling are mentioned, and a correlation between load cell data and sound data is noted, but no correlations or functional use of this knowledge is presented<sup>3</sup>. Fan

<sup>3</sup> D. Laboureur, L. Aprin, A. Osmont, J. M. Buchlin, and P. Rambaud, "Small scale thin-layer boilover experiments: Physical understanding and modeling of the water sub-layer boiling and the flame

et al. established the regimes and categorization mentioned in Laboureur et al. when examining boilover fires in oil tanks with a water sublayer. Audio in these experiments was collected with a dedicated external microphone and amplifier signal chain. Fan notes 3 basic stages of burning: quasi-steady, boilover premonitory, and boilover periods. Fan notes that audio signal data could be a viable method for early and/ or remote detecting of a likely boilover occurrence in a liquid pool fire<sup>45</sup>. Panetta et al. used acoustic transducers in crude oil burn experiments to prove the viability of using acoustic data to measure oil slick thickness. The technology proved viable to obtain slick thickness, instantaneous burn rate, and efficiency<sup>6</sup>.

A precedent for the utility of acoustic signals exists in the space of crude oil burning, and specifically crude over boilover burning. The objective of our exploration was to examine the viability of acoustic signals as another data source for evaluating FR performance in a burning crude oil pool fire. Two hardware options were tested, and success was demonstrated in various experiments.

### ***Hardware – acoustic sensors***

Two different audio sensor hardware options were tested in the February experiments. A standard instrument pickup piezoelectric sensor was tested first with limited results. Lack of water sealing led to sensor failure after a short amount of experimentation. An in-house constructed hydrophone, consisting of a modified piezoelectric sensor sealed into a watertight housing was then tested. This proved to be much more durable and produced a better signal-to-noise ratio.

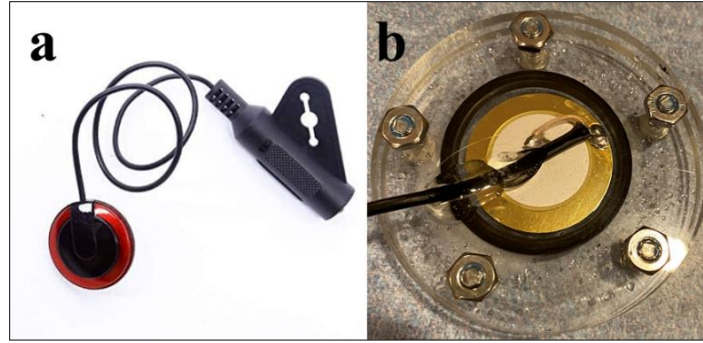
---

enlargement,” *J. Loss Prev. Process Ind.*, vol. 26, no. 6, pp. 1380–1389, 2013, doi: <https://doi.org/10.1016/j.jlp.2013.08.016>.

4 W. C. Fan, J. S. Hua, and G. X. Liao, “Experimental study on the premonitory phenomena of boilover in liquid pool fires supported on water,” *J. Loss Prev. Process Ind.*, vol. 8, no. 4, pp. 221–227, 1995, doi: [https://doi.org/10.1016/0950-4230\(95\)00012-P](https://doi.org/10.1016/0950-4230(95)00012-P).

5 J. S. Hua, W. C. Fan, and G. X. Liao, “Study and Prediction of Boilover in Liquid Pool Fires with a Water Sublayer using Micro-explosion Noise Phenomena,” *Fire Saf. J.*, vol. 30, no. 3, pp. 269–291, Apr. 1998, doi: [10.1016/S0379-7112\(97\)00025-8](https://doi.org/10.1016/S0379-7112(97)00025-8).

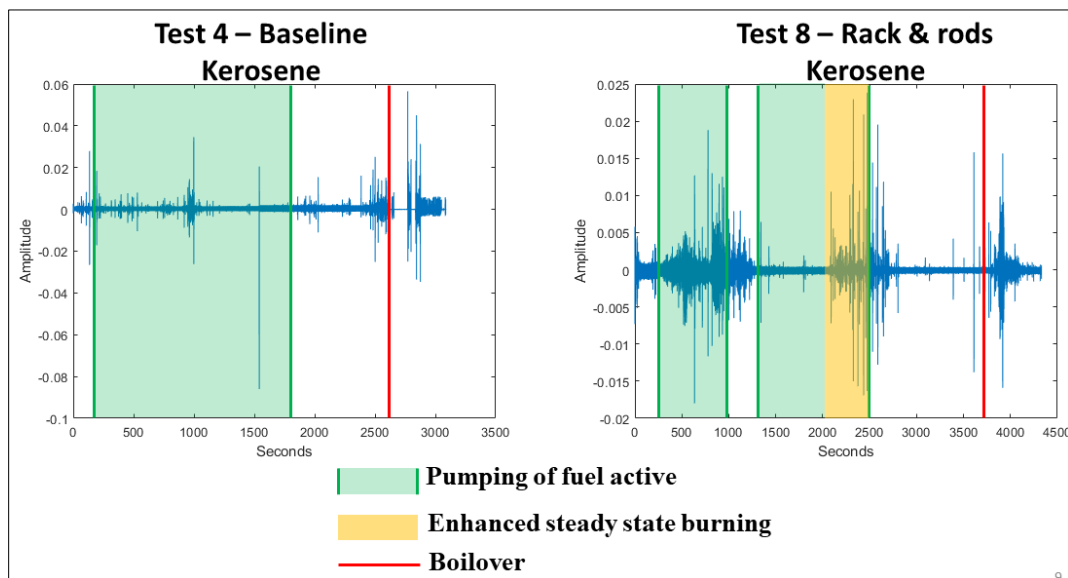
6 P. Panetta, R. Byrne, and H. Du, “Quantitative Measurement of In-Situ Burn (ISB) Efficiency and Rate,” Sep. 2018. Accessed: Apr. 19, 2021. [Online]. Available: <https://www.bsee.gov/research-reports/1074aa>.



**Figure 140 - (a) Commercially available instrument piezoelectric sensor (b) In-house-made waterproof piezoelectric disc sensor**

### ***Results***

The better acoustic sensor was only used for the latter half of the experiments, so available data is limited. But even so, we can demonstrate that using acoustic sensor data is useful in evaluating FR and burning pool performance. For example, we can compare the 70 cm Baseline Kerosene experiment and the Rack & 14 Rods Kerosene experiments data. Figure 141 below shows the audio amplitude data for each of these experiments over time. The baseline case, even being 70cm and significantly hotter, shows little audio disturbance over the course of the experiment up until boilover. However, the Rack and rods case show multiple zones where the audio picks up underwater boiling and seething sounds indicative of enhanced burning and hotter fuel-water interface temperatures. As well the boilover events are very distinct in the audio data, with usually a characteristic sound profile leading up to boil over. Indicating a possible utility of the audio data as a precursor to boil over.



**Figure 141 - Audio signal comparison for 70cm Baseline Kerosene (left) and 28cm Rack and rods Kerosene (right)**

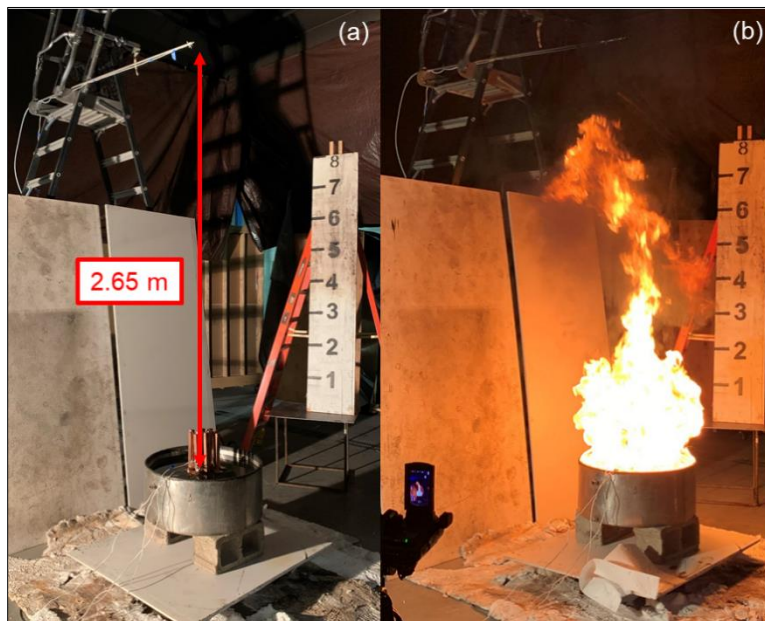
Subsurface sound signal data presents several promising signs as a new data source for FR analysis and pool burning analysis. This method will need further exploration and iteration as a data collection technique before it can reliably provide data for comparison across experimental platforms. As well an analytical method for reliably comparing data sets will need to be developed and vetted as viable.

## OGES

### Setup

#### *December WPI tests – 2020 (0.7m)*

The Outdoor Gas Emission Sampling (OGES) system sampling pipe was mounted at a height of 2.65 m above the pool. This height was selected based on flame height estimations for a 70 cm pool fire as well as experience from the previous large-scale tests performed at CRREL. To avoid saturation issues for the gas sensors along with the goal to obtain adequate data to study gas emissions within a smoke plume, the sampling location should be located above the flame tip and not within the flames. Based on regimes defined by McCaffrey, the sampling point should be in the intermittent zone. Fig. 142 below shows the OGES sampling pipe as mounted during the December burn tests.

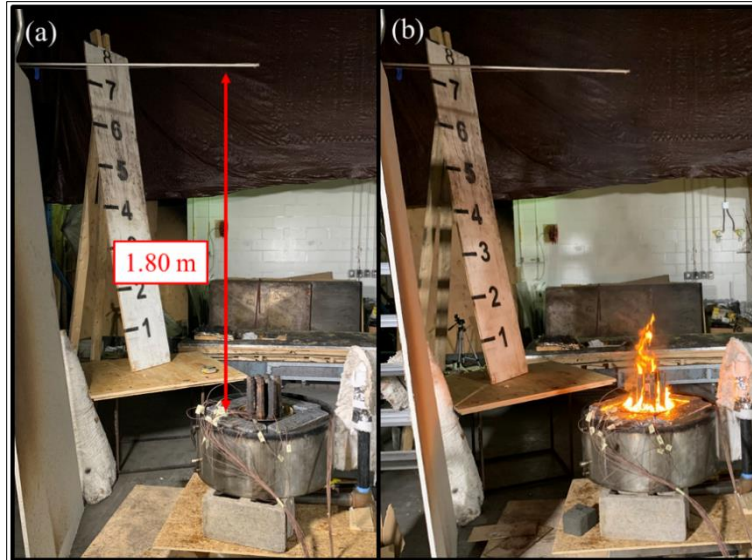


**Figure. 142 - December tests OGES system (a) Setup (b) Burn test.**

#### *February WPI tests*

Because of the smaller fire diameter for the February tests, the OGES system sampling pipe was situated at a lower height of 1.8 m above the base of the fire. This is because the anticipated flame height of a 28 cm fire would be much lower compared to the 70 cm fires performed in the December tests. Fig. 143 shows the OGES sampling pipe as mounted during the February burn tests.





**Figure 143 - February tests OGES system (a) Setup (b) Burn test.**

## Results and Discussion

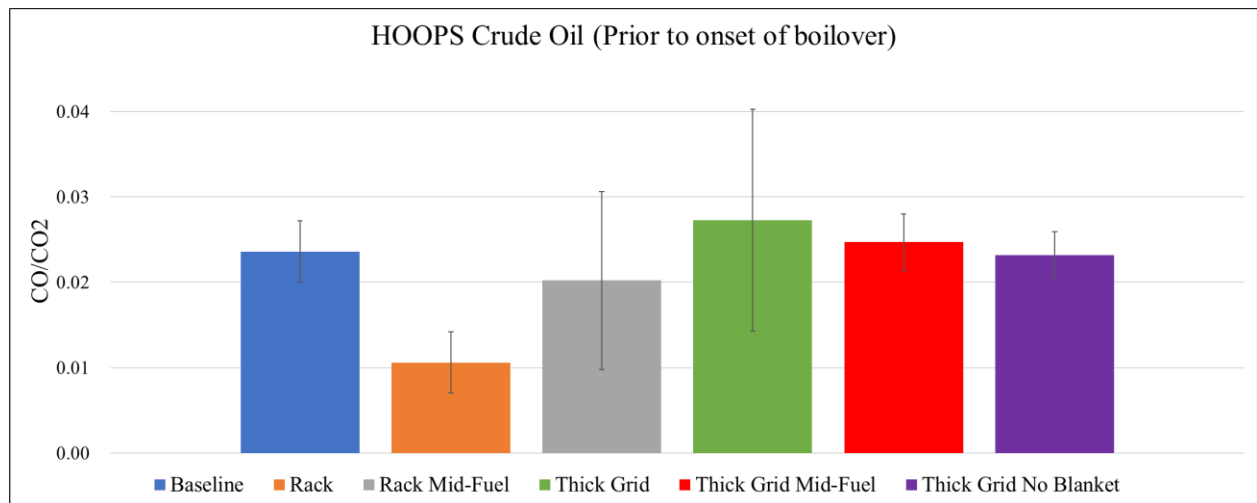
### *December WPI results*

#### *CO/CO<sub>2</sub> prior to the onset of boilover*

Table 18 and Fig 144 show the CO/CO<sub>2</sub> ratio for the discussed HOOPS crude oil cases at peak flame height just before the onset of boilover occurs as mentioned in the quarterly report; Table 19 and Fig. 145 are the results for the Kerosene cases at the same instance, just prior to the onset of boilover.

**Table 18 - Summary for December tests (HOOPS crude oil cases).**

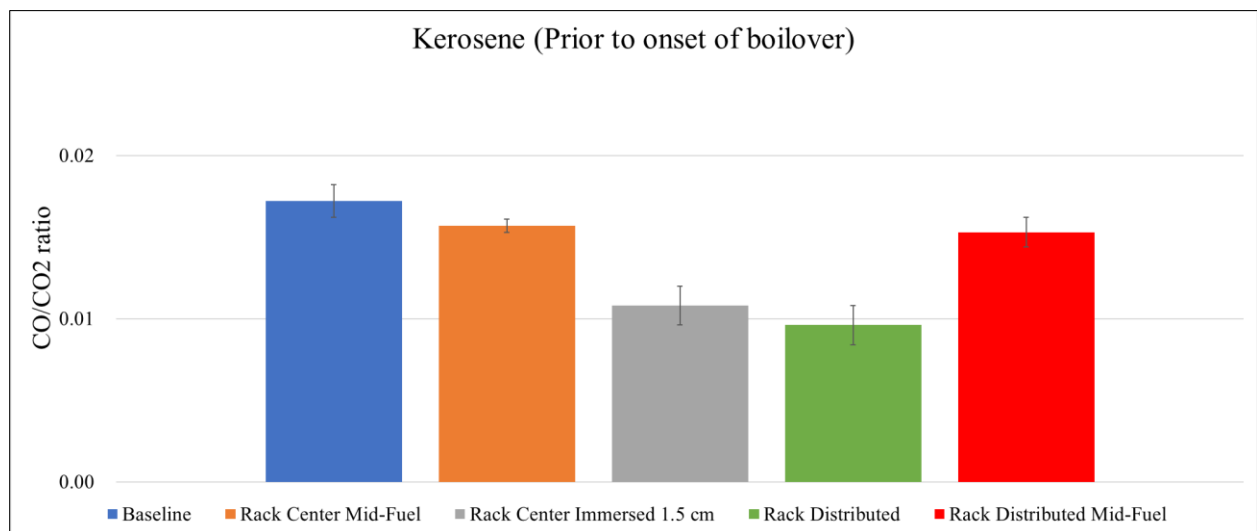
<b>CO/CO<sub>2</sub> (Prior to onset of boilover)</b>	<b>Average</b>
Baseline	$0.0236 \pm 0.0036$
Rack	$0.0106 \pm 0.0036$
Rack Mid-Fuel	$0.0202 \pm 0.0067$
Thick Grid	$0.0273 \pm 0.0130$
Thick Grid Mid-Fuel	$0.0247 \pm 0.0033$
Thick Grid No Blanket	$0.0232 \pm 0.0027$



**Figure 144 - Summary for December tests (HOOPS crude oil cases).**

**Table 19 - Summary for December tests (Kerosene cases).**

<b>CO/CO<sub>2</sub> (Prior to onset of boilover)</b>	<b>Average</b>
<b>Baseline</b>	$0.0172 \pm 0.0010$
<b>Rack Center Mid-Fuel</b>	$0.0157 \pm 0.0004$
<b>Rack Center Immersed 1.5 cm</b>	$0.0108 \pm 0.0012$
<b>Rack Distributed</b>	$0.0096 \pm 0.0012$
<b>Rack Distributed Mid-Fuel</b>	$0.0153 \pm 0.0009$



**Figure 145 - Summary for December tests (Kerosene cases).**

Purely observing the values on the surface, it would seem that for both HOOPS crude oil and kerosene, having the prototype touching the water actually improves the emissions the most in terms of CO/CO<sub>2</sub> ratio. On the contrary, having the prototype at mid-fuel yields the best

performance in terms of burn efficiency and burn time, but the improvement on gas emissions is much less pronounced.

However, due to the lack of a fuel replenishing system for these tests, the overall burn was transient in nature, never actually reaching a state where it would be deemed a steady state. Instead, these values were calculated based on the observation of an increased flame height just prior to the onset of boilover. If restricted to this period of study, the FR is no longer touching the fuel as a result of regressing fuel surface for the “Mid-fuel” cases, which is the reason for the seemingly lesser degree of emissions improvement when compared to data sets where the FR was touching the water layer. This can also be explained why the “Mid-fuel” cases have a CO/CO<sub>2</sub> ratio that is strikingly similar to baseline cases.

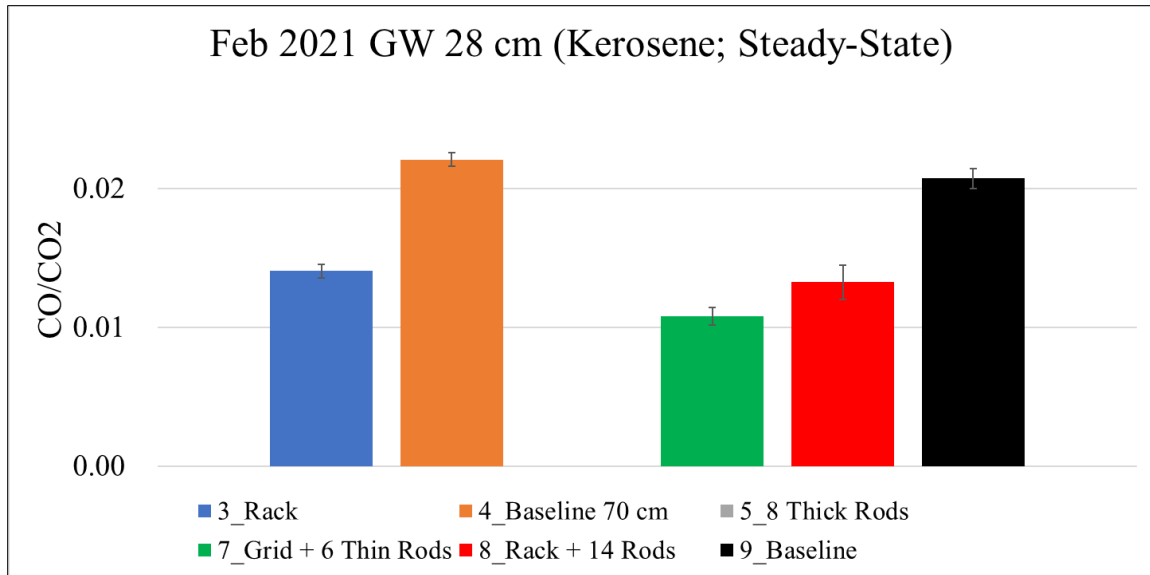
To better investigate the burning behavior improvement for all data sets, a time-dependent study should be performed for all the tests, especially the “Mid-fuel” cases. This allows provides the additional benefit of understanding when peak improvement is actually reached, and also understand when the fuel layer has regressed to a point where the FR is no longer touching the fuel and burning enhancement is reduced.

### February WPI results

Table 20 and Fig. 146 show the CO/CO<sub>2</sub> ratio for the February experiments at steady-state using kerosene as the fuel; Table 21 and Fig. 147 show the same study for HOOPS crude oil.

**Table 20 - Summary for February tests (Kerosene cases).**

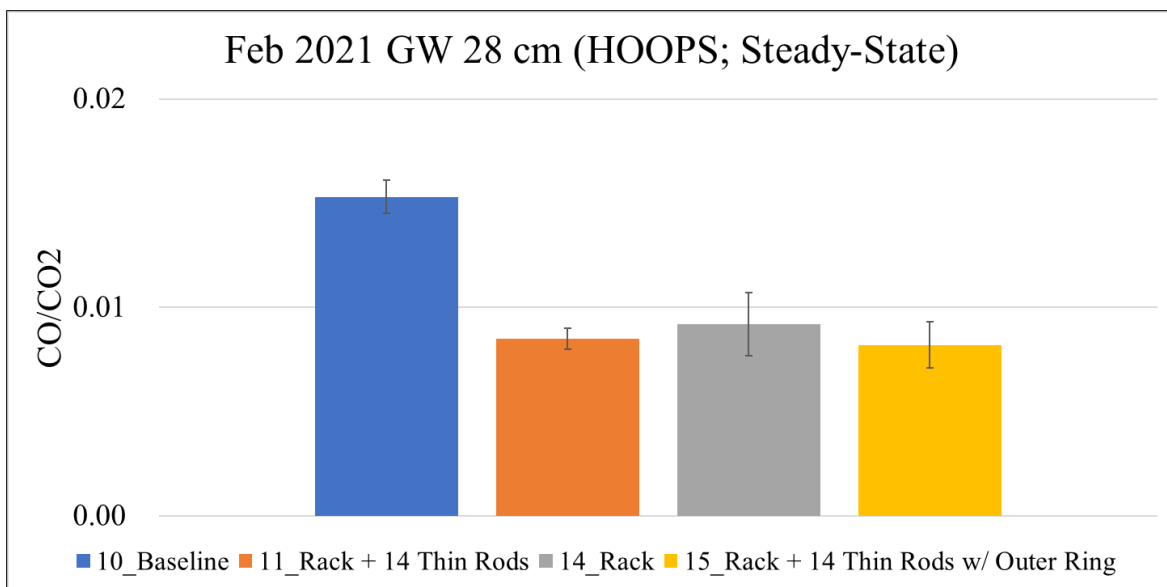
<b>CO/CO<sub>2</sub> (Steady-State)</b>	<b>Average</b>
<b>3_Rack</b>	0.0141 ± 0.0006
<b>4_Baseline (70 cm)</b>	0.0221 ± 0.0010
<b>5_8 Thick Rods</b>	
<b>7_Grid + 6 Thin Rods</b>	0.0108 ± 0.0006
<b>8_Rack + 14 Rods</b>	0.0133 ± 0.0012
<b>9_Baseline (28 cm)</b>	0.0207 ± 0.0007



**Figure 146 - Summary for February tests (Kerosene cases)**

**Table 21. Summary for February tests (HOOPS crude oil cases).**

CO/CO2 (Steady-State)	Average
10_Baseline	$0.0153 \pm 0.0008$
11_Rack + 14 Thin Rods	$0.0085 \pm 0.0005$
14_Rack	$0.0092 \pm 0.0015$
15_Rack + 14 Thin Rods w/ Outer Ring	$0.0082 \pm 0.0011$



**Figure 147 - Summary for February tests (HOOPS crude oil cases)**

With a replenishing system present, the steady-state study of the emissions data can be performed since the fuel is maintained at the same thickness throughout the experiments. This is in contrast to the December tests where it was transient in nature throughout the entire burn. This is evident as the values CO/CO<sub>2</sub> ratio are closer to as expected compared to the data sets from the December tests.

From Fig. 146, it can be observed that there is a missing data set using the “Thick Rods”. Visual observations noticed a much lower flame height than the baseline case, and therefore the gas concentrations sampled by the OGES system were too low to obtain a definitive CO/CO<sub>2</sub> ratio for this data set. With such a low flame height, excess dilution of the sampled gases resulted in CO/CO<sub>2</sub> ratios that were out of the reasonable range of such fires as reported by other studies. This is a similar observation to the experiments performed at CRREL where CO values approached zero.

For the other data sets, more reasonable CO/CO<sub>2</sub> ratios can be observed. This is especially evident when observing the baseline cases using Kerosene. The CO/CO<sub>2</sub> ratios for both 28 cm and 70 cm are identical, showing that this value is fuel-specific; and as long as the sampling distance is within the intermittent flame zone where excess dilution is not a significant factor, a similar CO/CO<sub>2</sub> ratio can be expected for the same fuel but different diameter fires.

Fig. 146 also shows the best performing FR to be the “Grid + 6 Thin Rods” case based on emissions, but mass loss data shows the degree of burning enhancement to be minimal compared to baseline. On the other hand, the “Rack + 14 Thin Rods” case indicates a similar CO/CO<sub>2</sub>, around 50% decrease compared to baseline, but also providing a substantial improvement in terms of mass loss rate compared to baseline. Data from Fig. 147 for HOOPS crude oil also supports this observation, yielding a decrease of 46% of CO/CO<sub>2</sub> ratio at steady-state. Therefore, in conclusion, the “Rack + 14 Thin Rods” shows to be the best overall performing FR in terms of both mass loss rate and emissions.

## **Conclusions from Phase III experiments performed at WPI during Dec 2020 and Feb 2021**

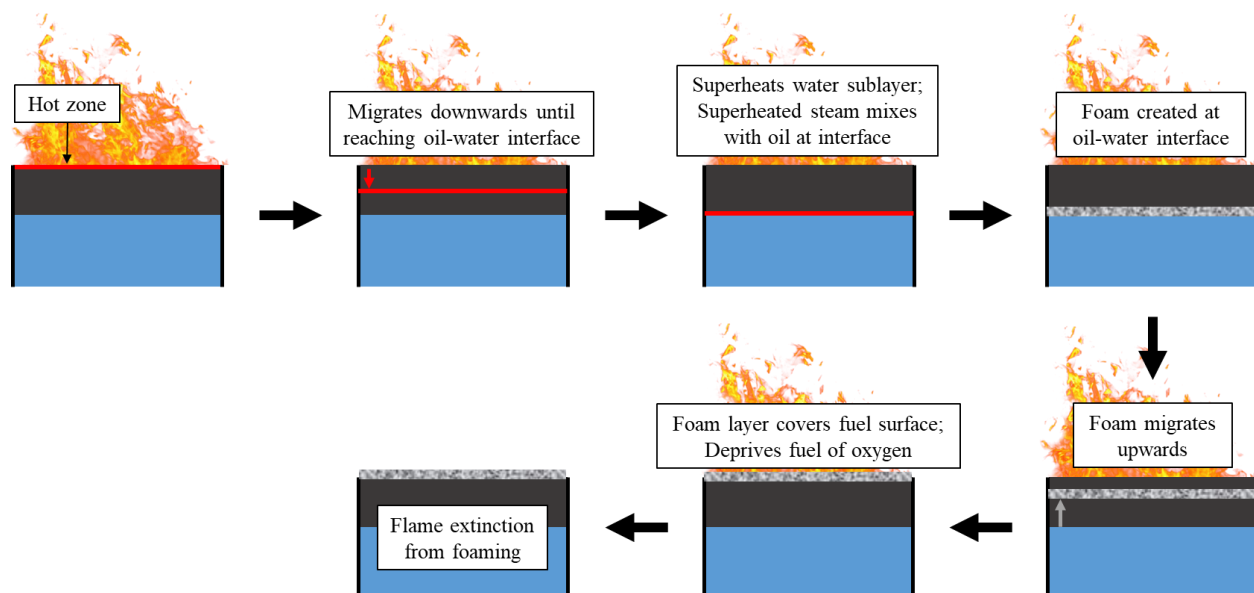
1. When the FR does not entirely cover the fuel surface, the heat transfer to the water sublayer can induce local water evaporation. This is especially true for fuels with a boiling point higher than that of water (100 °C), common with most oil slicks during in situ burning operations. We have observed this behavior for projection ratios  $< 0.6$ .
2. During combustion of an oil slick floating on water with an FR, the heat collected from the flame is at first efficiently transferred by the FR to the fuel, and burning is rapid. However, if or when the FR heater comes in contact with water, it loses its heat to the water faster than heating the fuel. The nucleate boiling of fuel on the heater surface stops, and instead, the water starts boiling. The resulting steam rises and causes an emulsification of the crude oil (foaming) and dilution of fuel vapor, thereby lowering the burning rate and causing the burning to slow down.
3. Experiments from Phase III show that there are only two solutions to the problem. A) Develop a floating control volume housing the FR's that is separated from the water sublayer. Or B) increase the coverage area of the FR such that it covers the entire fuel surface.



## 5. Foaming

### Introduction

During the Phase II experiments performed at CRREL in October 2020, visual observations during non-turbulent conditions (no waves) showed a foaming phenomenon of the HOOPS crude oil for all cases, even the baseline case where no FR was deployed. Foaming is hypothesized to occur when the water sublayer beneath the crude oil layer reaches and exceeds its boiling point. Buist et al. [1] observed boiling of water below an oil slick during in situ burning (ISB) in calm water with no current, which causes steam to mix vigorously with the remaining oil layer and eject oil droplets into the flame. They refer to this as the “vigorous burning phase” with observed increases in burn rate, flame height, and foaming behavior. However, Buist et al. [1] state that the cause of this phenomenon is a thinning oil slick that allows heat to reach the water sublayer. This behavior is in fact more analogous to the boilover phenomenon observed in liquid fuel storage tank fires, where Broeckmann and Schecker [2] observed violent fuel ejections, frothing over the tank, flame enlargements, and fireballs. Broeckmann and Schecker [2] hypothesize a zone of uniform temperature (hot zone) and an oil viscous enough to facilitate foaming as necessary conditions. However, they also observe a small amount of remaining fuel when the water below is heated to vaporization. This is in contrast to the observations at CRREL, where heating of the water sublayer occurs because of increased heat feedback from FR deployment, but the thicker fuel slick above is unable to allow steam to escape past the crude oil layer and result in a boilover. Instead, the force exerted induces mixing of the steam with the crude oil, resulting in a foam that migrates to the surface of the crude oil layer. This layer of foam blocks the ambient oxygen from reacting with the fuel below the foam, effectively suppressing the fire. An illustration of this hypothesized foaming mechanism is shown in Fig. 148.



**Figure 148 - Illustration of hypothesized foaming mechanism**

In the baseline case, the foaming caused the extinction of the flames after 20 min with an efficiency of 55%. This means nearly half of the fuel remained in the boom after the burn. With the Grid and Bimetal FR, foaming also resulted in the extinction of the flames. However, they reignited within 2 – 4 min, unlike the baseline case, causing the burning efficiency of the FR to reach 93 – 94%. Additionally, foaming would occur more quickly at the location of the FR because of more direct heat feedback in that area. This means foaming would initiate at the FR and migrate outwards. This also resulted in flames being pushed away from the FR since they would only be present in locations where the foam had not yet formed. However, the flames would reignite once the foam collapsed after a few minutes. During Phase III experiments at WPI, this phenomenon was observed once again for 70 cm pool fires with Rack prototypes using HOOPS crude oil with 3 cm initial fuel thickness. However, it should be noted that this foaming behavior did not occur during previous ISB experiments performed in Mobile, AL when the fuel was also HOOPS crude oil [3]. This may be because of continuous feeding and a lower fuel thickness of 1 cm, which causes boilover instead of foaming.

## Visual observations from CRREL experiments

### Foaming behavior

At present, only experiments without waves are discussed in this section, but oil foaming was also observed for wave cases at CRREL. As shown in Table 22, 12 out of 24 experiments were performed without the presence of waves, and foaming only occurred with HOOPS crude oil. Interestingly, an emulsion of HOOPS crude oil did not foam as shown in Table 22. This may be because of the smaller fuel thickness of only 2.5 cm compared to 8 cm used in the experiments where foaming was observed. A change in fuel properties because of emulsification may have also played a role. The table also details the time to foam for each data set, or time to extinction if foaming did not occur. This table divides the extinction behavior for these various experiments into three main types:

1. Foaming then extinction;
2. Foaming then reignition;
3. Extinction; no foaming.

**Table 22 - Summary of foaming times for no wave cases performed at CRREL**

Prototype	Fuel; Initial thickness	Time to foaming (or extinction)	Note
Baseline	HOOPS; 8 cm	16:30	Foaming then extinction
Ruffled metal	HOOPS; 8 cm	19:00	Foaming then extinction
Bimetal	HOOPS; 8 cm	19:30	Foaming then reignition (23:30)

Grid	HOOPS; 8 cm	28:00	Foaming then reignition (32:30)
Blanket	HOOPS; 8 cm	24:00	Foaming then extinction
Baseline	HOOPS Emulsion; 2.5 cm	09:00	Extinction; no foaming
Baseline	HOOPS Emulsion; 2.5 cm	08:30	Extinction; no foaming
Bimetal	HOOPS Emulsion; 4 cm	13:00	Extinction; no foaming
Baseline	HOOPS Emulsion; 4 cm	09:00	Extinction; no foaming
Baseline	Bunker; 1 cm	06:00	Extinction; no foaming
Bimetal	Bunker; 1 cm	08:00	Extinction; no foaming

“Foaming then extinction” is when a visible layer of foam is observed once flames are no longer present, and it is determined that the flames were extinguished caused by the presence of this foam. Similar to the mechanism utilized by foam-based fire suppression systems [4], foam on top of a liquid pool fire deprives the fuel of ambient oxygen. As the foam spreads and ultimately covers the entirety of the pool area, oxygen is completely cut off from the fuel and the extinction of the flames occur. Fig. 149 shows this situation during the baseline case where no FR was deployed, while Fig. 150 shows a similar photograph using the Ruffled metal FR. As seen in the photographs, a visible gray layer of foam is present, and no reignition occurs after several minutes.

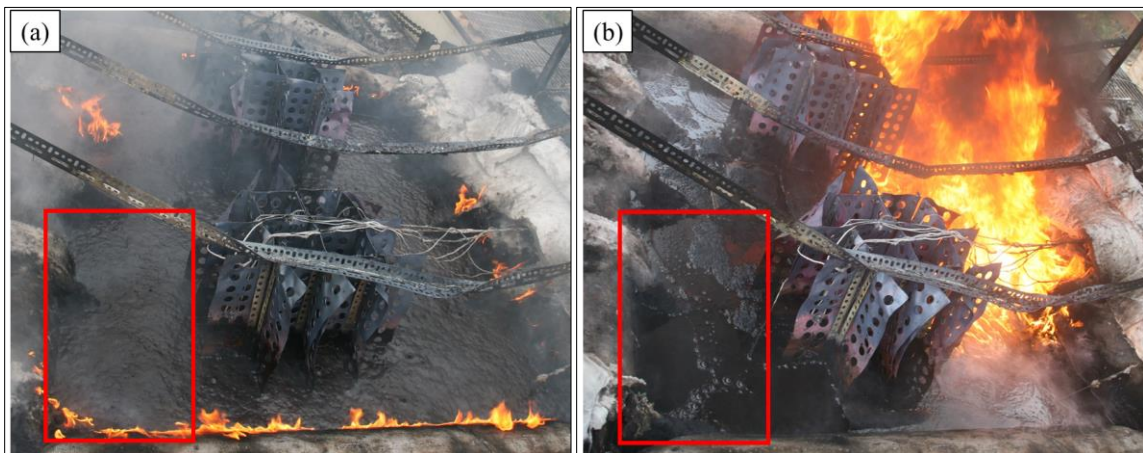


**Figure 149 - Foaming then extinction – Baseline (HOOPS crude oil; Pool dimensions: 1.7 m by 1.9 m)**



**Figure 150 - Foaming then extinction – Ruffled metal FR (HOOPS crude oil)**

“Foaming then reignition” is when the foam layer causes flame extinction, but the pool fire is reignited after several minutes. Fig. 151 shows this behavior when using the Grid FR with HOOPS crude oil. The foam layer causes extinction for the majority of the flames in Fig. 151 (a), but the surrounding residual flames reignite the pool several minutes later in Fig. 151 (b) after the bubbles in the foam have broken down to a certain degree. The highlighted area in red shows the contrast in appearance at the fuel surface. This behavior may also be because of the fact that the Grid FR remains at a high temperature of 500° C seven out of eight extinctions, providing a source of external heat flux to the fuel surface that facilitates reignition after the foam collapses. Temperature data showing the temperature history of the collector portion of the FR supports this hypothesis. Similar behavior is also observed with the Bimetal FR.

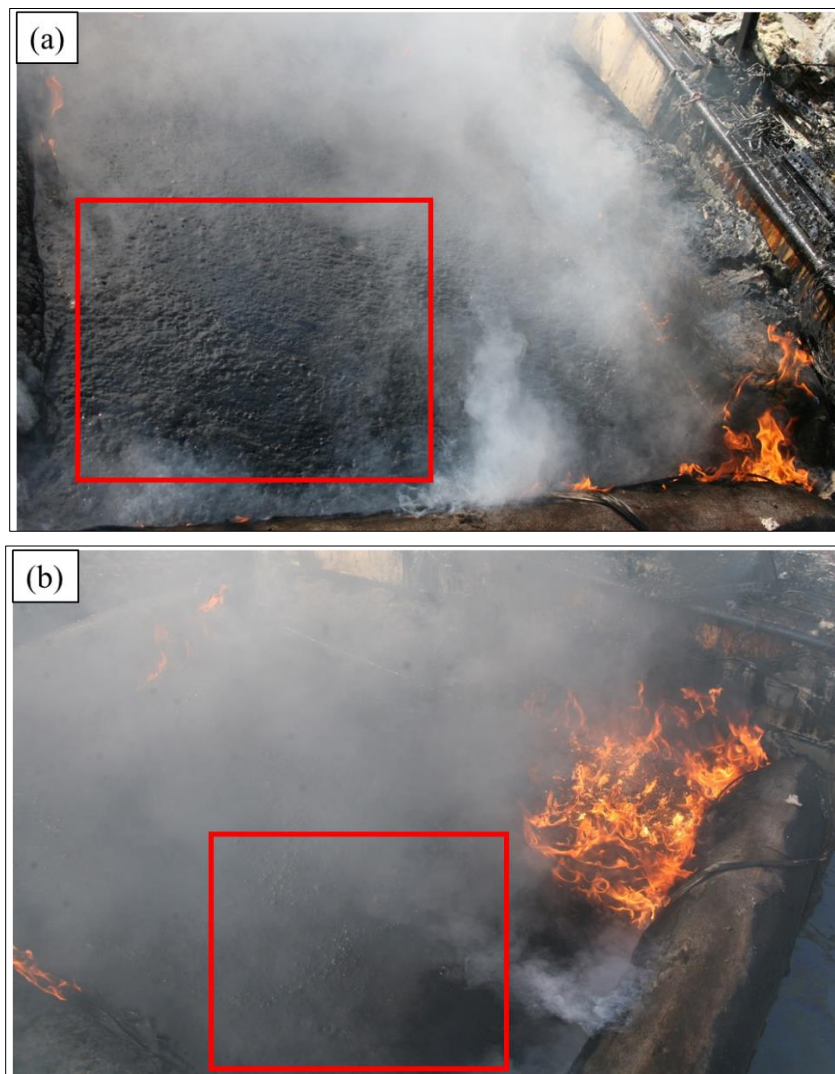


**Figure 151 - Foaming then reignition behavior – Grid FR (HOOPS crude oil)**

**(a) Initial extinction (b) Reignition**

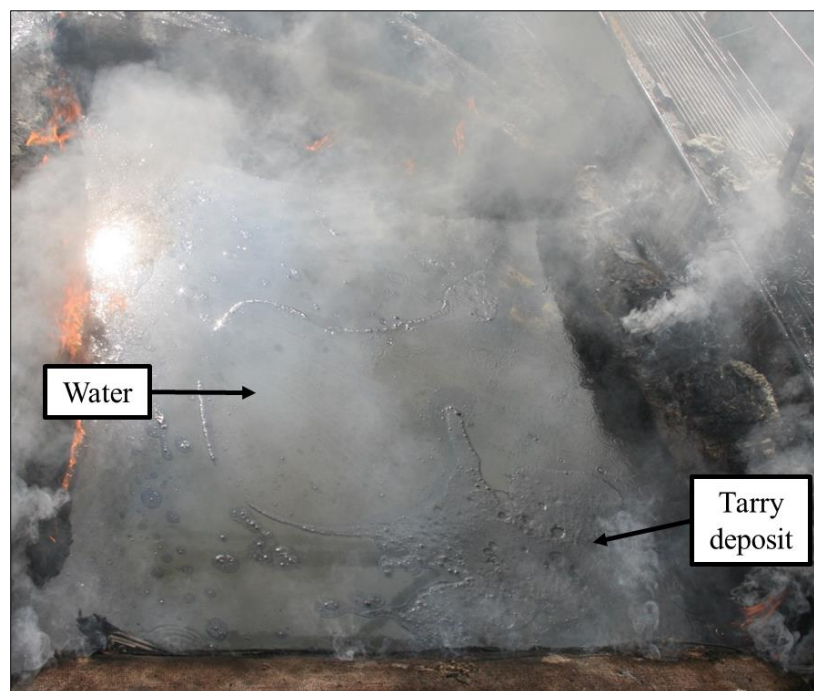


Certain wave cases also exhibit this behavior where foaming causes flame extinction, but reignition occurs after several minutes. Fig. 152 shows a similar phenomenon for the baseline case with Wave 2 using HOOPS crude oil. Interestingly, movement from the waves allows reignition to occur after the foam has broken down after several minutes. This is in stark contrast to the baseline case with no waves, where oil foaming caused complete extinction of the flames, which in turn resulted in a relatively low burn efficiency of 57%. The reignition behavior in the baseline case with Wave 2 yielded a much more satisfactory burn efficiency of 97%, showing that a potential solution to oil foaming is to create an environment where reignition is possible. Future studies on the effects of different wave profiles on oil foaming tendency and foam breakdown need to be performed to quantify this behavior.



**Figure 152 - Foaming then reignition behavior – Baseline (HOOPS crude oil) w/ Wave 2**  
**(a) Initial extinction (b) Reignition**

“Extinction; no foaming” is when the extinction of flames is visually observed to be caused by depletion of the fuel and not from a foam layer. For fuels such as emulsions, this foam layer never forms and the fuel is mostly burned off. Fig. 153 shows this behavior from a baseline burn using an emulsion between HOOPS crude oil and water (25% mixture). The water beneath the oil can be seen visually and there is minimal residue. However, it should be noted that the initial fuel thickness was only 2.5 cm in this case. As discussed earlier, there is a possibility this behavior may be caused by emulsion or a smaller initial fuel thickness compared to cases where foaming was observed. There may exist a critical initial fuel thickness that provides the conditions for foaming to occur. However, the deciding factors are currently unknown and require further research. This may be an important consideration especially in situations where thick oil layers can occur in stagnant pools, for example in marshy areas or ice cavities.



**Figure 153 - Extinction behavior – Baseline (Emulsion; 75% HOOPS crude oil, 25% water)**

### **Time to reignition**

As noted in Table 22 and Fig. 151, there are two experiments (Bimetal and Grid FR) where foaming was observed visually, but residual flames and retention of heat by the FR present in the surrounding boom material allowed for the possibility of reignition.

Fig. 154 shows a photo strip with corresponding times stamps for experiments with the Bimetal FR. This photo strip shows the initial flame reaching a fully developed state at around 1 min, while foaming begins to occur at around 19.5 min, and quickly causes the extinction of the flames in less than a minute. After about 4 min, the bubbles in the foam layer begin to subside and gradual reignition of the entire pool begins. However, since it takes another few minutes for the foam to disappear completely, in addition to the fact only mostly heavier and harder-to-burn hydrocarbons

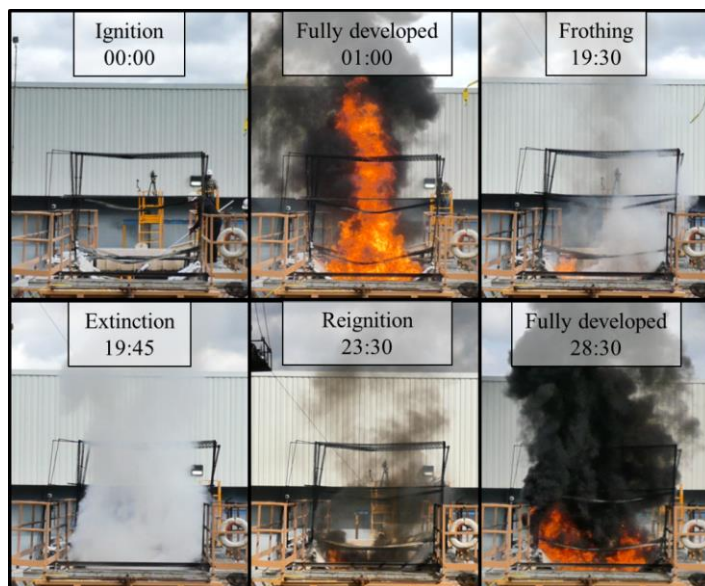


remain after the initial fire, it takes around 5 min before the fire becomes fully developed again. This can be verified by comparing the two fully developed fires at 1 min versus 28.5 min. The smoke plume in the latter fully developed fire is much thicker and darker compared to that of the earlier one, indicating that it is indeed the heavier components of the crude oil that are being burned during the latter stages of the fire, and lighter components had mostly burned off during the early stages. The in-depth temperature measurements also validate this fact.

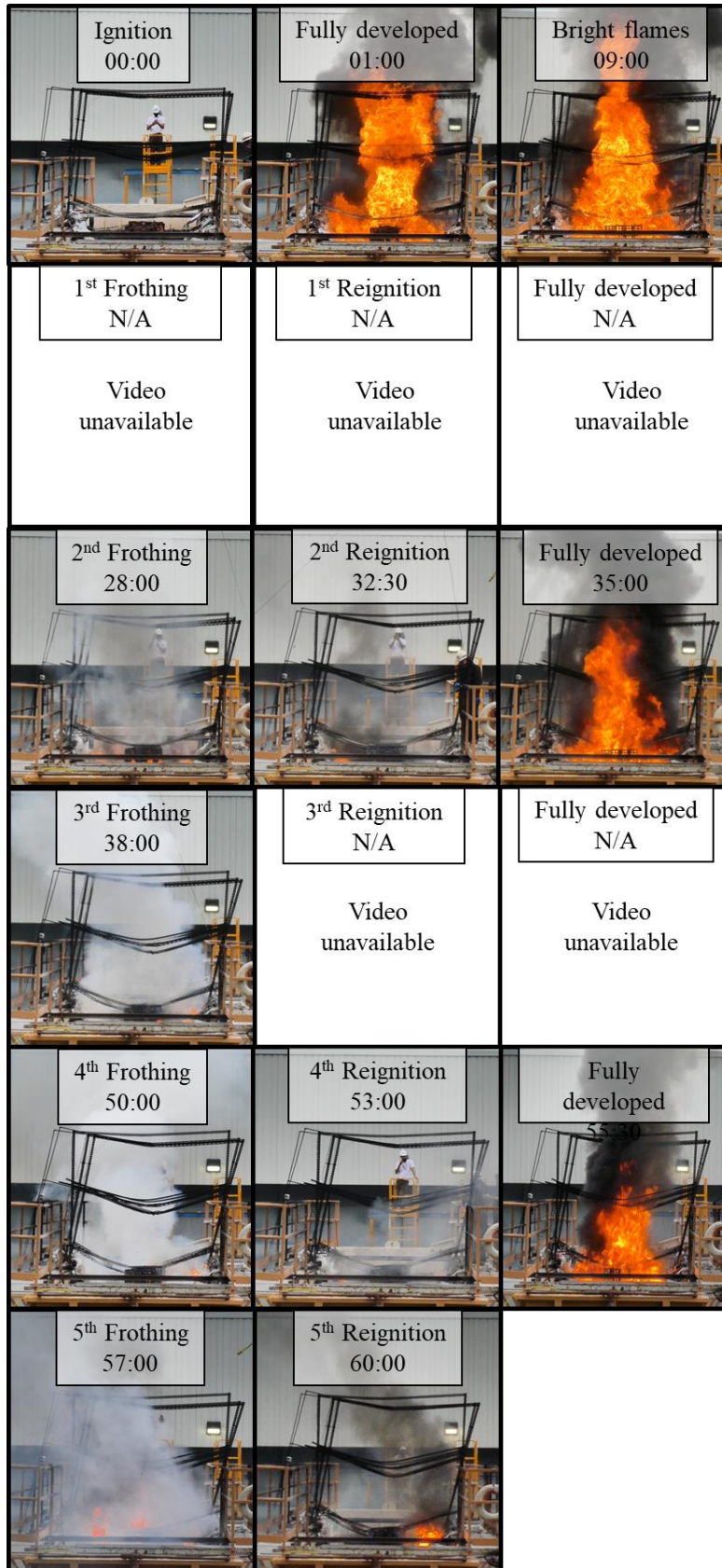
This experiment had two latter instances of foaming then reignition, however the video feed for this data set was only available for the first 30 min, therefore only the first instance of reignition is shown in Fig. 154. This observation of multiple reignitions will be shown for the Grid FR data set in Fig. 155.

A similar observation is made for the Grid FR, shown as a photo strip in Fig. 155. This experiment was interesting in that it had multiple occurrences of foaming then reignition behavior, a total of eight foaming instances, and seven reignitions. There were two instances where the video feed failed for a period of 6 min respectively, as labeled in the photo strip. However, this did not hinder the global observations for the foaming and subsequent reignition behavior. Similar conclusions to that of the Bimetal FR case are made for this data set as well. The cyclic behavior of the foaming in this data set shows that it takes approximately 3 to 4 min for the foaming to subside and allow the surrounding residual flames to reignite the pool. One additional observation noticed for this specific data set was that the flames were much hotter than any other data set at around 9 min, while the corresponding flame height was taller as well.

These qualitative observations from the video feed for time to foaming, time to reignition, and high temperatures at 9 min for the Grid FR case will be discussed further in the temperature data section.



**Figure 154 - Foaming then reignition behavior – Bimetal FR**



**Figure 155 - Foaming then reignition behavior – Grid FR**

### Contributing factors to foaming of crude oil and prior research

To achieve an improved understanding regarding the foaming behavior of crude oil, a literature review was performed on the factors that contribute to crude oil foaming, in addition to the comparison of the data sheets for ANS and HOOPS crude oil to explore the causes of foaming for HOOPS crude oil that is consistent with prior studies. Recall that previous experiments using HOOPS crude oil (Mobile, AL; 2017) [3] did not exhibit this type of foaming behavior. However, Phase II experiments at CRREL with 8 cm initial fuel thickness showed obvious foaming phenomena, while Phase III experiments at WPI with 3 cm initial thickness also exhibited similar behavior, indicating the need for further research on this topic. Fig. 156 shows foaming during Phase III experiments at WPI.



**Figure 156 - Foaming behavior during Phase III experiments at WPI**

The earliest instance of documenting the formation of oil foam was in a report by Scott [5] from Mobil Oil Company in 1967. Scott [5] shows that although oil foaming is mainly a result of mechanical means, characteristics of the oil, such as oil viscosity, can affect its foaming tendencies. A study by Callaghan et al. [6] used 16 different crude oils and showed extraction of these crudes with both alkali and acid indicated that the crude oil components responsible for foam stability were removed by the alkali extraction. Further examination of the alkali extract revealed it was the chloroform-soluble part of this extract (0.02 wt% of the whole crude) that was responsible for foaming. Further analysis of this extract indicated that the critical components were short-chain carboxylic acids and phenols with molecular weight  $\leq 400$ , presumably because they provide surface tension gradients and/or surface viscosity that promotes foam stabilization. Once stripped, all 16 crude oils no longer had the tendency to foam but retained their foaming tendencies once the extract was added back to the crude oil. Table 23 shows the foaminess indices for both stripped and complete crude oils. It can be seen from the data that alkali-stripped oils no longer have a tendency to foam.

**Table 23. Foaming indices of 16 crude oils in Callaghan et al. [6]**

	$\Sigma$ , minutes	
	Stripped Oil	Whole Oil
Bonny	0.0	0.4
Forcados	0.0	0.4
Basra	0.0	0.5
Umm Shaif	0.0	0.2
Zakum	0.0	0.4
Buchan	0.1	0.6
Ninian	0.0	0.5
Kuwait	0.0	0.7
Heather	0.0	0.4
Magnus	0.0	0.4
Alaskan (North Slope)	0.0	0.9
Iranian Heavy	0.0	0.8
Qatar	0.0	0.1
Forties	0.0	0.4
Murban	0.1	0.3
Iranian Light	0.0	0.6

Research by Poindexter et al. [7] provided the first systematic study directly using 20 different types of crude oil to investigate the factors that contribute to foaming. They attempted to correlate common crude oil properties such as density, bulk viscosity, surface tension, asphaltene, and resin contents to two critical foam parameters, foamability, and collapse slope. Sparge experiments were performed using a dynamic foam test. A 500 mL graduated cylinder (foam cylinder) is modified with a glass extension at the bottom, with 46 mL of crude oil added to this extension (reservoir). A gas dispersion tube was inserted through the bottom of the glass extension, with nitrogen serving as the sparge gas at gas flow rates of 100 or 250 mL/min. Foam volume, measured at the air-foam interface, was visually recorded. At the eight-minute mark, the gas flow was terminated, and the foam was allowed to collapse. Foamability simply relates to the maximum foam volume achieved during a fixed period of time, while collapse slope was determined by a least-squares fit of the linearly decreasing part of the curve after the termination of the sparge gas. Fig. 157 shows the results of the experimental study for six crude oil types.

Three main conclusions are made by Poindexter et al. [7] First, crude oils that have bulk viscosities at or above 150 cP at 37.8°C produced little or no foam, meaning crudes with high viscosities do not foam easily. This was observed at CRREL, where emulsion with HOOPS and highly viscous bunker fuel did not exhibit foaming. Table 24 shows a summary of the nine crudes used initially in the experiments performed by Poindexter et al. HO, SJV, and T1 crude fall into this criteria and show no foamability. As shown in Table 24, the foamability of these three oils is less than 10 mL. The resin content is around 20% for these three oils, compared to the others that have much lower resin content. This may play an important role in oil viscosity, as these three oils also have the highest viscosities of the crudes.



**Table 24 - Crude oil properties for the initial nine crudes in Poindexter et al. [7]**

crude oil	designation	density (g/mL)	viscosity (cP)	% asphaltenes	% resins	foamability (mL)	collapse slope (mL/min)
Alaska North Slope	ANS	0.8894	13	3.38	8.72	30	-9
Arab Berri	AB	0.8383	4	0.79	3.24	140	-220
Arab Heavy	AH	0.9460	34	6.68	7.46	200	-39
Canadon Seco	CS	0.9030	70	7.50	8.94	45	-8
Hondo	HO	0.9377	363	14.81	20.52	5	a
Malu Isan	MI	0.8448	38	0.18	4.86	75	-22
San Joaquin Valley	SJV	0.9792	1390	4.56	19.37	0	
Statfjord	SF	0.8328	3	0.09	4.02	120	-228
THUMS 1	T1	0.9516	152	5.09	18.70	0	

<sup>a</sup> Maximum foam volume was 5 mL. Upon terminating the gas flow, the foam immediately collapsed to 1 mL. A stable foam collar remained at 1 mL for the next 8 min.

Second, for Gulf of Mexico (GOM) crudes that contained asphaltenes of around 3 – 9% (GOM 1M - 4M), collapse slope was found to correlate with asphaltene content as well as crude oil density and viscosity. Foam volume did not show the same correlation, but these crudes tended to foam the most out of the 20 types used. Third, GOM crudes that had little to no asphaltenes (< 1%) (GOM 1A - 7A) showed foam volumes that were three to four times that of the ANS crude, but also possessed very steep collapse slopes, showing that foaming would subside rather easily after several minutes. Table 25 shows a summary for both categories of GOM crudes.

**Table 25 - Gulf of Mexico (GOM) crude oil properties in Poindexter et al. [7]**

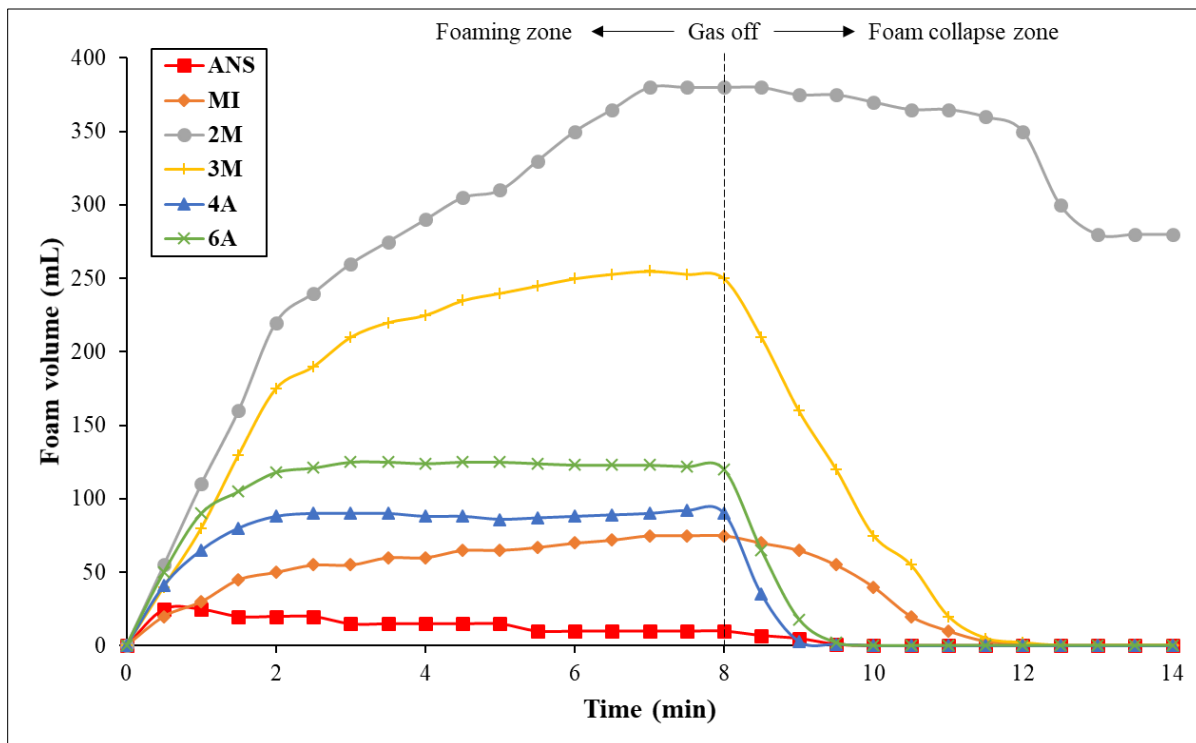
sample	designation	density (g/mL)	viscosity (cP)	surface tension (mN/m)	% asphaltenes <sup>a</sup>	% resins	foamability (mL)	collapse slope (mL/min)
GOM 1M	1M	0.8926	20	27.49	3.61	10.72	365	-80
GOM 2M	2M	0.9227	68	28.66	8.71	13.71	390	-19
GOM 3M	3M	0.8911	19	27.91	4.16	9.83	257	-74
GOM 4M	4M	0.9087	48	28.41	9.10	10.49	103	-30
GOM 1A	1A	0.8387	6	26.30	0.21	3.86	30	-88
GOM 2A	2A	0.8689	10	27.74	0.50	4.77	105	-94
GOM 3A	3A	0.8567	9	27.07	0.44	4.85	97	-97
GOM 4A	4A	0.8617	9	27.20	0.36	6.10	91	-106
GOM 5A	5A	0.8235	5	26.42	0.08	1.82	24	-76
GOM 6A	6A	0.8565	24	27.71	0.33	4.38	127	-106
GOM 7A	7A	0.8477	7	26.65	0.62	4.31	39	-108
toluene		0.8628	0.5 <sup>b</sup>	28.10	0	0	0	0
heptane		0.6804	0.3 <sup>b</sup>	19.91	0	0	0	0
octane		0.6991	0.4 <sup>b</sup>	21.30	0	0	0	0
mineral oil (heavy)		0.8772	68	31.32	0	0	126	-33

<sup>a</sup> As noted in the text, the GOM A crude asphaltenes are actually waxes. <sup>b</sup> Viscosities taken from the *Handbook of Chemistry and Physics*, 65th ed.; Weast, R. C., Ed.; CRC Press: Boca Raton, 1984–1985.

Comparing the data sheets provided by ExxonMobil for both ANS and HOOPS crude oil [8][9], it can be seen that ANS crude has a higher viscosity and asphaltene content (2.6%), while HOOPS crude has a lower viscosity and very low asphaltene content (0.3%). The study by Poindexter et al. [7] used ANS crude oil as one of the samples and showed ANS to produce little to no foam compared to the other samples. Although the study by Poindexter et al. [7] did not use HOOPS crude as one of their samples, the data sheet for HOOPS crude indicates oil characteristics closely resembling the seven non-asphaltenic crudes (GOM 1A - 7A) in that study. If we assume similar behavior, then it would be reasonable that HOOPS crude produced significantly more foam during

FR experiments compared to other crudes such as ANS. The same non-asphaltenic crudes show very steep collapse slopes, meaning the foam subsides quickly after the sparge gas is terminated. If we assume similar behavior for HOOPS, it is understandable why reignition was observed for the Bimetal and Grid FR after foaming had resulted in flame extinction. The foam breaks up quickly after the flames extinguish, but there are large amounts of residual heat on the FR, which results in reignition after the foam disappears.

Fig. 157 shows foam volume versus time plots to visually show the foamability and collapse slope of different crudes used in Poindexter et al. [7] Two crudes from each category are shown in the graph. It is interesting to note that the foam for one type of crude (GOM 2M) does not completely collapse after the sparge gas has been terminated for multiple minutes. Since an oil spill can occur for any type of crude oil, the worst-case scenario should be taken into consideration when considering the foaming capabilities of crude oil, which in this case is GOM 2M. Not only does it have the highest foamability compared to the other crudes, the collapsed slope is non-existent because the foam does not collapse completely even after extended amounts of time. The implication of this is the possibility that the foam will not subside after flame extinction has occurred and will hinder any possibility for reignition as observed in the Bimetal and Grid FR experiments. Crude oils with these characteristics need to be investigated specifically to understand the root cause of why the foam does not collapse and to design methods for mechanical breakdown of the foam if it were to occur during ISB.



**Figure 157 - Foam volume versus time for select crude oils in Poindexter et al. [7]**

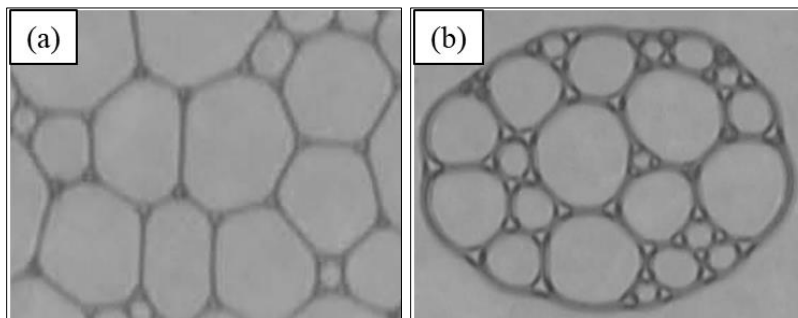


The study by Poindexter et al. [7] focused primarily on oil properties and the effect they have on crude oil foamability. However, there are certain key factors not considered in that study but relate to the experiments performed at CRREL. The first is the consideration of high temperatures. For example, foaming initiated at CRREL when the average oil temperature reached around 120 – 150 ° C, which shows that this was because of superheated steam. Elevated temperatures also significantly affect oil properties such as oil viscosity. The second factor is the influence of the initial thickness of the oil layer. As mentioned previously, foaming was observed at CRREL using an initial fuel thickness of 8 cm, but previous experiments performed in Mobile [3] with a 1 cm initial fuel thickness and replenishing system did not exhibit the same behavior. Buist et al. [1] also observed partial extinction of a burning oil slick initiated by foaming action. The burning oil slick foamed and extinguished over one area of the surface and was reignited later by adjacent flames. However, the fuel slicks were thinner than the experiments at CRREL, which is why foaming did not result in total extinction. Based on these two points, further research should be pursued on the topic for an improved understanding of foaming during ISB, particularly for thicker oil slick thicknesses.

Continuing the discussion of foaming, it should be noted that there are two classifications for liquid foams: dry and wet foams. Depending on the amount of liquid in the foam, bubbles can either be in contact or separated, and can often be empirically judged from the liquid fraction or shape of the bubbles [10]. For the case of dry foams, bubbles are substantially deformed and thin liquid films in contact with one another provide substantial mechanical stability to the foam. Bubble shapes also take the shape of polyhedrons. When the liquid fraction increases to a certain point, the shape of the bubbles becomes round and approaches circles, transitioning the foam to a wet foam. At this point, the bubbles are separated by the drainage of liquid between the bubbles due to gravity, causing bubbles to be destroyed more easily. Another way of articulating this is that wet foams are inherently less stable [10][11]. Fig. 158 shows a comparison from Furuta et al. [10] regarding the bubble shape for dry and wet foam. Callaghan et al. [12] use this observation for Ninian crude oil, but only makes the comparison for stabilized versus pipeline crude oil, and is therefore not a direct comparison to this current project.

In a three-dimensional system, Furuta et al. [10] state that liquid-gas (LG) foams are empirically recognized as a dry foam when the liquid fraction is below 5% and is considered to be in a state of wet foam when liquid fraction increase to 15% or above. The experiments at CRREL were performed with an oil slick floating on top of the water. For cases where foaming was observed, temperature data shows that the water sublayer indeed reaches and even exceeds the boiling point of water. It is assumed that this superheated steam moves upward into the crude oil layer and creates the foaming phenomenon observed at CRREL. At present, the hypothesis is that the foaming behavior observed at CRREL is in a state of wet foam since only a 15% liquid fraction is required for the foam to be in a state of wet foam. Both Furuta et al. [10] and Isert et al. [11] state that wet foams are inherently less stable and the bubbles break down more easily. This is validated

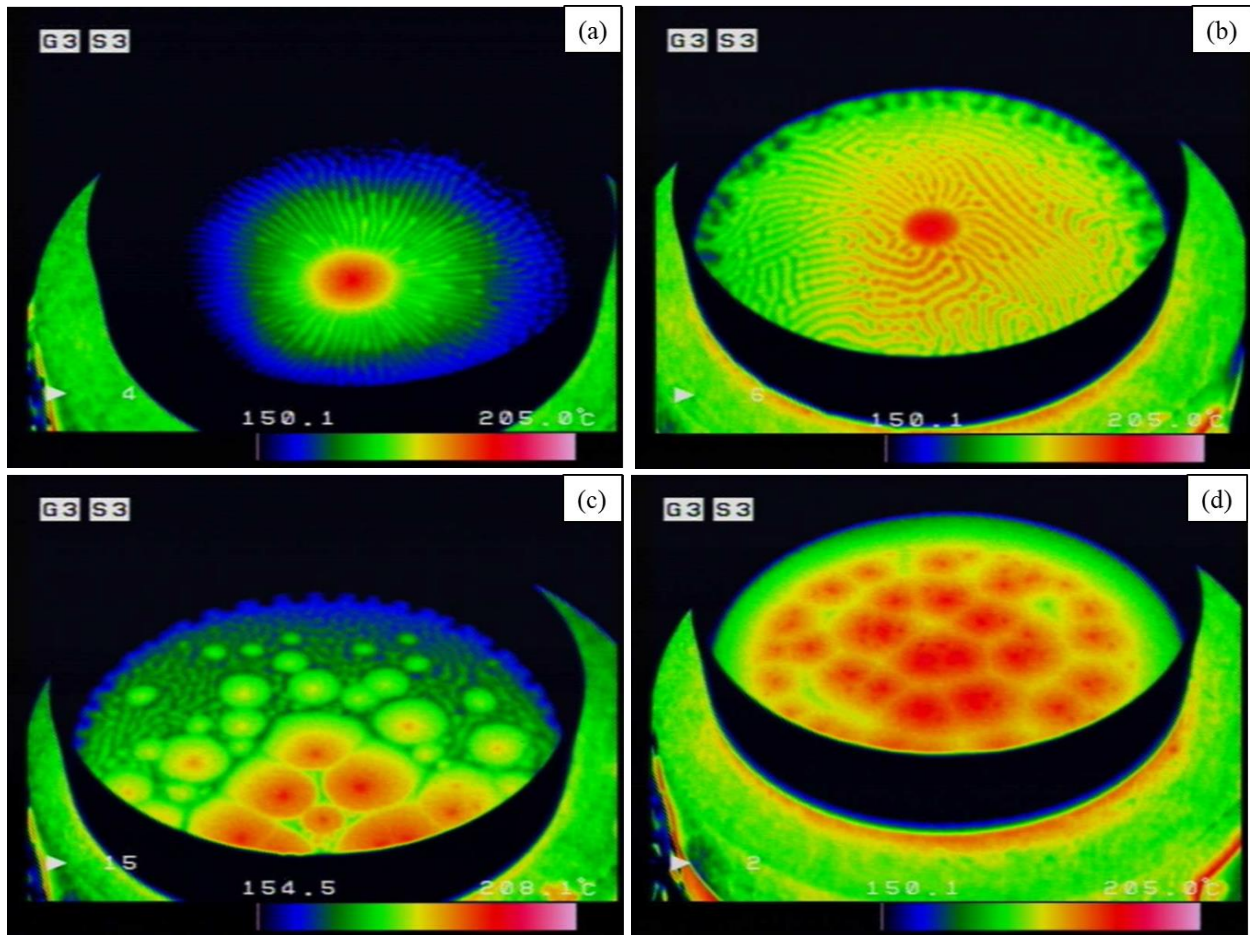
by the reignitions exhibited by the Grid and Bimetal FRs, as the foam subsided only a few minutes after flame extinction occurred.



**Figure 158 - Comparison in bubble shape from Furuta et al. [10]**  
**(a) dry foam – polyhedrons (b) wet foam – circles**

A study by Arnaudov et al. [13] discusses the effect of oily additives on the foamability and foam stability of surfactant solutions such as sodium dodecyl sulfate (SDS), a common ingredient used to make soap. They conclude that foamability is a nonmonotonic function of the oil concentrations based on a variety of variables such as dynamic surface tension. However, no direct correlation between the spreading behavior of the oils and their foam breaking ability was obtained. The solution used is also a surfactant and not crude oil, and therefore the results cannot be compared directly. Another study by Blazquez et al. [14] concluded that certain additives could be used to prevent the formation of foam (antifoams) or destroy foams that had already been created (defoamers) in crude oils. Scott [5] also documents this but states that these agents should only be used as a last resort when no mechanical or physical remedial action has proved effective.

A study by Mellema and Benjamins [15] attempts to explain the foaming behavior of triacylglycerol (TAG) oils in the presence of phospholipids when heated from the bottom via a hot plate. The foaming mechanism can be explained by relating the foaming tendency and interfacial elasticity to the occurrence of Benard-Marangoni (BM) convection patterns formed during heating, as a result of the Marangoni effect. To study the BM patterning, 20 mL of oil was placed in a 14 cm diameter shallow glass dish with 0.3 – 0.5 wt% of phospholipid additives and heated to 130° C on a heating plate. A stable pattern formation was usually observed within 2 min after the oil reached 130° C, and could be continuously observed for another 3 min. IR images of the experiments, as shown in Fig. 159, indicate that the BM patterns could take the form of rolls, necklaces, necklaces/hexagons, or large hexagons depending on the additive used in the oil. However, Mellema and Benjamins [15] do not have a water layer beneath the oil layer, and therefore more research is required regarding the viability of using this method to quantify crude oil foamability.



**Figure 159 - BM patterns via hot plate heating from the bottom at 130° C [15]**

**(a) Rolls (b) Necklaces (c) Necklaces/hexagons (d) Large hexagons**

## Conclusions

For the specific application regarding ISB of crude oil with FR deployment, further work is required to determine the exact parameters of crude oil to characterize foam volume, collapse slope, or some combination of the two parameters. Antifoams and defoamers are not ideal for this application, and therefore a mechanical solution needs to be developed to break down the bubbles within the foam if they were to occur during ISB. In the experiments at CRREL, oil foaming was still observed for wave cases. However, in contrast to the 57% burn efficiency for the baseline case with no waves, the baseline case with Wave 2 allowed for reignition to occur similar to the FR cases with no waves, which resulted in a 97% burn efficiency. The only difference was the addition of waves. It is currently unknown whether the presence of waves alone is responsible for allowing reignition to occur. Quantification for wave presence and wave intensity as it relates to oil foaming tendency and foam breakdown requires further investigation.

Studies relating BM patterns to foamability are based on a layer of oil with additives being heated from the bottom. It would be interesting to perform similar studies using various types of crude oil, especially HOOPS, to study foaming tendency versus BM patterns using IR images. Another possible study would be to consider heating from the top of the oil layer, which would relate the foamability of a given crude oil to a scenario where a fire is burning at the surface. Previous studies of dry and wet foam mostly focus on a premixed mixture of water and surfactant, such as SDS, to systematically quantify the liquid content in the foam. No prior studies exist discussing dry versus wet foam of crude oil due to boiling water at the water-fuel interface during a fire, as is the case with this project. Future research is required to allow categorization of the foam observed at CRREL as dry or wet foam and to study the mechanisms that result in the foaming behavior.

Moreover, this foaming behavior was not observed in the Mobile experiments, where HOOPS crude oil was also used as the fuel. However, one critical difference exists between the two projects. A fuel replenishing system was used in Mobile to maintain a constant fuel thickness of 1 cm, whereas, at CRREL, it was a thinning fuel slick with 8 cm initial fuel thickness. This suggests the possibility of fuel thickness or the presence of cold fuel at the water-fuel interface playing a role in the foaming tendency. This aspect also requires future work for a more fundamental understanding.

In the latter sections, temperature data from the CRREL experiments will also provide valuable insight into the time to foaming as well as the parameters for its cause.

## References

- [1] Arsava, K.S., et al. (2019). Application of Flame Refluxer<sup>TM</sup> Concept to ISB—Experimental Results of 5 Field Trials in Mobile, Alabama. In Proceedings-42nd AMOP Technical Seminar on Environmental Contamination and Response (pp. 568–587). Emergencies Science and Technology Section.
- [2] Buist, I., McCourt, J., Potter, S., Ross, S., & Trudel, K. (1999). In situ burning. *Pure and Applied Chemistry*, 71(1), 43-65.
- [3] Broeckmann, B., & Schecker, H. G. (1995). Heat transfer mechanisms and boilover in burning oil-water systems. *Journal of Loss Prevention in the Process Industries*, 8(3), 137-147.
- [4] Zalosh, R. G. (2003). *Industrial fire protection engineering* (pp. 230–234). Hoboken, NJ: Wiley.
- [5] Scott, J. K. B. (1967). Oil Foaming. *Proceedings of the Institution of Mechanical Engineers, Conference Proceedings*, 182(14), 260–261.
- [6] Callaghan, I.C., Mckechnie, A.L., Ray, J.E., & Wainwright, J.C. (1985). Identification of crude oil components responsible for foaming. The United States.
- [7] Poindexter, M., Zaki, N., Kilpatrick, P., Marsh, S., & Emmons, D. (2002). Factors Contributing to Petroleum Foaming. 1. Crude Oil Systems. *Energy & Fuels*, 16, 700-710.
- [8] Alaska North Slope, ANS17Y. <https://corporate.exxonmobil.com/crude-oils/crude-trading/alaska-north-slope>. Accessed July 22, 2021.
- [9] HOOPS Blend, HOOPS16F. <https://corporate.exxonmobil.com/Crude-oils/Crude-trading/HOOPS-Blend>. Accessed July 22, 2021.
- [10] Furuta, Y., Oikawa, N., & Kurita, R. (2016). The close relationship between a dry-wet transition and a bubble rearrangement in two-dimensional foam. *Scientific reports*, 6(1), 1-8.
- [11] Isert, N., Maret, G., & Aegerter, C. M. (2013). Coarsening dynamics of three-dimensional levitated foams: From wet to dry. *The European Physical Journal E*, 36(10), 1-6.
- [12] Callaghan, I. C., Gould, C. M., Reid, A. J., & Seaton, D. H. (1985). Crude-oil foaming problems at the Sullom Voe Terminal. *Journal of petroleum technology*, 37(12), 2211-2218.
- [13] Arnaudov, L., Denkov, N. D., Surcheva, I., Durbut, P., Broze, G., & Mehreteab, A. (2001). Effect of oily additives on foamability and foam stability. 1. Role of interfacial properties. *Langmuir*, 17(22), 6999-7010.

- [14] Blázquez, C., Emond, E., Schneider, S., Dalmazzone, C., & Bergeron, V. (2014). Non-aqueous and crude oil foams. *Oil & Gas Science and Technology–Revue d’IFP Energies nouvelles*, 69(3), 467-479.
- [15] Mellema, M., & Benjamins, J. (2004). Importance of the Marangoni effect in the foaming of hot oil with phospholipids. *Colloids and Surfaces A: Physicochemical and Engineering Aspects*, 237(1-3), 113-118.



## **6. Overall Conclusion and Future Work**



## **APPENDIX – A**

### **MODEL FOR PREDICTING THE INFLUENCE OF IMMERSED OBJECT ON POOL FIRE BURNING**

**Sharanya Nair<sup>\*</sup>, Glenn Mahnken, Kemal S. Arsava, Ali S. Rangwala**

<sup>\*</sup>Department of Fire Protection Engineering, Worcester Polytechnic Institute, Worcester, MA 01609, USA

#### **ABSTRACT**

The study presents a heat transfer model for prediction of the effect of immersed objects with high thermal conductivity (refluxer) on the mass burning characteristics of a pool fire. The refluxer forms a thermal loop between the flame and the fuel pool, enhancing the heat feedback to the fuel. Consequently, additional fuel vaporization occurs thus improving the burning characteristics. In the study, a theoretical model solves steady state energy equation to analyze the effectiveness of the refluxer by determining the heat transfer to the fuel pool based on parameters of refluxer parameters (material and dimensions) and fuel properties. The model solution also envisions an inverse design of a refluxer based on end-use of the refluxer.

**Keywords:** Pool fire; Heat transfer model; Mass loss rate enhancement; Inverse design.

#### **1. INTRODUCTION**

Pool fires have been studied extensively in terms of the mass burning rates, temperature, species, and flow fields. These are necessary for understanding the coupled behavior of heat transfer, mass transfer, and the reaction mechanism in pool fires. Due to this coupling, the fuel evaporation and burning are dependent on the flame heat feedback to the pool. Thus, a mechanism to enhance this heat transfer would improve the burning rate of the fuel. To accomplish this, the Flame Refluxer<sup>TM</sup> was developed [1], where a high conductivity material is placed the flame, which would assist in establishing a thermal loop from flame to preheat and burn the fuel in an enhanced manner. The technology was developed for with direct application to in-situ burning of oil spills where enhanced mass burning rates were observed [2 - 4]. Additionally, the method also has various applications where thermal storage in liquids or slurry is required, such as in anaerobic digester or in slurry sanitization.

Different scales of pool fire experiments have been conducted using the refluxer technology to determine the design parameters of the refluxer. The dimensions of the refluxer need to be optimized to ensure maximum heat transfer from the flame to the subcooled fuel. Studies have

shown a reduction in mass loss rate when the refluxer exceeds a particular height above the fuel pool [2, 5]. It was also shown that the thermal conductivity of the refluxer material played an important role where copper refluxers were more efficient than stainless steel ones [2]. Moreover, multiple refluxers immersed in the fuel pool also led to enhanced mass loss rate [2, 3].

Numerical modeling of the Flame Refluxer<sup>TM</sup> is valuable in understanding the effect of the governing parameters such as fuel characteristics and refluxer properties. A two-dimensional model was done by Sezer et al. [6], where the effect of an immersed aluminum rod in a hexane pool was studied. The enhanced mass loss rate due to the rod was predicted close to the experimental values. An integral model was developed by Arsava et al. [7] where the heating of the fuel in the presence of refluxers was analyzed through thermal penetration depth, and the optimization of the refluxer design was discussed for oil spill burning application. Fang et al. [5] predicted the mass loss rate using the *B*-number approach for aluminum plates in ethanol and heptane pools, where enhanced mass burning rates were observed. The present study proposes a predictive heat transfer model that solves steady state energy equation for the refluxer. The model can be utilized by an end-user for either (a) predicting the enhancement in the mass loss rate for a designed refluxer or (b) an inverse design of a refluxer prototype optimized to enhance the mass loss rate by a design amount.

## 2. MODEL DESCRIPTION

### 2.1. Problem specification

Figure 1(a) shows the heat transfer modes in a pool fire. The flame (*f*) heats the fuel surface through convection and radiation. This heat received on the fuel-air interface (*i*) is denoted by  $\dot{Q}_{f-i}$ . The in-depth conduction ( $\dot{Q}_{i-l}$ ) leads to sensible heating of the liquid fuel. The fuel evaporates from the surface and burns based on the flame heat feedback and the latent heating of the fuel. Thus, the energy balance is given by

$$\dot{Q}_{f-i} - \dot{Q}_{i-l} = \dot{m}L \quad (1)$$

where, *L* is the latent heat of vaporization of the fuel.

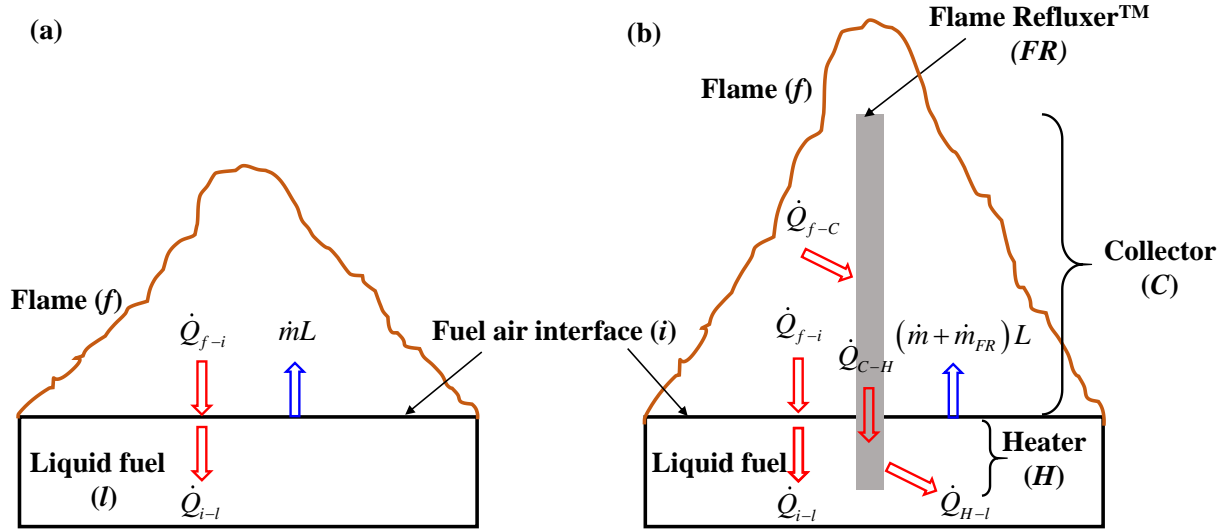


Figure 1: Heat transfer modes in a (a) pool fire, (b) pool fire with Flame Refluxer™

(f: flame, i: interface, l: liquid, C: collector, H: heater)

Figure 1(b) shows a pool fire burning with a Flame Refluxer™. In addition to the heat input from the flame to the fuel surface, heat is also transferred from the flame to the fuel through the high conducting refluxer. The part of the refluxer that is exposed to the hot combusting gases is the collector region (C). This heat is transferred to the fuel through the heater region (H) of the refluxer as shown in Fig. 1(b). The additional heat input into the liquid fuel causes sensible as well as latent heating of the fuel, leading to enhanced mass loss rate. The energy balance for the fuel in the presence of the refluxer is given by,

$$\dot{Q}_{f-i} - \dot{Q}_{i-l} + \dot{Q}_{H-l} = (\dot{m} + \dot{m}_{FR})L \quad (2)$$

It is seen that there is an additional mass loss rate due to the heat transfer from the immersed object. This paper aims to quantify and predict this enhancement based on a heat transfer model for the refluxer. For the refluxer region, the energy balance at steady state can be written as,

$$\dot{Q}_{f-c} = \dot{Q}_{c-h} = \dot{Q}_{H-l} \quad (3)$$

The enhancement of the mass burning rate of fuel with an immersed object depends on both fuel characteristics and the refluxer dimensions and properties. Further, from equation (3), it is seen that the problem can be studied from the perspective of the collector and heater sections separately. The heater section encompasses the conduction within the object and subsequent heat transfer to the fuel. Additionally, the heater would also act as sites for nucleate boiling [8] based on the degree of superheat. This would involve a complex coupled model to study the two-phase flow, fluid convection and heat transfer. Alternatively, the present work proposes a predictive model applied

to the collector region which involves a solid object heated in a gas phase. Hence, using equation (3), the term  $\dot{Q}_{H-l}$  in equation (2) can be re-written as,

$$\dot{Q}_{f-i} - \dot{Q}_{i-l} + \dot{Q}_{f-c} = (\dot{m} + \dot{m}_{FR})L \quad (4)$$

From equation (4), it is clear that if the heat input to the collector from the flame is known, the enhancement in mass loss rate can be predicted. Thus, the problem statement for the refluxer has been simplified into a collector model.

## 2.2. Model formulation

A fundamental model for the collector section of the refluxer is as shown in Fig. 2(a). A collector of length  $L_c$  is modeled in a constant heated temperature environment. This temperature is approximated to an effective flame temperature ( $T_f$ ). The heater section is simplified to a low temperature sink ( $T_s$ ) extracting heat from the defined collector region. The temperature along the collector ( $T_{FR}$ ) will be a function of height  $x$  above the heater, depending on the heat into the collector from the flame ( $\dot{Q}_{f-c}$ ) and the heat loss to sink ( $\dot{Q}_{c-h}$ ). Moreover, it is assumed that the temperature variation is more significant along x-direction as compared to the variation along the other directions of the collector.

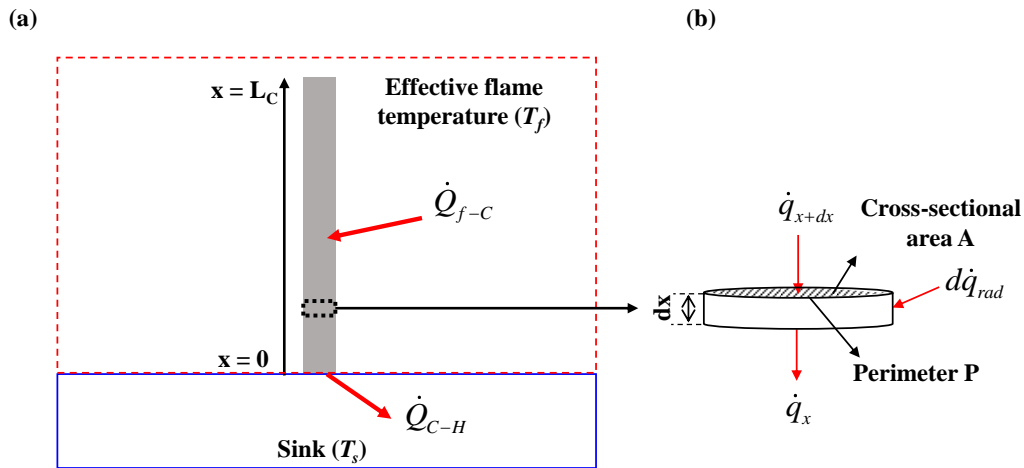


Figure 2: (a) Sketch showing the model for collector region of Flame Refluxer™, and (b) energy balance in a differential element of the collector

Fig. 2(b) shows a differential element of length  $dx$  at a distance  $x$  from the sink, with cross-sectional area  $A$  and perimeter  $P$ . It is to be noted here that the model is not specific to the shape of the collector and can be used if the cross-sectional area and perimeter of the refluxer are known. Heat conducts in negative  $x$ -direction as shown in Fig. 2(b). It is assumed the collector is heated through radiative mode of heat transfer. The radiative heat transfer to the collector element from the flame is also indicated in Fig. 2(b). The model simplifications and assumptions are summarized below:



1. The temperature variation in  $x$ -direction is more significant than the temperature variation in other directions.
2. The collector is assumed to be slender ( $A \ll P \times L_C$ , where  $P \times L_C$  is the side surface area of the collector) and major portion of the heat is collected by the side of the refluxer rather than the top of the collector.
3. The temperature of the surrounding of the collector is assumed to be at a specified effective flame temperature  $T_f$ .
4. The convective heat transfer from the flame is ignored as compared to the radiative heat flux, which is a valid assumption for medium to large pool fires.
5. A sink at constant temperature  $T_s$  is assumed at  $x = 0$ , which represents the heat lost from the collector to the heater section and to the fuel pool.
6. Transient heating of the system is not considered, and the results are based on the achievement of quasi-steady state.

As a result, the energy balance equation for the differential element at steady state can be written as,

$$\dot{q}_{x+dx} - \dot{q}_x + d\dot{q}_{rad} = 0 \quad (5)$$

Here, heat conduction at distance ( $x$ ) can be written from Fourier's Law as  $\dot{q}_x = kA \frac{dT_{FR}}{dx}$ , where  $k$  is the thermal conductivity of the refluxer material. The heat conduction at distance ( $x + dx$ ) can be written using Taylor series expansion as,

$$\dot{q}_{x+dx} = \dot{q}_x + \frac{d\dot{q}_x}{dx} dx = \dot{q}_x + kA \frac{d^2 T_{FR}}{dx^2} dx \Rightarrow \dot{q}_{x+dx} - \dot{q}_x = kA \frac{d^2 T_{FR}}{dx^2} dx \quad (6)$$

The radiant heat flux term ( $d\dot{q}_{rad}$ ) is given from Stephen-Boltzmann Law as,

$$d\dot{q}_{rad} = \sigma \varepsilon P dx (T_f^4 - T_{FR}^4) \quad (7)$$

where,  $\sigma$  is the Stephen-Boltzmann constant ( $5.67 \times 10^{-8} \text{ W/m}^2\text{-K}^4$ ),  $\varepsilon$  is the emissivity, and  $P \times dx$  denotes the surface area of the differential element exposed to radiant heating. Thus, equation (5) can be re-written as,

$$kA \frac{d^2 T_{FR}}{dx^2} + \sigma \varepsilon P (T_f^4 - T_{FR}^4) = 0 \quad (8)$$

Equation (8) shows a second order differential equation which must be solved to determine  $T_{FR}(x)$ .

### 2.3. Model solution

Equation (8) shows the temperature distribution ( $T_{FR}$ ) in terms of heat conduction term and the radiative heat transfer term. To solve this equation, the equation is simplified into two first order differential equations by defining the temperature gradient  $\frac{dT_{FR}}{dx} = \theta$ . Equations (9a) and (9b) show the two first order differential equations along with the known boundary conditions (BC) at  $x = 0$  and  $x = L_C$ . At  $x = 0$ , the temperature is the sink temperature ( $T_s$ ). From the slender refluxer assumption, the heat flux on the top of the collector is negligible resulting in an adiabatic condition at  $x = L_C$ .

$$\frac{dT_{FR}}{dx} = \theta, \quad BC : T_{FR}(x=0) = T_s \quad (9a)$$

$$\frac{d\theta}{dx} = -\frac{\sigma \varepsilon P}{kA} (T_f^4 - T_{FR}^4), \quad BC : \theta(x=L_C) = 0 \quad (9b)$$

Equation (9) can be solved numerically using Euler's method. However, Euler's method being a space-marching problem, requires the values of  $T_{FR}$  and  $\theta$  at  $x = 0$ . From the boundary conditions, we know that at  $x = 0$ ,  $T_{FR,0} = T_s$ . However,  $\theta_0$ , the temperature gradient at  $x = 0$ , is unknown. Hence, for the solution of the two differential equations, shooting method needs to be implemented, where a guess value of  $\theta_0$  is used and the solution is solved iteratively until the value of  $\theta(x=L_C) = 0$ . This can either be achieved by using goal seek procedure in MS excel or by using shooting method available in an in-house C code. The numerical solution gives the temperature distribution  $[T_{FR}(x)]$  and the temperature gradient distribution  $[\theta(x)]$  along the collector length.

### 2.4. Non-dimensional parameters

From the model solution for temperature and temperature gradient, the heat input to the collector,  $\dot{Q}_{f-C}$ , and heat output from collector to sink,  $\dot{Q}_{C-H}$ , as shown in Fig. 2(a) can be evaluated using equation (10). It should be noted that at steady state  $\dot{Q}_{f-C} = \dot{Q}_{C-H}$ .

$$\begin{aligned} \dot{Q}_{f-C} &= \sum_{x=0}^L \sigma \varepsilon (P dx) (T_f^4 - T_{FR}^4) \\ \dot{Q}_{C-H} &= kA \left. \frac{dT_{FR}}{dx} \right|_{x=0} = kA \theta|_{x=0} \end{aligned} \quad (10)$$

Subsequently, a non-dimensional parameter has been defined for associating the input parameters such as the collector dimensions and properties, and flame and sink temperatures given by,

$$\eta = L_c \sqrt{m \frac{(T_f^4 - T_s^4)}{(T_f - T_s)}} \quad (11)$$

where,  $\eta$  is non-dimensional, and  $m = \frac{\sigma \epsilon P}{kA}$ . It is to be noted that the parameter  $m$  is dependent on the collector geometry through parameters of  $P$  and  $A$ , and collector material property through thermal conductivity  $k$  and the emissivity  $\epsilon$ . Thus, a variation in  $m$  denotes an effective variation in the refluxer characteristics.

Similarly, the collector output given by  $\dot{Q}_{C-H} = kA \left. \frac{dT_{FR}}{dx} \right|_{x=0}$  can be non-dimensionalized using heat output evaluated for a side insulated refluxer,  $\dot{Q}_{ins}$ , such that the collector tip is at flame temperature. In this case,  $\dot{Q}_{ins} = kA \frac{(T_f - T_s)}{L_c}$ . Thus, the non-dimensional collector output can be defined as,

$$Q^* = \frac{\dot{Q}_{C-H}}{\dot{Q}_{ins}} = \frac{\left. \frac{dT}{dx} \right|_{x=0}}{\frac{(T_f - T_s)}{L_c}} \quad (12)$$

It is noted that parameter  $\eta$  involves all the input parameters and thus the non-dimensional collector output,  $Q^*$ , can be evaluated as a function of  $\eta$ . Figure 3(a) shows the variation of  $Q^*$  with  $\eta$ . Scatter plots are obtained by varying the different input parameters in terms of collector geometry parameters, the flame and sink temperature. The plot shows that  $Q^*$  can be increased by enhancing the value of  $\eta$ . This can be achieved by varying refluxer dimension by either (a) increasing collector length ( $L_c$ ) or by (b) increasing perimeter to area ( $P/A$ ) ratio. Additionally, the collector heat transfer to the sink ( $\dot{Q}_{C-H}$ ) in terms of Watt can be evaluated using equation (12) after obtaining  $Q^*$  as a function of  $\eta$ . Further, the temperature distribution obtained from the model solution can be non-dimensionalized such that it is a function of  $\eta$ . The temperature at  $x = L_c$  is denoted as  $T_{L_c}$  is non-dimensionalized in terms of flame temperature ( $T_f$ ) and sink temperature ( $T_s$ ) as shown in equation (13). The variation of  $T_{L_c}^*$  as a function of  $\eta$  is shown in Fig. 3(b) along with the polynomial fit. It is worthwhile to note that as the collector length increases,  $\eta$  increases to about 2.5,  $T_{L_c}^*$  asymptotes close to one, portraying that the temperature  $T_{L_c}$  approaches the effective flame temperature with increase in collector length.

$$T_L^* = \frac{(T_{L_c} - T_s)}{(T_f - T_s)} \quad (13)$$

The non-dimensional temperature distribution ( $T_x^*$ ) can be defined in terms of temperature at the top end ( $T_{L_c}$ ) as shown in equation (14). This non-dimensionalized distribution is seen to be fit by a second order polynomial as shown in Fig. 3(c).

$$T_x^* = \frac{(T_x - T_s)}{(T_L - T_s)} \quad (14)$$

The model procedure is summarized in the flow chart as shown in Fig. 4. As shown in Fig. 4, the non-dimensional parameter  $\eta$  is evaluated using the input parameters. Based on the value of  $\eta$ , the collector output  $\dot{Q}_{C-H}$  and the temperature distribution  $T_{FR}(x)$  can be evaluated using the model.

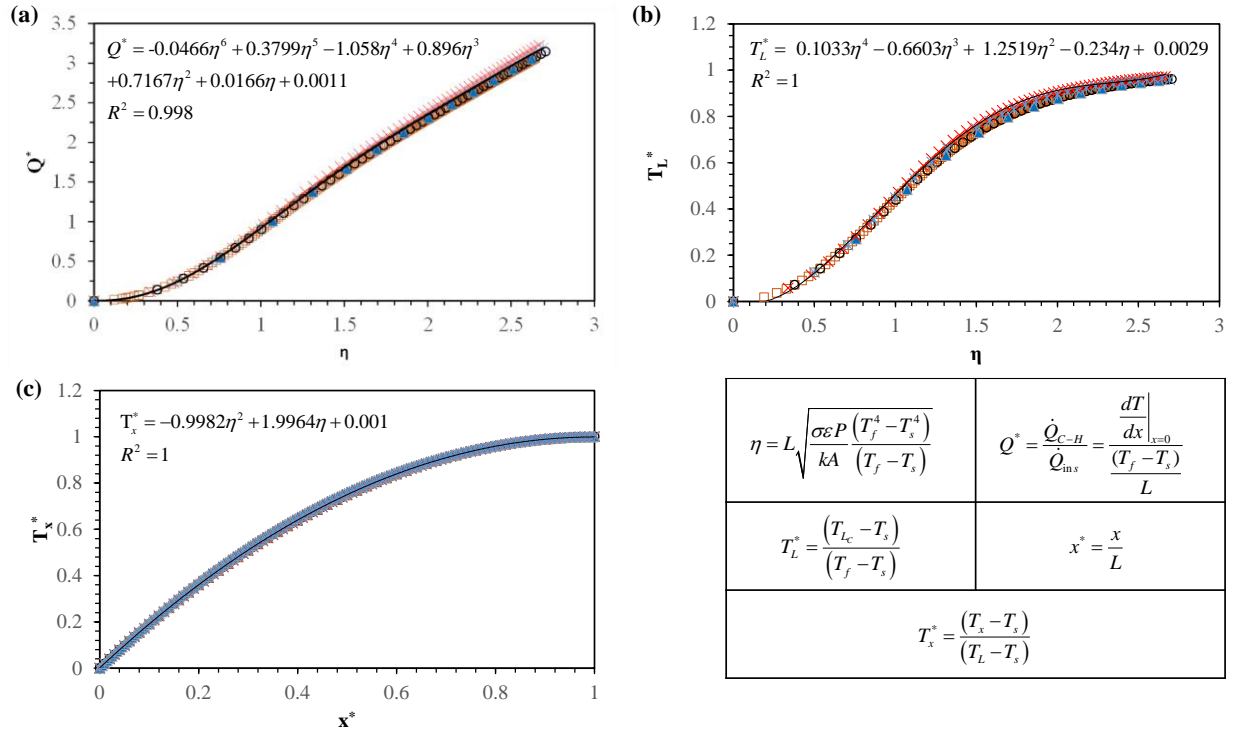


Figure 3: Model solution for non-dimensional (a) collector output ( $Q^*$ ), (b) temperature at  $x = L$ , and (c) temperature at  $x$

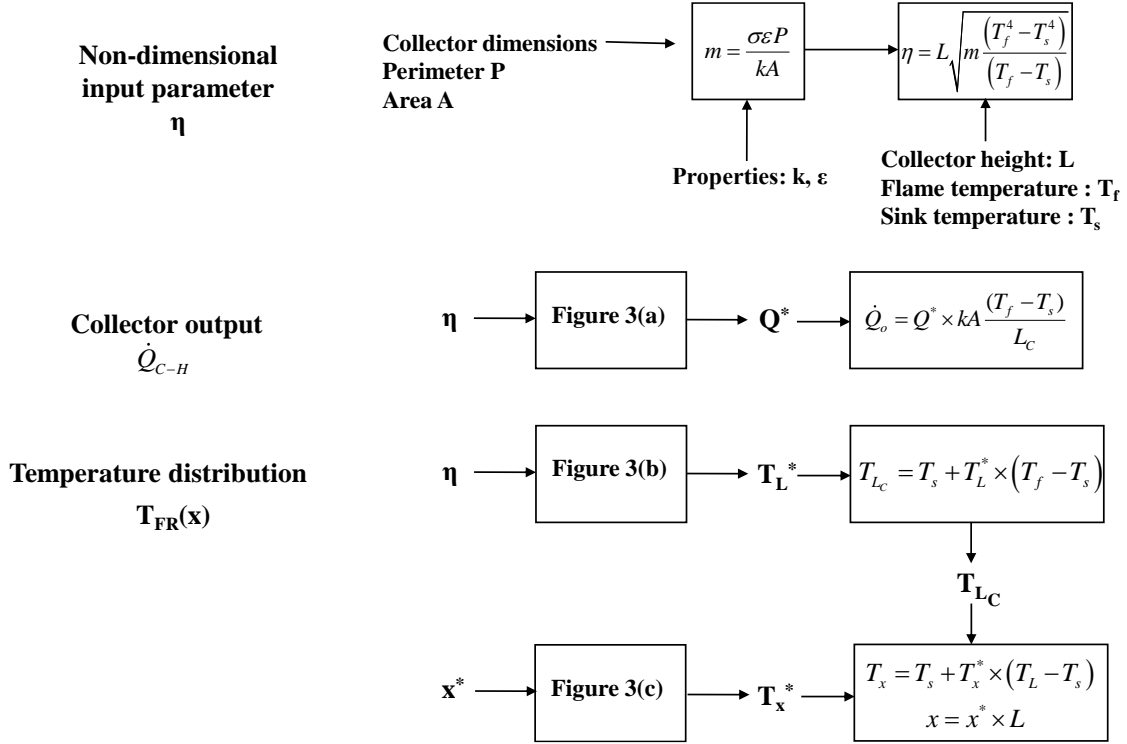


Figure 4: Flowchart showing the procedure for evaluating collector output  $\dot{Q}_{C-H}$  and temperature distribution  $T_{FR}(x)$  on the collector

### 3. RESULTS AND DISCUSSION

The model is used to study the effect of the governing parameters of refluxer characteristics and fuel properties on the mass loss rate enhancement in pool fires. Four case studies are considered to study the effect of (1) collector length, (2) multiple collectors, (3) collector material, and (4) fuel type. The final case study visualizes use of the model for inverse design of the collector.

#### 3.1. Case Study 1: Effect of collector length

An experiment was conducted [2] where an aluminum rod of diameter 1 cm was immersed in a hexane pool to analyze its effect on the mass loss rate. The collector length  $L_C$  was varied from 5 cm to 20 cm. The perimeter ( $P$ ) and the cross-sectional area ( $A$ ) of the rod is evaluated to be 0.031 m and  $7.85 \times 10^{-5} \text{ m}^2$ , respectively. Since  $A \ll P \times L_C$ , the slender rod assumption is valid for this case. Using thermal conductivity of aluminum ( $k = 220 \text{ W/m-K}$ ) and emissivity  $\varepsilon \sim 1$ , the parameter  $m$  can be evaluated as  $1.03 \times 10^{-7} \text{ m}^2\text{K}^{-4}$ . It is seen that the sink temperature and effective flame temperature used for evaluation of  $\eta$  is unknown. However, the temperature profile along the collector for  $L = 14 \text{ cm}$  collector is known through the experiment [2]. Assuming a sink temperature of 450 K and an effective flame temperature of 800 K,  $\eta$  is evaluated as 1.46 for  $L_C = 0.14 \text{ m}$ . The corresponding values of  $Q^*$ , and  $T_L^*$  are 1.51 and 0.67, respectively. Using these values, the temperature profile along the collector is obtained as shown in Fig. 8, as compared to the experimental data for  $L_C = 14 \text{ cm}$ . It is to be noted that the values of 450 K and 800 K for sink and flame temperatures have been obtained through a trial-and-error method, to match

experimental data. Using these temperature values  $\eta$  is evaluated, and the corresponding values of  $Q^*$ , and  $T_L^*$  are shown in Table 3 for different collector lengths. Further, the temperature distribution is plotted in Fig. 8 for different collector lengths as a function of  $x$ . It is seen that the FR tip temperature approaches  $T_f$  as collector length increases.

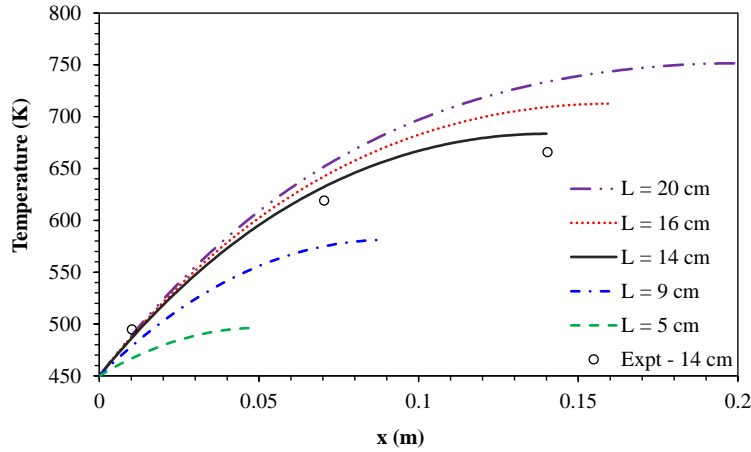


Figure 8: Temperature distribution along the rod for different collector lengths ( $L_C$  varying from 5 cm to 20 cm)

The collector output in terms of  $\dot{Q}_{C-H}$ , as evaluated from  $Q^*$  is also shown in Table 1 for different collector heights. The heat addition from the rod is seen to increase from about 32 W to 70 W as the collector height increases from 5 cm to 20 cm. If we assume that this heat is used in latent heating of the fuel, the additional mass loss rate due to the metal rod ( $\dot{m}_{FR}$ ) can be evaluated as shown in equation (15). This assumption is valid as the heater section acts as nucleation sites and the heat transferred from the collector to the heater section leads to formation of bubbles as shown by Pi et al. [8].

$$\dot{m}_{FR} = \frac{\dot{Q}_{C-H}}{L_{vap}} = \frac{Q^*}{L_{vap}} \times kA \frac{(T_f - T_s)}{L_C} \quad (15)$$

Here,  $L_{vap}$  is the latent heat of vaporization of the fuel (335 kJ/kg for hexane). Hence, the overall mass loss rate ( $\dot{m}$ ) is given by,

$$\dot{m} = \dot{m}_{baseline} + \dot{Q}_{C-H} / L_{vap} \quad (16)$$

where,  $\dot{m}_{baseline}$  represents the baseline mass loss rate for a pool fire without the rod. The experimental value for baseline mass loss rate is 0.11 g/s [2]. Using equation (16), the mass loss rates have been evaluated as shown in Table 1 and is compared with the experimental mass loss rate value at steady state. Further, the mass loss rate is plotted as a function of collector length in Fig. 9. The predicted values are seen to be in close proximity to the experimental values, showing that the model is able to ascertain the effectiveness of the refluxer in a quantitative manner.



Table 1: Predicted values of parameters for different collector lengths

( $L_C$  varying from 5 cm to 20 cm)

$L_C$ (cm)	5	9	14	16	20
$\eta$	0.52	0.94	1.46	1.67	2.08
$Q^*$	0.26	0.77	1.51	1.79	2.31
$T_L^*$	0.13	0.38	0.67	0.75	0.86
Heat from rod $\dot{Q}_{C-H}$ (W)	31.7	51.9	65.3	67.6	69.8
<b>Mass loss rate (g/s)</b>					
Predicted	0.2	0.26	0.3	0.31	0.32
Experiment	0.22	0.28	0.374	0.32	-
<b>Enhancement ratio (ER)</b>					
Predicted	1.82	2.36	2.72	2.82	2.9
Experiment	2	2.54	3.4	2.91	-

Moreover, an mass loss rate enhancement ratio (ER) can be defined as,

$$ER = \frac{\dot{m}}{\dot{m}_{baseline}} = 1 + \frac{\dot{Q}_{C-H}}{\dot{m}_{baseline} L_{vap}} \quad (17)$$

The predicted and experimental values of enhancement ratio are shown in Table 3, showing an increase in mass loss rate with collector length.

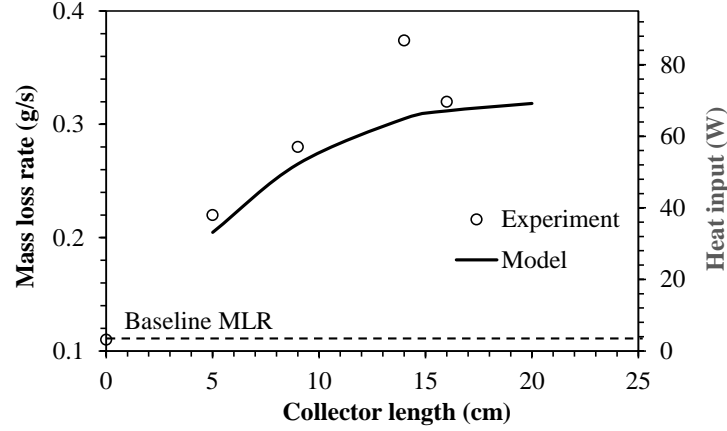


Figure 9: Variation of mass loss rate and heat input (open symbols indicate experimental data)

Another important observation from Table 1 is that the enhancement ratio is seen to asymptote to a value close to 3. This requires further study on impact of collector length  $L_C > 20$  cm. The data for higher values of  $L_C$  is shown in Fig. 10(a) where ER saturates to 3 beyond a collector length more than 30 cm. This is also explained by the coinciding temperature profiles for 30 cm and 50 cm collector length in Fig. 10(b). Thus, it is seen that the model can be used to optimize collector length. From Fig. 10(a), it is clear that the collector length in the range 20 cm - 30 cm ( $2.1 < \eta < 3.1$ ) can be considered optimal as the change in ER beyond this value of  $L_C$  is not significant. It is also interesting to note here that according to Fig. 3(b), the temperature at collector tip also asymptotes close to 1 around  $\eta \sim 2.5$ , which gives a collector length  $L_C = 25$  cm.

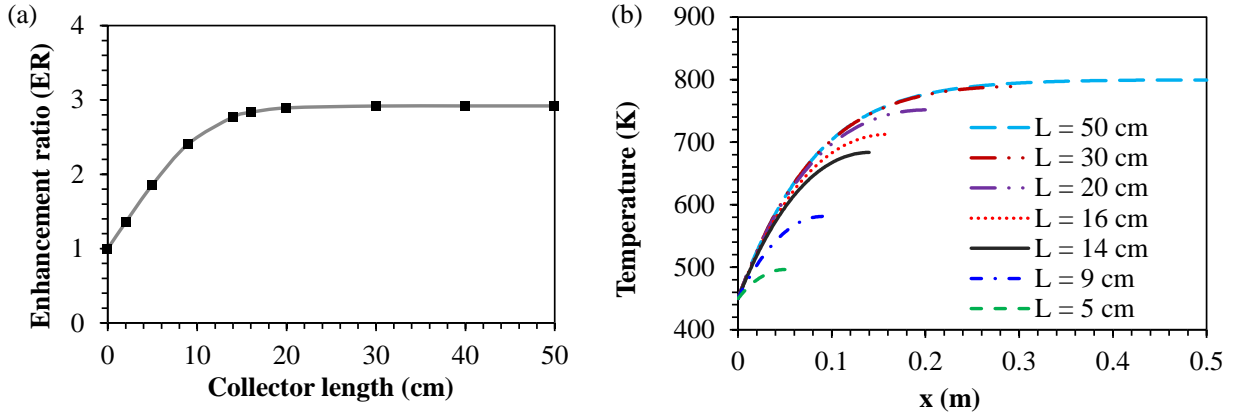


Figure 10: (a) Variation of enhancement ratio as a function of collector length, (b) temperature distribution along the rod for different collector lengths ( $L_C$  varying from 5 cm to 50 cm)

### 3.2. Case Study 2: Effect of multiple refluxers

In case study 1, a single refluxer was considered and the enhancement in mass loss rate was predicted. In addition to this in the same experimental setup [2], multiple aluminum rods of diameter 1 cm and height 14 cm were used as refluxers in a hexane pool. The number of rods is varied from 0 (no rod) to 9 rods in the experiment. Using the input parameters, the parameter  $\eta$  is

evaluated as 1.46 and the corresponding  $Q^*$  is 1.51 for each rod as dimensions and the properties are the same for each rod. However, the total heat from the refluxer is given by,

$$\dot{Q}_{C-H} = N \times Q^* \times kA \frac{(T_f - T_s)}{L} \quad (18)$$

where,  $N$  is the number of rods. The predicted values of heat from multiple rods, the corresponding mass loss rates and enhancement ratios are shown in Table 2. The mass loss rate and enhancement ratio as a function of number of FRs is shown in Fig. 11. It is seen that as the number of rods is increased, the enhancement in mass loss rates is higher. This is due to additional heat transferred from the flame that is transferred to the fuel by the rods.

Table 2: Predicted values of parameters for multiple collectors ( $N$  varying from 0 to 9)

<b>N</b>	0	1	2	3	4	5	9
<b><math>\eta</math></b>	1.46						
<b><math>Q^*</math></b>	1.51						
<b><math>T_L^*</math></b>	0.67						
<b>Heat from rods</b> <b><math>\dot{Q}_{C-H}</math> (W)</b>	0	65.3	130.6	195.9	261.2	326.5	587.7
<b>Mass loss rate (g/s)</b>							
<b>Predicted</b>	-	0.3	0.5	0.69	0.89	1.08	1.86
<b>Experiment</b>	0.11	0.374	0.51	0.71	0.95	1.23	1.64
<b>Enhancement ratio (ER)</b>							
<b>Predicted</b>	1	2.72	4.54	6.27	8.09	9.82	16.9
<b>Experiment</b>	1	3.4	4.64	6.45	8.64	11.2	14.9

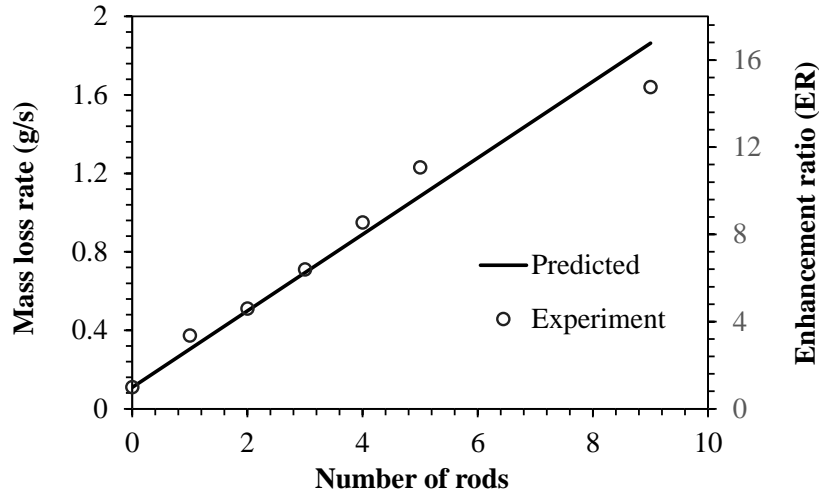


Figure 11: Variation of mass loss rate and enhancement ratio as a function number of rods

### 3.3. Case study 4: Effect of collector material

The collector property should be such that the heat incident on the rod is transferred in a fast and efficient manner to the heater section. This requires high conductivity materials such as copper or aluminum. Figure 12(a) shows the optimized rod length for materials with different thermal conductivities when the effective flame temperature is 800 K and sink temperature is about 450 K. It is seen that for the optimum length varies based on the refluxer material. Also, based on a baseline mass loss rate of 0.11 g/s [2], it is seen that a high conductivity material accounts for higher values of maximum enhancement ratio as shown in Fig. 12(b). These plots are also useful in predicting the diameter and collector length required if the enhancement ratio is specified. For instance, if the required ER is 4, Table 3 shows the different rod dimensions that could be used based on the chosen material. It is also seen that as thermal conductivity increases, slender and longer rods are optimum for mass loss rate enhancement.

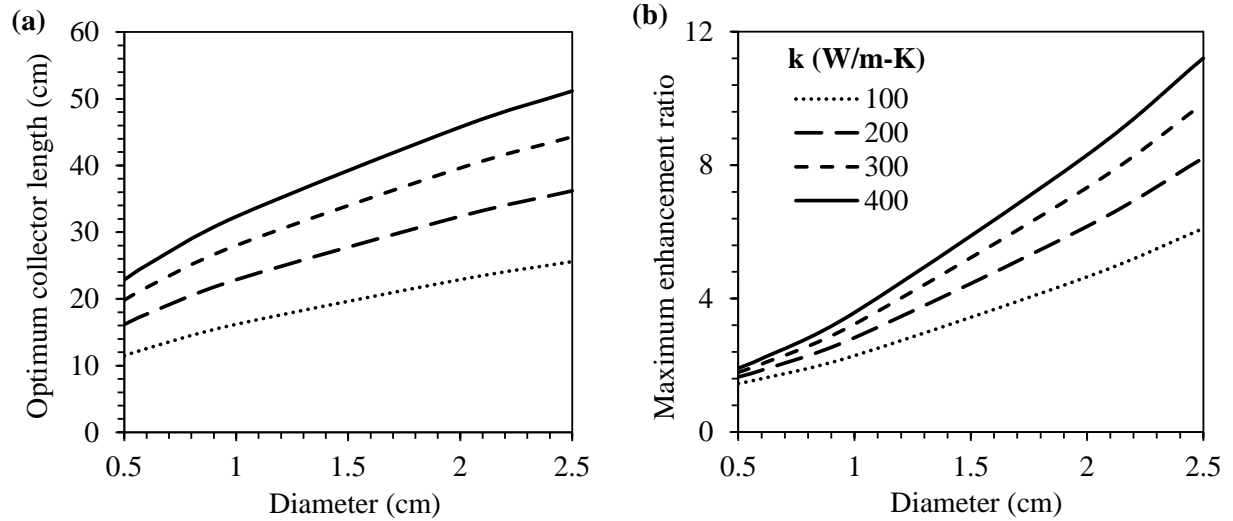


Figure 12: Variation of (a) optimum collector length, and (b) maximum enhancement ratio as a function of rod diameter for materials with different thermal conductivities

Table 3: Predicted values of rod dimensions based on required enhancement ratio

ER	4			
Thermal conductivity (W/m-K)	100	200	300	400
Rod diameter (cm) [Fig. 13(b)]	1.75	1.4	1.2	1.1
Optimum rod length (cm) [Fig. 13(a)]	21.4	27	31	34

### 3.4. Case Study 4: Effect of fuel type

The enhancement ratio in fuel vaporization and burning due to the refluxer depends on the type of fuel considered in the pool fire. The important thermo-physical properties of the fuel are thermal conductivity, specific heat and saturation temperature. The overall effect of these properties can be analyzed by varying the sink temperature. The optimum rod length for sink temperatures varying from 350 K to 500 K is shown in Fig. 13(a). The enhancement ratios for these cases are seen to almost coincide for the different case as shown in Fig. 13(b). The enhancement is evaluated based on baseline mass loss rate of 0.11 g/s [2]. Further, the effect of latent heat of vaporization is considered. Figure 14(a) shows the optimum length of an aluminum collector as a function of rod diameter when effective flame temperature is 800 K, and sink temperature is 450 K. The plots are seen to coincide for different fuels as the optimum

collector height is function of the refluxer properties. Figure 14(b) shows the variation in the maximum enhancement ratio for different fuels, as shown by varying the latent heat of vaporization. It is seen that the enhancement ratio is lower for fuels with higher requirement of latent heat.

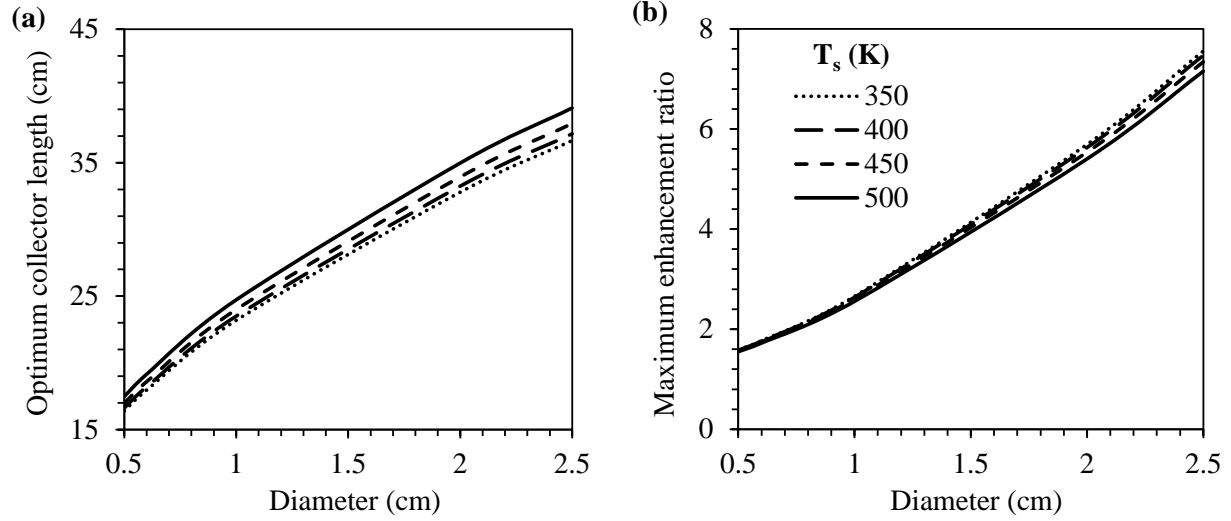


Figure 13: Variation of (a) optimum collector length, and (b) maximum enhancement ratio as a function of rod diameter for different sink temperatures

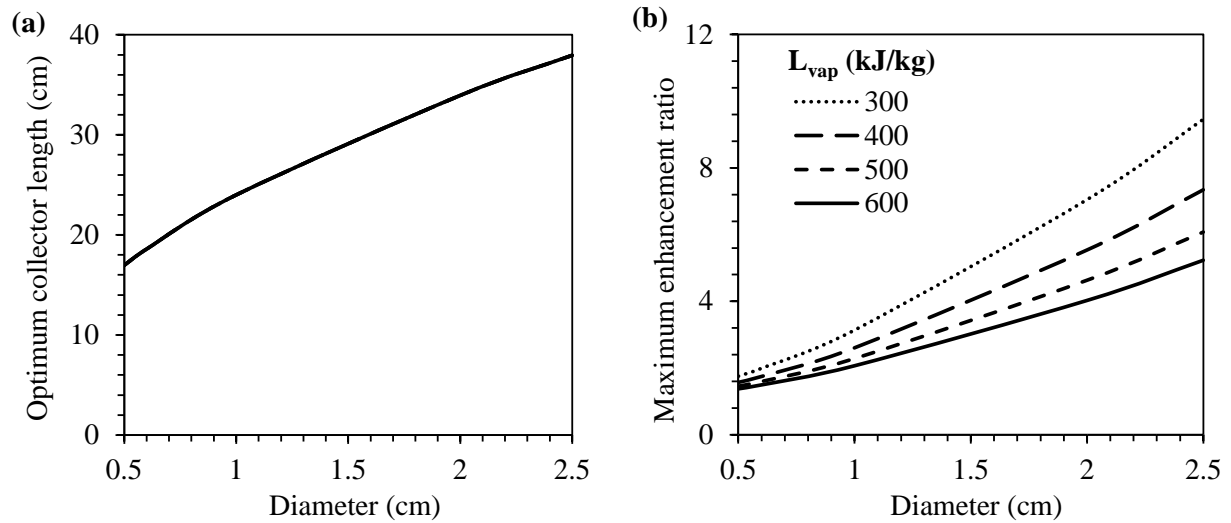


Figure 14: Maximum enhancement ratio for different latent heat of vaporization of fuels

### 3.5. Case Study 5: Inverse design of collector

Case studies 1 and 2 dealt with the prediction of enhancement in mass loss rate for a given collector dimension. This model can also be used to design a collector based on the maximum enhancement. From Fig. 3(b), it is seen that  $T_L^* \rightarrow 1$  when  $\eta \sim 2.5$  and this can be considered an optimal value for collector design. Considering this,

$$\eta = L_c \sqrt{\frac{\sigma \varepsilon P (T_f^4 - T_s^4)}{kA (T_f - T_s)}} \Rightarrow L_c \sim 2.5 \sqrt{\frac{kA}{h_R P}},$$

where  $h_R$  is the linearized radiation heat transfer coefficient defined as  $h_R = \sigma \varepsilon \frac{(T_f^4 - T_s^4)}{(T_f - T_s)}$ . The

corresponding  $Q^*$  for this value of  $\eta$  is about 2.8. The sink temperature is assumed to be about 450 K. The variation of the optimum collector length for an aluminum refluxer with the diameter or side length are shown in Figs. 15(a) and 15(c) for refluxers with circular, and square cross-sections respectively. It is seen that the optimum length is same for circular and square cross-sections. This is because the value of  $P/A$  is one-fourth of the characteristic length for both the cross-sections. The plots are also shown for different effective flame temperatures and it is seen that even a smaller collector is able to attain high ER values at higher flame temperatures.

Figs. 15(b) and 15(d) show the enhancement in the mass loss rate of hexane (considering a baseline mass loss rate of 0.11 g/s [2]). The enhancement ratio is given by,

$$ER = 1 + \frac{\dot{Q}_{C-H}}{\dot{m}_{baseline} L_{vap}} = 1 + \frac{2.8 \times kA (T_f - T_s) / L_c}{\dot{m}_{baseline} L_{vap}}$$

It is seen that for same characteristics dimensions, a square shaped refluxer shows better enhancement in the mass loss rate as shown in Fig. 15(d). This is due to higher surface area for a square refluxer.

Consequently, a plate type refluxer is envisioned. The plate is designed to match the enhancement ratio of the square refluxer. To accomplish this, a 2.5 cm thick plate is chosen such that the maximum enhancement ratio is about 20 when the effective flame temperature is 1000 K. Fig. 15(e) shows the variation of optimum collector length with its width for the aluminum plate and Fig. 15(f) shows the enhancement ratio for the plate. Table 4 shows the predicted values of refluxer dimensions based on ER of 8, and flame temperature of 800 K.

Table 4: Predicted values of refluxer dimensions based on required enhancement ratio

<b>ER</b>	8
-----------	---



<b>Refluxer type</b>	Circular rod	Square rod	Plate
<b>Diameter / Width (cm)</b>	2.4	2.01	1.6
<b>Optimum rod length (cm)</b>	37	34	38

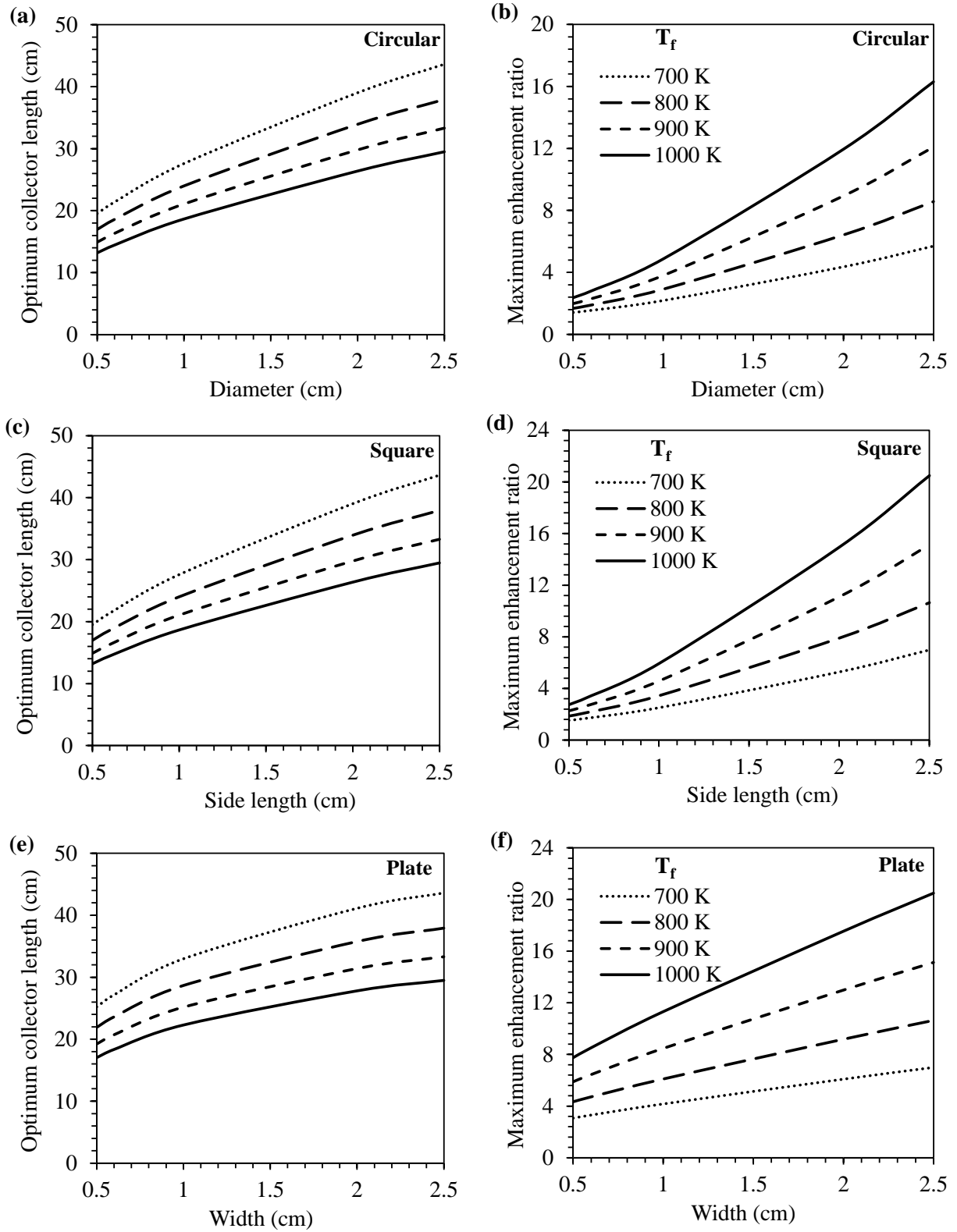


Figure 12: Variation of optimum collector length and maximum enhancement ratio as a function rod diameter for (a), (b) circular cross-section, (c), (d) square cross-section, (e), (f) plate refluxer

#### 4. CONCLUSIONS

The effect of refluxers in pool fires is analyzed using a heat transfer based model. Steady state energy equation is solved for the collector region of a the refluxer. The model solution has been used to define non-dimensional parameters based on the governing input (refluxer and fuel properties) and output characteristics (collector output, temperature distribution). These parameters have been correlated using polynomial fits which can be easily used to predict the refluxer effectiveness and enhancement in the mass loss rate. Further, the model has been used to analyze the effect of collector dimensions, multiple refluxers, refluxer material, and fuel type. The results have also been compared to experimental results from literature. Additionally, an inverse design approach is formulated where the optimized refluxer dimensions are predicted based on the collector output required.

#### REFERENCES

- [1] Rangwala, A.S., Shi, X., K.S. Arsava, G. Mahnken, Methods and Systems for Clean-up of Hazardous Spills, U.S. Patent No. 9772108, 2017.
- [2] Rangwala, A.S., Arsava, K.S., Mahnken, G., Shi, X., A Novel Experimental Approach to Enhance Burning of Oil-Water Emulsions by Immersed Objects, WPI & BSEE, Worcester, 2015. (<https://www.bsee.gov/sites/bsee.gov/files/research-reports//1049aa.pdf>)
- [3] Arsava, K.S., Sezer, H, Tukaew, P, Borth, T.J., Petrow, D.J., Kozhumal, S.P., Mahnken, G., Zalosh, R.G., Torero, J.L., Rangwala, A.S., Hansen, K.A., Fields, S., Chuck Clark, L.C., Stone, K., Laikin-Credno, C., New Technology for Enhanced Burning of Oil Slicks, WPI & BSEE, Worcester, 2017. (<https://www.bsee.gov/sites/bsee.gov/files/research-reports//1068aa.pdf>)
- [4] Arsava, K.S., Raghavan, V., and Rangwala, A.S., 2018, Enhanced oil spill clean-up using immersed thermally conductive objects, *Fire Technology*, 54(6), pp.1745-1758.
- [5] Fang, J., Zheng, S., Wang, J., Wang, K., Shah, H.R., and Wang, J., 2019, An analysis of heat feedback effects of different height embedded plates on promotion of pool fire burning using a variable B number, *International Journal of Thermal Sciences*, 145, p.106041.
- [6] Sezer, H., Arsava, K.S., Kozhumal, S.P., and Rangwala, A.S., 2017, The effect of embedded objects on pool fire burning behavior, *International Journal of Heat and Mass Transfer*, 108, pp. 537-548.
- [7] Arsava, K.S., Raghavan, V., and Rangwala, A.S., 2018, Enhanced oil spill clean-up using immersed thermally conductive objects, *Fire Technology*, 54(6), pp.1745-1758.
- [8] Pi, X., Chang, L., and Rangwala, A.S., 2021, The burning rate of a pool fire increased by bubble behaviors during nucleate boiling, *Fire Safety Journal*, 120, p.103097.

## APPENDIX – B

### Burning behavior analysis in meso- and large-scale oil slick fires with and without waves using Outdoor Gas Emission Sampling (OGES) system

#### Abstract

A new Outdoor Gas Emission Sampling (OGES) system was developed to serve as a low-cost alternative to expensive industrial gas sampling equipment. This research showed its effectiveness in sampling a smoke plume from multiple points simultaneously, obtaining gas concentration regression curves for common products of combustion such as CO<sub>2</sub> and CO in meso-scale experiments. The optimal height for combustion product sampling was determined based on a variety of factors, most notably CO/CO<sub>2</sub> ratio, which showed to be most consistent when located in the intermittent and plume regime of the McCaffrey plume. Large-scale field tests at U.S. Army Cold Regions Research and Engineering Laboratory (CRREL) in collaboration with the Environmental Protection Agency (EPA) demonstrated the potential of using the OGES system to evaluate the completeness of combustion for various fuels in a variety of settings. OC and CDG methods versus plume theory results show the potential of using point sampling within a smoke plume to estimate HRR for fires that exceed the capabilities of conventional calorimeters.

#### 1. Introduction

Heat release rate (HRR) is one of the most critical parameters in fire hazard evaluation [1]. Knowledge of HRR allows for further estimation of burning efficiency, convective and radiative losses, and emissions such as smoke and by-products, which may be harmful to the environment. Tsuchiya [2] summarizes multiple methods for determining HRR. The first is via thermal methods, which allows calculation of HRR based on specific heat ( $c_p$ ), temperature rise ( $\Delta T$ ), and mass flow rate of flue gases ( $\dot{m}$ ). The second is through gas analysis methods, which require the mass flow rate of air, fuel, and exhaust gases through a control volume. Another common method is shown in SFPE Handbook (SFPE HB) [3] using the product of mass burning rate ( $\dot{m}_{F,s}$ ) and heat of combustion ( $\Delta H_c$ ). Heat of combustion ( $\Delta H_c$ ) is defined as the enthalpy change because of reactants (fuel + oxygen) converting to products (CO<sub>2</sub> + H<sub>2</sub>O) through the process of combustion. This enthalpy change is assumed to be captured by change in  $c_p \Delta T$ . This sensible heating of air, expressed through  $c_p \Delta T$ , can be further expressed as  $\Delta H_c$ . As a result, heat of combustion is often studied and reported for different types of fuels and length scales [3].

One of the most commonly used apparatuses for quantifying HRR is through product gas calorimetry following ASTM E1354 [4]. It is used to evaluate various characteristics of materials such as HRR, effective heat of combustion, mass loss rate, and soot production. This is achieved with a gas analyzer, differential pressure probe, thermocouple, helium-neon laser, and load cell within the apparatus. The gas analyzer analyzes concentrations of combustion products within the

exhaust product stream such as CO<sub>2</sub>, CO, and O<sub>2</sub>. The differential pressure probe calculates the flow rate of exhaust product stream within the control volume. The thermocouple measures the temperature of the exhaust product stream. The helium-neon laser is part of a smoke obscuration measuring system that analyzes soot production. The load cell monitors mass loss rate of the burning sample, in turn obtaining mass burning rate ( $\dot{m}_{F,s}$ ).

Heat release measurements using this apparatus are based on oxygen consumption calorimetry [2][5], which is an HRR quantification technique that relies on a controlled indoor laboratory environment where there is an accurate sampling of the exhaust gases. This method utilizes the assumption that a constant amount of heat is released per unit mass of oxygen consumed, which is 13.1 kJ/g as demonstrated in a study by Huggett [6]. This is referred to as Oxygen Consumption (OC) calorimetry. Based on the formulation by Tewarson, Factory Mutual (FM) Global [3] developed a similar calorimetry method in the 1970s but instead focused on the generation of CO<sub>2</sub> and CO. In this method, HRR can be calculated from the amount of CO<sub>2</sub> and CO produced; this is referred to as Carbon Dioxide Generation (CDG) calorimetry. For simple organic compounds, Khan et al. [3] give average energy release constants for CO<sub>2</sub> and CO to be 13.3 kJ/g and 11.1 kJ/g respectively.

However, due to the variables required to establish HRR, this limits the size of the design fire because the entirety of the smoke plume needs to be collected to analyze the concentrations of the various exhaust gases. An amount of make-up air also needs to be provided to the burn space that is equivalent to the exhaust mass flow being extracted out the exhaust duct of the calorimeter hood. Cooper [9] states the ideal exhaust mass flow should be equal to the total mass flow of the plume for accuracy purposes.

Worcester Polytechnic Institute (WPI) possesses a large calorimeter capable of measuring a 5 MW fire at steady-state and upwards of 15 MW intermittently. National Institute of Standards and Technology (NIST) and Factory Mutual (FM) Global currently have the largest known commercial calorimeters in the US capable of measuring a continuous 20 MW fire for up to four hours, with a hood covering dimensions of 13.8 m by 15.4 m [7]. In many cases, larger fires are required to simulate realistic fire scenarios, such as in-situ burning (ISB) of crude oil in outdoor conditions, therefore rendering a cone calorimeter setup to be impractical as the plume cross-sectional area is expected to exceed several meters [8]. Assuming an oil spill with a burn area of 100 m<sup>2</sup>, with a burning regression rate of 4 mm/min, this corresponds to a fire of around 143 MW. Cooper [9] discussed the amount of make-up air needed in an ideal calorimeter hood design based on correlations by Heskestad [10]. For a design fire of this magnitude, the estimated amount of make-up air for the burn space would be around 450 m<sup>3</sup>/s. At present, the world's largest air compressor is capable of 277 m<sup>3</sup>/s. Both diameter and HRR of this expected fire far surpass the capabilities of any known calorimeter. This current knowledge gap is where improving a method for gas emissions point sampling to estimate HRR becomes valuable.

Previous studies by Tukaew [11] and Tukaew et al. [12] at Worcester Polytechnic Institute (WPI) were performed using an early design of the Outdoor Gas Emission Sampling (OGES) system to utilize point sampling within a smoke plume from a crude oil fire. A windsock covering a large metal frame with a gas sampling ring, differential pressure probe, and type-K thermocouple was mounted on an 8 m tall tower structure to serve as the singular gas sampling point. A pulley system was incorporated to maintain the windsock within the smoke plume as much as possible. The gas sampling ring was connected to a SERVOMEX 4200 industrial gas analyzer to record the gas concentration data. Field tests performed at U.S. Navy's Naval Research Laboratory (NRL) in Mobile, Alabama showed promise of the OGES system but also indicated the need for improvements in the sampling system design to systematically study completeness of combustion and possibly HRR.

A proper understanding of combustion product spatial distribution within a smoke plume is required to evaluate the applicability of point sampling on estimating burning efficiency and HRR. However, prior knowledge in this aspect is somewhat lacking. Previous studies regarding combustion production spatial distribution have been centered towards indoor scenarios related to tenable conditions for occupants [13], but little research has been performed outside this specific application. Early studies by McCaffrey [14] showed temperature and velocity distribution curves along the radial direction within a smoke plume, but no data regarding combustion product concentrations were published. Sibulkin and Malary [15] published concentration profiles of CO<sub>2</sub> and CO to study the completeness of combustion in MMA wall fires, but the focus was centered on the change in peak CO<sub>2</sub> and CO concentrations when varying the amount of oxygen on the fuel side of the flame. Tsuchiya [2] also published values for CO/CO<sub>2</sub> ratios in well-ventilated conditions, such as ASTM HRR apparatus and E-84 tunnel tests, but did not elaborate further on the practicality of such values.

The Environmental Protection Agency (EPA) has published many findings relating to gas emissions in outdoor fires [16 - 18]; however, the focus of such publications was related to particulates (PM) and other toxic substances released from such fires and not the completeness of combustion or HRR, which is the focus of this study. Hariharan et al. [19] observed particulate-matter emissions from liquid pool fires and fire whirls, however, similar to EPA, they emphasized cumulative release of carbon emissions (CO<sub>2</sub>, CO, and PM) rather than real-time emissions sampling.

## **2. Experimental setup and methods**

### *2.1 Setup*

#### *2.1.1 Sampling apparatus design*

The original iteration of the OGES system developed by Tukaew [11] and Tukaew et al. [12] utilized a flexible windsock attached to a rigid metal frame, which would alleviate issues of combustion product accumulation within the sampling apparatus. This would allow for the

differential pressure probe within the windsock to obtain a more accurate measurement of the mass flow rate through the control volume. The wind sock and frame were mounted to a pulley system which allowed for height adjustments to account for shifting winds. All gases gathered within the wind sock were transported via tubing to an industrial gas analyzer (SERVOMEX 4200 Industrial Gas Analyzer) to determine the real-time concentrations of the combustion products. It has an effective measurement range of 0 – 2.5% for CO<sub>2</sub>, 0 – 1% (0 – 10,000 ppm) for CO, and 0 – 25% for O<sub>2</sub>.

However, using the wind sock frame and gas analyzer for gas analysis and velocity measurements required long sampling tubes and wires, as well as exceeding 30 kg in weight. Furthermore, the primary assumption made for the wind sock design was that the control volume within the wind sock had the same gas concentrations as the entirety of the smoke plume. This assumption necessitates an empirical correction factor applied to mass flow rate calculations to account for the entire plume

One method of avoiding the use of an empirical correction factor is by using multiple sampling points, the control volume and gas analysis equipment needed to be designed in a way that required lower cost than using multiple industrial gas analyzers. The elimination of long tubes and wires was also desirable; because future research with multiple simultaneous sampling points would be made more convenient with wireless monitoring that could be performed remotely. This triggered a new iteration of the OGES system.

A new portable design was conceived as a substitute for the industrial gas analyzer, as well as the removal of the wind sock entirely. Small, portable sensors for CO<sub>2</sub> (GasLab TX 20% CO<sub>2</sub> Sensor), CO (GasLab AlphaSense CO-AF Sensor), and O<sub>2</sub> (GasLab TX 25% Oxygen Sensor) were purchased and placed within a sealed chamber. The measurement ranges were comparable to that of the industrial gas analyzer used in the previous iteration of the OGES system.

To prevent soot, water vapor, and other contaminants from entering the sensor module and affecting measurements, a sampling train with the proper filters was used. The first filter, referred to as coarse particle filter, was a polyester air filter foam often used in HVAC systems. These filters are designed to filter dust, dander, spores, and mold; and preliminary burn tests showed that they were very effective in filtering out the majority of soot particles. The foam was placed in a column to ensure that the entire system remained sealed and ambient air would not leak into the system. A 10 µm soot filter, or fine particle filter, was connected after the foam to filter any remaining particulates. Finally, calcium sulfate desiccants (Drierite) were used to filter out water vapor produced by the fire before the connected air pump (4.4 lpm) would transport the gases to the gas sensor module. This air pump had the same flow rate as the one used in the studies by Tukaew [11] and Tukaew et al. [12]. Fig. 1(a) shows a flow diagram for the new OGES system; Fig. 1(b) and (c) show a prototype of the gas sensor module and filter train used throughout the experiments.



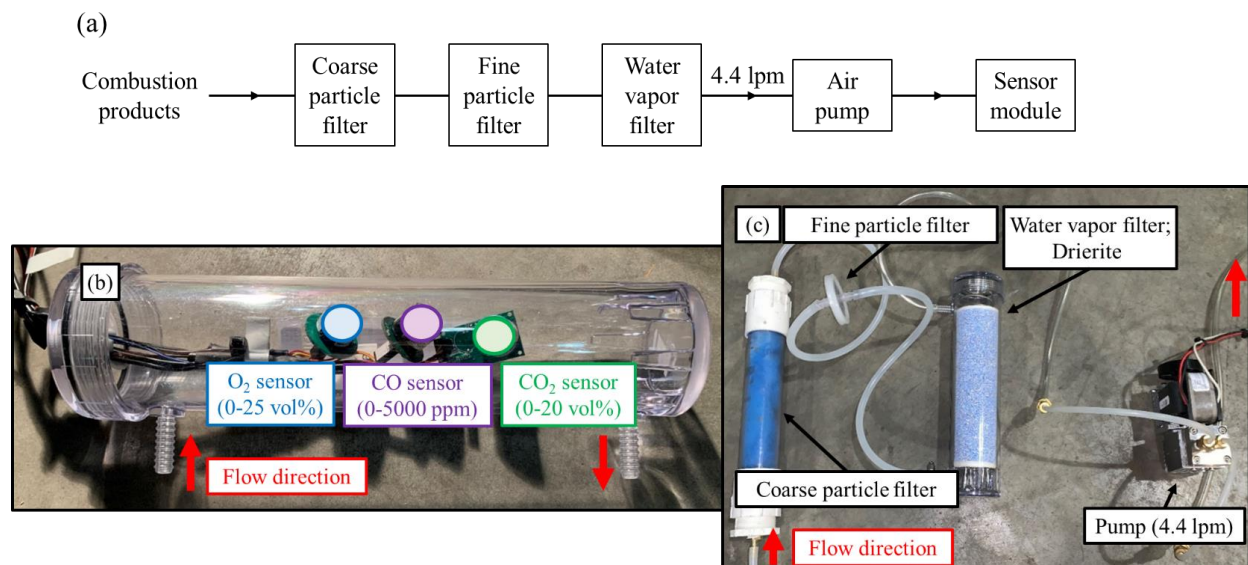


Fig. 1. New OGES system

(a) Flow diagram (b) Gas sensor module with CO<sub>2</sub>, CO, and O<sub>2</sub> sensors (a) Filter train.

Notable improvements over Tukaew [11] and Tukaew et al. [12] include size and weight, overall portability, and cost. The newfound portability of the new OGES system allowed for the gas sampling ports to be fixated on any structure without the worry of compromising its integrity, as there is a 50-fold decrease in overall system weight. Another scenario was to place sampling ports within a crane (or zip line when the crane was unavailable) as shown in Fig. 4. The crane would maneuver to sample the smoke plume continuously even during wind shifts in outdoor fires. This advantage was only made possible by the size and weight reduction of the new OGES system. Another limitation to the original OGES system was the singular sampling point. To achieve improved results for the development of a combustion product spatial distribution model, more simultaneous sampling points are required. However, industrial gas analyzers are expensive and therefore make it impractical to purchase multiple systems while also being hindered by their lack of mobility. The use of low-cost, portable gas sensors decreases the cost of equipment by 20-fold compared to an industrial gas analyzer, which allows for simultaneous deployment of multiple systems.

One of the most important factors to validate beforehand was the accuracy of the portable sensors compared to industrial equipment. Fig. 2 shows a validation burn experiment (75 cm pool fire) using the new OGES system with the existing SERVOMEX industrial gas analyzer. Plots show that these portable gas sensors provide readings that are in good agreement with industrial equipment at gas concentrations around this range. Therefore, results reported in the latter portion of this study will be concentrations obtained from the portable sensor readings.

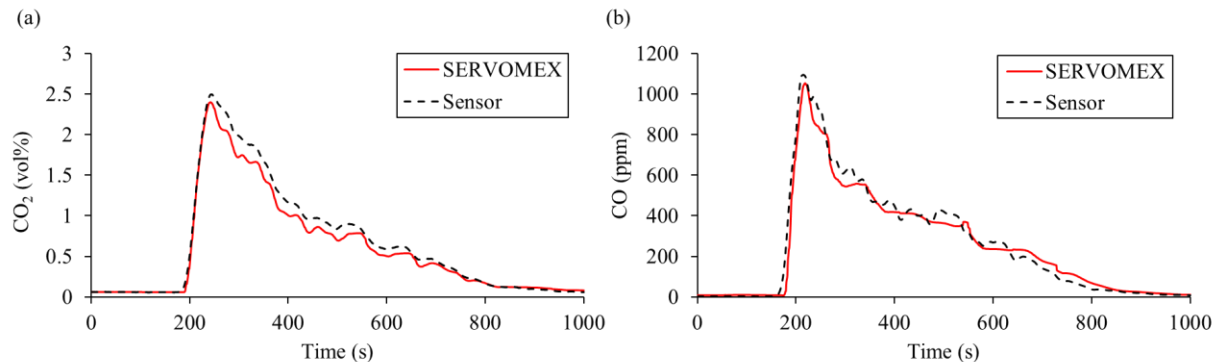


Fig. 2. Validation burn experiment (a) CO<sub>2</sub> (b) CO. Pool diameter = 75 cm; Fuel = ANS crude oil; Initial fuel thickness = 5 cm; Fuel volume = 22 L; Sampling height = 1.5 m above pool surface.

## 2.2 Experimental methods

### 2.2.1 Combustion product spatial distribution study

Meso-scale burn experiments were designed to investigate the spatial distribution of certain combustion products such as CO<sub>2</sub> and CO within a smoke plume. A burn pan of 75 cm in diameter was placed on a load cell to obtain mass loss rate. Two types of fuel were used for these experiments: ANS crude oil and 87-octane regular gasoline. The fuel volume was 22 L, which equaled an initial fuel thickness of 5 cm

The indoor laboratory environment at WPI provided a vertical plume that was undisturbed by wind, therefore six to nine sampling locations along the centerline of the plume could be studied simultaneously. This aspect of a vertical plume in tandem with centerline sampling points allowed for additional validation of sensor readings with plume theory correlations [3] to obtain HRR.

Fig. 3 illustrates the sampling locations throughout this series of experiments. Nine sampling locations were selected for the ANS crude oil experiments. Three repeat experiments were performed for all locations to ensure repeatability of gas concentrations at specific heights above the pool surface. Experimental results discussed later include standard deviation for different heights above the pool surface.

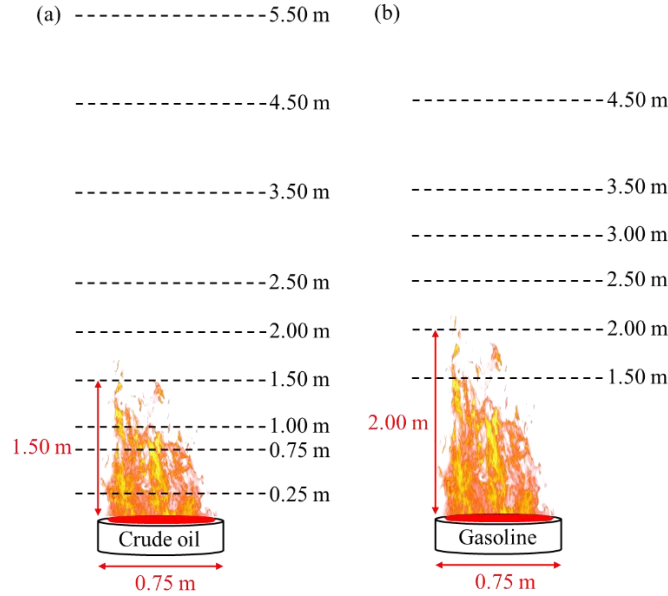


Fig. 3. Sampling locations for meso-scale 75 cm burn experiments  
(a) ANS crude oil (b) 87-octane regular gasoline.

### 2.2.2 Large-scale field study

A large-scale field study was performed at U.S. Army Cold Regions Research and Engineering Laboratory (CRREL) in a large wave tank with a burn area of 1.9 m by 1.7 m. Two types of fuel were burned in the field trials: HOOPS crude oil and bunker fuel. The fuel was burned floating on top of water bound by a boom. Fuel volumes for HOOPS crude oil and bunker fuel were 260 L and 32 L respectively, equating to respective initial fuel thicknesses of 8 cm and 1 cm. Three wave profiles were used in the experiments (wave period; wave height): Wave 1 – 2.5 s, 7 cm; Wave 2 – 4 s, 14 cm; Wave 3 – 1 s, 4 cm. Wave 1 and 3 were faster but shorter waves; Wave 2 was slower but taller. The OGES system was set up in an attempt to continue research of completeness of combustion for various fuels, as well as estimate HRR based on gas concentration readings. The main purpose of the parametric study with the presence of waves was to investigate the influence of waves on emissions; this was to see if using the same methods to calculate HRR for wave cases would yield a similar agreement to cases with no waves.

Similar to the meso-scale experiments, the large-scale nature of the CRREL field trials piqued interest in combustion product distribution at different heights above a fire. A sampling point on the superstructure at 2.80 m above the pool was selected as the sampling point. This sampling location was chosen based on the presence of an existing Thermocouple (TC), which allowed for gas emission data to be compared to temperature data during data analysis. The superstructure above the pool will be referred to as TC tree in the subsequent text; this sampling point is denoted as OGES TC tree.

EPA was present for several burn experiments to perform burn emission sampling with the aid of a crane at locations much higher than the TC tree. In light of this, another sampling point was added in the crane to provide an additional data set for the WPI studies and collaborate with EPA data when needed, denoted OGES Crane. The concept of crane sampling is similar to the studies by Tukaew [11] and Tukaew et al. [12]. However, fixating the sampling point on the crane was only made possible as a result of decreased size and weight of the new OGES system.

To visualize the overall setup, Fig. 4(a) shows an overview of the layout at CRREL, while Fig. 4(b) is a side view. The sampling tube for the OGES TC tree was connected to the filter train and gas sensor module located within a control shed next to the wave tank. In addition, this control shed housed the data logging equipment for the gas sensor data, temperature data, and controller for the wave tank paddle. On the other side of the wave tank was the EPA station where EPA personnel were situated during burn experiments to monitor data streams. Fig. 5(a) shows an overview photo of the wave tank; Fig. 5(b) shows a detailed photo of the OGES TC tree sampling point. The OGES Crane sampling point, as shown in Fig. 6, was connected via sampling tube to gas sensor data logging equipment located in the EPA station. Table 1 summarizes the locations of the sampling points relative to the fuel surface.

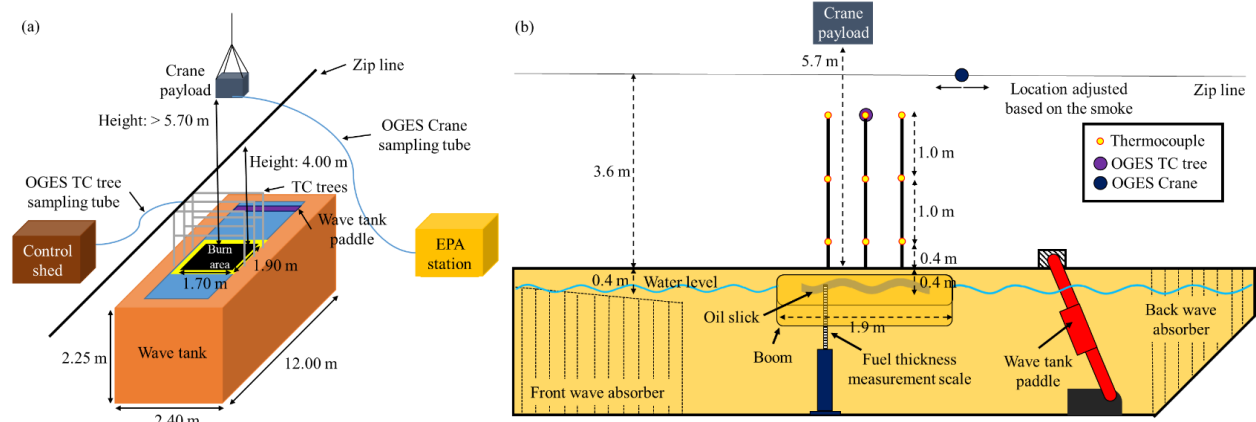


Fig. 4. Diagram of layout and OGES system connections at CRREL (a) Overview (b) Side view.

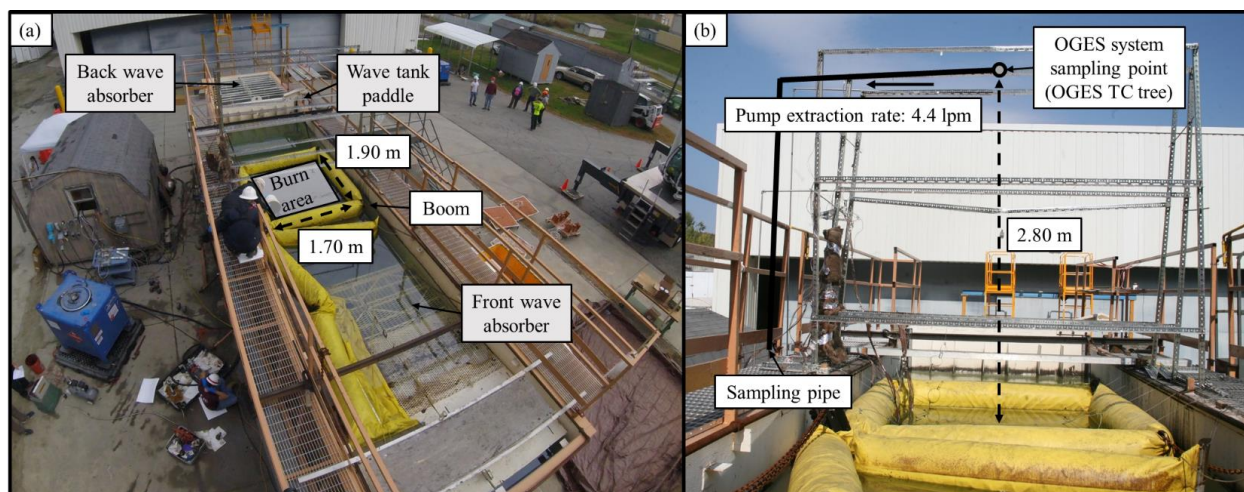


Fig. 5. OGES system setup on (a) TC tree (b) Crane.

Table 1. OGES system sampling points for CRREL experiments.

OGES system sampling point	Location
TC tree	<b>Height:</b> 2.80 m <b>Position:</b> Centerline
Crane	<b>Varies:</b> Crane operator attempts to maintain payload within smoke plume as much as possible

A main source of concern would be the difference in tube length, especially the TC tree sampling point versus the crane sampling point, which would result in different time delays recorded by the data logging equipment. This concern was alleviated by comparing the gas sensor data to the temperature data to consider the amount of time delay within the sampling lines.

Out of five total experiments, EPA personnel and the crane operator were only present for two experiments. For subsequent experiments, a zip line was mounted at the facility to mimic the crane as much as possible. The OGES Crane sampling point was fixed to this zip line at a height of 4.00 m above the pool surface, the highest possible height at this facility. A string of metal wire was used to pull OGES Crane along the zip line to maintain its presence within the smoke plume during wind shifts. The location of the zip line is shown in Fig. 4.

A more detailed photograph of the sampling point for OGES Crane as well as the sampling rigs used by EPA, called the Flyer, is shown in Fig. 6. The OGES system sampling tube is fixated on an aluminum frame next to the Flyer, while its tip is reinforced with a barbed metal hose connector to ensure the tip does not deform and collapse in the case of higher temperatures when the crane moves to close proximity of the flames. The Flyer was developed in-house by EPA and can measure CO<sub>2</sub>, CO, PM<sub>2.5</sub> (particulate matter of mass median diameter 2.5 μm or less), Black Carbon (BC), total carbon/organic carbon/elemental carbon (TC/OC/EC), polycyclic aromatic



hydrocarbons (PAHs), volatile organic compounds (VOCs), and polychlorinated dibenzo-p dioxins/polychlorinated dibenzofurans (PCDD/PCDF) from the smoke plumes. As shown in the previous figure, the sampling instrumentation was suspended and maneuvered via crane into the smoke plume with guidance from the Flyer's operator, who monitored real-time temperature and CO<sub>2</sub> levels. In particular, this study compared measured CO<sub>2</sub> and CO values with EPA.

The main goal of EPA was the accumulation study of toxic gases and particulates throughout a burn experiment, while the OGES system was focused on real-time gas emissions sampling. The Flyers were limited by the capacity of the particulate filters, and sampling would need to be terminated once the filters were saturated, which was around 45 min. One of the advantages of the OGES system over the Flyers is that it only measured gas emissions, and therefore the setup of a coarse and fine particulate filter could allow for continuous sampling of burns that well exceeded 60 min. Moreover, the Flyers needed to be maintained under 50°C for equipment longevity purposes, therefore the crane held the payload at an average height of 5.70 m above the pool surface, as shown in Fig. 4. A clear disadvantage of this is the susceptibility to non-continuous sampling caused by sudden wind shifts. Experimental results discussed later will also show that gas sampling at this distance may lead to results that are not representative of the actual burning behavior. This is another advantage of the OGES system in that it was much more flexible in terms of system placement compared to the Flyers, even near flames. **(PERHAPS DR. GULLETT CAN PROVIDE SOME FURTHER DETAILS REGARDING THE FLYERS AND CLARIFY THE MAXIMUM SAMPLING TIME)**

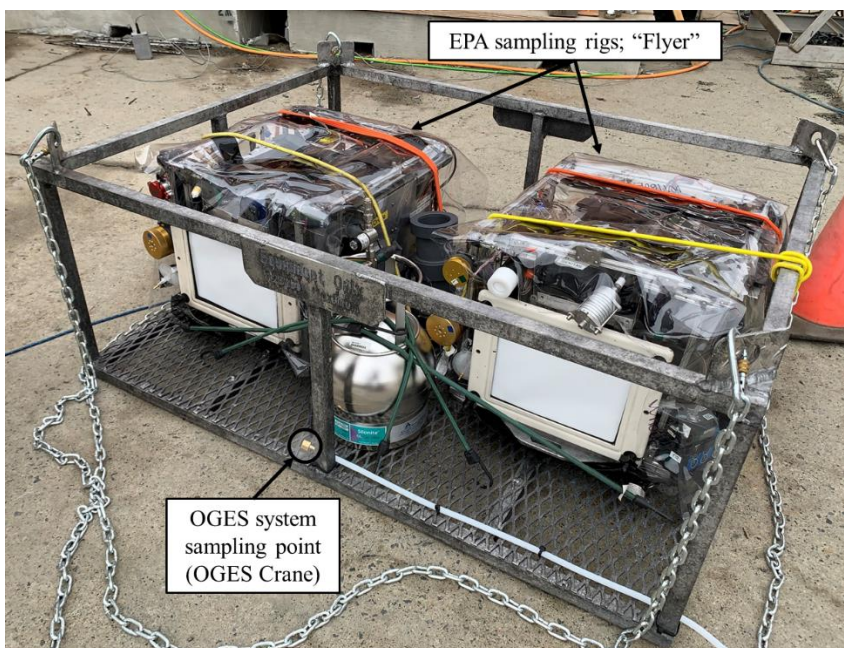


Fig. 6. Detailed depiction of OGES system and EPA setup on the crane.

### 3. Results and discussion

### 3.1 Meso-scale 75 cm indoor experiments

#### 3.1.1 Combustion product spatial distribution

Fig. 7 shows the vertical distribution along the centerline for CO<sub>2</sub> and CO emissions for the meso-scale 75 cm burn experiments. Fig. 7(a) shows the results for ANS crude oil and Fig. 7(b) for 87-octane gasoline. Heights below 1.00 m were omitted as a result of being in too close proximity to the base of the fire, yielding concentrations that exceeded the capabilities of the gas sensors and industrial gas analyzers. The shaded regions correspond to the intermittent zone defined by McCaffrey [14][20]. This will be important in a later discussion regarding HRR.

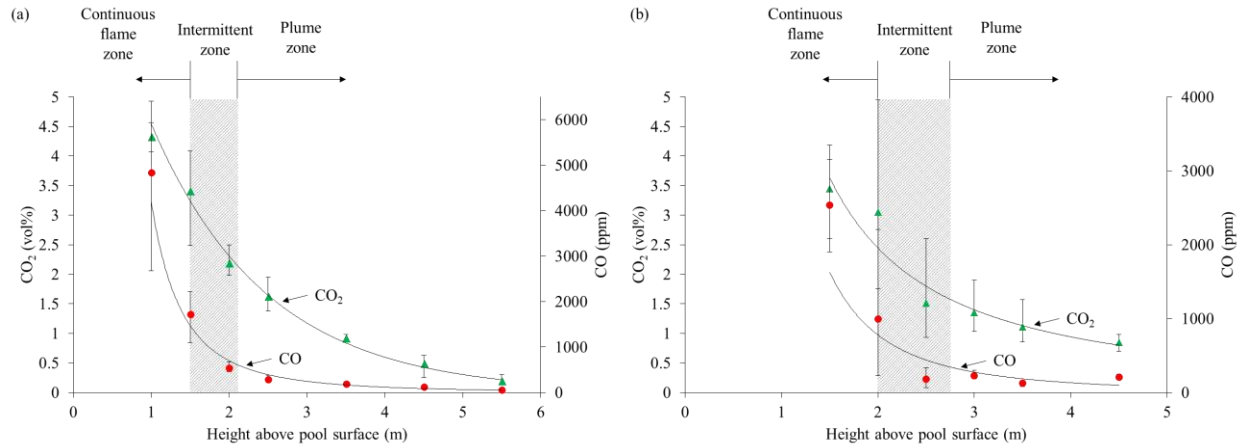


Fig. 7. Vertical distribution of CO<sub>2</sub> and CO concentrations within the smoke plume of 75 cm pool fire

(a) ANS crude oil (b) 87-octane gasoline.

Interestingly, trends for both types of fuels are similar with respect to vertical distance from the pool surface, but the trends between CO<sub>2</sub> and CO are drastically different. Observations for both ANS crude oil and 87-octane gasoline show concentration of CO<sub>2</sub> seems to decrease in a relatively linear fashion with respect to height, while CO concentration decreases exponentially. Since this trend is consistent for both types of fuel, observations suggest this trend is species-specific and not fuel-specific. This is elaborated further in the large-scale experiments at CRREL when discussing the validity of OGES TC tree and OGES Crane data.

#### 3.1.2 CO/CO<sub>2</sub> ratio

Another method for burning behavior analysis is the comparison of CO/CO<sub>2</sub> ratio. Before comparing between data sets, the CO/CO<sub>2</sub> ratios at different heights along the centerline of a smoke plume should be evaluated to determine the optimal sampling point above a fire that will serve as



a basis for further burning behavior analyses. Table 2 and Fig. 8 show the CO/CO<sub>2</sub> ratios for a 75 cm pool fire using ANS crude oil and 87-octane gasoline at the different sampling heights mentioned in the previous section. Normalized plots are shown in Fig. 8 by dividing sampling height over observed flame height.

Table 2. Average CO/CO<sub>2</sub> ratio at different heights above pool surface for 75 cm indoor pool fire experiments with two different fuels.

Height above pool surface (m)	ANS Crude Oil	87-Octane Gasoline
1	0.1119 ± 0.07	
1.5	0.0504 ± 0.0042	0.0736 ± 0.0011
2	0.0245 ± 0.0015	0.0327 ± 0.0131
2.5	0.0173 ± 0.0017	0.0121 ± 0.0025
3		0.0169 ± 0.0009
3.5	0.0201 ± 0.0032	0.0116 ± 0.0011
4.5	0.0233 ± 0.0105	0.0241 ± 0.0004
5.5	0.0253 ± 0.0042	

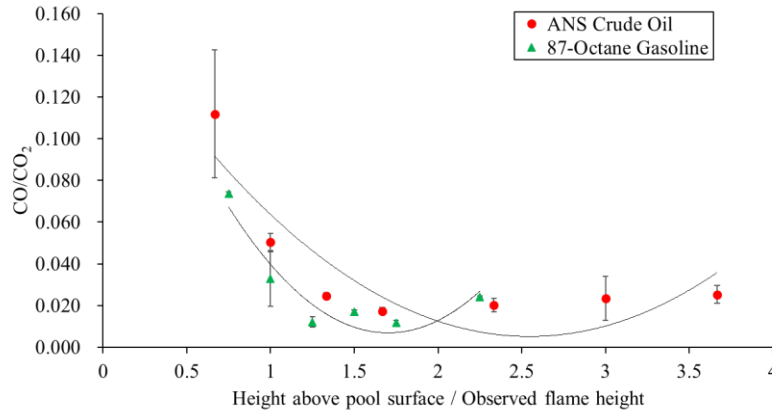


Fig. 8. Summary of CO/CO<sub>2</sub> ratios for 75 cm indoor pool fire experiments with two different fuels.

As indicated in Fig. 3, the flame height for the 75 cm ANS crude oil fire was approximately 1.5 m. Observing CO/CO<sub>2</sub> ratios for ANS crude oil, there is an obvious difference between the values obtained above the flame tip compared to below it. There is a visible decrease in CO/CO<sub>2</sub> ratio once above the flame tip at 1.5 m. This can be attributed to the fact that at heights of 1.5 m and below, it is the continuous flame zone, and therefore ongoing flame chemistry is still a significant factor that is affecting the results of emissions sampling. The standard deviation also reflects this as ongoing combustion results in rapid changing of gas species, and therefore sampled gas concentrations show immense fluctuations between repeat tests.

For 87-octane gasoline, Fig. 3 shows the flame height to be approximately 2 m. With that knowledge, a visible cutoff point past the location of the flame tip is observed once again. Similar to the ANS crude oil cases, the standard deviation between repeat tests is much larger for heights in the continuous flame zone, where combustion is ongoing. In contrast, the standard deviation for heights in the plume zone is rather small.

At heights above the flame tip, where only the smoke plume is present and there are no flames, average CO/CO<sub>2</sub> ratios along the centerline of the fire maintain consistent values between 0.0173 and 0.0253. Even at heights where effects from the ambient environment begin to cause significant dilution of the sampled gas species, the standard deviation is rather small between repeat tests compared to locations in the continuous flame zone. Tsuchiya [2] measured and reported CO/CO<sub>2</sub> ratios from experiments performed in an ASTM HRR apparatus and E-84 tunnel for various solid fuels, such as particleboard, asbestos board, and red oak. Values reported in literature indicate that for well-ventilated indoor scenarios, the three solid fuels mentioned above yielded CO/CO<sub>2</sub> ratios between 0.002 and 0.300. The CO/CO<sub>2</sub> ratios obtained in this study show consistency with values reported by Tsuchiya.

CO/CO<sub>2</sub> ratios maintain rather consistent values above the flame tip; however, it can be observed that the value begins to deviate when the normalized height exceeds 2. The hypothesis from observations is that CO concentration decays exponentially with height, while CO<sub>2</sub> concentration decays in a relatively linear fashion. At heights exceeding two times the flame height, rapid dilution of CO gas may yield results that are not representative of the actual burning behavior.

Using the crude oil and gasoline data sets as a baseline, the optimal sampling heights for meso-scale experiments should be above the flame tip but no more than two times that of the observed flame height. This ensures only gas emissions from the smoke plume are sampled but the effects from ambient dilution are minimized, particularly for CO. This corresponds to the intermittent and plume regime of the McCaffrey plume [14].

### *3.2 Large-scale outdoor experiments at CRREL*

Five burn experiments were performed at CRREL. The first three experiments were performed using HOOPS crude oil to compare between a baseline case and two wave profiles. The latter two experiments consisted of bunker fuel, as well as a third wave profile.

Densities for HOOPS crude oil and bunker fuel were 784 kg/m<sup>3</sup> and 940 kg/m<sup>3</sup> respectively. The three wave profiles are described using wave period and wave height. Wave 1 – 2.5 s, 7 cm; Wave 2 – 4 s, 14 cm; Wave 3 – 1 s, 4 cm.

#### *3.2.1 OGES TC tree data*

OGES TC tree was 2.8 m above the surface of the pool and located at the centerline of the fire. Table 5 is a summary of the combustion product measurements sampled by OGES TC tree throughout the five experiments. For the case of CO<sub>2</sub>, the value is reported after deducting 0.046

vol% from the measured concentration. For CO, this value is 0 vol%. Since there is a consumption of O<sub>2</sub> instead of production, the reported value is obtained after deducting the measured O<sub>2</sub> concentration from 20.80 vol%.

In Table 3, peak values represent the peak amount of gas concentration measured by the OGES system. For CO<sub>2</sub> and CO, it represents the peak amount produced. In the case of O<sub>2</sub>, it represents the peak amount consumed. Average (Avg) values represent sampled gas concentrations averaged over the entire burn experiment.

Table 3. Summary of combustion product concentrations measured at 2.8 m above pool surface.

Fuel	Initial thickness	Wave number	Peak/Avg Produced CO <sub>2</sub> (vol%)	Peak/Avg Produced CO (vol%)	Peak/Avg Consumed O <sub>2</sub> (vol%)	Soot <sup>^</sup> (g)	Regression rate (mm/min)	Burn time (min)	Burn efficiency (%)
HOOPS	8 cm		4.637/1.415	0.460/0.098	7.500/2.081	0.01	1.54	30.0	57
HOOPS*	8 cm	Wave 1	4.540/1.817	0.475/0.118	7.834/2.946	0.10	1.86	42.0	95
HOOPS	8 cm	Wave 2	2.798/1.137	0.299/0.054	5.331/1.685	0.01	1.45	54.0	97
Bunker	1 cm		1.943/0.705	0.106/0.035	2.797/1.107		1.25	5.5	74
Bunker	1 cm	Wave 3	1.122/0.405	0.053/0.019	1.523/0.653	0.02	1.72	6.0	86

\* Rain

<sup>^</sup> Fine particle filter in Fig. 1

Fig. 9 shows the CO<sub>2</sub>, CO, and O<sub>2</sub> concentration curves throughout the entirety of the burn for the first three experiments sampled from by OGES TC tree at 2.8 m above the pool surface. The plots shown were readings from the portable gas sensors.

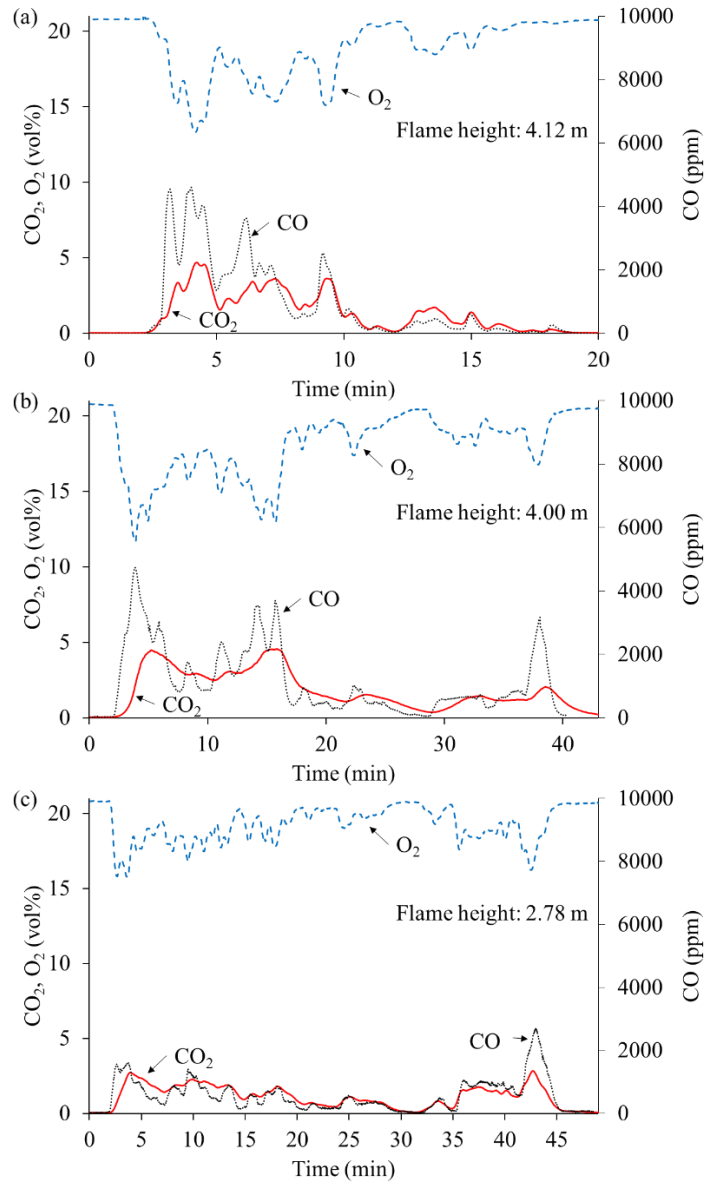


Fig. 9. CO<sub>2</sub>, CO, and O<sub>2</sub> concentration curves throughout the entirety of the burn experiment at 2.8 m along centerline  
 (a) HOOPS crude oil without wave  
 (b) HOOPS crude oil with Wave 1  
 (c) HOOPS crude oil with Wave 2.

Fig. 10 provides timeline photographs to explain the gas concentration curves for Fig. 9(c). At 1 min, there is a very tall initial flame height. This is attributed to the lighter components in the crude oil being burned off in the early stages of the fire. The CO<sub>2</sub> and CO values reflect this as there is a peak at the start of the fire. At 10 min, the flame height has decreased slightly because the fire is now burning slightly heavier components. There is a corresponding decrease in CO<sub>2</sub>, however, CO values have increased because heavier components tend to have a higher degree of incomplete

combustion. At 30 min, oil foaming from boiling water below the oil causes the flames to extinguish temporarily. However, the foam breaks down after a few minutes and the surrounding residual flames allow reignition of the entire pool to occur. At 40 min, there is a steady flame, but the smoke is much thicker and darker compared to earlier photos. At 43 min, the fuel slick is now very thin and allows boilover to occur, resulting in a very tall flame for a short period before complete extinction of the fire.

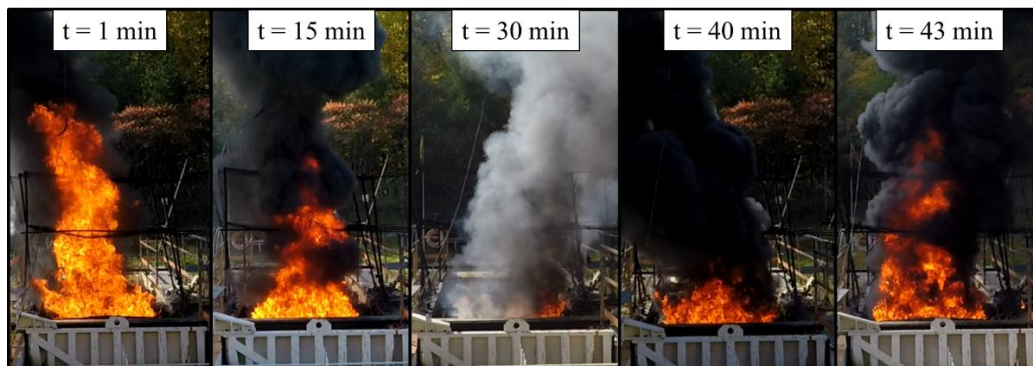


Fig. 10. Timeline photograph of HOOPS crude oil with Wave 2. Flame heights concur with measured gas concentrations at labeled time stamps.

### 3.2.2 OGES Crane data

For the first two experiments, EPA utilized a crane to collect data regarding emissions from outdoor pool fires, specifically particulate matter (PM) and volatile organic compounds (VOC). Similar to this study, EPA also sampled CO and CO<sub>2</sub> concentrations but focused on cumulative amounts rather than concentrations at specific times throughout the burn. For three experiments, the crane was not present and the zip line was used, as shown in Fig. 5. Table 6 is a summary of the combustion product measurements sampled at a height of 4.00 m (zip line) or around 5.70 m (crane) throughout the five experiments. The measurements were not made along the centerline but followed the plume trajectory.

Table 4. Summary of combustion product concentrations measured by OGES Crane.

Fuel	Initial thickness	Wave number	Peak/Avg Produced CO <sub>2</sub> (vol%)	Peak/Avg Produced CO (ppm)	Peak/Avg Consumed O <sub>2</sub> (vol%)	Soot <sup>^</sup> (g)	Regression rate (mm/min)	Burn time (min)	Burn efficiency (%)
HOOPS <sup>a</sup>	8 cm		0.247/	33/	0.117/	0.01	1.54	30.0	57

HOOPS <sup>a*</sup>	8 cm	Wave 1	0.858/0.45 5	105/34	0.292/	0.10	1.86	42.0	95
HOOPS <sup>b</sup>	8 cm	Wave 2	2.197/0.65 1	224/50		0.01	1.45	54.0	97
Bunker <sup>b</sup>	1 cm		1.860/0.49 0	113/49			1.25	5.5	74
Bunker <sup>b</sup>	1 cm	Wave 3	2.146/0.65 9	1420/460		0.02	1.72	6.0	86

\* Rain

^ Fine particle filter in Fig. 1

<sup>a</sup> Crane

<sup>b</sup> Zip line

As noted in Fig. 5 in the experimental setup section, the crane was not in a static position. The crane operator would maneuver the crane to allow for the sampling point to be completely engulfed by the smoke plume depending on the direction of the wind. However, as seen from Table 5, this was not without its challenges. Initially, the crane operator required some repetitions to maintain the sampling apparatuses within the smoke plume. In addition, obstruction from the dark smoke limited visibility and required external communication. This caused slight delays, which would result in gaps of missing data points during sudden wind shifts. Because of this, an average value for the combustion product concentrations could not be reasonably calculated for the first experiment.

Table 4 shows sampled concentrations to be relatively higher when using the zip line compared to the crane. This is because the zip line was situated at a height of 4.0 m above the pool, while the average height for the cases with a crane was approximately 5.7 m. The sampling apparatuses used by EPA required that the ambient temperature around the equipment be maintained below 50°C to ensure accuracy and longevity. This meant that the crane could not lower the sampling points too close to the flames, as it would easily exceed the limiting temperature. This difficulty did not exist with OGES. Using Heskestad plume correlations [10] for the 1.9 m by 1.7 m crude oil pool fire at CRREL, the estimated minimum height to maintain a temperature below 50°C is around 5.7 m.

However, recall the conclusion from the meso-scale experiments concerning optimal sampling height. It should be above the flame tip but no more than two times that of the observed flame height. Visual observations from video footage showed the average flame height to be around 2.7 m. Since 5.7 m was the minimum height for the crane, it consistently exceeded this value, which resulted in sampling heights that exceeded the optimal range for the OGES system. Recall from meso-scale experiments that CO concentrations decay exponentially with height, diffusing much quicker than CO<sub>2</sub> as height increases. This shows the possibility for skewed results, especially when sampling heights exceed a certain range.

### 3.2.3 Comparison with EPA results

As mentioned previously, EPA was only present for the first two experiments, therefore only two cases will be compared to EPA data in this section. Using Modified Combustion Efficiency (MCE) to compare burning behavior for different experiments,

$$MCE = \frac{CO_2}{CO_2 + CO}, \quad (1)$$

where  $CO_2$  and  $CO$  are in vol%.

MCE is a different way of expressing the  $CO/CO_2$  ratio. In general, a higher  $CO/CO_2$  ratio represents a higher degree of incomplete combustion, while a higher MCE represents the opposite. Both terms can be compared since the included variables are the same. Fig. 11 shows a comparison between calculated MCE values obtained from both OGES TC tree and OGES Crane. Both peak and average concentrations values are reported in the figure. EPA values were obtained from the final report [22].

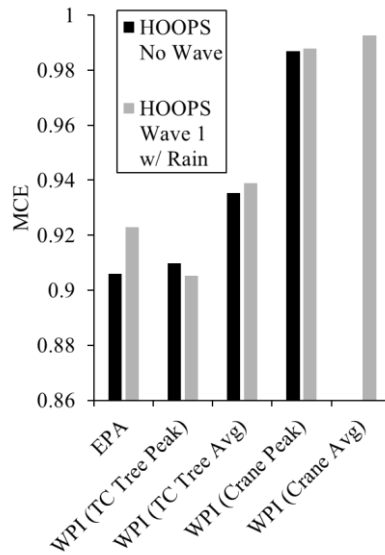


Fig. 11. MCE comparison between WPI and EPA reported values.

An initial assumption is that increased convective cooling from wave behavior would lower the combustion efficiency of a fire. Interestingly, EPA and WPI data seem to both suggest the effect is negligible, and perhaps increases the combustion efficiency by a slight margin. More observations on the influence of waves are given in the latter HRR discussion.

It is observed that OGES TC tree yielded MCE values that were consistent with the reported values by EPA. Both peak and average concentrations from OGES TC tree produced reasonable results.



At the same time, however, one cannot ignore that OGES Crane yielded results that are not in good agreement with other values. It is also noted that the values approach unity, meaning OGES Crane only captured relatively low amounts of CO compared to CO<sub>2</sub>. A possible reason is that wind shifts affected OGES Crane more than OGES TC tree. The fact that OGES TC tree was in much closer proximity to the fire aided in its ability to be fully engulfed within the smoke plume compared to OGES Crane during wind shifts. Another contributor to uncertainty can be attributed to the same CO sensors being used simultaneously for OGES TC tree and OGES Crane. The CO sensors were calibrated for higher concentrations upwards of 5000 ppm, but CO concentrations at the average crane height of 5.7 m were in the range of 100 ppm. The sensors likely had less sensitivity at low concentrations.

However, the same report by EPA [22] reported peak CO concentrations of approximately 150 ppm in the same sampling location. The peak CO concentration of 105 ppm sampled by OGES Crane was within a similar range. A reasonable hypothesis stems from the results shown in the meso-scale experiments. CO concentrations show exponential decay with respect to height compared to CO<sub>2</sub> concentrations. This shows that sampling locations that exceed a certain height may yield CO/CO<sub>2</sub> ratios, or MCE values in this case, that is not representative of the actual burning behavior.

A solution to this would be to develop a system that can withstand extreme heat similar to OGES TC tree so that gas sampling can be performed closer to the fire, and metrics such as MCE or CO/CO<sub>2</sub> ratio are more representative of the actual burning behavior. Another consideration arises when considering other harmful combustion products, such as nitrogen oxides (NO<sub>x</sub>) and sulfur oxides (SO<sub>x</sub>). It is currently unknown whether these gas species diffuse in a manner that is similar to CO<sub>2</sub> or CO, therefore future studies on combustion product sampling should be performed while including these gas species.

### *3.3 Heat Release Rate (HRR)*

HRR based on point measurements of fire products. Six different methods can be used to establish the HRR ( $\dot{Q}$ ) or energy release rate of the process, as shown in Fig. 12.

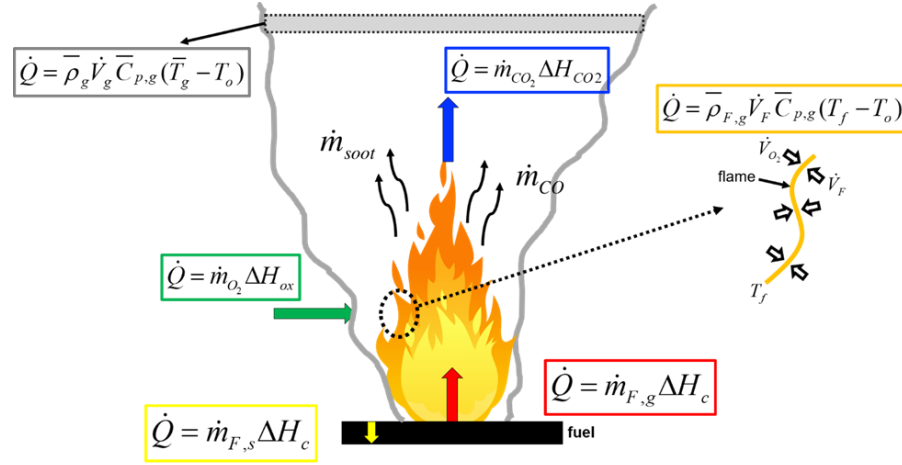


Fig. 12. Six different methods for establishing HRR. The first two methods multiply heat of combustion ( $\Delta H_c$ ) and mass of fuel consumed ( $\dot{m}_{F,s}$ ) or mass of fuel vapor released ( $\dot{m}_{F,g}$ ) per unit time. The third method is based on the amount of consumed oxygen. The fourth method uses produced  $CO_2$ . The fifth method assumes energy released by combustion is used to heat the gas to a flame temperature at the flame location. The sixth method is based on the temperature rise of the exhaust gasses passing through the control volume.

This research used three methods to calculate HRR: Oxygen Consumption (OC) method, Carbon Dioxide Generation (CDG) method, and Mass Burning Rate (MBR) method. First is the OC method from Tsuchiya [2], which is represented by the product of mass flow rate of oxygen ( $\dot{m}_{O_2}$ ) through the control volume and heat release per unit mass of oxygen ( $\Delta H_{ox}$ ). Second is the CDG method using the formulation by Tewarson [3], which is generally represented by the product of mass flow rate of oxygen ( $\dot{m}_{CO_2}$ ) through the control volume and heat release per unit mass of  $CO_2$  ( $\Delta H_{CO_2}$ ). In the CRREL experiments, however, sampled CO concentrations were rather high compared to small- and meso-scale fires, which represents a larger degree of incomplete combustion. This needed to be accounted for and therefore an additional term for the production of CO was added to the CDG method equation. HRR based on the OC method is shown as Eqn. (2), while HRR based on the CDG method is shown as Eqn. (3).  $\dot{m}^0$  terms represent the mass flow rate of individual gas species in ambient air. Huggett [6] showed that  $\Delta H_{ox}$  is constant for most hydrocarbon fires, which is 13.1 kJ/g. Khan et al. [3] showed  $\Delta H_{CO_2}$  and  $\Delta H_{CO}$  to also be consistent for most hydrocarbon fires, which are 13.3 kJ/g and 11.1 kJ/g respectively.

$$\dot{Q}_{OC} = \Delta H_{O_2} (\dot{m}_{O_2}^0 - \dot{m}_{O_2}), \quad (2)$$

$$\dot{Q}_{CDG} = \Delta H_{CO_2} (\dot{m}_{CO_2} - \dot{m}_{CO_2}^0) + \Delta H_{CO} (\dot{m}_{CO} - \dot{m}_{CO}^0). \quad (3)$$

Eqn. (2) and (3) show HRR calculations based on OC and CDG method require mass flow rate through the control volume. Plume theories derived by Heskestad [10] and McCaffrey [20] were used to estimate mass flow rates along the centerline of the fire at different heights. In addition, profiles of vertical velocity across the horizontal direction of the plume are assumed to be uniform based on integral formulations by Morton et al. [21]. This results in a simplification where a uniform “top hat” profile was used when estimating mass flow rate at a certain height. This assumption also means a radial distribution of CO<sub>2</sub>, CO, and O<sub>2</sub> is not needed.

McCaffrey [14][20] divides a buoyant diffusion flame into three distinct regimes: continuous flame zone, intermittent zone, and plume zone. Continuous flame zone is the zone where the flame is always present. Intermittent zone is the zone where the eruption and break from the anchored flame with a regular flicker of a few Hz can be observed. Plume zone is the zone above the visible flame where flames are no longer present. The regime is determined based on height above the burner ( $z$ ) and total HRR ( $\dot{Q}$ ). McCaffrey [20] provides equations to calculate mass flow rate ( $\dot{m}$ ) along the centerline of the fire based on the regime, as shown in Table 2.

Table 2. Summary of mass flow rate correlations for a buoyant diffusion flame from McCaffrey [14]

Regime	$z / \dot{Q}^{2/5}$ [m/kW <sup>2/5</sup> ]	Correlation
Continuous Flame	< 0.08	$\dot{m} / \dot{Q} = 0.011(z / \dot{Q}^{2/5})^{0.566}$
Intermittent	0.08 – 0.20	$\dot{m} / \dot{Q} = 0.026(z / \dot{Q}^{2/5})^{0.909}$
Plume	> 0.20	$\dot{m} / \dot{Q} = 0.124(z / \dot{Q}^{2/5})^{1.895}$

McCaffrey [14] also provides equations for centerline velocity and temperature of a buoyant diffusion flame, shown as Eqn. (4) and (5) respectively. Table 3 shows the constants used for the three distinct regimes.  $u_0$  is centerline velocity;  $g$  is gravitational acceleration, or 9.81 m/s<sup>2</sup>;  $T_0$  is ambient temperature;  $\Delta T_0$  is temperature rise above ambient;  $C$  is an empirical correction factor, or 0.9;  $\eta$  is an empirical exponent coefficient.

$$u_0 / \dot{Q}^{1/5} = k(z / \dot{Q}^{2/5})^\eta, \quad (4)$$

$$2g\Delta T_0 / T_0 = (k / C)^2 (z / \dot{Q}^{2/5})^{2\eta-1}. \quad (5)$$

Table 3. Summary of centerline constants for a buoyant diffusion flame from McCaffrey [14]

Regime	$k$	$\eta$	$z / \dot{Q}^{2/5}$ [m/kW <sup>2/5</sup> ]	$C$
--------	-----	--------	---	-----

Flame	6.8 [m <sup>1/2</sup> /s]	1/2	< 0.08	0.9
Intermittent	1.9 [m/kW <sup>1/5</sup> · s]	0	0.08 – 0.20	0.9
Plume	1.1 [m <sup>4/3</sup> /kW <sup>1/3</sup> · s]	- 1/3	> 0.20	0.9

The third method of calculating HRR is taking the product of mass burning rate ( $\dot{m}_{F,s}$ ) and heat of combustion ( $\Delta H_c$ ) for a given fuel [3]. SFPE HB [3] gives the heat of combustion for crude oil as 42,600 kJ/g. The mass burning rate (MBR) was calculated based on the average observed regression rate of the fuel layer throughout the experiments. Using that as a baseline HRR value, this study calculated HRR based on measured combustion products concentrations.

HRR can also be obtained by using empirical constants reported by Babrauskas [3][23] for large-scale pool fires,

$$\dot{Q} = \Delta H_c \dot{m}_\infty'' (1 - e^{-k\beta D}) \times A. \quad (6)$$

Outside of the heat of combustion for a given fuel, two additional empirical constants need to be determined. First is the asymptotic mass loss rate per unit area ( $\dot{m}_\infty''$ ). The mass loss rate per unit area approaches asymptotic as the pool diameter increase towards infinity. Generally, this equation can be applied to pool fires that are 1 m in diameter or greater. The second constant is the product of extinction-absorption coefficient and beam-length corrector ( $k\beta$ ). However, it is noted that this correlation yields an HRR value solely based on pool diameter and fuel type, which in this study is identical across cases that use the same fuel. It cannot account for external factors such as waves.

### 3.3.1 Meso-scale 75 cm indoor experiments

Using Babrauskas [3][23] correlation for the meso-scale indoor experiments, a 75 cm ANS crude oil fire would have an HRR of 350 kW, while an 87-octane gasoline fire would be 720 kW. This set of experiments only measured combustion product concentrations. However, the fact that sampling points were located at the centerline allowed for McCaffrey plume correlations [14][20] to be used to estimate mass flow rate at the sampling point, as shown in Table 2 and Eqn. (4) (5). Once these variables were obtained, HRR was approximated using CDG method with measured CO<sub>2</sub> and CO concentrations. Fig. 13 shows estimated HRR from CDG method using measured gas concentrations at different heights. The horizontal lines represent HRR approximated by Babrauskas [3][23] for a 75 cm pool fire.

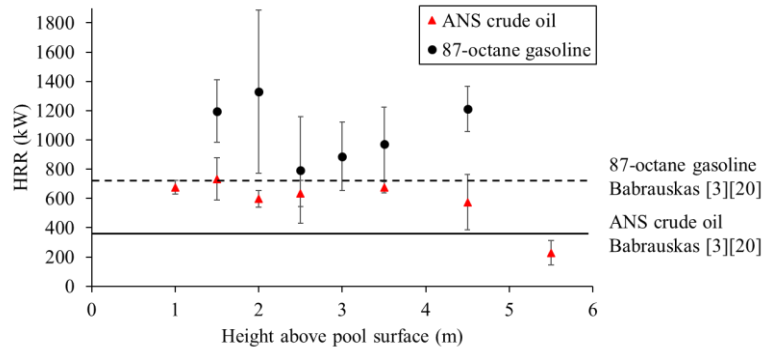


Fig. 13. Estimated HRR for meso-scale 75 cm indoor pool fire experiments. Measured gas concentrations at different heights were used with CDG method to obtain HRR values.

From Fig. 13, it is interesting to see that using CDG method from the OGES system measured  $\text{CO}_2$  and CO concentrations yielded HRR values that consistently overestimated for both ANS crude oil and 87-octane gasoline when compared to Babrauskas [3][23] values. Other measurement methods such as oxygen data, temperature data, and fuel regression rate were lacking, so other methods of validation were not present for this set of experiments.

However, the takeaway from these results is that there is a similar trend for calculated HRR with respect to sampling height. In the continuous flame zone (1 – 1.5 m for ANS crude oil, 1.5 – 2 m for 87-octane gasoline), the calculated HRR increases, moving further away from the HRR predicted by existing correlations. However, once in the intermittent zone (1.5 – 2 m for ANS crude oil, 2 – 2.5 m for 87-octane gasoline), the calculated HRR values decrease and are closer to expected values. Once the plume zone is reached at further distances (> 2 m for ANS crude oil, > 2.5 m for 87-octane gasoline), the HRR calculated by CDG method again begins to deviate farther from the expected value. The conclusion drawn from these observations is that OGES system gas emissions sampling for HRR measurement purposes should be performed in the intermittent zone of the fire, as that yields values that are closest to plume theory correlations.

### 3.3.2 Large-scale outdoor experiments at CRREL

Based on Babrauskas [3][23], HRR is estimated to be 5.9 MW for HOOPS crude oil. SFPE HB [3] does not report values for bunker fuel specifically, but it states that bunker fuel falls under the category of heavy fuel oil. Using the constants for heavy fuel oil, the estimated HRR for bunker fuel is 4.3 MW. As stated previously, this correlation yields an HRR value solely based on pool diameter and fuel type, which means an identical HRR will be obtained across cases that use the same fuel. However, this is not the case with external factors such as waves and is one of the limitations of this correlation.

As mentioned in previous sections, this study relied on existing plume theories such as McCaffrey plume [14][20] to estimate mass flow rate, velocity, and temperature along the centerline at the sampling height, as shown in Table 2 and Eqn. (4) (5). Once these variables were obtained, HRR was approximated using CDG method with measured  $\text{CO}_2$  and  $\text{CO}$  concentrations, or OC method with  $\text{O}_2$  concentrations. Recall that OGES TC tree was located along the centerline of the fire at 2.8 m above the pool surface. This is why McCaffrey plume could be used to obtain variables not measured in this study. However, for the same reason, HRR could not be obtained using OGES Crane data, since the crane was not always situated along the centerline of the plume.

Based on the three distinct flame regimes from McCaffrey [14][20], Table 2 shows that OGES TC tree was located in the intermittent zone for all five experiments. MBR provided a baseline value for HRR calculation; the value was then used to estimate the mass flow rate along the centerline using Table 2.  $\dot{m}_{\text{CO}_2}$ ,  $\dot{m}_{\text{CO}}$ , and  $\dot{m}_{\text{O}_2}$  could then be calculated using measured gas concentrations from OGES TC tree, after which these values were used to estimate HRR using OC and CDG method.

Initially, HRR was calculated using OC and CDG method respectively using both peak or average gas concentration values. However, results showed using peak gas concentrations sampled by the OGES system did not yield HRR values that were in good agreement with the HRR based on MBR. Using peak values consistently resulted in a significant overestimation of HRR. However, average gas concentration values yielded HRR values that were much more reasonable for this fire size. This made sense, as the MBR was calculated based on an average regression rate of the fuel layer. For the three cases with HOOPS crude oil, HRR based on MBR was in good agreement with the two HRR values predicted by OC and CDG method within a reasonable degree of error when average gas concentrations were used. Fig. 14 plots calculated HRR values using the different methods; HRR calculated using peak gas concentrations are omitted.

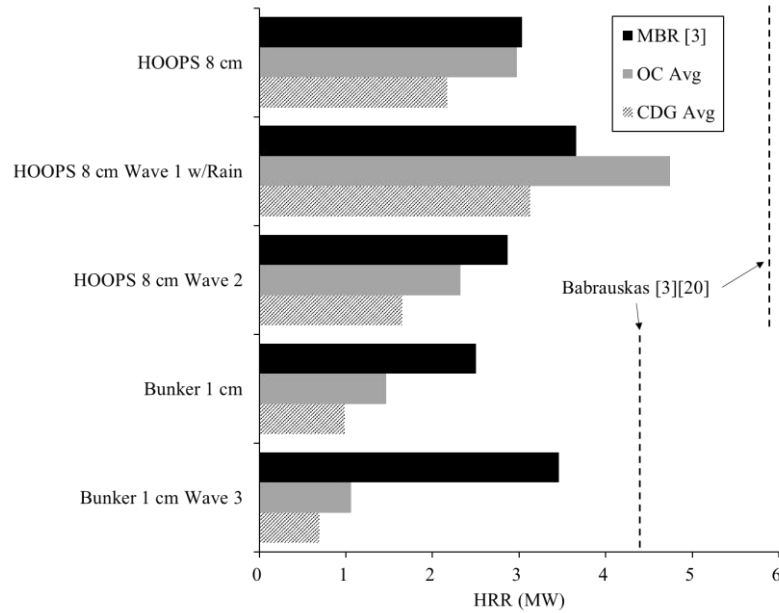


Fig. 14. Four HRR calculation methods for five experiments at CRREL.

It can be observed that OC method yields HRR values that are in good agreement for HOOPS crude oil cases, even with the inclusion of waves. CDG method yields consistently lower values, which suggests other products of combustion, such as soot production, need to be quantified as well. This is especially important for the fire size used at CRREL, as a higher degree of incomplete combustion is expected.

Similar to the comparison with EPA data, both MCE and HRR calculations seem to suggest that a fast but short wave like Wave 1 allows more complete combustion of the fire. However, a slow but tall wave like Wave 2 causes HRR to decrease slightly. Regardless of the wave, the OGES system shows the capability to capture combustion products and effectively estimate HRR based on OC and CDG methods even with the presence of waves. Quantification of waves is out of the scope of this study, but future research is needed to quantify the effect of waves on oil slicks burning above water.

It is interesting to observe that these same methods underestimate HRR for bunker fuel by a considerable margin. For bunker fuel, this suggests a thin fuel layer of 1 cm allows for very fast heat penetration to the water sublayer under the fuel, which promotes burning phenomena such as boilover as the water reaches its boiling point. The boiling water in conjunction with the waves atomizes the fuel quicker since the fuel slick thickness is very thin initially; this enhances the burn rate compared to a calm scenario. The hypothesis of why OC and CDG methods are underestimating the HRR is that the vaporizing water content is a significant component in the flue gases and should be quantified in further studies to more accurately predict HRR using point sampling.



Although currently limited to certain fuels, the OGES system has demonstrated a low-cost but effective alternative to expensive industrial gas analyzers for HRR estimation, especially in large-scale outdoor fire scenarios where complete encapsulation of the plume is unfeasible and only point sampling is possible. Further refinement of this system, such as measurement of mass flow rate at the sampling location and quantification of water vapor content, can allow it to become applicable for more types of fuels.

#### **4. Conclusion**

The newly developed OGES system displays a new alternative method for gas emissions sampling in outdoor fires. In the meso-scale tests, it showed an ability to obtain a vertical distribution of combustion products along the centerline of a fire, obtaining a regression curve for gas concentrations versus height. Results suggest CO<sub>2</sub> dilutes in a relatively linear fashion with respect to height, while CO dilutes exponentially. Further studies are required regarding other combustion products not considered in this study, such as NO<sub>x</sub> and SO<sub>x</sub>, to better understand the dilution of combustion products with respect to height.

In the large-scale field tests at CRREL, measured combustion product concentrations and comparison with reported EPA data suggest that OGES TC tree was in a more optimal gas sampling location for HRR measurements. Significant dilution of CO concentration at higher locations above the fire made it difficult for consistent point sampling to be performed.

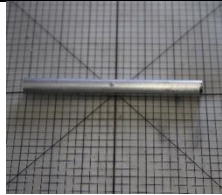

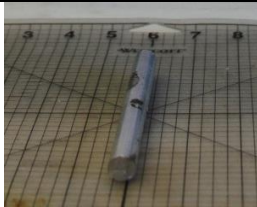
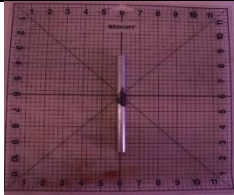
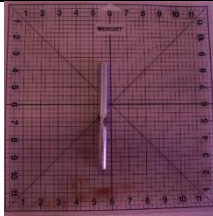
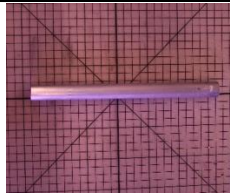
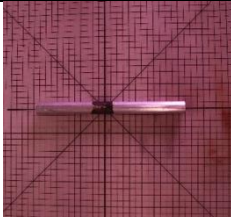
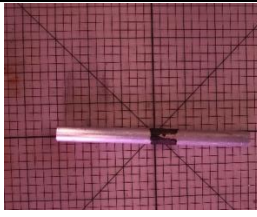
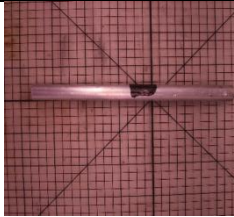
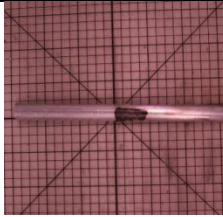


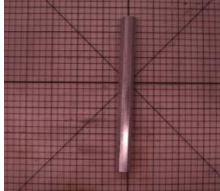
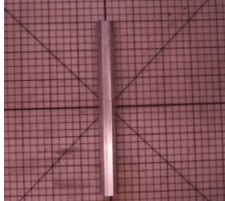
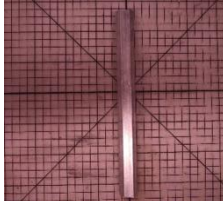
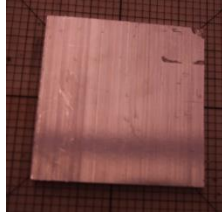
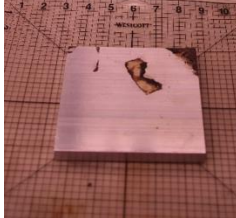

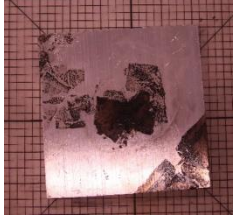
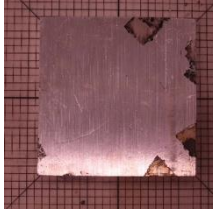
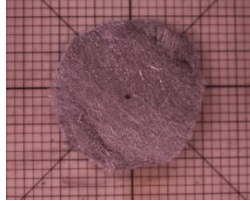
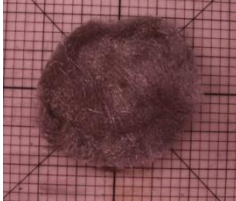
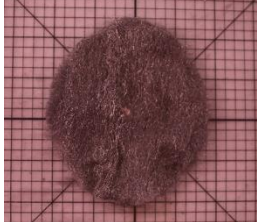
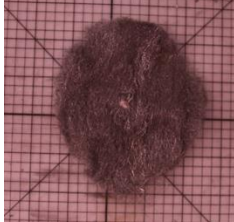
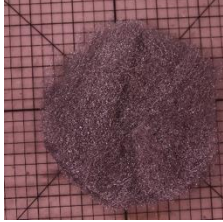
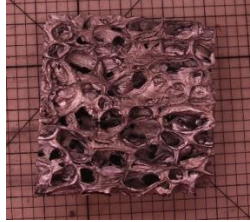
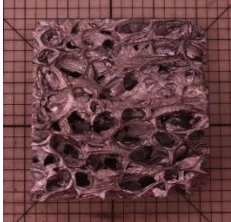
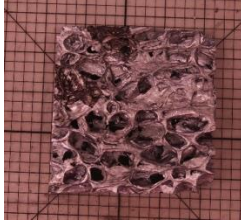

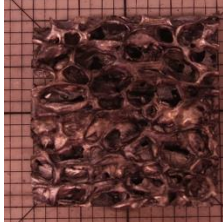
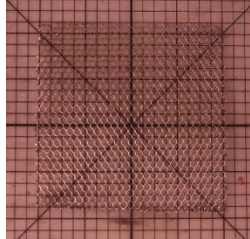
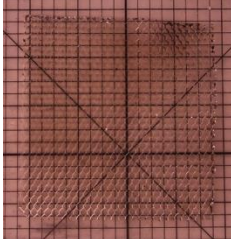
When combined with plume theories, such as McCaffrey plume, using average values of CO<sub>2</sub>, CO, and O<sub>2</sub> captured by the OGES TC tree yielded HRR values that were in good agreement with mass burning rate data for HOOPS crude oil. Larger underestimations with bunker fuel suggest other products of combustion not measured in this study, and further research should be pursued on this topic. However, at present, the OGES system has shown to be a low-cost but effective way to measure HRR in large-scale outdoor fire scenarios where only point sampling is feasible.

## References



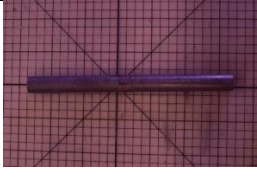
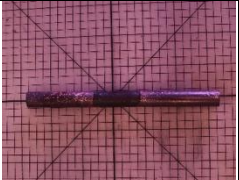
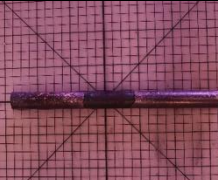
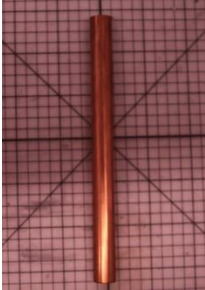

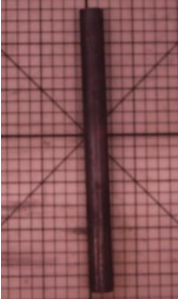
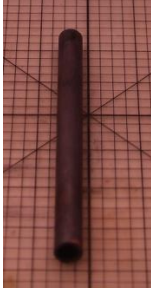
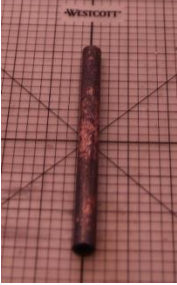
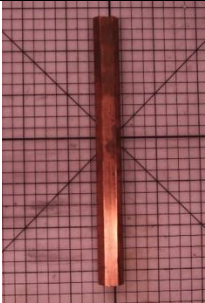


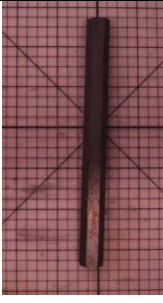
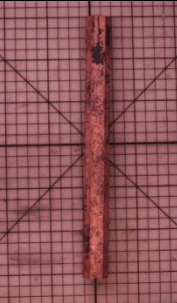
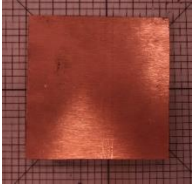
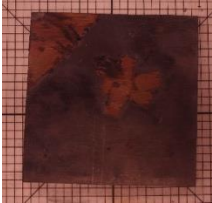
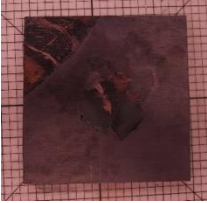
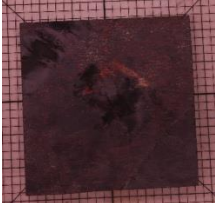
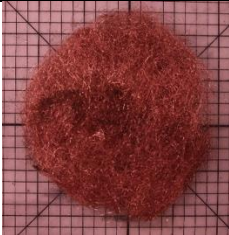
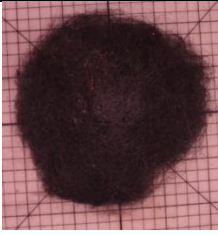
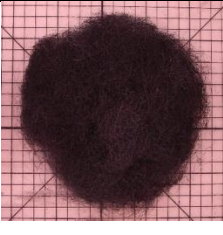
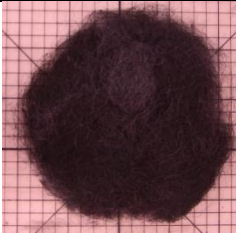
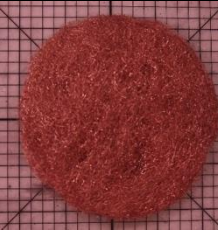
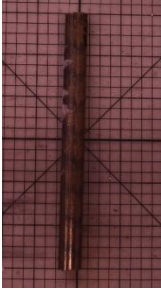




- [1] Babrauskas, V., & Peacock, R. D. (1992). Heat release rate: the single most important variable in fire hazard. *Fire safety journal*, 18(3), 255-272.
- [2] Tsuchiya, Y. (1982). Methods of determining heat release rate: State-of-the-art. *Fire Safety Journal*, 5(1), 49-57.
- [3] Hurley, M. J., Gottuk, D. T., Hall Jr, J. R., Harada, K., Kuligowski, E. D., Puchovsky, M., ... & WIECZOREK, C. J. (Eds.). (2015). *SFPE handbook of fire protection engineering*. Springer.
- [4] ASTM, S. (2016). Standard test method for heat and visible smoke release rates for materials and products using an oxygen consumption calorimeter. E1354-16a.
- [5] Babrauskas, V., & Grayson, S. J. (Eds.). (1990). *Heat release in fires*. Taylor & Francis.
- [6] Huggett, C. (1980). Estimation of rate of heat release by means of oxygen consumption measurements. *Fire and Materials*, 4(2), 61-65.
- [7] Bryant, R. and Bundy, M. (2019), The NIST 20 MW Calorimetry Measurement System for Large-Fire Research, Technical Note (NIST TN), National Institute of Standards and Technology, Gaithersburg, MD.
- [8] Evans, D. D., Mulholland, G. W., Baum, H. R., Walton, W. D., & McGrattan, K. B. (2001). In Situ Burning of Oil Spills. *Journal of research of the National Institute of Standards and Technology*, 106(1), 231–278.
- [9] Cooper, L. Y. (1994). Some factors affecting the design of a calorimeter hood and exhaust. *Journal of Fire Protection Engineering*, 6(3), 99-111.
- [10] Heskestad, G. (1984). Engineering relations for fire plumes. *Fire Safety Journal*, 7(1), 25-32.
- [11] Tukaew, P. (2017). Outdoor Gas Emission Sampling System: A Novel Method for Quantification of Fires in Outdoor Conditions. *Fire Protection Engineering*.
- [12] Tukaew, P., K.S. Arsava, S.L. Fields, A.S. Rangwala, “Outdoor Gas Emission Sampling System –Performance during Large Scale Fire Tests in Mobile Alabama”, in *Proceedings of the Thirty ninth AMOP Technical Seminar on Environmental Contamination and Response*, Environment Canada, Halifax, Nova Scotia, In-Press, 2019.
- [13] Lizhong, Y., Wenxing, F., & Junqi, Y. (2008). Experimental research on the spatial distribution of toxic gases in the transport of fire smoke. *Journal of fire sciences*, 26(1), 45-62.
- [14] McCaffrey, B. J., & Flames, P. B. D. (1979). Some Experimental Results. Nbsir.
















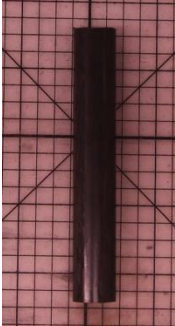



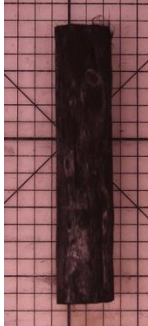
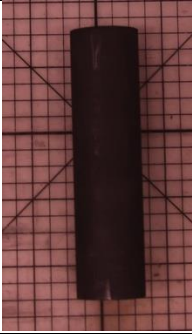


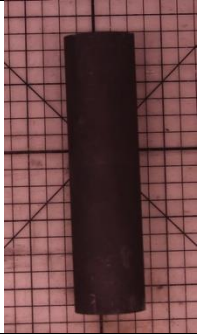

- [15] Sibulkin, M., Malary, S. F. (1984). Investigation of completeness of combustion in a wall fire. *Combustion Science And Technology*, 40(1-4), 93-106.
- [16] Aurell, J., & Gullett, B. K. (2010). Aerostat sampling of PCDD/PCDF emissions from the Gulf oil spill in situ burns. *Environmental science & technology*, 44(24), 9431-9437.
- [17] Aurell, J., Gullett, B. K., Pressley, C., Tabor, D. G., & Gribble, R. D. (2011). Aerostat-lofted instrument and sampling method for determination of emissions from open area sources. *Chemosphere*, 85(5), 806-811.
- [18] Aurell, J., Gullett, B. K., & Yamamoto, D. (2012). Emissions from open burning of simulated military waste from forward operating bases. *Environmental science & technology*, 46(20), 11004-11012.
- [19] Hariharan, S. B., Farahani, H. F., Rangwala, A. S., Dowling, J. L., Oran, E. S., & Gollner, M. J. (2021). Comparison of particulate-matter emissions from liquid-fueled pool fires and fire whirls. *Combustion and Flame*, 227, 483-496.
- [20] McCaffrey, B. J. (1983). Momentum implications for buoyant diffusion flames. *Combustion and Flame*, 52, 149-167.
- [21] Morton, B. R., Taylor, G. I., & Turner, J. S. (1956). Turbulent gravitational convection from maintained and instantaneous sources. *Proceedings of the Royal Society of London. Series A. Mathematical and Physical Sciences*, 234(1196), 1-23.
- [22] Aurell, J., Gullett, B. Analysis of Emissions and Residue from Methods to Improve Combustion Efficiency of In Situ Oil Burns, Heat Transfer Technology: Flame Refluxer. Final Report (2021).
- [23] Babrauskas, V. (1983). Estimating large pool fire burning rates. *Fire technology*, 19(4), 251-261.

# **APPENDIX – C Samples tests in small scale experiments (PHASE Ia)**

Material	Test 1	Test 2	Test 3	Test 4	Test 5
Al – Cyl. Bar					
Al - Hollow Bar					
Al – Hex. Bar					
Al - Plate					
Al - Wool					
Al - Foam					
Al - Honeycom b			Fell apart, no further tests	Fell apart, no further tests	Fell apart, no further tests

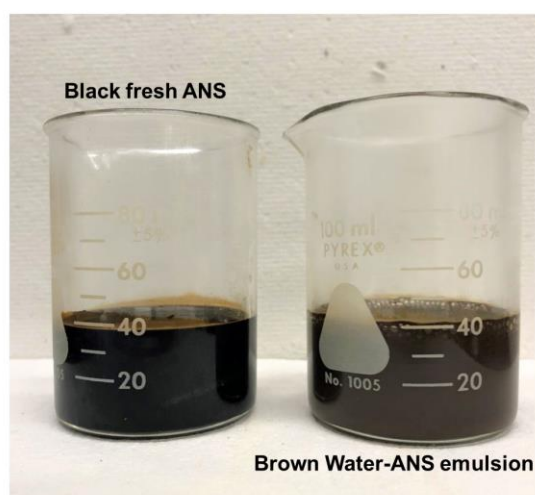
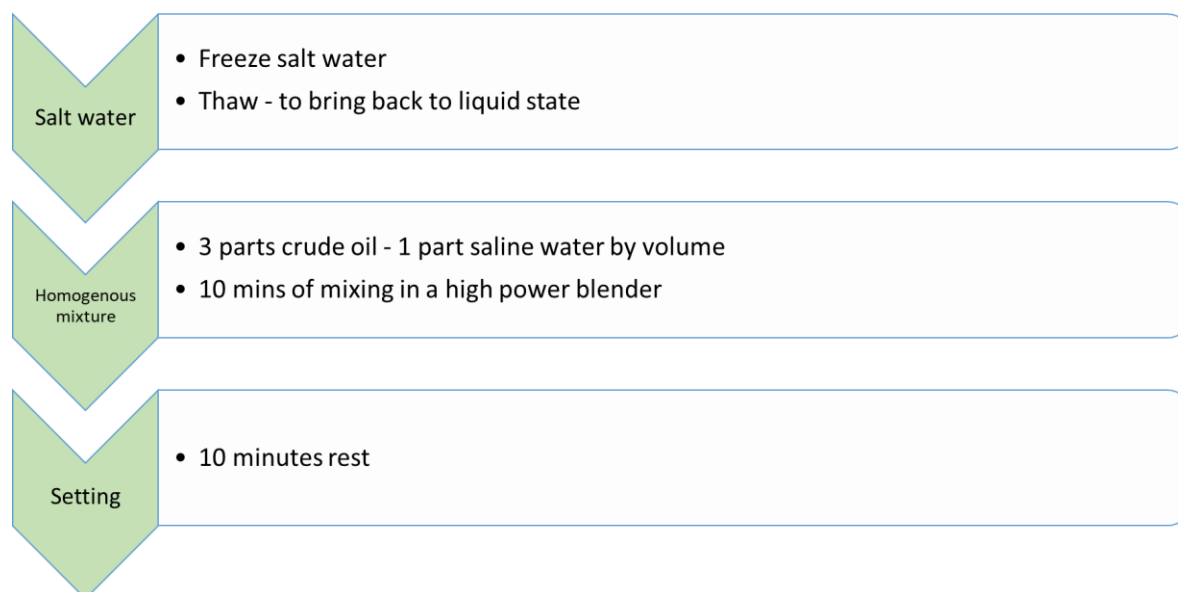


Cu – Cyl. Bar					
Cu - Hollow Bar					
Cu – Hex. Bar					
Cu - Plate					
Cu - Wool					
Bronze Oil Rod					
Ceramic Board					

Bronze Solid Graphite					
Bronze Hollow Graphite					
Macor- Glass- Ceramic Rod					
Carbon Fiber Rod					
Graphite Rod					

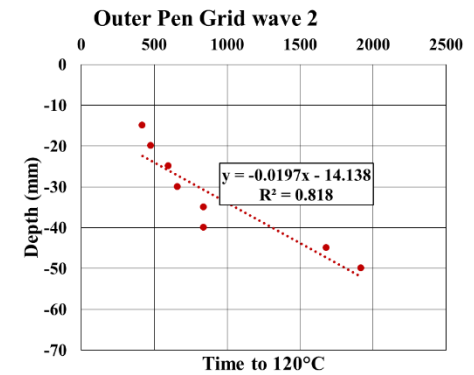
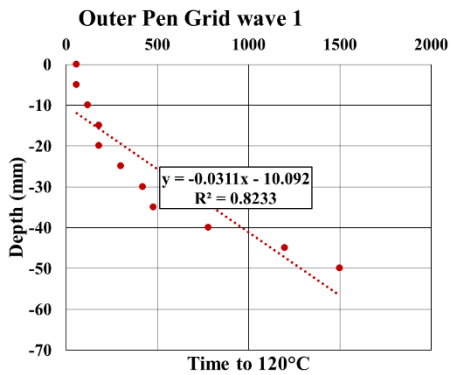
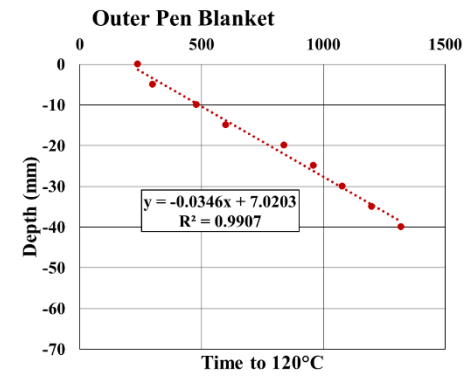
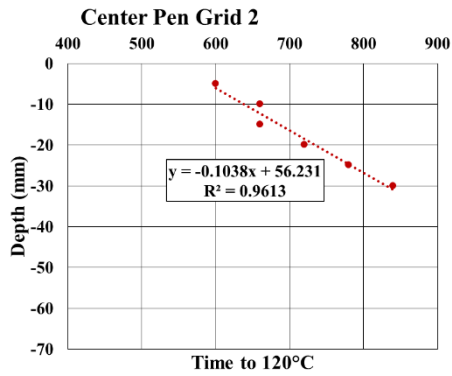
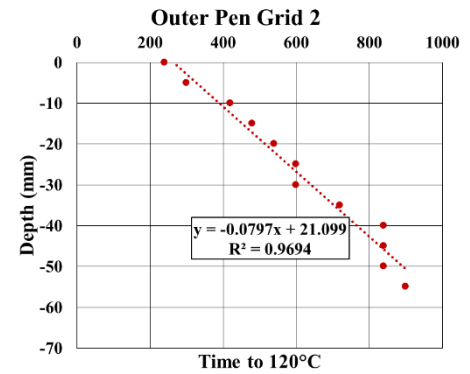
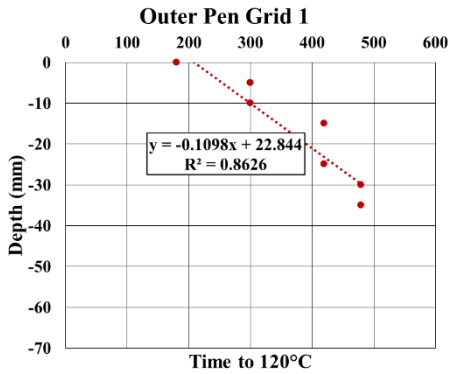
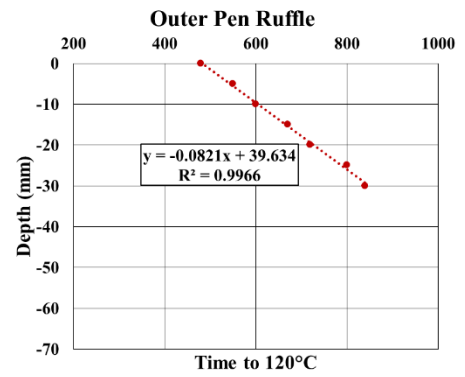
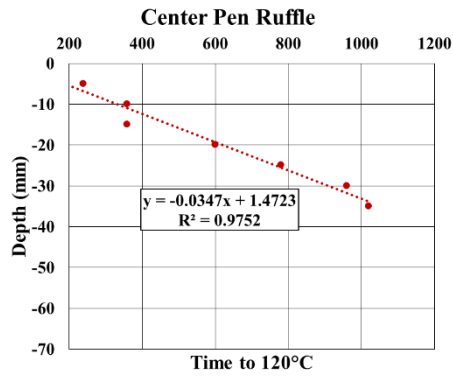


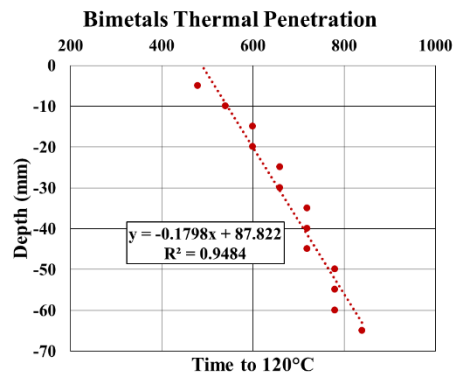
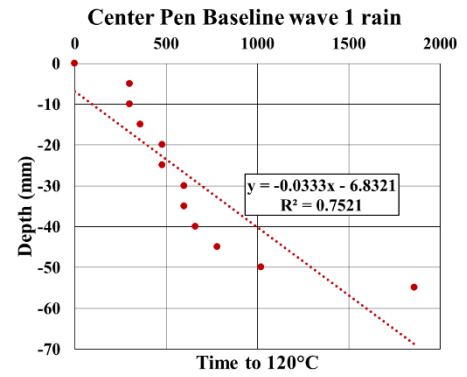
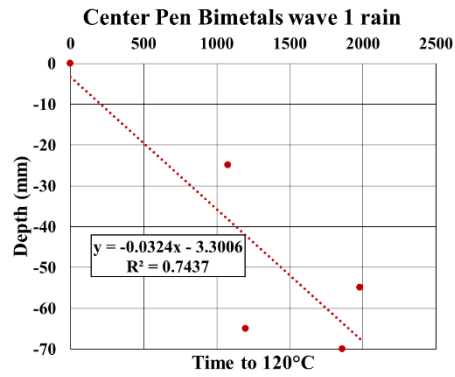
## APPENDIX – D (Emulsion Preparation – PHASE Ib)





## APPENDIX – E (Additional Figures – PHASE II)





Baseline (Flame1)					Bimetal (Flame1)				
175.6	160.4	142.3	129.5	101.8	325.1	314.8	292.7	219.7	265.6
F1_10	F1_11	F1_12	F1_13	F1_14	F1_10	F1_11	F1_12	F1_13	F1_14
337.8	295.0	243.0	150.7	137.7	468.4	507.4	512.9	330.1	318.8
F1_5	F1_6	F1_7	F1_8	F1_9	F1_5	F1_6	F1_7	F1_8	F1_9
334.3	453.7	608.6	555.7	330.4	477.5	160.2	958.5	927.4	937.0
F1_0	F1_1	F1_2	F1_3	F1_4	F1_0	F1_1	F1_2	F1_3	F1_4

Grid (Flame1)				
360.1	327.6	253.0	209.0	285.8
F1_10	F1_11	F1_12	F1_13	F1_14
518.4	630.3	532.8	252.3	1096.9
F1_5	F1_6	F1_7	F1_8	F1_9
464.7	664.5	670.7	690.8	555.5
F1_0	F1_1	F1_2	F1_3	F1_4

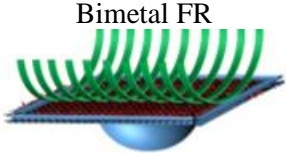
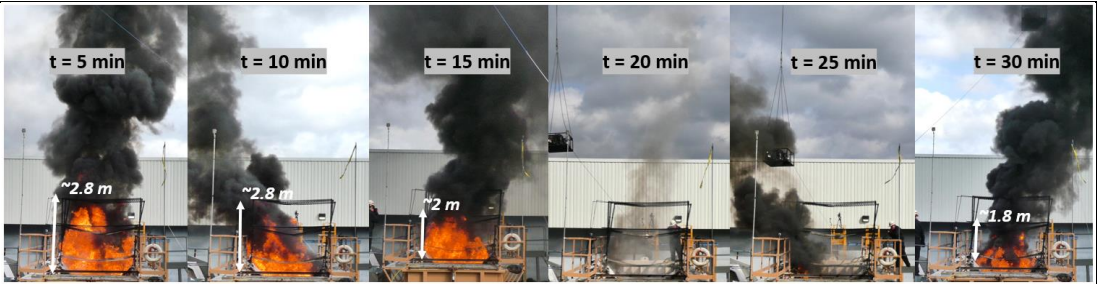
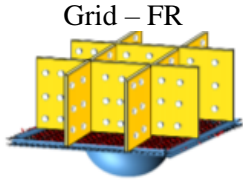
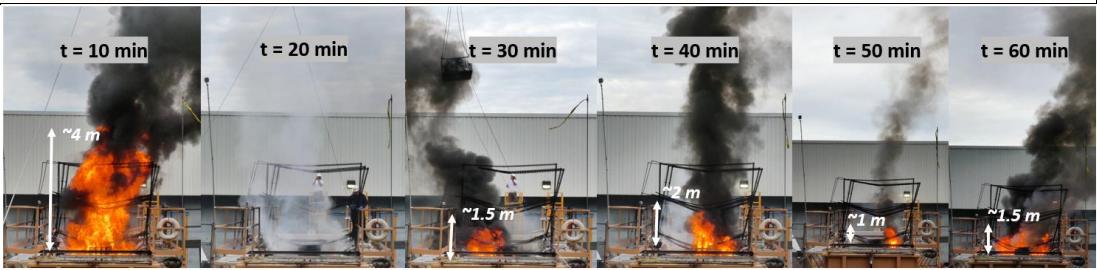
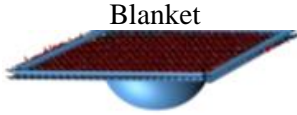
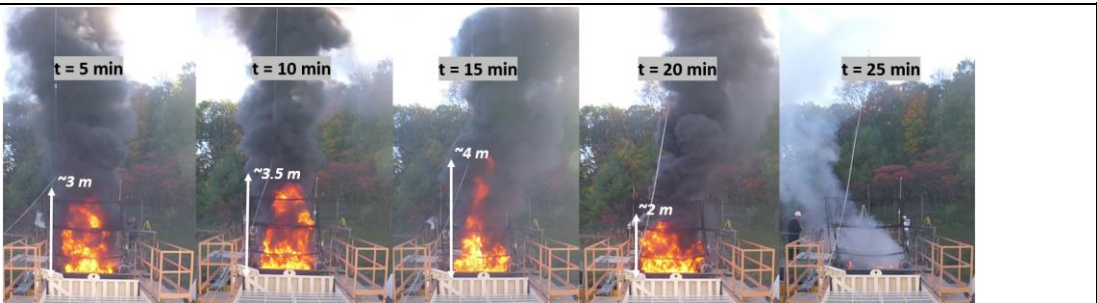
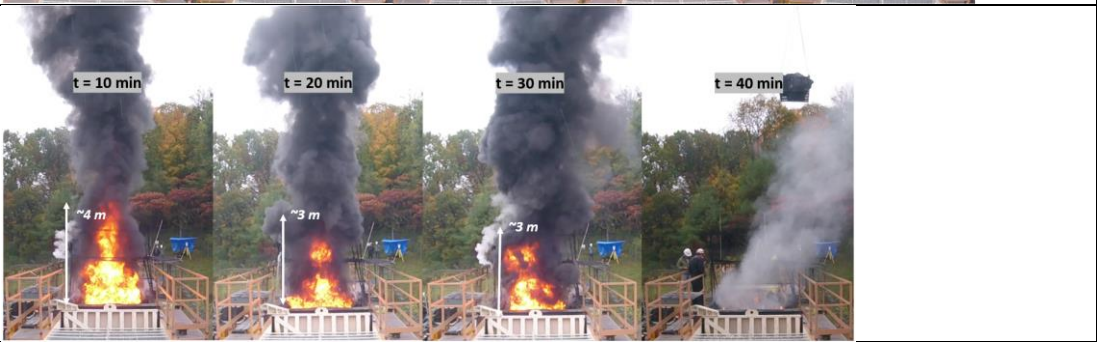
Baseline (Flame3)					Bimetal (Flame3)				
114.8	357.4	261.3	165.6	169.5	316.9	286.3	235.9	195.5	141.1
F3_10	F3_11	F3_12	F3_13	F3_14	F3_10	F3_11	F3_12	F3_13	F3_14
676.7	616.3	684.9	447.9	578.7	493.0	484.2	525.4	563.3	625.7
F3_5	F3_6	F3_7	F3_8	F3_9	F3_5	F3_6	F3_7	F3_8	F3_9
72.4	644.5	714.5	710.7	675.0	562.8	745.4	725.5	752.4	780.5
F3_0	F3_1	F3_2	F3_3	F3_4	F3_0	F3_1	F3_2	F3_3	F3_4

Grid (Flame3)				
488.7	477.1	277.4	208.2	265.0
F3_10	F3_11	F3_12	F3_13	F3_14
584.7	722.3	484.0	1083.3	855.5
F3_5	F3_6	F3_7	F3_8	F3_9
756.0	1045.5	991.4	1047.9	1334.2
F3_0	F3_1	F3_2	F3_3	F3_4

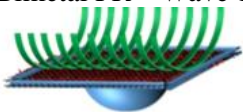
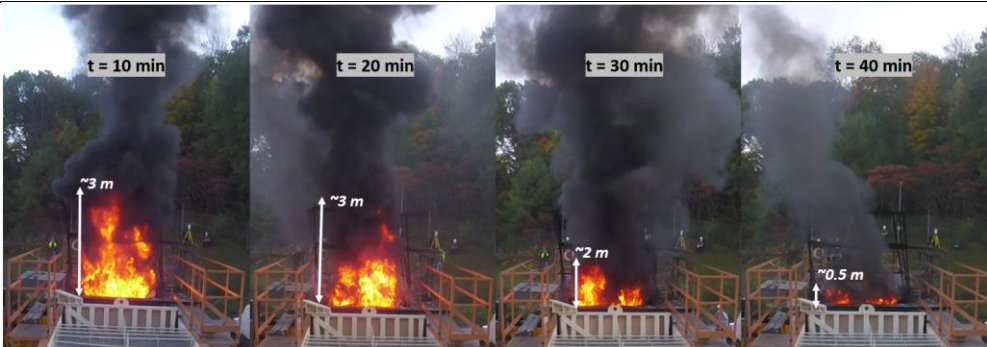
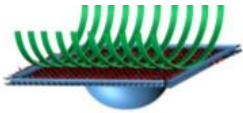
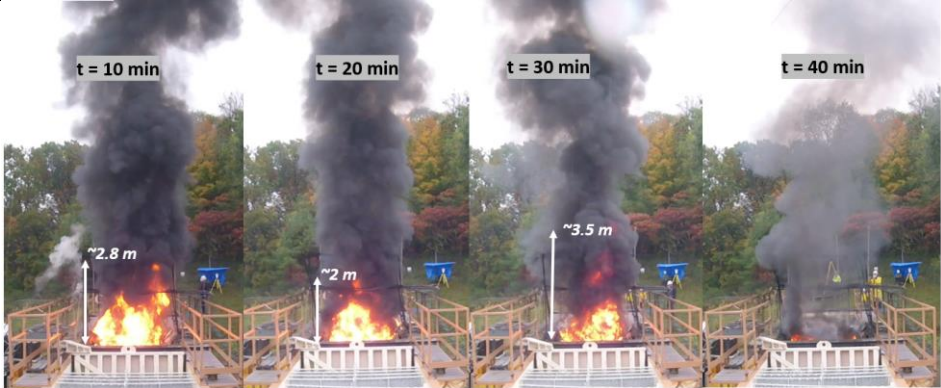
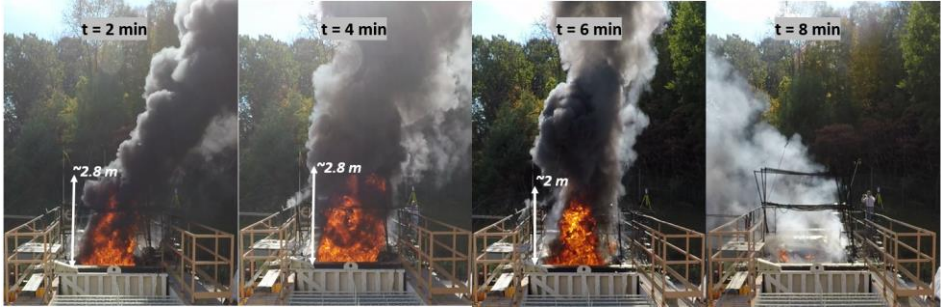
# APPENDIX – F (Phase II – Test Summary)

#	Test Date	Fuel Thickness (cm)	Test	
1	Sept 28, 2020 Fuel: HOOPS	8	Baseline	
2	Sept 28, 2020 Fuel: HOOPS		Ruffled FR 	
3	Sept 28, 2020 Fuel: HOOPS		Grid FR 	

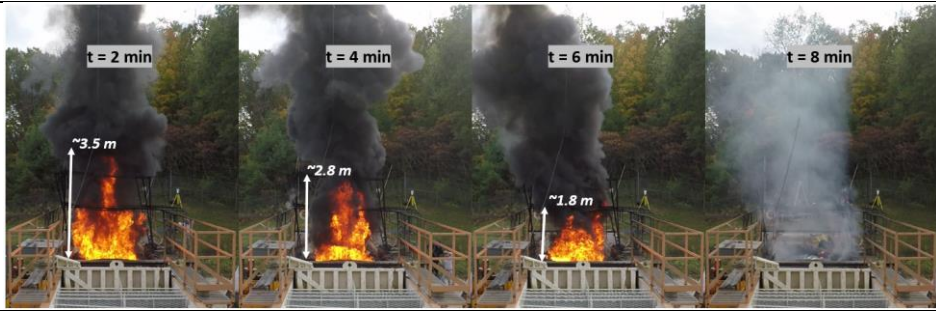
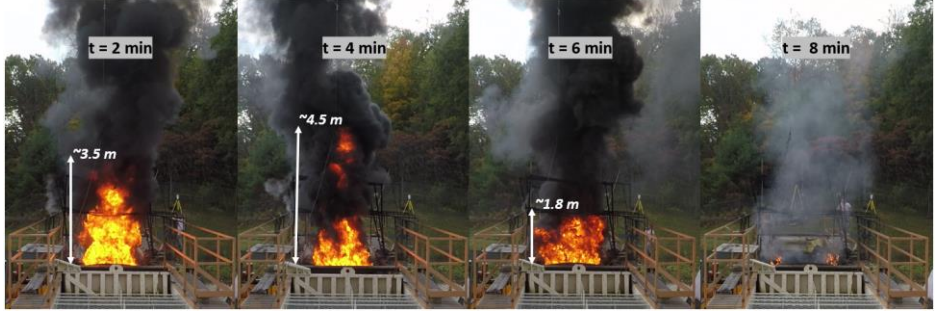
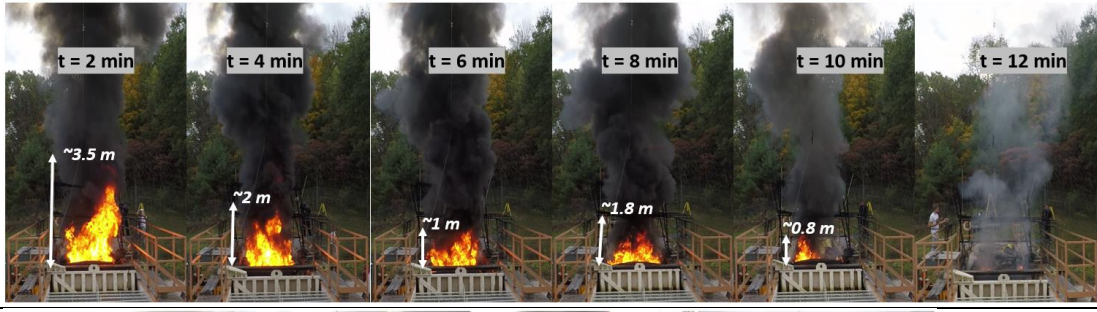
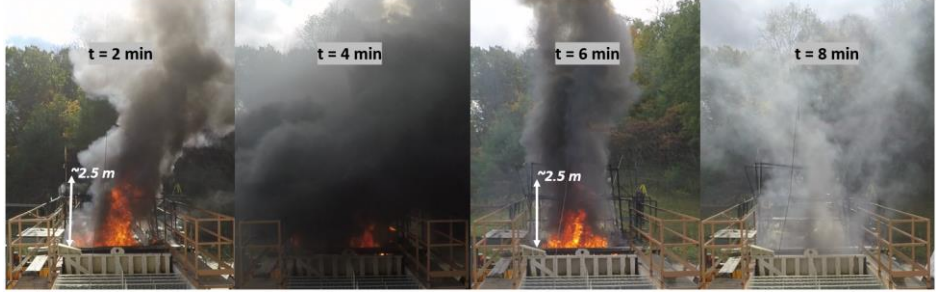
4	Sept 29, 2020 Fuel: HOOPS	8	 <p>Bimetal FR</p>	
5	Sept 29, 2020 Fuel: HOOPS		 <p>Grid - FR</p>	
6	Sept 30, 2020 Fuel: HOOPS		 <p>Blanket</p>	
7	Oct 2, 2020 Fuel: HOOPS		<p>Baseline – Wave 1</p>	

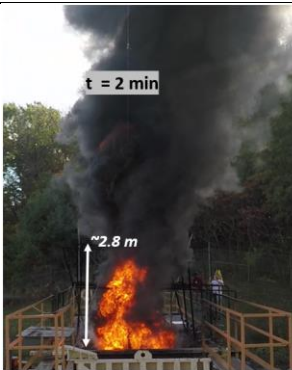


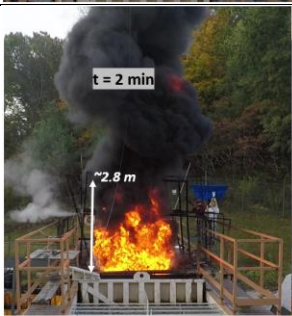


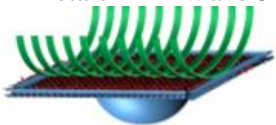
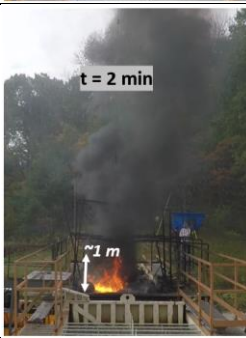


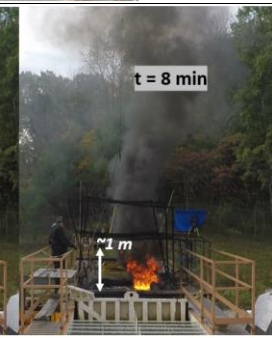


8	Oct 5, 2020 Fuel: HOOPS		Baseline – Wave 2	
9	Oct 1, 2020 Fuel: HOOPS		Grid Wave 1 	
10	Oct 1, 2020 Fuel: HOOPS	8	Grid Wave 2 	
11	Oct 1, 2020 Fuel: HOOPS		Solo Grid – Wave 1 	

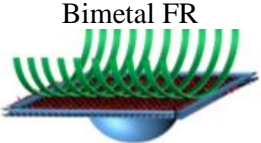

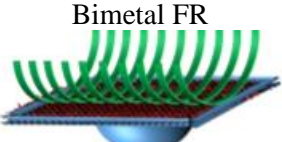
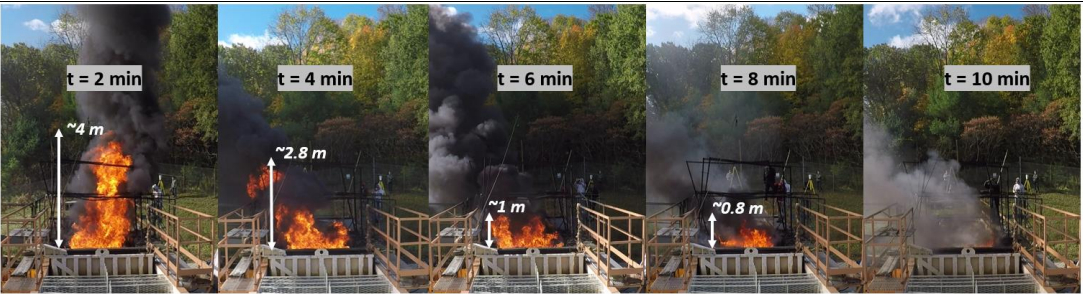
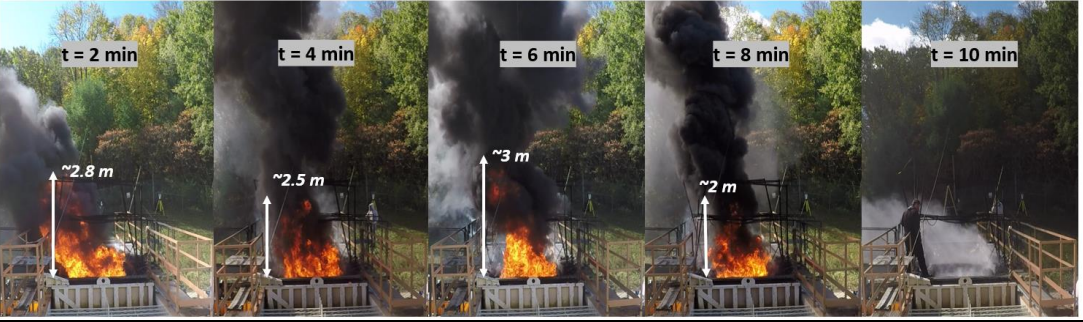
12	Oct 1, 2020 Fuel: HOOPS		Bimetal FR – Wave 1 	
13	Oct 2, 2020 Rainy Fuel: HOOPS	8	Bimetal FR – Wave 1 	
14	Oct 5, 2020 Fuel: 25% Emulsion	2.5	Baseline	



15	Oct 5, 2020 Fuel: 25% Emulsion	2.8	Baseline – Wave 3	
16	Oct 5, 2020 Fuel: 25% Emulsion	2.5	Baseline – Wave 4	
17	Oct 5, 2020 Fuel: 25% Emulsion	2.5	Baseline wave 5	
18	Oct 6, 2020 Fuel: 25% Emulsion		Baseline	

19	Oct 6, 2020 Fuel: Bunker	1	Baseline	  
20	Oct 7, 2020 Fuel: Bunker		Baseline – Wave 3	  
21	Oct 7, 2020 Fuel: Bunker	1	Bimetals FR – Wave 3 	   



22	Oct 7, 2020 Fuel: Bunker		 <p>Bimetal FR</p>	 <p>t = 2 min ~4 m</p> <p>t = 4 min ~5 m</p> <p>t = 6 min</p>
23	Oct 8, 2020 Fuel: 25% Emulsion	4	 <p>Bimetal FR</p>	 <p>t = 2 min ~4 m</p> <p>t = 4 min ~2.8 m</p> <p>t = 6 min ~1 m</p> <p>t = 8 min ~0.8 m</p> <p>t = 10 min</p>
24	Oct 8, 2020 25% Emulsion		Baseline	 <p>t = 2 min ~2.8 m</p> <p>t = 4 min ~2.5 m</p> <p>t = 6 min ~3 m</p> <p>t = 8 min ~2 m</p> <p>t = 10 min</p>

## APPENDIX – E (Repository)

Efforts were made in constructing an online repository for WPI-BSEE projects, instruments, and research applications that are done in the past. Most of the information currently was passed down from person to person or by personal documents used by individuals. There was a need for centralizing information, and transparency for knowledge transfer. The repository in construction was built as a starting point for anyone looking to find information on specific topics with case studies and real-time application examples that were previously done as a part of research at WPI. The repository site is an ongoing effort, last updated on *May 11<sup>th</sup>, 2020*. Below attached is the link to redirect to the live online repository.

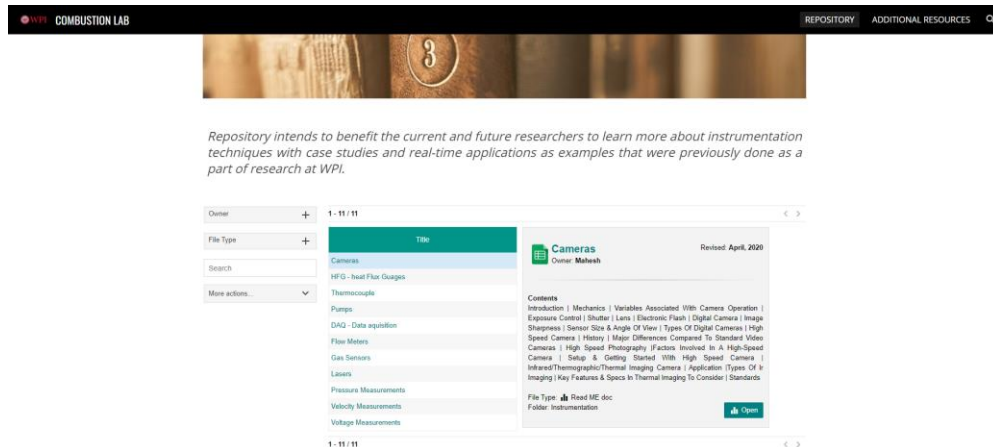
<https://sites.google.com/view/combustion-lab/repository>

The projects that being analyzed were first chosen, following which the instrumentation used in all of the projects were summarized and sectioned into categories as follows,

- |                     |                     |
|---------------------|---------------------|
| 1. Camera           | 7. Lasers           |
| 2. Thermocouple     | 8. Pressure         |
| 3. Pumps            | 9. Velocity         |
| 4. Data Acquisition | 10. Heat Flux Gauge |
| 5. Flow Meters      | 11. Voltage         |
| 6. Gas Sensors      |                     |

An introductory literature review (*READ ME doc*) was documented to discuss a broader perspective of the topics categorized above. Further, these topics were provided and linked with an additional set of case study documents, consisting of examples of previous research using these instrumentation techniques wherever further understanding was necessary of its applications and implementations in the research scenario for most of the topics.

Fig. 1 shows the overview of the repository site online (alpha version). It can be seen that eleven topics are listed in a table format with filters in place for ease of selection. Each of the documents listed gives a content overview, type of file, and the editor to review information first hand. The interface also allows filtering the contents of the table by project lead (owner), the type of file (readme Doc, Final report, examples, etc.), and by specific documents required in the search bar for navigation. More topics and content will be added for selection in the future for references.



**Figure1 - Overview of the interface for the repository online with the topics covered (last updated – May 2020)**

The primary objective of the repository was to benefit the present and future researchers to learn about previous projects and instrumentation techniques used for the specific experiments, fundamentally a local library database unique to research efforts at combustion lab, WPI. The site online is still in its infant alpha version, and the project will be continued as an ongoing project. An effort in continuous contribution towards the repository from present and incoming researchers will help in preserving the research efforts done in the past.